

1  
2  
3  
4  
5  
6  
7  
8  
9  
10  
11  
12  
13  
14  
15  
16  
17  
18  
19  
20  
21  
22  
23  
24  
25  
26  
27  
28  
29  
30  
31  
32  
33  
34  
35  
36  
37  
38  
39  
40  
41  
42  
43  
44  
45  
46  
47  
48  
49  
50  
51  
52  
53  
54  
55  
56  
57  
58  
59  
60

## New Generation Cadmium-Free Quantum Dots for Biophotonics and Nanomedicine

Gaixia Xu<sup>1,5†</sup>, Shuwen Zeng<sup>2,5†</sup>, Butian Zhang<sup>2</sup>, Mark T. Swihart<sup>3\*</sup>,  
Ken-Tye Yong<sup>2\*</sup> and Paras N. Prasad<sup>4\*</sup>

<sup>1</sup>*Key Laboratory of Optoelectronics Devices and Systems of Ministry of Education/Guangdong Province, College of Optoelectronic Engineering, Shenzhen University, Shenzhen, P. R. China*

<sup>2</sup>*School of Electrical and Electronic Engineering, Nanyang Technological University, Singapore 639798, Singapore*

<sup>3</sup>*Department of Chemical and Biological Engineering, State University of New York at Buffalo, Buffalo, New York 14260, United States*

<sup>4</sup>*Institute for Lasers, Photonics, and Biophotonics and Department of Chemistry, University at Buffalo, State University of New York, Buffalo, NY 14260, USA*

<sup>5</sup>*CINTRA CNRS/NTU/THALES, UMI 3288, Research Techno Plaza, 50 Nanyang Drive, Border X Block, Singapore 637553, Singapore*

†These authors equally share the first authorship

\*Corresponding authors: Mark T. Swihart ([swihart@buffalo.edu](mailto:swihart@buffalo.edu)), Ken-Tye Yong ([kt Yong@ntu.edu.sg](mailto:kt Yong@ntu.edu.sg)) and Paras N. Prasad ([pnprasad@buffalo.edu](mailto:pnprasad@buffalo.edu))

## Abstract

This review summarizes recent progress in the design and applications of cadmium-free quantum dots (Cd-free QDs), with an emphasis on their role in biophotonics and nanomedicine. We firstly present the features of Cd-free QDs and describe the physics and emergent optical properties of various types of Cd-free QDs whose applications are discussed in subsequent sections. Section 3 discusses selected specific QD systems, while Section 4 covers preparation of these Cd-free QDs in a form useful for biological applications, including recent advances in achieving high photoluminescence quantum yield (PL QY) and tunability of emission color. Section 5 summarizes biophotonic applications of Cd-free QDs in optical imaging, photoacoustic imaging, sensing, optical tracking and photothermal therapy. Section 6 discusses recent progress in the use of Cd-free QDs for nanomedicine applications such as drug/gene delivery, protein/peptide delivery, image-guided surgery, diagnostics and medical devices. Section 7 focuses on the pharmacokinetics and biodistribution of Cd-free QDs. Section 8 summarizes recent studies on the *in vitro* and *in vivo* toxicity of Cd-free QDs. Finally, Section 9 provides perspectives on the overall current status, challenges, and future directions in this field.

## Table of Contents

|  |    |
|--|----|
| Table of Contents.....   | 3  |
| 1.0 Introduction and Background .....  | 5  |
| 1.1 Introduction to Quantum Dots .....   | 5  |
| 1.2 Biophotonics Applications.....   | 8  |
| 1.3 Applications in Nanomedicine.....  | 9  |
| 1.4 Pharmacokinetics and Biodistribution .....                                       | 11 |
| 1.5 <i>In vitro</i> and <i>in vivo</i> Toxicity.....                                 | 12 |
| 1.6 Review Outline .....   | 13 |
| 2.0 Features of Cadmium-Free Quantum Dots .....                                      | 15 |
| 2.1 Quantum Confinement Effects .....  | 15 |
| 2.2 Core/Shell Architecture .....  | 17 |
| 2.3 Tunability in the Biological Transparency Window.....                            | 22 |
| 2.4 Opportunity to Introduce Tunable Plasmonic Features .....                        | 25 |
| 2.5 Doping to Achieve Enhanced Emission from Dopant States .....                     | 26 |
| 2.6 Magnetic Doping to Introduce Magnetic Imaging Capability.....                    | 29 |
| 2.7 Relationship of Quantum Dot Physics, Properties, and Applications .....          | 32 |
| 3.0 Selected Quantum Dot Systems.....  | 34 |
| 3.1 InP and InP/ZnS Quantum Dots .....   | 36 |
| 3.2 CuInS <sub>2</sub> and CuInS <sub>2</sub> /ZnS Quantum Dots .....                | 40 |
| 3.3 Ag <sub>2</sub> S and Ag <sub>2</sub> Se Quantum Dots.....                       | 44 |
| 3.4 ZnS-AgInS <sub>2</sub> (ZAIS) Quantum Dots.....                                  | 48 |
| 3.5 Silicon Quantum Dots.....  | 49 |
| 3.6 Graphene Quantum Dots.....   | 51 |
| 3.7 Doped ZnS/ZnSe Quantum Dots .....  | 54 |
| 3.8 Plasmonic Copper Chalcogenide Quantum Dots.....                                  | 58 |
| 4.0. Preparation of Biocompatible Cadmium-Free Quantum Dots.....                     | 64 |
| 4.1. InP and InP/ZnS Quantum Dots .....  | 64 |
| 4.2. CuInS <sub>2</sub> , CuInS <sub>2</sub> /ZnS and CuInZnS/ZnS Quantum Dots ..... | 66 |
| 4.3. Ag <sub>2</sub> S and Ag <sub>2</sub> Se Quantum Dots.....                      | 70 |
| 4.4. ZnS-AgInS <sub>2</sub> (ZAIS) Quantum Dots.....                                 | 79 |
| 4.5. ZnSe/InP/ZnS Quantum Dots .....   | 81 |

|    |  |     |
|----|--|-----|
| 1  |  |     |
| 2  |  |     |
| 3  |  |     |
| 4  | 4.6. InAs/InP/ZnSe Quantum Dots .....  | 82  |
| 5  | 4.7. Silicon Quantum Dots.....   | 83  |
| 6  | 4.8. ZnO Quantum Dots.....   | 86  |
| 7  | 4.9. WS <sub>2</sub> Quantum Dots.....   | 87  |
| 8  | 4.10. Graphene Quantum Dots.....   | 88  |
| 9  | 4.11. Doped ZnS/ZnSe Quantum Dots .....  | 93  |
| 10 | 4.12. Plasmonic Copper Chalcogenide Quantum Dots.....                              | 95  |
| 11 | 5.0. Biophotonic Applications .....  | 99  |
| 12 | 5.1. Optical Imaging .....   | 102 |
| 13 | 5.2. Photoacoustic Imaging.....  | 117 |
| 14 | 5.3. Biosensing.....   | 123 |
| 15 | 5.4. Optical Tracking .....  | 131 |
| 16 | 5.5. Photothermal Therapy.....   | 139 |
| 17 | 5.6. Multimodal Imaging .....  | 145 |
| 18 | 6.0. Nanomedicine Applications.....  | 152 |
| 19 | 6.1. Drug Delivery .....   | 157 |
| 20 | 6.2. Gene Delivery .....   | 165 |
| 21 | 6.3. Protein and Peptide Delivery .....  | 168 |
| 22 | 6.4. Cancer Nanotechnology.....  | 169 |
| 23 | 6.5. Imaging Guided Surgery.....   | 175 |
| 24 | 6.6. <i>In vitro</i> Diagnostics.....  | 179 |
| 25 | 6.7. Infectious Diseases.....  | 185 |
| 26 | 7.0. Pharmacokinetics and Biodistribution of Cadmium-Free Quantum Dots .....       | 190 |
| 27 | 7.1 Biodistribution of Non-targeted Cadmium-Free Quantum Dots .....                | 195 |
| 28 | 7.2 Biodistribution of Targeted Cadmium-Free Quantum Dots .....                    | 203 |
| 29 | 8.0. <i>In vitro</i> and <i>in vivo</i> Toxicity of Cadmium-Free Quantum Dots..... | 208 |
| 30 | 8.1 <i>In vitro</i> Toxicity .....   | 214 |
| 31 | 8.2 <i>In vivo</i> Toxicity .....  | 220 |
| 32 | 8.3 Mechanism of Toxicity.....   | 224 |
| 33 | 9.0. Concluding Remarks and Perspectives.....                                      | 231 |
| 34 | 10.0 References.....   | 243 |
| 35 |  |     |
| 36 |  |     |
| 37 |  |     |
| 38 |  |     |
| 39 |  |     |
| 40 |  |     |
| 41 |  |     |
| 42 |  |     |
| 43 |  |     |
| 44 |  |     |
| 45 |  |     |
| 46 |  |     |
| 47 |  |     |
| 48 |  |     |
| 49 |  |     |
| 50 |  |     |
| 51 |  |     |
| 52 |  |     |
| 53 |  |     |
| 54 |  |     |
| 55 |  |     |
| 56 |  |     |
| 57 |  |     |
| 58 |  |     |
| 59 |  |     |
| 60 |  |     |

## 1.0 Introduction and Background

### 1.1 Introduction to Quantum Dots

Quantum dots (QDs) are semiconductor nanocrystals (typically 2-10 nm in diameter) that exhibit size-dependent optical properties, including absorbance and photoluminescence (PL). They have proven useful in many biophotonic and nanomedical applications including imaging and sensing.<sup>1</sup> A single QD typically contains hundreds to thousands of atoms of group II-VI elements (*e.g.* CdTe, CdSe, CdS, ZnS, ZnSe, or ZnTe), group III-V elements (*e.g.* InP or InAs), group I-III-VI<sub>2</sub> elements (*e.g.* CuInS<sub>2</sub> or AgInS<sub>2</sub>), group IV-VI elements (*e.g.* PbSe, PbS, or PbTe) or group IV elements (*e.g.* Si, C, or Ge). QDs are large in comparison to conventional organic dyes, but can be comparable in size to fluorescent proteins and other large biomolecules. QDs have unique advantages relative to organic dyes as luminescent labels for biological applications.<sup>2,3</sup> Specifically, QDs of different sizes or compositions can all be excited by a single light source, to produce separate emission colors over a wide spectral range with minimal spectral overlap, making them particularly attractive for multiplex imaging.<sup>4</sup> Also, unlike organic dyes, most QDs are highly resistant to photobleaching, which allows them to be used for long term *in vitro* and *in vivo* imaging.<sup>5-7</sup> More importantly, these nanocrystals can be engineered to emit at wavelengths ranging from 450 to 1500 nm by tailoring their size, shape, and composition.<sup>8-11</sup> QDs can be prepared as dispersions in either organic or aqueous media, depending on their intended application. The basic features of QDs are described in greater detail in section 2 of this review.

For biological applications, QDs must be water-dispersible. When QDs are initially synthesized as colloidal dispersions in a nonpolar organic media, surface modification is required to render them dispersible in aqueous biological media. Ligand exchange and encapsulation of

1  
2  
3 QDs using hydrophilic/amphiphilic molecules or polymers are common strategies for preparing  
4 water-dispersible QDs from hydrophobic QDs.<sup>12-15</sup> The QDs can then be functionalized with a  
5 variety of biomolecules (*e.g.* proteins, antibodies, peptides, DNA, and vitamins) through  
6 established conjugation techniques. The large surface area of each QD, relative to organic dyes  
7 and other small molecules, provides many surface attachment sites for conjugation.<sup>16-18</sup> This  
8 opens up possibilities for multivalent binding via multiple targeting moieties. Flexibility in  
9 surface chemistry as well as in emission wavelength of bioconjugated QDs enables their use as  
10 nanoprobe or traceable nanocarriers for broad applications in biophotonics and nanomedicine,  
11 including near-IR deep tissue imaging (*e.g.* 700-900 nm),<sup>19,20</sup> PL imaging in the second near-IR  
12 window (*e.g.* 1000-1400 nm),<sup>21,22</sup> single cell detection,<sup>23</sup> and controlled release of drugs.<sup>24-26</sup>  
13  
14 However, to date, the majority of QD-related research in biology and medicine has employed  
15 Cd-based QDs including CdSe, CdTe, CdS, and CdTe/CdSe core/shell QDs, often with  
16 additional protective shells of ZnS and/or ZnSe.<sup>27,28</sup> The popularity of these Cd-based QDs is  
17 primarily due to their ease of synthesis using readily available precursors and straightforward  
18 solution phase synthesis methods. Protocols for preparing and using these QDs have been  
19 somewhat standardized. They are also readily available commercially in formats optimized for  
20 specific biological assays and applications.  
21  
22

23  
24  
25 With the rapidly developing biological applications of Cd-based QDs, their potential toxicity  
26 has become a subject of serious discussion and debate. Some studies have demonstrated that Cd-  
27 based QDs can degrade in a biological environment, releasing highly cytotoxic Cd<sup>2+</sup> ions.<sup>29,30</sup>  
28 Other studies suggest that the observed degradation results from the poor quality (*i.e.* insufficient  
29 stability or encapsulation) of the QDs employed.<sup>31,32</sup> Researchers ranging from biomedical  
30 engineers to clinicians have raised doubts about the possible use of Cd-based QDs for clinical  
31  
32  
33  
34  
35  
36  
37  
38  
39  
40  
41  
42  
43  
44  
45  
46  
47  
48  
49  
50  
51  
52  
53  
54  
55  
56  
57  
58  
59  
60

1  
2  
3 applications such as *in vivo* diagnostics and surgery, due to toxicity concerns associated with  
4 their Cd content. At present, two approaches are being pursued to address these concerns. The  
5 first approach involves the use of one or more biocompatible and long-lasting polymeric layers  
6 to encapsulate the QDs and prevent their breakdown *in vivo*.<sup>33-35</sup> The second approach, which is  
7 arguably more challenging and time consuming as it requires advances in material science and  
8 nanochemistry, is to create Cd-free QDs with performance comparable to or even better than  
9 existing Cd-based QDs.<sup>36-38</sup> Currently, many research groups are developing and applying  
10 nanochemistry methods to design and fabricate Cd-free QDs with tunable emission color, and are  
11 testing them in applications ranging from diagnostics, to imaging, to traceable drug delivery.  
12  
13 Nonetheless, matching the high brightness, narrow PL emission spectrum, and high PL quantum  
14 yield of Cd-based QDs remains a challenge. Even when optical properties are comparable, Cd-  
15 based QDs have the benefits of longer history and the resulting better-developed encapsulation  
16 and surface functionalization strategies and better optimized protocols for specific applications.  
17  
18  
19  
20  
21  
22  
23  
24  
25  
26  
27  
28  
29  
30  
31  
32  
33

34 With advances in solution phase synthesis methods over the past few years, a variety of Cd-  
35 free QDs have been prepared from materials including indium phosphide (InP),<sup>39-42</sup> copper  
36 indium sulfide (CuInS<sub>2</sub>),<sup>36,43,44</sup> silver indium sulfide (AgInS<sub>2</sub>),<sup>45,46</sup> silver sulfide (Ag<sub>2</sub>S),<sup>21,47</sup>  
37 doped Zn chalcogenides,<sup>48,49</sup> graphene,<sup>50-52</sup> and silicon.<sup>53,54</sup> These QDs share many of the  
38 advantages of conventional Cd-based QDs with respect to their optical properties, colloidal  
39 stability, PL stability, and surface chemistry. The QD research community has begun to use these  
40 Cd-free QDs for biological applications and evaluate their potential in numerous *in vitro* and *in*  
41 *vivo* models such as cultured cells, tissues, and small animals. However, additional effort will be  
42 required to improve the performance of Cd-free QDs in biomedical applications and to optimize  
43 them for specific applications. This will facilitate their adoption by mainstream biomedical  
44  
45  
46  
47  
48  
49  
50  
51  
52  
53  
54  
55  
56  
57  
58  
59  
60

1  
2  
3 researchers and, ultimately, clinicians. The synthesis of QDs and their preparation for biological  
4 applications are addressed in sections 3 and 4 of this review.  
5  
6

## 7 8 **1.2 Biophotonics Applications** 9

10 Biophotonics is a multidisciplinary research frontier<sup>2</sup> that employs light for medical  
11 diagnostics,<sup>55</sup> bioimaging,<sup>56</sup> biosensing,<sup>57</sup> laser tissue engineering,<sup>58</sup> and light activated therapy.<sup>59</sup>  
12 It involves the study of light activated processes, from molecular, to cellular, to tissue levels. The  
13 unique optical properties of QDs make them useful as optical probes or optically trackable  
14 biomolecule carriers for *in vitro* and *in vivo* studies.<sup>60,61</sup> By conjugating appropriate functional  
15 biomolecules onto their surface, one can use QDs to target specific sites *in vitro* and *in vivo*.<sup>62-64</sup>  
16 For example, bioconjugated QDs have been applied in targeted cell labeling,<sup>65,66</sup> tissue  
17 imaging,<sup>6,67</sup> *in vivo* tumor detection,<sup>36,68</sup> photodynamic therapy,<sup>69,70</sup> sensing of biomolecules,<sup>71</sup>  
18 monitoring the biodistribution of drugs,<sup>25</sup> and drug delivery.<sup>72</sup> Moreover, bioconjugated QDs can  
19 be used with a wide variety of optical imaging techniques such as near field microscopy,  
20 confocal microscopy, multiphoton microscopy, and CARS microscopy, to study structure and  
21 dynamics from cellular to tissue levels.<sup>6,73-76</sup> QDs have also been used in multimodal imaging  
22 studies to derive fundamental molecular-level insights into biological processes such as cell  
23 replication, transcription, translation and apoptosis.<sup>31,77,78</sup> To facilitate the use of QDs for  
24 multimodal imaging, QDs can be integrated with other contrast agents (*e.g.* gold nanoparticles,  
25 Raman tags, gadolinium chelates, or <sup>125</sup>I radioactive labels). These probes have been engineered  
26 and studied for imaging of cells and small animals using two or more imaging modalities.<sup>79-83</sup> In  
27 studies to date, *in vitro* and *in vivo* biophotonic imaging and sensing studies using QDs have  
28 aimed to create an understanding of cell localization and interaction, biomolecule and drug  
29 biodistribution, mechanism of drug action, and real time monitoring of disease progression or  
30  
31  
32  
33  
34  
35  
36  
37  
38  
39  
40  
41  
42  
43  
44  
45  
46  
47  
48  
49  
50  
51  
52  
53  
54  
55  
56  
57  
58  
59  
60

1  
2  
3 response to a therapy. The flexibility and versatility of QDs will surely provide keys to answer  
4 critical biological and medical questions and thereupon improve diagnosis and treatment of  
5 human diseases. Applications of QDs in biophotonics provide unprecedented opportunities for  
6 resolving many current challenges in disease theranostics. Section 5 of this review focuses on  
7 applications of Cd-free QDs in biophotonics.  
8  
9

### 10 11 12 **1.3 Applications in Nanomedicine** 13 14

15  
16 Nanomedicine employs specifically designed nanoplatfoms to achieve minimally or non-  
17 invasive diagnosis, targeted and controlled delivery of therapeutics, improved efficacy of an  
18 existing therapy, real-time monitoring of a treatment, or evaluation of *in vivo*  
19 pharmacokinetics.<sup>3,84-88</sup> QDs have been used as nanoplatfoms for targeted delivery of  
20 pharmaceutical, therapeutic, and diagnostic nanoprobcs. For example, identifying specific targets  
21 (*e.g.*, endothelial cells, tumor cells, or tumor neovasculature) using an appropriate choice of QD-  
22 based nanoprobe can guide site-specific therapy.<sup>89-92</sup> *In vivo* diagnosis using biofunctionalized  
23 QDs also offers the benefit of combining different functions into a single nanoparticle (NP)  
24 platform. For example, conjugating or co-encapsulating drugs and MRI or PET imaging contrast  
25 agents with QDs allows detailed disease profiling based on molecular, structural, and  
26 morphological changes as a disease evolves.<sup>93-96</sup> Specific targeting of QDs to the disease site  
27 allows use of a lower dose of QD probes for diagnosis, and thereby minimizes the potential  
28 toxicity of the designed nanocarrier. QDs are expected to contribute to development of  
29 nanomedicine *via* design of new therapeutic modalities and by increasing the effectiveness of  
30 existing therapies. For example, QD nanoformulations can be integrated with magnetic therapy  
31 using magnetic NPs, and with photothermal therapy using metallic NPs.<sup>94,97,98</sup> As an example of  
32 improving the efficacy of an existing therapy, QDs can be designed as nanocarriers to alter the  
33  
34  
35  
36  
37  
38  
39  
40  
41  
42  
43  
44  
45  
46  
47  
48  
49  
50  
51  
52  
53  
54  
55  
56  
57  
58  
59  
60

1  
2  
3 biodistribution and circulation of a hydrophobic drug in order to localize a large concentration of  
4 the drug at the disease site. Additional benefits offered by QD nanocarriers include controlled  
5 and sustained release of a drug.<sup>25,99,100</sup> The controlled release of drugs from QD nanocarriers can  
6 be achieved *via* external stimulation using light, magnetic fields, heat, or radio-frequency  
7 stimulation.  
8  
9

10  
11  
12  
13  
14  
15 Theranostics is an emerging paradigm that combines diagnosis with therapy to enable a see,  
16 treat, and see therapeutic modality. This can enable a clinician to follow a medical treatment,  
17 surgery, or other procedure in real time, using the same material or device for both diagnosis and  
18 therapy. Nanoparticle technology allows creation of new theranostics in a single nanoformulation.  
19 QDs with their size- and compositionally-tunable emission and ease of surface functionalization  
20 can provide a useful platform for nanotheranostics. The optical and electronic properties of QDs  
21 provide a basis for multiplexed imaging and sensing, while surface functionalization and  
22 encapsulation enable them to carry therapeutic payloads.  
23  
24  
25  
26  
27  
28  
29  
30  
31  
32  
33

34 The Cd-free QDs covered in this review are particularly suitable for theranostics. First,  
35 without the toxicity concerns associated with Cd, they can more readily be considered for *in vivo*  
36 applications. Many of the materials covered in this review are ternary semiconductors in which  
37 compositional variation can provide wide spectral tuning of optical properties, providing  
38 emission in the near IR range to enable deep tissue imaging and optical tracking of drug or gene  
39 delivery. In some cases, their optoelectronic properties can be exploited for biosensing and  
40 functional imaging. Magnetic impurities can be introduced to provide contrast for magnetic  
41 resonance imaging. Their excitation dynamics can also be manipulated for use in light-induced  
42 therapies. Ease of surface functionalization enables conjugation with various therapeutic  
43 payloads such as drugs, genes, and RNA. In addition, a therapeutic agent can be coencapsulated  
44  
45  
46  
47  
48  
49  
50  
51  
52  
53  
54  
55  
56  
57  
58  
59  
60

1  
2  
3 with QDs in a biocompatible and biodegradable shell. Section 6 of this review discusses  
4  
5 nanomedical applications of Cd-free QDs in greater detail.  
6  
7

#### 8 **1.4 Pharmacokinetics and Biodistribution**

9

10 The pattern of distribution among organs over time, *i.e.* the biodistribution, is a key  
11 characteristic of any nanoparticle or drug formulation. Biodistribution measurements provide key  
12 information on the accumulation of a NP formulation at the targeted site and in other sites where  
13 the accumulation may not be desirable. Several factors contribute to the specific localization of  
14 NPs in different organs, including the hydrodynamic size of NPs, plasma protein binding to NPs,  
15 hydrophobicity of the NPs, the ligands or polymers used to stabilize the NPs in the biological  
16 environment, and the types of biomolecules conjugated to the surface of NPs. Most often,  
17 biodistribution studies are carried out using radioactively or fluorescently labeled NPs that are  
18 injected into animals. Subsequently, the animals are sacrificed, and various organs are harvested  
19 and analyzed for the localization of the NPs by fluorescence, magnetic resonance, and/or nuclear  
20 imaging (*e.g.* PET and SPECT). Bioconjugation and size control of QDs provide the ability to  
21 create desired biodistribution patterns for specific applications using both active and passive  
22 targeting approaches. More importantly, in many cases the bright PL of QDs and the ability to  
23 combine them with other contrast agents can enable *in vivo* multimodal imaging in real time to  
24 monitor the biodistribution pattern. Such real-time monitoring allows rapid optimization of  
25 delivery and targeting strategies, compared to *ex vivo* measurements and eliminates the animal-  
26 to-animal variability associated with sacrificing animals for *ex vivo* measurements at different  
27 time points. We discuss the details of biodistribution studies of Cd-free QDs in section 7 of this  
28 review.  
29  
30  
31  
32  
33  
34  
35  
36  
37  
38  
39  
40  
41  
42  
43  
44  
45  
46  
47  
48  
49  
50  
51  
52  
53  
54  
55  
56  
57  
58  
59  
60

### 1.5 *In vitro and in vivo Toxicity*

Toxicity of QDs is a function of many factors including not only their composition, but also their size, shape, encapsulation, and surface functionalization. Toxicity studies assess the response of specific cell types, tissues, organs, and organisms to varying doses of a given QD formulation. In the context of this review, we are concerned with the toxicity of QDs used in biophotonics and nanomedicine. Noting the importance of understanding the potential toxicity of QDs, many research teams worldwide have been devoting effort to elucidating underlying mechanisms of QD toxicity *in vitro* and *in vivo*, and many articles are being published on this subject.<sup>31</sup> In this review, we focus only on toxicity studies of Cd-free QDs. The toxicity of QDs is of two main types: (1) that directly associated with the intact QDs themselves and (2) toxicity associated with their chemical constituents. In the first case, the physical and surface properties of the QDs generate responses that can depend upon size, shape, surface charge, and surface coatings. Because the surface-to-volume ratio in NPs is very large, surface-initiated processes are significantly enhanced compared to larger structures. Their small size also alters immune-system response. Thus, size and shape play critical roles in determining the intact particle toxicity. In the second case, the toxicity is generated by the chemical constituents of the QDs. For example, the release of Cd<sup>2+</sup> ions from CdSe or CdTe QDs can cause significant damage to cells and tissues. Because the toxicity of QDs can have multiple origins and mechanisms and depends on multiple physico-chemical properties, and also because even within one formulation QDs are not all identical, assessing their toxicity can be much more complex than assessing the toxicity of a small molecule. Testing the toxicity for every possible combination of size, shape, composition, and surface modification of a given type of QD is generally not possible, and this can make

1  
2  
3 guaranteeing the biocompatibility of a QD formulation difficult. Toxicity of Cd-free QDs is  
4  
5 discussed in section 8 of this review.  
6  
7

### 8 **1.6 Review Outline**

9

10  
11 This review summarizes recent progress in the design and applications of Cd-free QDs, with  
12 an emphasis on their role in biophotonics and nanomedicine (**Figure 1**). In addition, we discuss  
13 current challenges and opportunities faced in using these QDs for *in vitro* and *in vivo*  
14 applications. Section 2 presents features of Cd-free QDs, describing the physics and emergent  
15 optical properties of various types of Cd-free QDs whose applications are discussed in  
16 subsequent sections. Section 3 discusses specific QD systems, while Section 4 covers preparation  
17 of these Cd-free QDs in a form useful for biological applications. It discusses recent advances in  
18 achieving high PL QY and tunability of emission color, along with stable dispersion in biological  
19 media. Section 5 presents applications of Cd-free QDs for biophotonics, summarizing recent  
20 advances in biophotonic applications of Cd-free QDs in optical imaging, photoacoustic imaging,  
21 sensing, optical tracking, photothermal therapy, and multimodal imaging. Section 6 discusses  
22 recent progress in the use of Cd-free QDs for nanomedicine applications such as drug delivery,  
23 gene delivery, protein and peptide delivery, cancer nanotechnology, image-guided surgery,  
24 diagnostics, medical devices, and drug screening. Section 7 focuses on the pharmacokinetics and  
25 biodistribution of Cd-free QDs. Section 8 summarizes recent studies on the *in vitro* and *in vivo*  
26 toxicity of Cd-free QDs. Finally, Section 9 concludes by providing perspectives on the overall  
27 current status, challenges, and future directions in this field.  
28  
29  
30  
31  
32  
33  
34  
35  
36  
37  
38  
39  
40  
41  
42  
43  
44  
45  
46  
47  
48  
49  
50  
51  
52  
53  
54  
55  
56  
57  
58  
59  
60

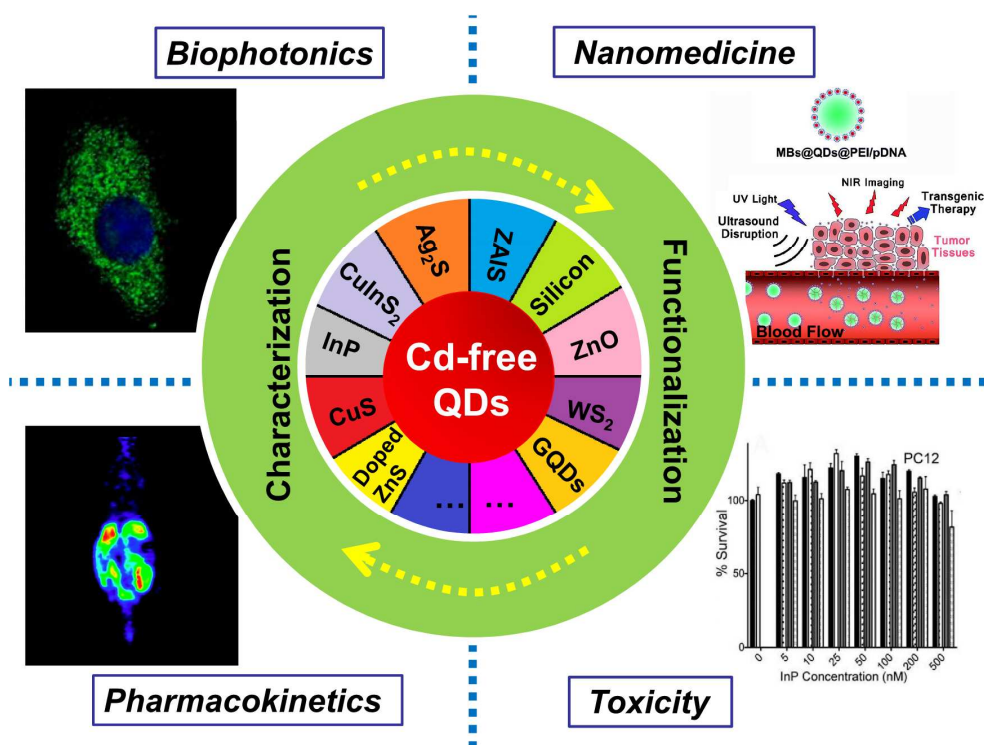


**Figure 1.** Cd-free QDs discussed in this review and representative applications in biophotonics and nanomedicine.

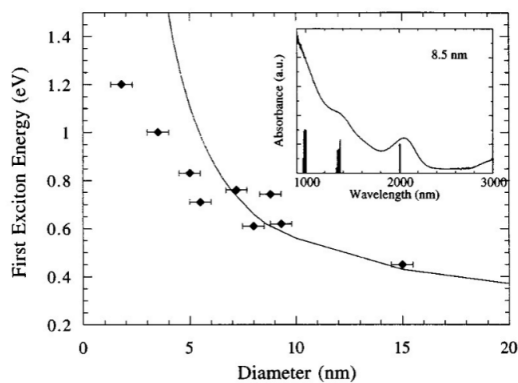
## 2.0 Features of Cadmium-Free Quantum Dots

### 2.1 Quantum Confinement Effects

QDs are semiconductor nanocrystals whose size, in all three dimensions, is comparable to the exciton Bohr radius of the material from which they are prepared.<sup>1</sup> The exciton Bohr radius ( $a_B$ ) is the average separation of the excited electron and hole that make up an exciton in a bulk semiconductor. In analogy to the Bohr model of the hydrogen atom, it can be written as:

$$a_B = \frac{\hbar^2 \varepsilon}{e^2} \left( \frac{1}{m_e} + \frac{1}{m_h} \right) \quad (1)$$

where  $\varepsilon$  is the dielectric constant of the semiconductor,  $\hbar$  is the reduced Planck constant,  $e$  is the charge of an electron,  $m_e$  is the effective mass of the electron, and  $m_h$  is the effective mass of the hole. Because the dielectric constant and effective masses of the hole and electron are material-dependent, the exciton Bohr radii for different semiconductors vary substantially (e.g., 2.3 nm for ZnO,<sup>101</sup> 4.1 nm for CuInS<sub>2</sub>,<sup>102</sup> 18 nm for PbS,<sup>103</sup> and 46 nm for PbSe<sup>104</sup>). When the radius of a semiconductor nanocrystal approaches the exciton Bohr radius, the motions of the electron and hole are confined, within the particle, to dimensions smaller than in the bulk.<sup>105</sup> The electronic structure and optical properties of QDs differ significantly from their bulk counterparts due to this quantum confinement effect (**Figure 2**).<sup>104,106-109</sup>



1  
2  
3 **Figure 2** Measured (symbols) and calculated (line) energies of the lowest energy exciton for  
4 PbSe QDs of varying size. The inset shows the measured absorption spectrum (line) and  
5  
6  
7  
8  
9  
10  
11  
12  
13  
14  
15  
16  
17  
18  
19  
20  
21  
22  
23  
24  
25  
26  
27  
28  
29  
30  
31  
32  
33  
34  
35  
36  
37  
38  
39  
40  
41  
42  
43  
44  
45  
46  
47  
48  
49  
50  
51  
52  
53  
54  
55  
56  
57  
58  
59  
60  
from Lipovskii *et al.*<sup>104</sup> Copyright 1997 AIP Publishing LLC.

The quasi-continuous states (energy bands) of the bulk semiconductor evolve into discrete levels in QDs, corresponding to hybridization of a finite number of atomic orbitals.<sup>110</sup> The energy gap between the bottom of the conduction band and the top of the valence band in QDs expands with decreasing size.<sup>111</sup> This increase in energy associated with exciton generation/recombination produces a blue-shift of both absorbance and PL spectra with decreasing size. Because of the atom-like discrete structure of electronic states under strong quantum confinement, QDs are sometimes described as artificial atoms, with their discrete energy levels interpreted in a manner analogous to the discrete energy levels of an atom. The strongly size-tunable properties of QDs make them very useful for biomedical applications. Related properties of QDs, such as size-dependent Stokes shift, long lifetime of band-edge luminescence, and magnetic field-induced lifetime shortening can also be exploited in some biophotonic and nanomedicine applications. Factors such as QD shape, lattice asymmetry, electron-hole exchange interaction, impurities, defects, and external fields affect these properties,<sup>112-114</sup> as well as the fine structure of their absorbance and PL spectra, especially in the strong confinement regime, in which the QD radius is significantly smaller than the exciton Bohr radius.

Cadmium-free QDs typically range from 1 to 10 nm in diameter. The size dependence of optical and electronic properties is similar to that of Cd-based QDs, but varies in detail due to

1  
2  
3 differences in bulk band structure, electron and hole effective masses, and other factors. The PL  
4 wavelength in Cd-free QDs can be tuned from the ultraviolet to mid-IR region by changing QD  
5 composition, size, and shape. Generally, the QD composition sets the range of wavelengths that  
6 are accessible, because quantum confinement can only produce a blue-shift in the PL relative to  
7 the optical band gap energy of the bulk material. For a particular composition, the degree to  
8 which the PL emission can be tuned depends upon the Bohr radius of the material and the range  
9 of sizes that can be practically produced. Manipulating the composition and shape of the QDs  
10 requires control of the chemistry of QD synthesis and capping. For most Cd-free QDs, as for Cd-  
11 based QDs, the PL lifetimes and two-photon absorbance cross-sections are much greater than  
12 those of the traditional organic dyes.<sup>115-117</sup> These features make QDs very useful for two-photon  
13 imaging of deep tissues, with reduced autofluorescence background.<sup>6,118,119</sup> The PL lifetime and  
14 two-photon cross-section, like the PL spectrum, vary with composition, size, and shape.

## 31 **2.2 Core/Shell Architectures:**

32  
33 Core/shell QD structures consist of a QD core of one semiconductor material coated by one  
34 or more shells of different composition. These have several advantages relative to single  
35 composition (core-only) QDs. Most importantly, surface-related quenching by surface defects  
36 and by solvent phonon-induced relaxation are minimized by reducing interaction between the  
37 exciton and the outer surface of the nanocrystal. In addition, the various possible relationships  
38 between energy levels in the core and shell provide control of the PL wavelength, lifetime, and  
39 QY that is not available in single-component QDs.

40  
41 In general, core/shell QDs can be divided to three types based upon the band alignment of  
42 valence and conduction bands between their constituent materials (*i.e.*, type-I, type-II and quasi  
43 type-II, **Figure 3**).<sup>120,121</sup> Type-I (*e.g.*, InP/ZnS and CdSe/ZnS) and type-II core/shell QDs (*e.g.*,

1  
2  
3 CdTe/CdSe) are the most-commonly prepared and have been widely used for biological  
4 applications. In conventional type-I core/shell QDs, the conduction band of the shell is at higher  
5 energy than that of the core, whereas the valence band of the shell is at lower energy than that of  
6 the core (**Figure 3a**). As a result, both holes and electrons are confined within the QD core. This  
7 architecture has been widely applied in recently-developed Cd-free QDs, *e.g.*, InP/ZnS,  
8 CuInS<sub>2</sub>/ZnS, AgInS<sub>2</sub>/ZnS, and ZnSe/ZnS core/shell QDs. Encapsulation of a core QD in a higher  
9 bandgap material to create a type-I core/shell QD can greatly reduce non-radiative recombination,  
10 thereby dramatically increasing PL QY. For example, Kang *et al.* improved the QY of AgInS<sub>2</sub>  
11 QDs from 3.6-11.6% to 18.4-39.1% by adding a ZnS shell.<sup>45</sup> Similarly, Chen *et al.* observed a  
12 QY increase from 1.4% to 48% upon adding a ZnS shell to CuInS<sub>2</sub> QDs.<sup>122</sup> ZnS has been the  
13 most common shell material in type-I core/shell QDs. A key advantage of this type-I architecture  
14 is enhanced stability and prolonged shelf life due to the high chemical stability of ZnS. In type-II  
15 QDs, both the conduction and valence bands are at higher energy in one material than in the  
16 other (**Figure 3b**). Thus, one carrier type (electron or hole) is mainly confined to the core while  
17 the other is mainly confined to the shell. This spatial separation of carriers can produce  
18 properties that are quite different from those of type-I QDs. Type-II QDs can be prepared to emit  
19 at near-IR wavelengths using materials with band gaps that are too wide to provide near-IR  
20 emission in a Type I QD structure. Typical Cd-based type-II QDs include CdSe/CdTe and  
21 CdSe/ZnTe core/shell QDs, which exhibit NIR emission due to electron-hole recombination  
22 across the core/shell interface.<sup>123</sup>

23  
24  
25  
26  
27  
28  
29  
30  
31  
32  
33  
34  
35  
36  
37  
38  
39  
40  
41  
42  
43  
44  
45  
46  
47  
48  
49  
50  
51  
52  
53  
54  
55  
56  
57  
58  
59  
60

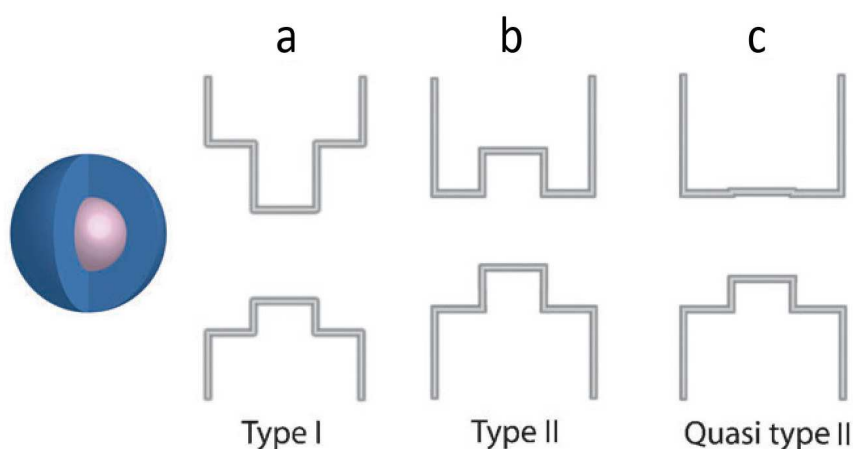


**Figure 3.** Schematic band diagrams of representative core-shell QDs: type-I (a); type-II (b); quasi-type-II (c). Adapted with permission from Deutsch *et al.*<sup>120</sup> Copyright 2011 Royal Society of Chemistry.

Recently, a handful of studies have explored preparation of Cd-free Type-II QDs.<sup>124,125</sup> Bang *et al.* prepared ZnTe/ZnSe QDs with PL colors from blue to amber by simply varying the shell thickness (**Figure 4**).<sup>124</sup> This sensitivity of PL emission wavelength to shell thickness is a characteristic of type-II core/shell QDs. Another distinguishing feature of type-II QDs is their extended exciton lifetime. However, compared to type-I QDs, most type-II QDs exhibit lower QY. Carrier separation slows radiative recombination due to reduced overlap of the hole and electron wavefunctions, extending the lifetime of the exciton. However, this longer radiative lifetime inherently increases the time during which nonradiative recombination can occur, lowering QY.

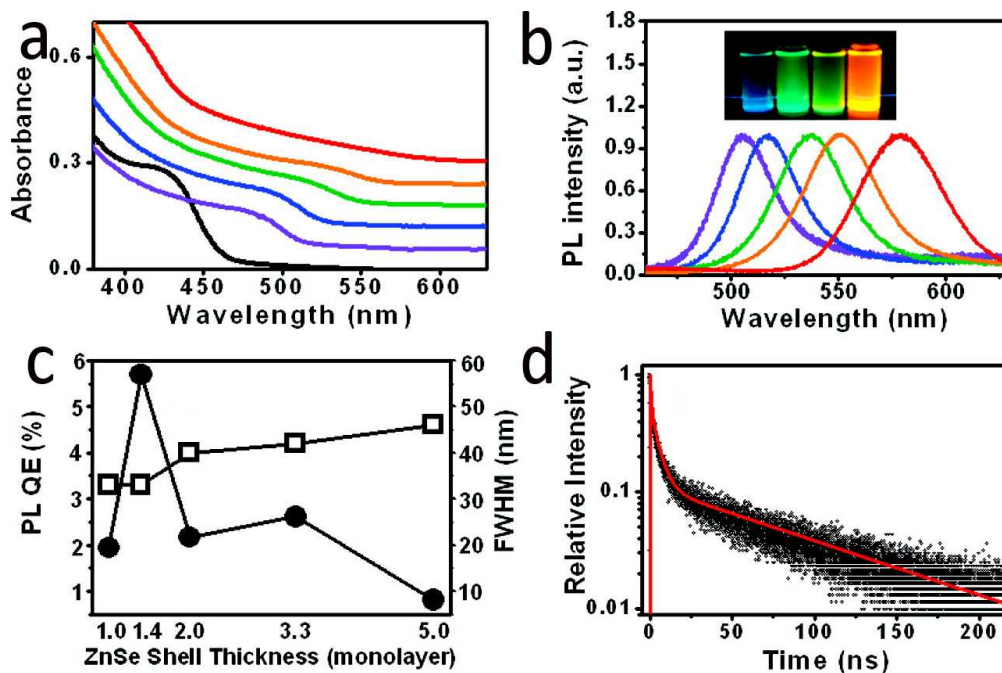


**Figure 4.** (a) Absorption and (b) emission spectra of ZnTe cores (black), ZnTe/ZnSe core/shell QDs that have same ZnTe cores and 1.0 (violet), 1.4 (blue), 2.0 (green), 3.3 (orange), and 5.0 (red) monolayers of ZnSe shells. The inset in panel (b) shows various ZnTe/ZnSe (core/shell) QD samples under UV illumination. (c) Photoluminescence quantum efficiencies (PL QE, closed circle) and full widths at half-maximum (FWHM, open squares) for ZnTe/ZnSe QDs. (d) Room-temperature normalized photoluminescence decay of ZnTe/ZnSe QDs dispersed in hexanes. Reprinted with permission from Bang *et al.*<sup>124</sup> Copyright 2009 American Chemical Society.

In an exception to the general rule of low QY from type-II core-shell QDs, Tyrakowski *et al.* achieved bright type-II QDs with 61% QY based on a novel ZnSe/CdS/ZnS structure. In this case the intermediate CdS shell has a type-II alignment with the ZnSe inner core and a type-I alignment with the ZnS outer shell.<sup>126</sup> Interestingly, the high QY was found to be a result of increased radiative recombination rate, rather than suppression of defect-related nonradiative

1  
2  
3 recombination. In another study, Soni *et al.* synthesized CdSe/CdS/ZnSe QDs that could achieve  
4 both type-I and type-II emission simultaneously.<sup>127</sup> Investigation of their optical properties  
5 demonstrated that the intermediate CdS layer formed a type-I structure with the inner CdSe core  
6 while it also formed a type-II structure with the outermost ZnSe shell. While these two examples  
7 are for Cd-containing structures, the principles demonstrated in them are applicable to Cd-free  
8 core-shell QDs as well.  
9

10  
11 In addition to band alignment, several other factors should be considered when designing and  
12 synthesizing core/shell QDs. In general, reaction conditions during shell growth, including the  
13 reaction temperature, precursor concentration, ligand identities and concentrations, and shell  
14 precursor injection rate must be optimized and controlled to obtain core/shell QDs without  
15 nucleation of separate NPs of the shell material, formation of “dumbbell”-like heterodimers, or  
16 undesired alloying of the core and shell materials. The core and shell materials must have  
17 commensurate crystalline structures and tolerable lattice mismatch. Large lattice mismatch  
18 induces strain at the core/shell interface, which can be relieved by defect formation, or can even  
19 cause a strain-induced transition between the type-I and type-II band alignment.<sup>128</sup> Lattice  
20 mismatch is an important parameter for evaluating the feasibility of shell growth on a given core  
21 material. Large lattice mismatch (>12%) typically makes epitaxial growth of a shell difficult and  
22 leads to the formation of many interface defects that degrade the optical properties of the  
23 QDs,<sup>129,130</sup> or even to the formation of separate NPs of the shell material. Effects of lattice  
24 mismatch can be partially ameliorated by growth of an intermediate layer between the core and  
25 shell to form multi-shell QDs, *e.g.* CdSe/CdS/ZnS QDs and CdSe/ZnSe/ZnS QDs. In analogy to  
26 these multi-shell Cd-based QDs, Ippen *et al.* developed Cd-free InP/ZnSe/ZnS QDs with 50%-  
27 70% QY.<sup>131</sup> ZnSe has a lattice constant between those of InP and ZnS, making it useful as a  
28  
29  
30  
31  
32  
33  
34  
35  
36  
37  
38  
39  
40  
41  
42  
43  
44  
45  
46  
47  
48  
49  
50  
51  
52  
53  
54  
55  
56  
57  
58  
59  
60

1  
2  
3  
4  
5  
6  
7  
8  
9  
10  
11  
12  
13  
14  
15  
16  
17  
18  
19  
20  
21  
22  
23  
24  
25  
26  
27  
28  
29  
30  
31  
32  
33  
34  
35  
36  
37  
38  
39  
40  
41  
42  
43  
44  
45  
46  
47  
48  
49  
50  
51  
52  
53  
54  
55  
56  
57  
58  
59  
60

buffer material or “lattice adapter” in that study. The multi-shell, or “sandwiched” InP/ZnSe/ZnS QDs showed improved PL intensity compared with InP/ZnS QDs.

### 2.3 Tunability in the Biological Transparency Window

A major limitation in the application of UV and visible light-based biotechnology is the very limited penetration of light of these wavelengths through most tissues. Effects limiting light propagation through biological media include both absorption by its constituent materials and scattering by the many heterogeneous structures present in tissues. Both effects are strongly wavelength-dependent. **Figure 5** shows the attenuation coefficient vs. wavelength for typical biological media. There are two optical transmission windows in the IR region where the attenuation is minimized. Transmission window I is from 650 nm to 950 nm and transmission window II is from 1000 nm to 1350 nm.<sup>132</sup>

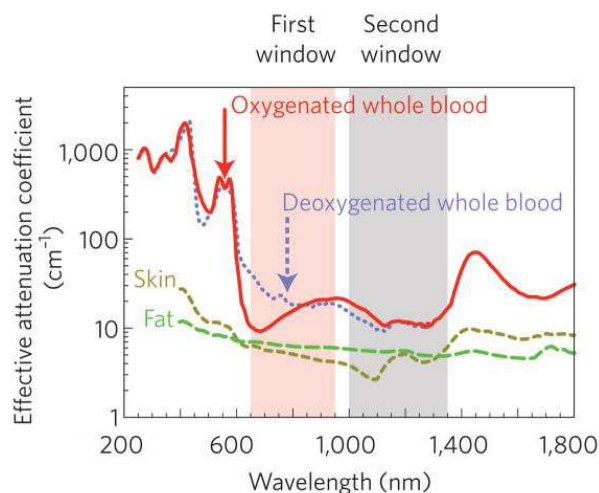


**Figure 5.** Effective attenuation coefficient (on a logarithmic scale) versus wavelength in a typical biological medium. Absorption and scattering from oxygenated blood, deoxygenated

1  
2  
3 blood, skin and fatty tissue is lowest in either the first (pink) or second (grey) near-IR window.

4  
5 Reprinted with permission from Smith *et al.*<sup>132</sup> Copyright 2009 Nature Publishing Group.  
6  
7

8  
9  
10 Many Cd-free QDs are based on narrow bandgap semiconductors. Their bandgap can be  
11 tuned by varying composition and size so that the QDs both absorb and emit at near-IR  
12 wavelengths where attenuation in tissues is minimized. Chalcopyrite AgInS<sub>2</sub>, with 1.87 eV  
13 bandgap, and CuInS<sub>2</sub>, with 1.55 eV bandgap can emit in the first NIR transmission window.  
14  
15 Recently, Dai and co-workers prepared AgInS<sub>2</sub> QDs with PL emission peak tunable from 650 to  
16  
17 850 nm by varying the Ag:In precursor ratio. The blue shift of the absorbance and PL spectra  
18 upon decreasing the Ag content was attributed to lowering of the valence band maximum.<sup>133</sup>  
19  
20 Several studies of CuInS<sub>2</sub> QDs found similar effects of composition on absorbance and emission  
21 wavelength, while other studies reported the size-dependence of their optical properties. Chen *et*  
22  
23 *al.* observed a blue shift of the PL peak of CuInS<sub>2</sub> QDs from 760 to 650 nm upon decreasing the  
24  
25 Cu:In ratio from 1.6 to 0.3.<sup>134</sup> In another study on CuInS<sub>2</sub> QDs, Li *et al.* obtained bright CuInS<sub>2</sub>  
26  
27 QDs with PL emission tunable from 630-780 nm by controlling the size while fixing the Cu:In  
28  
29 ratio close to 1:1.<sup>135</sup> The emission wavelengths of CuInS<sub>2</sub> and AgInS<sub>2</sub> can be further tuned to  
30  
31 longer wavelengths through substitution of S by Se. In both materials, Se substitution narrows  
32  
33 the band-gap, producing a red shift of the PL. Allen *et al.* obtained Cu-In-Se QDs with PL  
34  
35 emission peaks from 650 to 975 nm. They also achieved similar tunable PL by optimizing the  
36  
37 synthesis of Ag-In-Se QDs. Cassette *et al.* fabricated Cu-In-Se/ZnS QDs with PL from 700 to  
38  
39 1030 nm by varying the synthesis temperature.<sup>136</sup> Another strategy for tuning emission of these  
40  
41 ternary I-III-VI QDs is to incorporate Zn to generate quaternary QDs. For example, Deng *et al.*  
42  
43  
44  
45  
46  
47  
48  
49  
50  
51  
52  
53  
54  
55  
56  
57  
58  
59  
60

1  
2  
3 tuned the emission of Zn-Ag-In-Se QDs from 660 to 800 nm by varying the Zn:Ag precursor  
4 ratio from 5:0.5 to 0.5 :2.<sup>137</sup>  
5  
6

7  
8 Compared to the NIR-I transmission window, the NIR-II window can provide improved  
9 signal-to-noise ratio in bioimaging due to minimal biological autofluorescence as well as reduced  
10 scattering.<sup>132</sup> Ag<sub>2</sub>S and Ag<sub>2</sub>Se QDs are promising optical probes for use in the NIR-II window.  
11  
12 Jiang *et al.* fabricated Ag<sub>2</sub>S QDs with tunable PL from 690 to 820 nm. To extend the emission to  
13 longer wavelengths, they used their NIR-I emitting Ag<sub>2</sub>S QDs as seeds for a second growth  
14 process that produced larger Ag<sub>2</sub>S QDs with PL in the NIR-II range (1227 nm).<sup>138</sup> Tan and co-  
15 workers produced Ag<sub>2</sub>Se QDs with visible-NIR absorption (**Figure 6a**) and 966-1228 nm PL  
16 with a narrow spectral width (**Figure 6b**).<sup>22</sup> The multidentate polymer capped Ag<sub>2</sub>Se QDs were  
17 administered to nude mice and provided good *in vivo* image contrast in the NIR-II range (**Figure**  
18 **6c, d, e**). Using Ag<sub>2</sub>Se QDs with emission centered at 1300 nm, Dong *et al.* performed an *in vivo*  
19 imaging study in mice and achieved high-resolution imaging of both the vascular structure and  
20 organs at a depth of ~100 μm, demonstrating the potential of these NIR Ag<sub>2</sub>Se QDs for use in  
21 deep imaging applications.<sup>139</sup>  
22  
23  
24  
25  
26  
27  
28  
29  
30  
31  
32  
33  
34  
35  
36  
37  
38  
39  
40  
41  
42  
43  
44  
45  
46  
47  
48  
49  
50  
51  
52  
53  
54  
55  
56  
57  
58  
59  
60

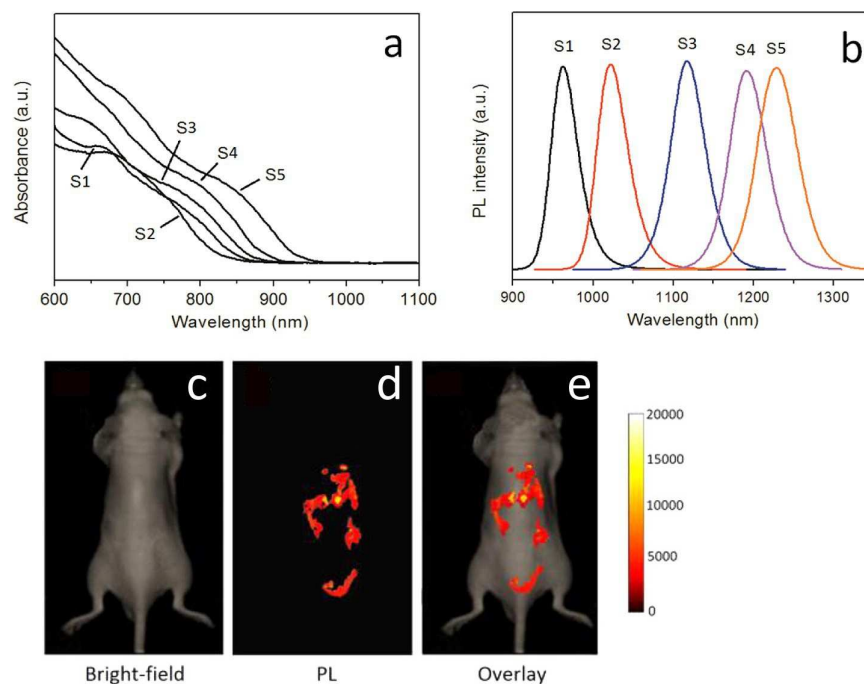


**Figure 6.** (a) Visible–NIR absorption and (b) emission spectra of multidentate polymer capped  $\text{Ag}_2\text{Se}$  QDs produced at different reaction times (S1–S5: 0.5, 1, 1.5, 2, and 3 h). (c) Bright-field image, (d) *in vivo* PL image, and (e) overlaid images of a nude mouse 12 h after tail vein injection of  $\text{Ag}_2\text{Se}$  QDs. Reprinted with permission from Tan *et al.*<sup>22</sup> Copyright 2014 American Chemical Society.

## 2.4 Opportunity to Introduce Tunable Plasmonic Features

Some of the QDs discussed here can be prepared with a nonstoichiometric ratio of constituents (*i.e.* can be vacancy-doped) or can be doped with impurity atoms to produce a high concentration ( $> 10^{21} \text{ cm}^{-3}$ ) of free charge carriers, either holes or electrons. Such degenerately-doped semiconductor nanocrystals can exhibit localized surface plasmon resonance (LSPR), derived from oscillations of free charge carriers, at near-IR wavelengths. LSPR absorbance and scattering in these nanocrystals can be used in many biological applications. Moreover, when

1  
2  
3 they are sufficiently small, quantum confinement effects can produce quantized excitonic states,  
4  
5 in addition to LSPR, in these degenerately-doped QDs. In one of the first examples of such  
6  
7 materials, free carrier-doped Cd-free QDs exhibiting LSPR were fabricated by Luther *et al.*<sup>140,141</sup>  
8  
9  
10 This discovery enabled the generation of LSPR at wavelengths up to 1800 nm in Cd-free QDs  
11  
12 with an average size smaller than 5 nm. In comparison to noble metal nanostructures with near-  
13  
14 IR LSPR (>50 nm in at least one dimension) that have been employed for *in vivo* photothermal  
15  
16 therapy and photoacoustic imaging, these smaller QDs can allow rapid excretion and better  
17  
18 circulation/biodistribution profiles, while providing similar optical performance. Moreover, these  
19  
20 plasmonic QDs maintain their excitonic absorbance, which is also subject to quantum  
21  
22 confinement. Kriegel *et al.* studied the plasmonic and excitonic properties of copper  
23  
24 chalcogenide QDs, showing the coupling between the excitonic and plasmonic modes.<sup>142</sup> Doping  
25  
26 of the Cu<sub>2</sub>E (E = S, Se, or Te) QDs, by oxidizing them to generate oxygen vacancies and free  
27  
28 holes creates Cu<sub>2-x</sub>E QDs that exhibit LSPR. However, the PL of the stoichiometric Cu<sub>2</sub>E QDs  
29  
30 decreases in intensity and ultimately disappears as the doping level increases. The high hole  
31  
32 concentration in the QDs enables Auger-like non-radiative recombination of excitons. Thus,  
33  
34 while having both PL and LSPR from the same QDs is unlikely, one can imagine QDs that  
35  
36 initially exhibit efficient PL but, upon oxidation, show PL quenching and the appearance of  
37  
38 LSPR absorbance. This could enable interesting combinations of short-term optical and longer-  
39  
40 term photoacoustic imaging methods.  
41  
42  
43  
44  
45  
46  
47

### 48 **2.5 Doping to Achieve Enhanced Emission from Dopant States**

49

50  
51 The finite dimensions of QDs lead to relaxation of the *k*-selection rule in indirect bandgap  
52  
53 semiconductors as well as significant enhancement of oscillator strength due to the overlap of the  
54  
55 electron and hole wavefunctions. This can produce efficient PL from materials that are not  
56  
57  
58  
59  
60

1  
2  
3 ordinarily considered good light emitters. Confinement of excitons also produces more efficient  
4  
5 photosensitization of impurity bands, allowing for high QY emission from impurity states  
6  
7 introduced by dopant atoms. Such doped QDs can also produce multiple emission peaks, which  
8  
9 can be useful for multichannel bioimaging. For instance, zinc chalcogenides (*i.e.*, ZnS and ZnSe)  
10  
11 doped with Cu, Mn, Eu, or Ga have attracted attention for biophotonic applications due to their  
12  
13 large Stokes shifts, which minimize re-absorbance of emitted photons. Cooper and co-workers<sup>143</sup>  
14  
15 prepared codoped core/shell ZnSe/ZnS QDs using Cu<sup>+</sup> as a primary dopant with trivalent co-  
16  
17 dopants including Al<sup>3+</sup>, Ga<sup>3+</sup>, and In<sup>3+</sup>. The peak emission wavelengths ranged from 430 nm to  
18  
19 570 nm with a narrow FWHM of ~80 nm. The codopant strategy combined with a novel  
20  
21 bidentate thiol ligand led to a significant improvement of both the PL intensity and the shelf life  
22  
23 of the QDs. The authors explained that the tunability of the emission arises from changes in  
24  
25 donor and acceptor energy levels. Specifically, the trivalent codopant provided donor states  
26  
27 within the bandgap while acceptor states were provided by the Cu dopant. Emission arose from  
28  
29 recombination of donor–acceptor pairs (DAPs), whose energy varied with codopant identity.  
30  
31 Note that, in general, quantum confinement effects change both the band energies of the host  
32  
33 semiconductor and the energies of donor and acceptor states relative to the band edges and to one  
34  
35 another.  
36  
37  
38  
39  
40  
41  
42

43 Zeng *et al.* reported aqueous synthesis of Cu-doped ZnSeS/ZnS core/shell QDs with a high  
44  
45 PL QY of 40% (**Figure 7**).<sup>144</sup> The QDs showed good stability, retaining 90% of their initial PL  
46  
47 intensity after 30 days of continuous air exposure. The outer ZnS shell not only helped to confine  
48  
49 excitons to the core, but also served as a passivation layer to prevent photo-degradation. PL  
50  
51 saturation at higher Cu content was attributed to defect formation and increased Cu-Cu  
52  
53 interactions. The emission also red-shifted with increasing Cu doping. Doping of QDs with  
54  
55  
56  
57  
58  
59  
60

Mn<sup>2+</sup> can similarly produce dopant-related PL. Song *et al.*<sup>125</sup> found that the QY of Mn<sup>2+</sup>-doped core/shell ZnTe/ZnSe QDs improved from 5.3% for undoped QDs to 7% for Mn<sup>2+</sup>-doped QDs. The PL emission from the doped QDs was dominated by the dopant-related emission, peaking at 593 nm, rather than the host emission near 450 nm.

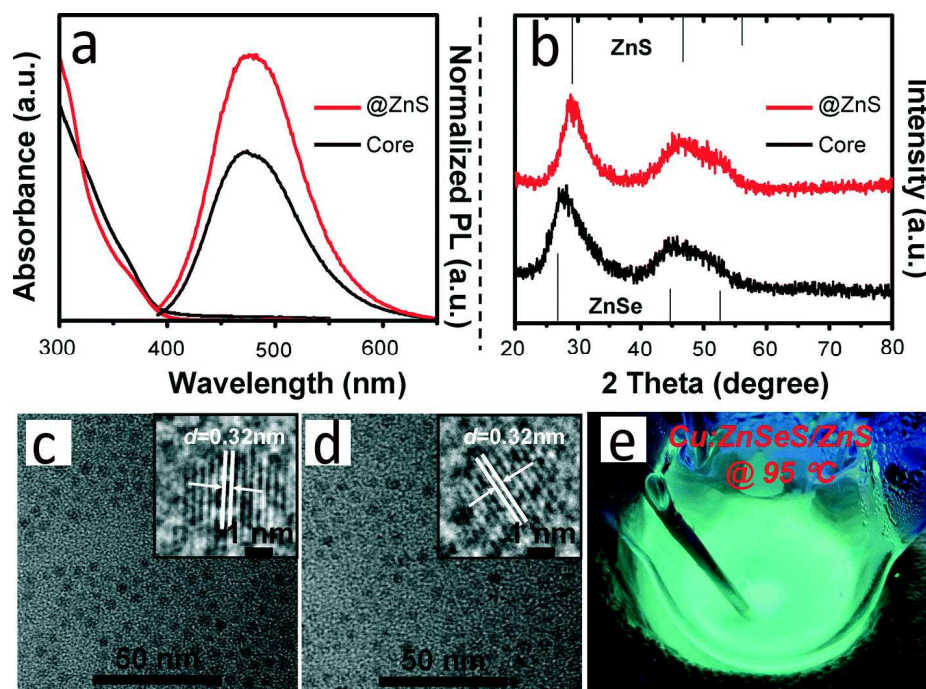


**Figure 7.** (a) Absorbance and emission spectra and (b) XRD patterns of Cu:ZnSeS and Cu:ZnSeS/ZnS QDs. TEM images of (c) Cu:ZnSeS and (d) Cu:ZnSeS/ZnS QDs, and (e) a photograph of Cu:ZnSeS/ZnS QDs under a 365 nm UV lamp at 95 °C. Reprinted with permission from Zeng *et al.*<sup>144</sup> Copyright 2014 Royal Society of Chemistry.

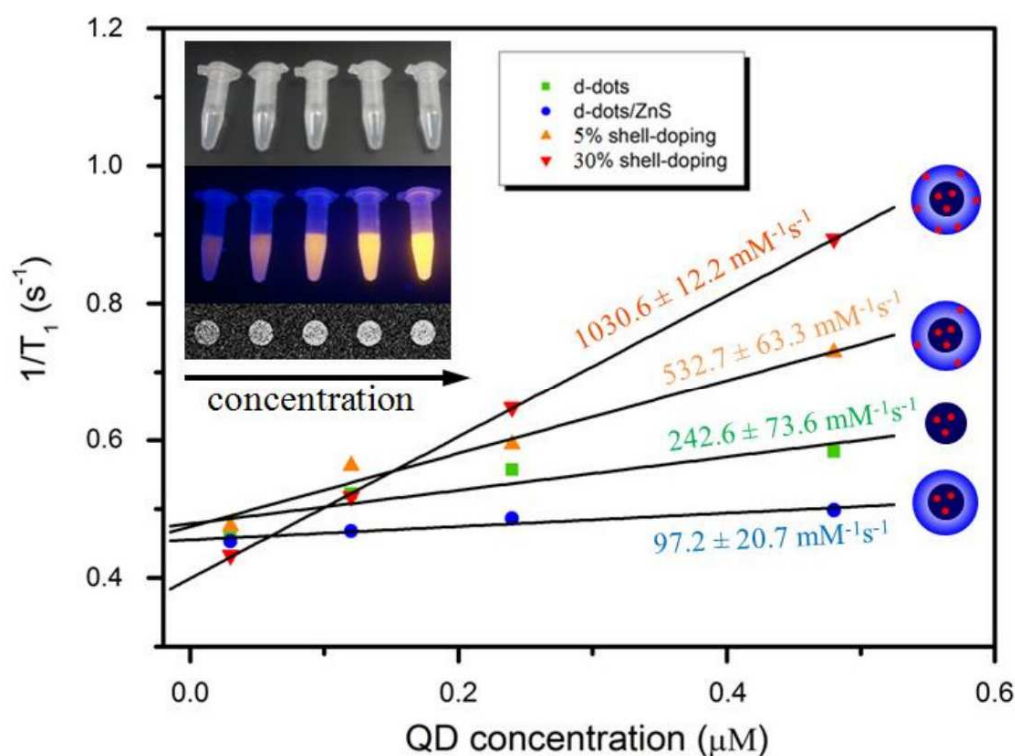
## 2.6 Magnetic Doping to Introduce Magnetic Imaging Capability

QDs can be endowed with magnetic functionality to provide contrast in magnetic resonance imaging (MRI), thereby achieving multimodal imaging with a single nanostructure. Magnetic functionality generally originates from paramagnetic ions or magnetic nanoparticles that are incorporated within or linked to the QDs. MRI plays a critical role in clinical diagnostics, because it allows monitoring of morphological changes of soft tissues at the whole organism level.<sup>145,146</sup> MRI is commonly employed for profiling the state of a disease or injury.

MRI relies on the nuclear magnetic resonance of spin states of hydrogen protons present in water. When a paramagnetic contrast agent is introduced and accumulates in the tissue of interest, it produces changes in the spin-lattice relaxation ( $T_1$  contrast) and/or the spin-spin relaxation ( $T_2$  contrast) dynamics of protons in nearby water molecules.<sup>147,148</sup> This change allows one to differentiate the tissue of interest from others. Contrast agents are called either  $T_1$  or  $T_2$  agents, depending on whether the relative change in relaxation times is greater for  $T_1$  or  $T_2$ . The performance of the contrast agent is described by its relaxivity ( $r_1$  or  $r_2$ ), which is the change in  $1/T_1$  or  $1/T_2$  of protons per unit concentration of the contrast agent.<sup>149</sup> Typical paramagnetic ions used as contrast agents include manganese ( $\text{Mn}^{2+}$ ) and gadolinium ( $\text{Gd}^{3+}$ ).<sup>150,151</sup> A QD formulation containing such ions can have advantages including targeted delivery to the tissue of interest for improving MRI contrast and reduced toxicity of the paramagnetic ions, when they are embedded within the QDs. Note that caution must be exercised in comparing relaxivity values between studies, because they are reported using different definitions and measurements of concentration. Some studies report relaxivity in terms of the concentration of paramagnetic ions,

1  
2  
3 while others use the concentration of QDs. The relaxivity per QD is larger than the relaxivity per  
4  
5  
6 ion simply because each QD can host many ions.

7  
8 An example of a QD formulation containing Mn is Mn-doped ZnS in which the manganese  
9 ions within the QDs influence the relaxation times of protons in the water surrounding them.<sup>152</sup>  
10 Another type of formulation prepared by our group utilizes Mn:ZnSe/ZnS/ZnMnS sandwiched  
11 QDs for combined MRI and optical imaging (**Figure 8**).<sup>153</sup> In this core/shell co-doped system,  
12 paramagnetic Mn<sup>2+</sup> ions are employed in the core to produce Mn photoluminescence while those  
13 in the shell provide the magnetic resonance imaging contrast. The  $T_1$  relaxivity of the  
14 nanocrystals can be enhanced by raising the shell doping level. Under optimized conditions, a  $T_1$   
15 relaxivity of  $r_1 = 1030.6 \text{ mM}^{-1}\text{s}^{-1}$  can be produced by these Mn-doped nanocrystals. By  
16 packaging these QDs within liposomes and conjugating them with folic acid, our group was able  
17 to use these sandwiched QDs for MR imaging of Panc-1 tumor cells, capturing excellent MR  
18 signals from the treated tumor cells.  
19  
20  
21  
22  
23  
24  
25  
26  
27



1  
2  
3 **Figure 8.**  $T_1$  relaxation rate ( $R_1 = 1/T_1$ ) plotted against Mn:ZnSe/ZnS/ZnMnS QD concentration.  
4  
5  
6 Insets are MR images and photographs of the QD samples under room light and UV excitation.  
7  
8 Adapted from Wang *et al.*<sup>153</sup> Copyright 2016 John Wiley and Sons.  
9

10  
11  
12 Mn-doped ZnS QDs, designed and prepared by Jahanbin *et al.* for MR imaging<sup>154</sup> generated  
13  $T_1$  contrast enhancement that could be manipulated by changing the Mn dopant content, at  
14 concentrations below 0.1 mM. CuInS<sub>2</sub>-Zn<sub>1-x</sub>Mn<sub>x</sub>S core/shell QDs<sup>155</sup> displayed a  $T_1$  relaxivity of  
15  $r_1 = 7.2 \text{ mM}^{-1} \text{ s}^{-1}$ . MR imaging of BXPC-3 cells showed that the Mn concentration in the  
16 nanocrystals was sufficient to generate MR contrast from QDs taken up by the cells. Similarly,  
17 CuInS<sub>2</sub>@ZnS:Mn QDs<sup>156</sup> with a gradient of Zn concentration in the core showed reduced Mn-  
18 based quenching of PL. This architecture optimized both the optical and magnetic functionalities  
19 of the QDs.  
20  
21  
22  
23  
24  
25  
26  
27  
28  
29  
30

31  
32 Another type of copper-based QD formulation for MR imaging is Gd-doped CuInS/ZnS<sup>157</sup>.  
33 Gd doped into the QD matrix produced MR relaxivity. The QDs were packaged within  
34 PEGylated dextran-stearic acid polymeric lipid vesicles for *in vivo* imaging experiments. The  
35 QDs possessed excellent near-IR PL and relatively high  $T_1$  relaxivity in water. *In vivo*  
36 experiments demonstrated application of these QDs for targeted MR imaging of tumors. Based  
37 on a similar concept, Zheng *et al.* reported water-dispersible Gd-doped CuInS<sub>2</sub> QDs.<sup>158</sup> Their  
38 QDs had a reasonable  $T_1$  relaxivity of  $12.84 \text{ mM}^{-1} \text{ s}^{-1}$  and further engineering these particles to  
39 incorporate targeting ligands and drugs may allow their use as dual optical and MR probes.  
40  
41  
42  
43  
44  
45  
46  
47  
48  
49  
50

51 ZnO is another promising QD host for incorporation of Gd ions. Gd-doped ZnO QDs have  
52 been engineered for MR imaging.<sup>94</sup> The size of these nanoparticles ranged from 4 to 6 nm,  
53 implying that they may be cleared from the body through renal filtration. In MRI studies, these  
54  
55  
56  
57  
58  
59  
60

1  
2  
3 particles exhibited a large  $T_1$  relaxivity of  $16 \text{ mM}^{-1} \text{ s}^{-1}$ . Subsequently, these particles were used  
4  
5 for MR imaging of HeLa cells. The  $T_1$ -weighted MR image of HeLa cells treated with QDs was  
6  
7 much brighter than that of untreated ones, demonstrating that the QDs were indeed being taken  
8  
9 up by the HeLa cells.  
10

11  
12  
13 Zn–Cu–In–(S, Se)/Zn<sub>1-x</sub>Mn<sub>x</sub>S core–shell QDs are another type of nanocrystals with magnetic  
14  
15 functionality that can be used for MR imaging.<sup>159</sup> The incorporation of Mn ions into the QDs  
16  
17 makes them paramagnetic. These QDs have  $T_1$  relaxivities<sup>159</sup> up to  $1400 \text{ mM}^{-1} [\text{QD}] \text{ s}^{-1}$  at 7 T  
18  
19 and 300 K. They were applied for MR imaging of regional lymph nodes in mice.  
20

## 21 22 **2.7 Relationship of Quantum Dot Physics, Properties, and** 23 24 **Applications** 25

26  
27  
28 Before moving on, we briefly summarize the relationship between the QD physics described  
29  
30 in the preceding subsections, the resulting properties, and the applications that depend on those  
31  
32 properties, as illustrated schematically in **Figure 9**. The defining feature of QDs, whether Cd-  
33  
34 based or Cd-free, is their size-dependent electronic band structure, which allows them to exhibit  
35  
36 narrow, tunable PL emission spectra combined with broad PL excitation spectra. Core-shell  
37  
38 structures are often employed to enhance this feature, by tuning the confinement and providing a  
39  
40 high-quality (defect free) interface between the QD core and its immediate surroundings. When  
41  
42 the semiconductor from which the QDs are prepared has a narrow band gap, the PL emission can  
43  
44 be tuned to match the NIR windows in which tissue absorbance and scattering is minimized.  
45  
46 Together, these properties allow multiplexed and NIR optical imaging by a variety of imaging  
47  
48 modalities in contexts from single cells to live animals. One can also employ QDs as hosts for  
49  
50 dopants. Dopants or defects can lead to emissive states that provide another means of accessing  
51  
52 NIR emission, or can introduce magnetic features that provide MRI contrast for multimodal  
53  
54  
55  
56  
57  
58  
59  
60

1  
2  
3  
4  
5  
6  
7  
8  
9  
10  
11  
12  
13  
14  
15  
16  
17  
18  
19  
20  
21  
22  
23  
24  
25  
26  
27  
28  
29  
30  
31  
32  
33  
34  
35  
36  
37  
38  
39  
40  
41  
42  
43  
44  
45  
46  
47  
48  
49  
50  
51  
52  
53  
54  
55  
56  
57  
58  
59  
60

imaging. Very high dopant concentrations can produce NIR LSPR absorbance, opening up an additional range of applications including photoacoustic and photothermal imaging and photothermal therapy. Finally, the size range of QDs allows their surface to accommodate multiple targeting groups, which can be identical or different, to enable multivalent targeting of particular biomolecules, cells, and tissues that is not possible with smaller structures, such as molecular dyes.

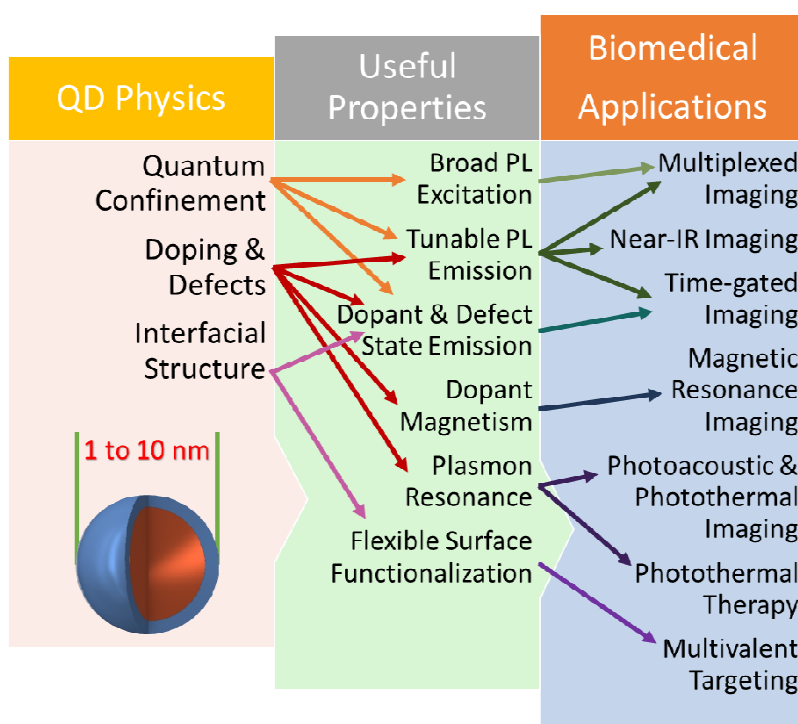


**Figure 9.** Schematic illustration of the relationships between the physics associated with quantum dot structures, the resulting QD properties, and biomedical applications enabled by these properties.

### 3.0 Selected Quantum Dot Systems

This chapter describes the different types of Cd-free QDs that have been studied for biological applications (discussed in Chapters 5 & 6) in recent years. **Table 1** summarizes the various materials, material properties, and key references discussed in the subsequent sections.

**Table 1. Summary Cd-free QD types, properties, and synthesis methods.**

| QD type <sup>a</sup>                                   | Exciton Bohr radius <sup>b</sup> (nm) | Bulk Bandgap (eV) | Synthesis method      | Size <sup>c</sup> (nm) | Emission wavelength (nm) | Quantum yield                  | Ref     |
|--|---------------------------------------|-------------------|-----------------------|------------------------|--------------------------|--------------------------------|---------|
| <b>InP</b>   | 20                                    | 1.35              | hot colloidal         | 2.8                    | 480-750                  | 1-30%                          | 160     |
|  |                                       |                   | hot colloidal         | 2.8-3.2                | –                        | Not luminescent                | 161     |
| <b>InP/ZnS</b>   | –                                     | 1.35              | hot colloidal         | 4.5                    | 480-735                  | up to 60%                      | 160     |
|  |                                       |                   | hot colloidal         | 6                      | 510-630                  | up to 80%                      | 161     |
| <b>CuInS<sub>2</sub></b>                               | 4.1                                   | 1.5               | hot colloidal         | 2-4                    | 630-780                  | 5-10%                          | 135     |
|  |                                       |                   | hot colloidal         | 2.5                    | 620-870                  | up to 18%                      | 36      |
|  |                                       |                   | hydrothermal          | 2.2                    | 660                      | 3.3%                           | 162     |
| <b>CuInS<sub>2</sub>/ZnS and ZnS-CuInS<sub>2</sub></b> | –                                     | 1.5-3.7           | hot colloidal         | 7                      | 550-815                  | up to 60%                      | 163     |
|  |                                       |                   | hot colloidal         | 4                      | 550-800                  | 20-80%                         | 36      |
|  |                                       |                   | continuous flow       | 3.0                    | 432-615                  | up to 40%                      | 164     |
|  |                                       |                   | hydrothermal          | 3.8±0.3                | 543-625                  | 20-38%                         | 165     |
|  |                                       |                   | microwave             | 3.3                    | 540-680                  | up to 24%                      | 166     |
| <b>AgInS<sub>2</sub></b>                               | 5.5                                   | 1.87              | hot colloidal         | 2.5-4.3                | 770-855                  | 36-63%                         | 167,168 |
| <b>AgInS<sub>2</sub>/ZnS and ZnS-AgInS<sub>2</sub></b> | –                                     | 1.87-3.7          | hot colloidal         | 1.4-5.2                | 620-815                  | 1.5 ±0.1%                      | 169     |
|  |                                       |                   | thermal decomposition | 4.1-4.4                | 540-720                  | up to 24%                      | 170     |
|  |                                       |                   | sonochemical          | 12 ± 1.3               | 480-700                  | 57.6-336% relative to CdSe/ZnS | 171     |

|    |                               |          |         |                 |           |                |             |     |
|----|-------------------------------|----------|---------|-----------------|-----------|----------------|-------------|-----|
| 1  |                               |          |         |                 |           |                |             |     |
| 2  |                               |          |         |                 |           |                |             |     |
| 3  | <b>Cu<sub>2</sub>S</b>        | 3-5      | 1.2     | sono-           | 12.1-     | NIR Abs        |             | 172 |
| 4  |                               |          |         | electrochemical | 18.1      | peak >1100 nm  |             |     |
| 5  |                               |          |         | hot colloidal   | 2.5-6     | NIR Abs        |             | 140 |
| 6  |                               |          |         |                 |           | peak >1796 nm  |             |     |
| 7  |                               |          |         |                 |           |                |             |     |
| 8  | <b>CuInSe<sub>2</sub></b>     | 10.6     | 1.04    | hot colloidal   | 2-3.5     | 650-975        | up to 25%   | 173 |
| 9  |                               |          |         |                 |           |                |             |     |
| 10 |                               |          |         |                 |           |                |             |     |
| 11 | <b>Ag<sub>2</sub>S</b>        | 2.2      | 0.9-1.1 | hot colloidal   | 5.6       | 1200           | 16%         | 174 |
| 12 |                               |          |         | hot colloidal   | 1.5-4.6   | 690-1227       | 0.18%       | 138 |
| 13 |                               |          |         | hydrothermal    | 2.6-3.7   | 687-1096       | 14.2-16.4%  | 73  |
| 14 |                               |          |         | hydrothermal    | 1.5-6.3   | 510-1221       | up to 2.1%  | 8   |
| 15 |                               |          |         |                 |           |                |             |     |
| 16 |                               |          |         |                 |           |                |             |     |
| 17 | <b>Ag<sub>2</sub>Se</b>       | 2.9      | 0.15    | aqueous at      | 3.4-5.9   | 966-1228       | 11.1-12.2%  | 22  |
| 18 |                               |          |         | room            |           |                |             |     |
| 19 |                               |          |         | temperature     |           |                |             |     |
| 20 |                               |          |         | hot colloidal   | 3.4       | 1300           | 29.4% after | 139 |
| 21 |                               |          |         |                 |           |                | phase       |     |
| 22 |                               |          |         |                 |           |                | transfer    |     |
| 23 |                               |          |         |                 |           |                |             |     |
| 24 | <b>ZnS-AgInSe<sub>2</sub></b> | –        | 1.2-3.7 | hot colloidal   | 5         | 660-800        | up to 50%   | 137 |
| 25 |                               |          |         |                 |           |                |             |     |
| 26 | <b>Mn:ZnSe</b>                | 4.5      | 2.7     | hydrothermal    | 3.8       | 410,480,570    | 2.4%        | 175 |
| 27 |                               |          |         | hydrothermal    | 7.0       | 400,480,590    | up to 17%   | 153 |
| 28 |                               |          |         |                 |           |                |             |     |
| 29 | <b>Mn:ZnS</b>                 | 2.5      | 3.7     | hot colloidal   | 3.8 ±     | 585            | 51.3%       | 176 |
| 30 |                               |          |         |                 | 0.2       |                |             |     |
| 31 |                               |          |         |                 |           |                |             |     |
| 32 | <b>Cu:ZnS</b>                 | 2.5      | 3.7     | hydrothermal    | –         | 482            | 4.2%        | 48  |
| 33 |                               |          |         |                 |           |                |             |     |
| 34 | <b>ZnSe/InP/ZnS</b>           | –        | 2.7     | hot colloidal   | 5.4       | 430-610 (for   | 60%         | 177 |
| 35 |                               |          |         |                 |           | ZnSe/InP)      |             |     |
| 36 |                               |          |         |                 |           |                |             |     |
| 37 | <b>Silicon</b>                | 4        | 1.1     | pulsed laser    | 4         | 450            | 0.4%        | 178 |
| 38 |                               |          |         | ablation        |           |                |             |     |
| 39 |                               |          |         | microemulsion   | 3.5-4.3   | 420-280        | 5.2%        | 179 |
| 40 |                               |          |         | gas-phase       | 2.8-5.2   | 700-1000       | 0.3-10.2%   | 180 |
| 41 |                               |          |         |                 |           |                |             |     |
| 42 |                               |          |         |                 |           |                |             |     |
| 43 | <b>ZnO</b>                    | 2.3      | 3.3     | sol-gel         | 2.85-     | 450-550        | 23-61%      | 181 |
| 44 |                               |          |         |                 | 12.16     |                |             |     |
| 45 |                               |          |         | sol-gel         | 3-4       | 520-550        | 20-50%      | 182 |
| 46 |                               |          |         |                 |           |                |             |     |
| 47 | <b>WS<sub>2</sub></b>         | –        | 1.35    | chemical        | 8-15      | 369-461        | 4%          | 183 |
| 48 |                               |          |         | exfoliation     | (lateral) |                |             |     |
| 49 |                               |          |         |                 |           |                |             |     |
| 50 | <b>Graphene</b>               | Infinite | 0       | hydrothermal    | 5-25      | 377-493 ( Exc: | 28%         | 184 |
| 51 |                               |          |         |                 |           | 300-400 )      |             |     |
| 52 |                               |          |         | pyrolysis       | 4.66±     | 415-580 and    | up to 54.5% | 185 |
| 53 |                               |          |         |                 | 1.24      | 800-850 (Exc:  |             |     |
| 54 |                               |          |         |                 |           | 320-540 )      |             |     |
| 55 |                               |          |         |                 |           |                |             |     |
| 56 |                               |          |         |                 |           |                |             |     |
| 57 |                               |          |         |                 |           |                |             |     |
| 58 |                               |          |         |                 |           |                |             |     |
| 59 |                               |          |         |                 |           |                |             |     |
| 60 |                               |          |         |                 |           |                |             |     |

<sup>a</sup>For simplicity, ideal chemical formulae are provided to represent the QDs even when the actual QDs are not stoichiometric, *e.g.*, Cu<sub>2</sub>S can represent Cu<sub>x</sub>S and CuInS<sub>2</sub> can represent Cu<sub>x</sub>In<sub>y</sub>S.

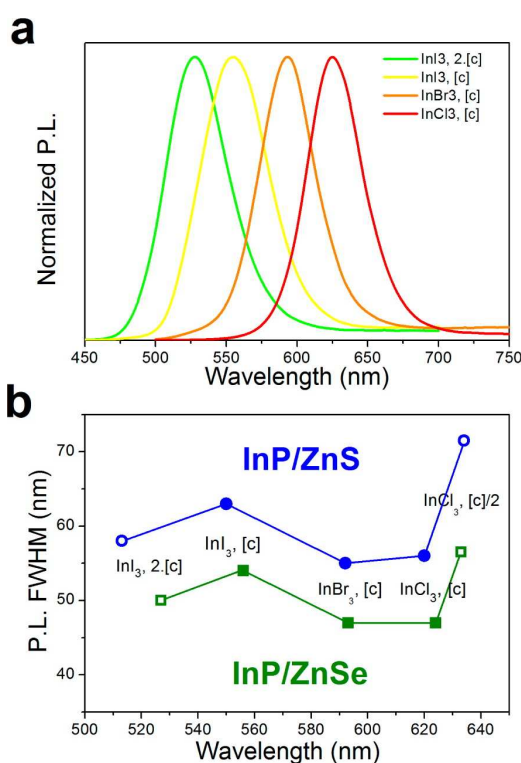
<sup>b</sup>For doped QDs, the Bohr radii of the host materials are provided.

<sup>c</sup>Sizes from TEM imaging or calculated from absorption spectra are given here. Hydrodynamic diameters in solution are inevitably larger.

### 3.1 InP and InP/ZnS Quantum Dots

QDs of group III-V semiconductors, particularly InP QDs, are generally more robust and stable than QDs of II-VI materials such as CdSe, because the bonding in III-V materials is less ionic and more covalent than in II-VI QDs.<sup>37,186-190</sup> However, the PL intensity and the QY of InP QDs have generally been lower than those of CdSe and other II-VI QDs, due to less effective passivation of dangling bonds and surface defects.<sup>191-194</sup> To overcome this challenge, the InP core QDs can be coated with a shell of a wider bandgap semiconductor like ZnS or ZnSe. Tessier *et al.*<sup>161</sup> produced InP/ZnSe and InP/ZnS core/shell QDs with emission peaks tunable from 510 nm to 630 nm and narrow full widths at half-maximum (FWHM) ranging from 46 to 63 nm (**Figure 10**). The bare core InP QDs, 3.2 nm in diameter, showed negligible PL. However, their absorbance spectra showed two excitonic features separated by 0.3 eV. The first excitonic absorbance peak of InP core QDs was at 570 nm. The two excitonic features correspond to the two transitions from the highest occupied state (h1, HOMO) to the first and second unoccupied states (e1 and e2, LUMO and LUMO+1). After coating the InP QDs with a 1.5 nm ZnS shell, the first exciton transition was red-shifted by 60 meV, and the PL QY increased to 60%. The emission linewidth was 56 nm. The size of the resulting InP/ZnSe QDs with the same precursor concentration was larger than that of InP/ZnS QDs due to a smaller lattice mismatch of 3.2% between InP and ZnSe. The smaller bandgap of 2.7 eV for ZnSe compared to 3.6 eV for ZnS led to a larger redshift of the first exciton transition, by 120 meV, due to weaker confinement by the ZnSe shell. The resulting InP/ZnSe had a narrower emission FWHM of 48 nm and a slightly

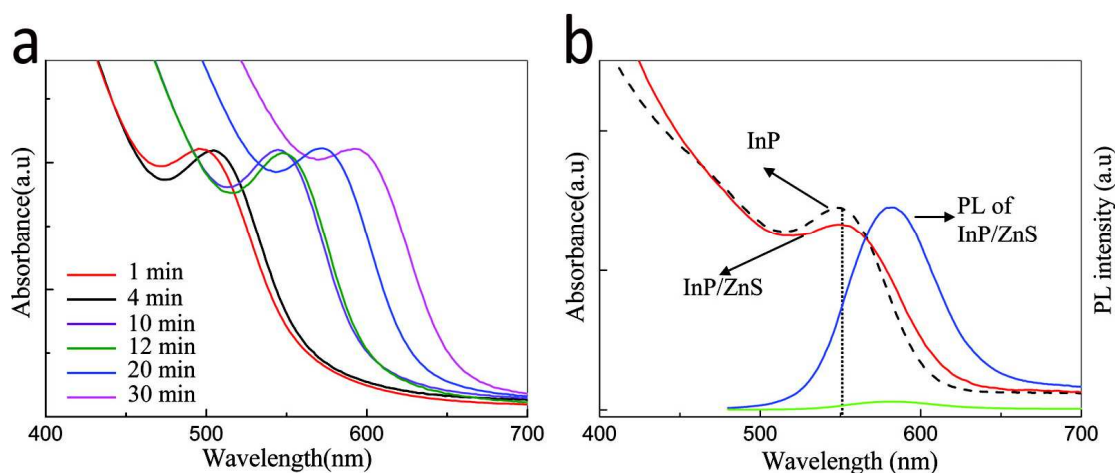
1  
2  
3 lower QY of 50%. The authors attributed the narrower emission to the lower lattice mismatch  
4 between InP and ZnSe (3.2%) than that between InP and ZnS (7.7%). Moreover, a broadened  
5 FWHM up to 70 nm and increased QY up to 80% were observed in the InP/ZnS QDs upon  
6 further increasing the shell thickness. Increasing the shell thickness of InP/ZnSe QDs only  
7 increased the QY. These results revealed the advantage of a ZnSe shell relative to a ZnS shell for  
8 maintaining narrow emission spectra.  
9  
10  
11  
12  
13  
14  
15  
16



47  
48  
49  
50  
51  
52  
53  
54  
55  
56  
57  
58  
59  
60

**Figure 10.** (a) PL emission spectra of InP/ZnSe QDs (b) Full-width at half maximum (FWHM) of InP/ZnS and InP/ZnSe using different In halides and different precursor concentrations ([c] corresponds to 0.09 M In precursor). Reprinted with permission from Tessier *et al.*<sup>161</sup> Copyright 2015 American Chemical Society.

1  
2  
3  
4 The temperature dependence of PL emission from InP/ZnS QDs was studied by  
5 Narayanaswamy and co-workers.<sup>195</sup> They focused on the bandgap change, *i.e.*, the energy change  
6 of the e1-h1 (HOMO-LUMO) transition over a temperature range from 300 K to 525 K. They  
7 showed that the energy decreased as the temperature increased, due to coupling between the e1-  
8 h1 exciton and acoustic phonon modes. The experimental results were fit with an empirical  
9 function from which the average phonon energy and Huang-Rhys factor were derived. The  
10 FWHM of the QD PL spectra broadened with increasing temperature, and this broadening was  
11 analyzed with an equation that described the temperature dependence of the energy of the  
12 lowest-lying exciton. For a fixed temperature of 300 K, the absorption and PL peaks red-shifted  
13 with increasing QD size. The Stokes shift, defined as the energy difference between the first  
14 absorbance and PL peaks, increased with decreasing QD diameter as 101.3 meV, 133.6 meV and  
15 191.2 meV for InP/ZnS with diameters of 3.2 nm, 2.8 nm and 2.3 nm (**Figure 11**).



50 **Figure 11.** (a) Temporal evolution of the UV-vis absorption spectra of InP QDs with synthesis  
51 time in ODE. (b) UV-vis absorption and PL spectra of InP (black dashed line and green solid  
52 line) and InP/ZnS QDs (red solid line and blue solid line). Reprinted with permission from  
53 Narayanaswamy *et al.*<sup>195</sup> Copyright 2008 American Chemical Society.

1  
2  
3  
4  
5  
6  
7  
8  
9  
10  
11  
12  
13  
14  
15  
16  
17  
18  
19  
20  
21  
22  
23  
24  
25  
26  
27  
28  
29  
30  
31  
32  
33  
34  
35  
36  
37  
38  
39  
40  
41  
42  
43  
44  
45  
46  
47  
48  
49  
50  
51  
52  
53  
54  
55  
56  
57  
58  
59  
60

Copper-doped InP/ZnS core/shell QDs were fabricated by Zhang *et al.* to achieve broadband emission from visible to near-IR wavelengths under a single excitation wavelength.<sup>196</sup> Their Cu-doped InP/ZnS/InP/ZnS core/barrier/quantum well/shell QDs had two PL peaks that respectively resulted from the Cu-doped InP core and the InP quantum well layer. The dual emission peaks were tuned by changing the core size and the thickness of the quantum well. The ZnS layer inside the QDs was placed between the InP core and the InP quantum well and worked as a barrier to decouple the QD core and the quantum well. The outer layer of ZnS at the QD surface enhanced the QY and photostability of emission from the quantum well. The PL peak of the Cu-doped InP core (1.8 nm) at 690 nm was unchanged upon coating with 3 monolayers of ZnS (to 3.8 nm diameter) and then 1.5 layers of InP (to 4.9 nm diameter) to form Cu:InP/ZnS/InP. The new PL peak at 530 nm was obtained only upon surface passivation of the InP quantum well layer by growth of the outer ZnS shell, which increased the overall QD diameter to 6.2 nm. The lifetime of the first PL peak was measured to be 499 ns, which is much longer than that of the second PL peak of 46 ns. The large lifetime difference confirmed the role of the ZnS barrier in decoupling of the dual emission channels in the particle. By changing the thickness of the InP quantum well layer from 0.35 nm to 1.2 nm, the second PL peak could be tuned from 480 nm to 600 nm. In addition, the first PL peak could be tuned from 600 nm to 800 nm by only changing the diameter of the core InP QD from 1.5 nm to 2.6 nm. This illustrates the effect of quantum confinement on the energy of the Cu dopant states in the QD.

Recently, Thomas and co-workers<sup>197</sup> systematically studied the Förster resonance energy transfer (FRET) from InP QDs to different fluorescent dyes including rhodamine 101 (Rh101), Texas red cadavarine C5 (TxRed) and lissamine rhodamine B ethylene diamine (LiRh). The

1  
2  
3 efficient energy transfer observed in that study illustrates the potential of InP QDs for harvesting  
4 energy in biophotonics and photovoltaics. Chemical groups like the amine groups on TxRed and  
5  
6 LiRh and the carboxyl group on Rh101 can coordinate directly to the QD surface. From the  
7  
8 steady-state and time-resolved emission spectra, large quenching constants of  $10^{13}$ - $10^{14}$   $M^{-1} s^{-1}$   
9  
10 were observed upon anchoring of the dyes to InP/ZnS core/shell QDs. A rapid PL decay  
11  
12 followed by increased acceptor emission with a rise time of 200 ps was observed under 405 nm  
13  
14 excitation. Thus, the mechanism of energy transfer was non-radiative. The excitation energy of  
15  
16 the InP/ZnS QDs was transferred to the fluorescent dyes *via* FRET. The authors demonstrated  
17  
18 that the energy transfer rate varied with the QD size. For example, the InP/ZnS QDs with  
19  
20 maximum PL at 530 nm showed a higher energy transfer rate than those whose PL spectrum  
21  
22 peaked at 500 nm, due to better overlap between QD emission and dye absorbance for the 530  
23  
24 nm emitting QDs.  
25  
26  
27  
28  
29  
30

### 31 **3.2 CuInS<sub>2</sub> and CuInS<sub>2</sub>/ZnS Quantum Dots**

32  
33  
34 CuInS<sub>2</sub> (CIS) QDs have a Bohr exciton radius of 4.1 nm and thus quantum confinement  
35  
36 effects can be observed when their diameter falls below 8 nm<sup>166,198-200</sup>. The molar absorptivity of  
37  
38 CIS is relatively high across the entire visible spectral range (*e.g.*,  $10^5$   $cm^{-1}$  at 500 nm). However,  
39  
40 bare CIS QDs are not stable in air or water and show a low PL QY<sup>201-203</sup>. Chen *et al.*<sup>122</sup>  
41  
42 demonstrated that the PL intensity of the CIS QDs could be improved dramatically by coating  
43  
44 with a ZnS shell. The signal enhancement was attributed to passivation of defects at the core QD  
45  
46 surface. The PL QYs for the core and core/shell QDs were 1.4% and 48%, respectively, under  
47  
48 460 nm excitation. The large bandgap difference between ZnS (3.2eV) and CIS (1.5eV) leads to  
49  
50 strong confinement of excitons within the CIS core, and thus significant QY enhancement. A 100  
51  
52 nm blue shift of the emission peak was observed after the ZnS shell coating due reduction in size  
53  
54  
55  
56  
57  
58  
59  
60

1  
2  
3 of the CIS core during the ZnS shell growth reaction. Encapsulation of the QDs with *O*-  
4 carboxymethylchitosan (OCMCS) made the CIS/ZnS QDs water-dispersible, with a  
5 hydrodynamic diameter of ~200 nm. Many QDs were enclosed within each OCMCS spheroid.  
6  
7 After encapsulation, the PL emission peak shifted to the near-IR biological window (~700 nm),  
8 which is favorable for *in vivo* imaging. Rao *et al.*<sup>204</sup> showed that doping the ZnS shell with  
9 aluminum could significantly improve the photostability and QY of the CuInS<sub>2</sub>/ZnS core/shell  
10 QDs (**Figure 12**). The active Al introduced at the surface of the ZnS shell was oxidized to an  
11 Al<sub>2</sub>O<sub>3</sub> layer that protected the QDs from degradation under long-term irradiation. The optimum  
12 molar ratio between Al and Zn was found to be 0.5. Addition of too much Al may reduce the  
13 stability of the ZnS/Al shell due to the formation of less stable Al-S bonds. A red shift of the PL  
14 peak of the CIS/ZnS QDs without aluminum doping after 30 min of light excitation was  
15 attributed to corrosion of ZnS. The PL peak of the CIS/ZnS-Al QDs remained unchanged under  
16 the same conditions.  
17  
18  
19  
20  
21  
22  
23  
24  
25  
26  
27  
28  
29  
30  
31  
32  
33  
34  
35  
36  
37  
38  
39  
40  
41  
42  
43  
44  
45  
46  
47  
48  
49  
50  
51  
52  
53  
54  
55  
56  
57  
58  
59  
60

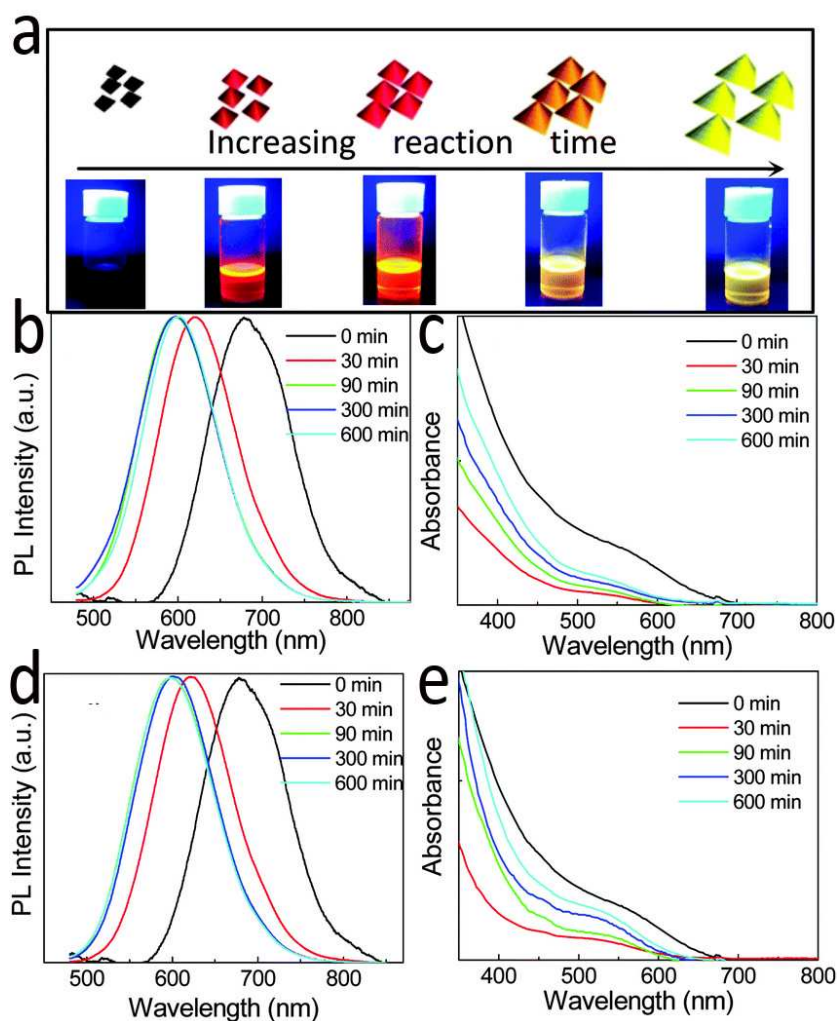
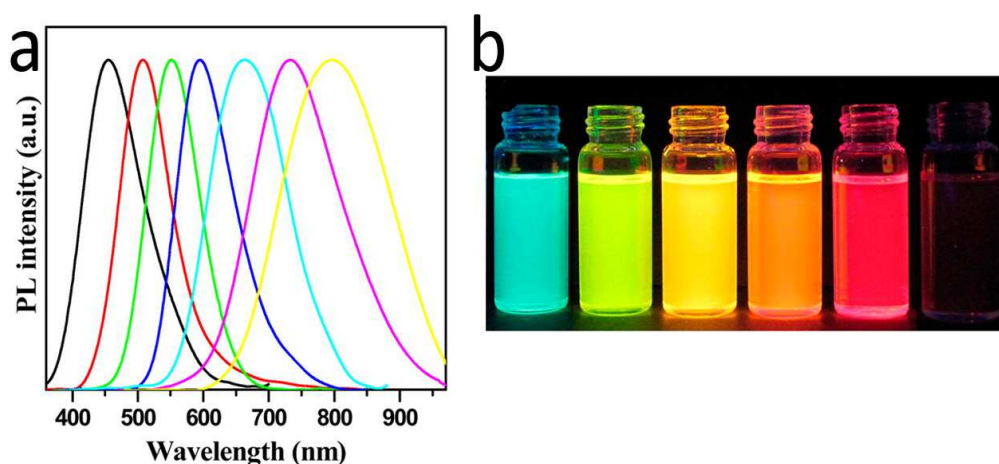


**Figure 12.** (a) Crystal growth process and color change of CIS@ZnS:Al QDs; (b) PL and (c) UV-vis absorbance spectra of CIS@ZnS QDs; (d) PL and (e) UV-vis absorbance spectra and CIS@ZnS:Al QDs with a Al/Zn molar ratio of 0.5. Reprinted with permission from Rao *et al.*<sup>204</sup> Copyright 2015 Royal Society of Chemistry.

The QY of hydrophobic CIS/ZnS QDs synthesized in organic solvents has reached 80% in some studies, and their PL emission wavelength is widely tunable across the visible to NIR spectral region (**Figure 13**).<sup>205</sup> However, in most cases the QY dropped dramatically after the

1  
2  
3 hydrophobic to hydrophilic ligand exchange process required to make the QDs water-dispersible.  
4  
5 Recently, Jiang *et al.*<sup>206</sup> reported Cu-doped Zn–In–S/ZnS core/shell QDs (CZIS/ZnS QDs)  
6  
7 fabricated directly in water, with a QY up to 35%. In this study, the absorbance and PL peaks of  
8  
9 the QDs showed a redshift with decreasing Zn and In precursor concentrations and increasing Cu  
10  
11 precursor concentration. The QD PL emission wavelength was tunable from 465 to 700 nm.  
12  
13 Changes in the Zn<sup>2+</sup> precursor concentration induced a larger shift in the emission peak  
14  
15 wavelength of QDs than changes in the In<sup>3+</sup> precursor concentration. Before coating with ZnS  
16  
17 shells, a shoulder PL peak was observed at 700 nm and attributed to recombination of trapped  
18  
19 electrons with holes in the acceptor level of zinc vacancies. The ZnS shell suppressed this  
20  
21 shoulder peak, suggesting that electron traps and zinc vacancies were eliminated.  
22  
23  
24  
25  
26  
27



45 **Figure 13.** (a) Normalized PL emission spectra ( $\lambda_{\text{ex}} = 350$  nm) of Zn-Cu-In-S/ZnS QDs  
46  
47 synthesized in organic solvents. (b) Photograph of samples under UV illumination. Reprinted  
48  
49 with permission from Zhang *et al.*<sup>205</sup> Copyright 2014 American Chemical Society.  
50  
51

52  
53  
54 The optical properties of CuInS<sub>2</sub>/ZnS quantum rods (QRs) can also be tuned by changing the  
55  
56 precursor ratios during synthesis. Li *et al.*<sup>207</sup> found that the absorbance spectra and PL peaks of  
57  
58  
59  
60

1  
2  
3 CuInS<sub>2</sub>/ZnS QRs were strongly dependent on the zinc precursor concentration in the seed growth  
4 process rather than the final diameter and length of the QRs. In comparison to pure CIS QRs, the  
5 absorbance spectra of CuInS<sub>2</sub>/ZnS QRs were shifted to shorter wavelengths. The optical bandgap  
6 of the QRs increased from 1.82 eV to 2.27 eV with increasing ZnS:CIS ratio from 1:2 to 2:1,  
7 while the PL peaks of CuInS<sub>2</sub>/ZnS QRs were blue-shifted from 760 nm to 520 nm under 450 nm  
8 excitation. Currently, quaternary CuInZnS/ZnS QDs with reproducible size and QY can be  
9 obtained even at large scale (gram scale). Li *et al.*<sup>164</sup> designed a continuous-flow synthesis  
10 method using a stainless steel cannula (1.6 mm diameter × 400 mm long needle) as the reaction  
11 chamber, a geometry similar to the narrow channels in microfluidic chips.<sup>208</sup> For the QD  
12 synthesis, the Cu, In and Zn precursors were mixed with oleylamine (OAm) and pumped into a  
13 commercial stainless steel cannula. The CuInZnS/ZnS core/shell QDs were formed with a high  
14 yield of 82-85%. The emission wavelengths of the QDs could be tuned from 432 to 615 nm by  
15 varying the fraction of each precursor during synthesis. The maximum PL QY of the  
16 CuInZnS/ZnS QDs from the continuous-flow reaction was ~40%.

### 3.3 Ag<sub>2</sub>S and Ag<sub>2</sub>Se Quantum Dots

37  
38  
39 Ag<sub>2</sub>S and Ag<sub>2</sub>Se QDs are based on I–VI semiconductors with narrow bandgaps of 0.85 and  
40 0.15 eV<sup>209-213</sup>. They are known as NIR-II emitting probes (950 to 1400 nm) which are often more  
41 suitable for deep tissue imaging than NIR-I emitters (650 to 950 nm). Reduced autofluorescence  
42 and other background in the NIR-II window allow larger penetration depths and higher imaging  
43 fidelity<sup>214-216</sup>. Also, the optical absorbance and scattering by biological tissues are significantly  
44 reduced in the NIR-II window. Silver ions were ultraslowly released into the biological  
45 environment, ensuring high biocompatibility of the Ag<sub>2</sub>S and Ag<sub>2</sub>Se QDs. Recently, the exciton  
46 Bohr radius of Ag<sub>2</sub>S QDs was determined to be 2.2 nm from both experimental and theoretical  
47  
48  
49  
50  
51  
52  
53  
54  
55  
56  
57  
58  
59  
60

1  
2  
3 results<sup>217</sup>. Thus, Ag<sub>2</sub>S QDs below 4.4 nm diameter are in the quantum confinement regime and  
4  
5 show size-dependent PL emission and excitation spectra. Sun and co-workers<sup>218</sup> studied  
6  
7 multiple-exciton generation in Ag<sub>2</sub>S QDs and found that their lifetimes were 1-2 orders of  
8  
9 magnitude longer than those of PbS QDs.  
10

11  
12 Li *et al.*<sup>174</sup> reported that PEGylated Ag<sub>2</sub>S QDs with an average size of 5.6 nm showed a PL  
13  
14 peak at 1200 nm and QY of 16% (**Figure 14**). Compared to indocyanine green (ICG), an organic  
15  
16 dye with NIR-I emission, the Ag<sub>2</sub>S QDs with NIR-II emission showed a narrower feature width  
17  
18 in a tissue phantom study when immersed in high concentration of intralipid solution. A spatial  
19  
20 resolution of 40 μm was achieved by using these QDs for *in vivo* angiogenesis imaging of blood  
21  
22 vessels (43 μm) in a small tumor (2 to 3 mm). The QDs retained 70% of their peak PL intensity  
23  
24 after 2 h irradiation at 808 nm by a laser diode at a flux of 123.8 mW/cm<sup>2</sup>. Using these QDs, a  
25  
26 penetration depth of 1.1 cm was achieved in a phantom model, with an injection concentration of  
27  
28  
29  
30  
31  
32 0.1 mg/mL.  
33  
34  
35  
36  
37  
38  
39  
40  
41  
42  
43  
44  
45  
46  
47  
48  
49  
50  
51  
52  
53  
54  
55  
56  
57  
58  
59  
60

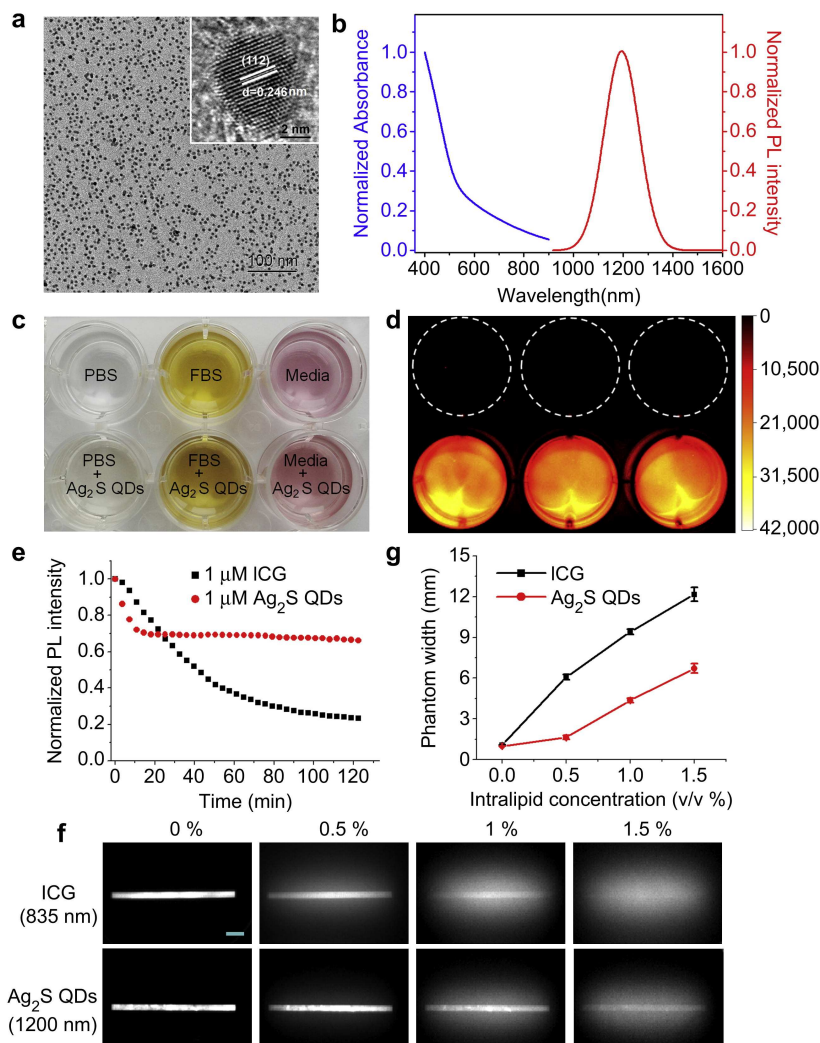


**Figure 14.** Characterization of PEGylated Ag<sub>2</sub>S QDs. (a) TEM and HR-TEM (inset) image, (b) absorbance and PL spectra of PEGylated Ag<sub>2</sub>S QDs. (c and d) Dispersion (0.1 mg/mL) of PEGylated Ag<sub>2</sub>S QDs in PBS, FBS, and cell culture media and their NIR-II PL images. (e) Photostability of PEGylated Ag<sub>2</sub>S QDs and ICG under irradiation of an 808 nm laser. (f) Fluorescent images of ICG at 835 nm and Ag<sub>2</sub>S QDs at 1200 nm immersed in different concentration of intralipid solutions. Scale bar: 0.5 cm. (g) Phantom width of Ag<sub>2</sub>S QDs and ICG capillary images corresponding to (f), showing a narrower feature width of NIR II-emitting Ag<sub>2</sub>S

1  
2  
3 QDs in comparison with the NIR I-emitting ICG. Reprinted with permission from Li *et al.*<sup>174</sup>

4  
5  
6 Copyright 2014 Elsevier.

7  
8  
9  
10 Gui *et al.*<sup>219</sup> fabricated thiol-multidentate polymer functionalized Ag<sub>2</sub>S QDs with sizes  
11 ranging from 2.6 to 3.7 nm and QY of 14.2–16.4%. Their PL emission was tuned across a wide  
12 range from deep red to NIR-II (687 nm to 1096 nm) making the Ag<sub>2</sub>S QDs an ideal candidate for  
13 multicolor targeted imaging. Tan *et al.*<sup>22</sup> demonstrated the tunability of PL multidentate polymer  
14 (MDP) functionalized Ag<sub>2</sub>Se QDs from 966 to 1228 nm by changing the reaction time from 0.5  
15 to 3 h. Upon increasing the growth time, the absorbance and emission spectra were red-shifted.  
16 As a result, the PL emission of the QDs could be excited within the NIR-I window, which is  
17 preferable for *in vivo* imaging. The longer reaction time also led to broadening of the size  
18 distribution and the PL emission spectrum. The Ag<sub>2</sub>Se QDs synthesized in water had a relatively  
19 high QY of 12.2% and a long PL lifetime of 135.3 ns. The photostability of the MDP-  
20 functionalized Ag<sub>2</sub>Se QDs was compared ICG. The fluorescence intensity of the ICG was fully  
21 bleached after 3 h of excitation, while the QDs suffered only a 20% decrease in PL intensity  
22 under the same conditions. The effects of different capping ligands including 1-octanethiol,  
23 oleylamine (OAm), and tetradecylphosphonic acid (TDPA) on formation of Ag<sub>2</sub>Se QDs were  
24 demonstrated by Zhu *et al.*<sup>220</sup> They found that among the three ligands, 1-octanethiol was most  
25 effective for producing highly monodisperse and photostable Ag<sub>2</sub>Se QDs. This is attributed to  
26 differences in interaction between the ligands and the Ag precursor. The Ag(I) precursor is a soft  
27 Lewis acid and 1-octanethiol is soft Lewis base ligand, while OAm and TDPA are hard Lewis  
28 base ligands. In this case, the Ag(I) precursors could be effectively stabilized at a higher reaction  
29  
30  
31  
32  
33  
34  
35  
36  
37  
38  
39  
40  
41  
42  
43  
44  
45  
46  
47  
48  
49  
50  
51  
52  
53  
54  
55  
56  
57  
58  
59  
60

1  
2  
3 temperature during the nucleation and growth process. The Ag<sub>2</sub>Se QDs exhibited NIR-II PL  
4  
5 emission wavelengths from 1080 to 1330 nm.  
6  
7

### 8 **3.4 ZnS-AgInS<sub>2</sub> (ZAIS) Quantum Dots**

9

10  
11 AgInS<sub>2</sub> QDs are ternary I-III-VI<sub>2</sub> QDs that are similar to CuInS<sub>2</sub> QDs.<sup>221-223</sup> AgInS<sub>2</sub> can  
12  
13 exist in two crystal phases: chalcopyrite and orthorhombic. The chalcopyrite phase has a  
14  
15 tetragonal unit cell and in the bulk is thermodynamically stable below 620°C, while the  
16  
17 orthorhombic phase is more stable at higher temperatures. Thus, AgInS<sub>2</sub> QDs are mainly  
18  
19 produced in the chalcopyrite phase, which has a direct bandgap of 1.87 eV (663 nm), with high  
20  
21 absorption coefficient. The bandgap of AgInS<sub>2</sub> QDs was tuned from 1.87 eV to 2.03 eV by  
22  
23 changing the Ag:In precursor ratio during synthesis<sup>221</sup>. Water-dispersible AgInS<sub>2</sub>/ZnS core/shell  
24  
25 QDs with a long PL lifetime of 170 ns and a high QY of 20% were recently fabricated by  
26  
27 Regulacio and co-workers.<sup>224</sup> To achieve water dispersibility, they modified the QD surface with  
28  
29 mercaptoacetic acid (MAA) and polyacrylic acid (PAA). Hamanaka *et al.*<sup>168</sup> investigated the  
30  
31 effect of AgInS<sub>2</sub> QD size on the PL QY and radiative recombination rate. They found that the  
32  
33 QY of AgInS<sub>2</sub> QDs increased with decreasing size from 4.3 nm to 2.5 nm, reaching 60% for 2.5  
34  
35 nm QDs. The authors concluded that the low reaction temperature used in preparing the smaller  
36  
37 QDs might increase the number of donor-acceptor recombinations trapped by defects sites,  
38  
39 leading to a higher QY. Using a low reaction temperature of 165°C and a small amount of zinc  
40  
41 precursor (8 atom %) in the reaction system, the NIR emission peak of AgInS<sub>2</sub>/ZnS core/shell  
42  
43 QDs was tuned to 815 nm. Zinc can not only prevent aggregation of the QDs at higher reaction  
44  
45 temperature, but can also reduce the number of defects formed on the QD surface through cation  
46  
47 exchange by zinc ions and ZnS shell growth. The optimum Ag/In/Zn precursor ratio reported by  
48  
49  
50  
51  
52  
53  
54  
55  
56  
57  
58  
59  
60

1  
2  
3 Mao *et al.*<sup>169</sup> was 1:0.68:0.08 for preparing ZAIS QDs with an average diameter of 2.5 nm and  
4  
5  
6 high QY.  
7

### 8 **3.5 Silicon Quantum Dots**

9

10  
11 In contrast with the Cd-free QDs discussed in the previous subsections, Si QDs have an  
12  
13 indirect bulk bandgap that leads to reduced radiative recombination of electrons and holes in the  
14  
15 bulk state due to mismatch between the wave vectors at the valence band maximum and  
16  
17 conduction band minimum. Matching is required by the *k*-selection rule for an optical transition  
18  
19 between them. However, finite size effects in the quantum confinement regime<sup>225-228</sup> relax the  
20  
21 wave vector matching requirement, as the valence and conduction bands become discrete states.  
22  
23  
24 If the QD surface is well passivated so that no other recombination routes are available, SiQDs  
25  
26 can exhibit efficient size-tunable PL emission, when their radius is below the exciton Bohr radius  
27  
28 of 4.2 nm.<sup>226,229-236</sup> Because of strong covalent bonding in Si, fabrication at temperatures  
29  
30 accessible in solution-phase synthesis is difficult, and high-temperature gas-phase and solid-  
31  
32 phase synthesis methods have been developed.<sup>233,235,237,238</sup> The PL QY of Si QDs produced in the  
33  
34 gas-phase, then surface passivated by covalent attachment of organic ligands and dispersed in  
35  
36 organic solvents, can exceed 60%.<sup>236</sup> Two-photon and three-photon excited PL have also been  
37  
38 demonstrated using Si QDs produced in the gas phase followed by solution-phase etching and  
39  
40 surface functionalization.<sup>239</sup> This opens up the possibility of multiphoton imaging using Si QDs.  
41  
42 Solution-phase synthesized Si QDs often exhibit blue PL associated with oxide defects at the QD  
43  
44 surface, and blue PL can also be produced by oxidation of gas-phase synthesized QDs.<sup>240,241</sup> Our  
45  
46 group introduced a combination of bottom-up gas-phase synthesis of Si nanoparticles from silane  
47  
48 gas with solution phase (top-down) etching and surface passivation which allowed production of  
49  
50 high quality, high quantum yield SiQDs with relatively narrow emission spanning the visible and  
51  
52  
53  
54  
55  
56  
57  
58  
59  
60

1  
2  
3 near-IR spectral ranges.<sup>65,231-233,242</sup> The bandgap and emission wavelengths of Si QDs can be  
4  
5  
6 tuned by functionalizing the NP surface with different ligands. For example, Zhou and co-  
7  
8 workers<sup>243</sup> successfully produced a 70 nm redshift of the PL peak of Si QDs by conjugating the  
9  
10 particle surface with organic moieties like 4-ethynyl-N,N-bis(4-methoxyphenyl)aniline  
11  
12 (MeOTPA). Due to the indirect band structure of Si QDs, their absorption efficiency in the  
13  
14 visible wavelength region is relatively low in comparison to that in the UV region, where silicon  
15  
16 has direct transitions<sup>244</sup>. Sugimoto *et al.*<sup>180</sup> demonstrated that co-doping Si QDs with boron (*p*-  
17  
18 type dopant) and phosphorus (*n*-type dopant) enhanced radiative transitions by producing donor-  
19  
20 acceptor states associated with the B and P atoms. The diameter of the co-doped Si QDs was  
21  
22 tuned from 2.8 to 5.2 nm by changing the annealing temperature from 1050°C to 1150°C during  
23  
24 Si QD preparation. The peak of the PL spectra redshifted from 760 nm to 1000 nm and the PL  
25  
26 lifetime of QDs were wavelength dependent (**Figure 15**). The PL spectra of the co-doped Si QDs  
27  
28 were not affected by the solvent polarity or pH (from 2-10), when dispersed in water or methanol  
29  
30 solutions or in acidic or alkaline media. A QY of 10.2% and long lifetime of 30  $\mu$ s were obtained  
31  
32 for the Si QDs with an average size of 2.8 nm and emission peak of 760 nm.  
33  
34  
35  
36  
37  
38  
39  
40  
41  
42  
43  
44  
45  
46  
47  
48  
49  
50  
51  
52  
53  
54  
55  
56  
57  
58  
59  
60

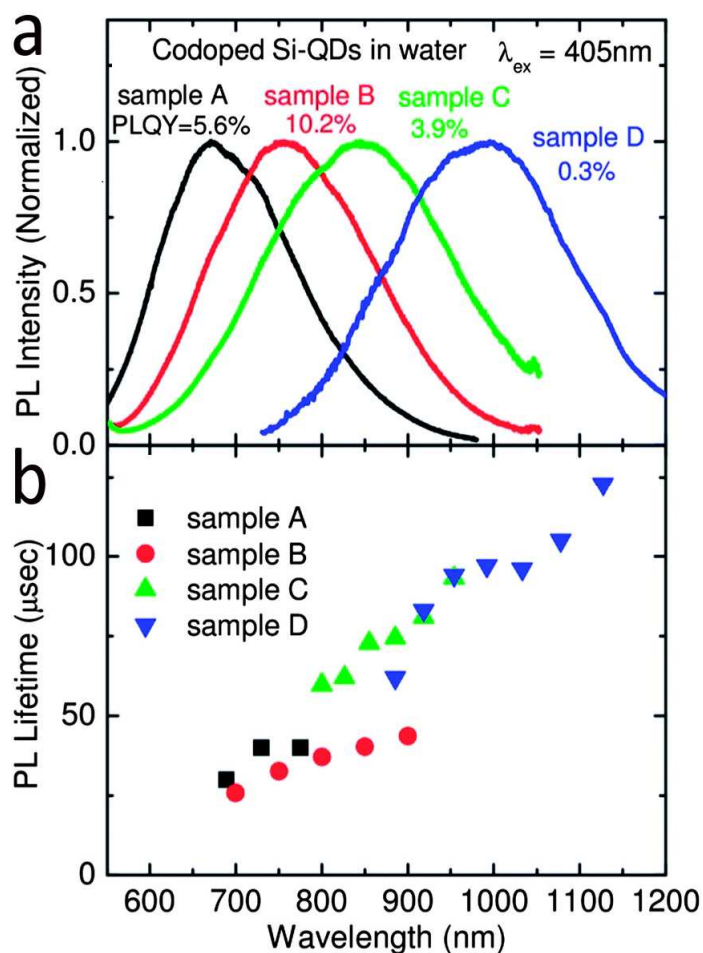


**Figure 15.** (a) PL spectra of Si QDs prepared under annealing temperature 1050°C to 1150°C. (b) PL lifetimes of Si QDs as a function of detection wavelength. Reprinted with permission from Sugimoto *et al.*<sup>180</sup> Copyright 2014 Royal Society of Chemistry.

### 3.6 Graphene Quantum Dots

Pristine graphene consists of a single layer of carbon atoms arranged in a hexagonal lattice.<sup>245</sup> The bandgap of graphene is zero and its exciton Bohr radius is infinite due to its linear

1  
2  
3 dispersion relation with conduction and valence bands that meet at Dirac points.<sup>245,246</sup>  
4  
5 Nonetheless, quantum confinement effects emerge in graphene layers of nanometer lateral  
6 dimensions, which have finite band gaps. In such graphene QDs (GQDs) PL emission can be  
7  
8 tuned by varying the size in the two lateral dimensions. The emission peaks of GQDs shift to  
9  
10 longer wavelengths with the increasing size. For example, the PL peak wavelengths of zigzag-  
11  
12 edged GQDs can be tuned to cover the entire visible spectrum by changing their diameter from  
13  
14 0.89 to 1.80 nm<sup>247</sup>. GQDs exhibit broad absorption in the UV-visible region (from 400 to 700  
15  
16 nm). Ge *et al.*<sup>70</sup> reported that the Stokes shift of GQDs was up to 205 nm, which minimizes self-  
17  
18 absorbance of their PL emission. The PL QY and lifetime measured in air or nitrogen were  
19  
20 higher than those measured in oxygen.  
21  
22

23  
24  
25  
26 According to density-functional theory (DFT) calculations, the emission peak of pristine  
27  
28 GQD with an average diameter of 2 nm should be in the red region<sup>247</sup>. However, exfoliation-  
29  
30 based preparation of graphene from bulk graphite can disrupt the sp<sup>2</sup>-hybridized carbon network  
31  
32 and introduce defects and functional groups that result in blue and green emission. Kumar and  
33  
34 co-workers demonstrated that the PL spectra 5-7 nm GQDs that were edge-functionalized with  
35  
36 amino groups depended strongly on excitation wavelength (**Figure 16a**)<sup>248</sup>. They further studied  
37  
38 the mechanism of the excitation-dependent PL emission in terms of the GQD energy band  
39  
40 variation using first principles calculations. The amino functionalization at the GQD surface  
41  
42 edges led to (i) zigzag effect (*i.e.*, band-to-band  $\pi^*-\pi$  transition at 429 nm) and (ii) interstate to  
43  
44 band transitions ( $n-\pi$  transitions at 497 nm) (**Figure 16b**). This edge functionality-induced PL  
45  
46 was also observed when the size of the GQD increased to a dimension larger than 20 nm.  
47  
48  
49  
50  
51  
52  
53  
54  
55  
56  
57  
58  
59  
60

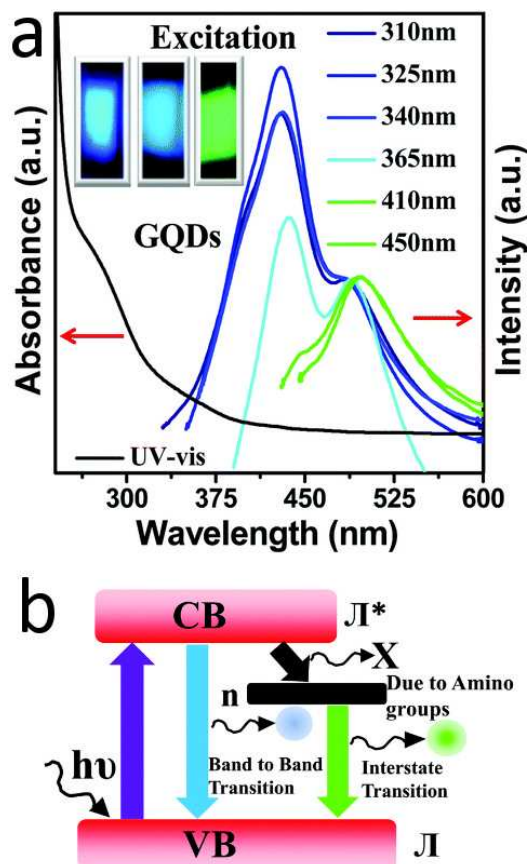


**Figure 16.** (a) UV-vis absorption and excitation dependent PL spectra of amino-functionalized GQDs. (b) Schematic representation of the energy band diagram model to explain  $\pi^*-\pi$  and  $n-\pi$  transitions. Reprinted with permission from Kumar *et al.*<sup>248</sup> Copyright 2014 Royal Society of Chemistry.

Recently, Huang *et al.*<sup>99</sup> demonstrated shifts in absorbance and PL of GQDs due to surface functionalization with folic acid. After conjugation with folate groups, the absorbance peak of the GQDs shifted from 290 nm to 370 nm. The peak at 290 nm was attributed to the  $\pi^*-\pi$  transition of aromatic carbon-carbon bonds, while the redshifted absorption peak at 370 was due

1  
2  
3 to the  $\pi^*-\pi$  transition and  $n-\pi$  transitions involving the folate molecules. The PL emission peak  
4 for the folate-conjugated GQDs was at 517 nm under 350 nm excitation. Two other factors that  
5 influence the PL spectra of GQDs, are the pH of their environment and heteroatom doping (e.g.  
6 with N).<sup>249</sup> The PL intensity of the GQDs was greater under alkaline conditions (pH=10) than  
7 under acidic conditions (pH=3), because the emissive triplet carbene state was disrupted by  
8 protonation of the free zigzag sites at the GQD surface in acid, but was restored at high pH. Sun  
9 *et al.*<sup>250</sup> reported that nitrogen doping in the aromatic rings of GQDs can significantly enhance  
10 their PL intensity and resulted in a high QY of 74% through the  $n-\pi^*$  transition between the  
11 doped nitrogen atom and the graphene structure.  
12  
13  
14  
15  
16  
17  
18  
19  
20  
21  
22  
23

### 24 **3.7 Doped ZnS/ZnSe Quantum Dots**

25  
26  
27 Doped semiconductor QDs with low intrinsic toxicity are mostly based on zinc  
28 chalcogenides doped with  $\text{Mn}^{2+}$ ,  $\text{Eu}^{2+}$ ,  $\text{Cu}^{2+}$  or  $\text{Ga}^{2+}$ .<sup>251-254</sup> The Stokes shift of these doped QDs is  
29 much larger than in conventional QDs, because the QD host absorbs the excitation light, but  
30 emission is from the dopant atom. This reduces self-absorbance and PL self-quenching. The PL  
31 emission peaks of these doped QDs can be tuned by changing the dopant concentration. Doping  
32  $\text{Mn}^{2+}$  into ZnS QDs produces strong dopant emission centered around 575 nm, by transitions  
33 between the  $\text{Mn}^{2+}$   ${}^4\text{T}_1$  first excited state and its  ${}^6\text{A}_1$  ground state.<sup>255,256</sup> Recently, Yu *et al.*<sup>257</sup>  
34 demonstrated that  $\text{Mn}^{2+}$  doped ZnS QDs had a large three-photon cross-section ( $1.3(\pm 0.5) \times$   
35  $10^{-79} \text{ cm}^6 \text{ s}^2$ ) that enabled imaging with spatial resolution exceeding the single-photon diffraction  
36 limit (**Figure 17**). The  $\text{Mn}^{2+}$  concentration in their study was 1.1%, and the QD diameter was 5.5  
37 nm. The three-photon (3P) excited PL with Mn emission at 580 nm was excited at 920 nm using  
38 a Ti:sapphire pulsed laser. The 3P PL was attributed to absorbance via the  $1\text{S}_e-1\text{S}_h$  exciton  
39 transition of the ZnS QDs followed by energy transfer to  $\text{Mn}^{2+}$ . The 3P cross-section was 10,000  
40  
41  
42  
43  
44  
45  
46  
47  
48  
49  
50  
51  
52  
53  
54  
55  
56  
57  
58  
59  
60

times that of conventional UV dyes, which allowed the use of much lower excitation power than would be possible using dyes. This reduces phototoxicity during long-term imaging studies.

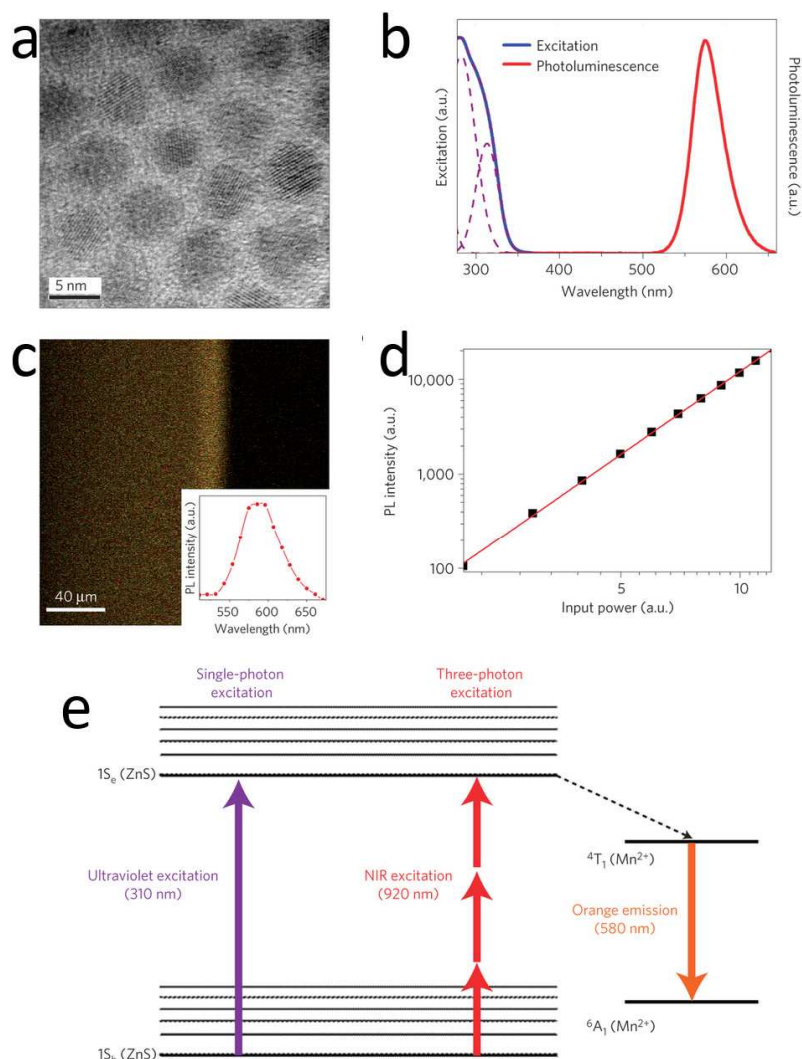


**Figure 17.** (a) TEM image of 5.5 nm ZnS:Mn QDs. (b) Normalized one-photon PLE (blue) and PL (red) spectra of ZnS:Mn QDs. The Gaussian fit to the PLE spectrum (purple dashed line) matches the  $1S_e-1S_h$  transition peaked at 314 nm. (c) Multi-photon PL image of the ZnS:Mn QD thin film under 920 nm laser excitation. Inset: luminescence spectrum extracted from the image.

1  
2  
3 (d) Log–log plot of the power dependence of PL intensity. (e) Jablonski diagram of one-photon  
4 and three-photon excited luminescence in ZnS:Mn QDs. Reprinted with permission from Yu *et*  
5  
6  
7  
8 *al.*<sup>257</sup> Copyright 2013 Nature Publishing Group.

9  
10 PL quenching of Mn-doped ZnS QDs by an anticancer drug molecule called idarubicin (IDA)  
11 was demonstrated by Ertas and co-workers<sup>258</sup>. The Mn-doped ZnS QDs had an average diameter  
12 of 3.5 nm and two absorbance peaks at 209 nm and 290 nm. Their PL peak under 290 nm  
13 excitation was ~590 nm. The hybrid IDA/Mn-doped QDs were sensitive to the presence of target  
14 double stranded DNA (dsDNA), because the IDA drug preferentially adsorbs to the dsDNA. The  
15 desorption of IDA from the QD restored the QD PL. In this manner, double stranded DNA was  
16 detected at concentrations ranging from 1.2 mM to 6.0 mM. Song *et al.* prepared Mn-doped  
17 type-II core/shell ZnTe/ZnSe QDs with emission wavelengths from blue to orange.<sup>125</sup> The QY of  
18 ZnTe/ZnSe core/shell QDs improved from 5.3% to 7% upon doping with Mn<sup>2+</sup> ions. Aqueous  
19 Cu-doped ZnSeS/ZnS QDs with a QY of 40% and impressive photostability were also fabricated  
20 by Zeng *et al.*<sup>144</sup> These QDs retained 90% of their PL intensity after 30 days of exposure to air  
21 and light. The maximum QY was obtained with a 0.43% Cu<sup>+</sup> cation fraction (Cu/(Cu+Zn) atomic  
22 ratio). Further increasing the dopant concentration decreased the QY due to nonradiative decay  
23 via interaction between Cu<sup>+</sup> ions. Emission from the doped QDs redshifted with increasing Cu<sup>+</sup>  
24 dopant concentration. Doping an element such as Cu<sup>+</sup> into ZnSe and ZnS QDs could generate  
25 charge imbalance because the preferred oxidation state differs from that of the cation of the host  
26 lattice.<sup>259</sup> The charge imbalance can produce compensating effects like lattice distortion and  
27 vacancies that can reduce PL QY. To overcome this challenge, trivalent cations have been used  
28 as codopants in Cu<sup>+</sup> doped ZnSe/ZnS QDs to form a neutral lattice. Cooper *et al.*<sup>143</sup> fabricated  
29 codoped core/shell ZnSe/ZnS QDs with Cu<sup>+</sup> as the primary dopant and In<sup>3+</sup>, Ga<sup>3+</sup>, and Al<sup>3+</sup> as  
30  
31  
32  
33  
34  
35  
36  
37  
38  
39  
40  
41  
42  
43  
44  
45  
46  
47  
48  
49  
50  
51  
52  
53  
54  
55  
56  
57  
58  
59  
60

1  
2  
3 codopants. The resulting QDs showed tunable PL emission from 430 nm to 570 nm with an  
4  
5 average PL FWHM of 80 nm (**Figure 18**). The PL from the core 8 nm diameter ZnSe QDs was  
6  
7 weak, but improved after coating with a 2 nm ZnS shell. The PL intensity of the doped QDs was  
8  
9 enhanced tenfold after surface functionalization with bidentate thiol-based ligands. This may  
10  
11 indicate that the ligands could further passivate defects at the QD surface. The undoped  
12  
13 core/shell ZnSe/ZnS had a PL peak at 437 nm. The emission peak intensity decreased after  
14  
15 doping with  $\text{Cu}^+$ , but increased with further addition of  $\text{Al}^{3+}$ . A green PL peak at 509 nm and a  
16  
17 yellow peak at 550 nm were obtained for  $\text{Cu}^+ - \text{Al}^{3+}$  codoped QDs and  $\text{Cu}^+ - \text{Ga}^{3+}$  codoped QDs.  
18  
19 The largest redshift in the PL peak, to 570 nm was achieved with  $\text{Cu}^+ - \text{In}^{3+}$  codoped QDs. The  
20  
21 PL lifetime for undoped ZnSe was 9.3 ns, but significantly increased lifetimes of 480 ns, 710 ns  
22  
23 and 940 ns were observed for the  $\text{Cu}^+ - \text{Al}^{3+}$ ,  $\text{Cu}^+ - \text{Ga}^{3+}$  and  $\text{Cu}^+ - \text{In}^{3+}$  co-doped QDs. The  
24  
25 longer lifetime demonstrated that elimination of compensation effects by codoping could  
26  
27 effectively stabilize the photogenerated carriers.  
28  
29  
30  
31  
32  
33  
34  
35  
36  
37  
38  
39  
40  
41  
42  
43  
44  
45  
46  
47  
48  
49  
50  
51  
52  
53  
54  
55  
56  
57  
58  
59  
60

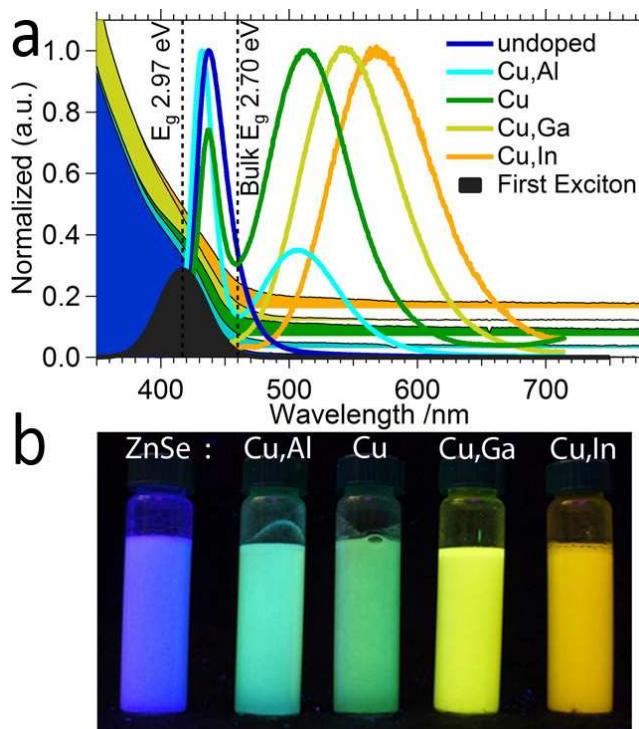


**Figure 18.** (a) Normalized absorbance and PL spectra of ZnSe/ZnS (undoped), Cu and Al-doped ZnSe/ZnS (Cu,Al), Cu-doped ZnSe/ZnS (Cu), Cu and Ga-doped ZnSe/ZnS (Cu,Ga), Cu and In-doped ZnSe/ZnS (Cu,In) QDs.  $E_g$  and bulk  $E_g$  represent the absorbance onset of the ZnSe/ZnS QDs and bandgap of bulk ZnSe, respectively. (b) Photograph of the codoped ZnSe/ZnS QD dispersions under UV excitation. Reprinted with permission from Cooper *et al.*<sup>143</sup> Copyright 2015 American Chemical Society.

### 3.8 Plasmonic Copper Chalcogenide Quantum Dots

Degenerately doped semiconductor QDs, especially copper chalcogenide QDs (*i.e.*,  $\text{Cu}_{2-x}\text{S}$ ,  $\text{Cu}_{2-x}\text{Se}$ ,  $\text{Cu}_{2-x}\text{Te}$ , etc.), have recently emerged as a new type of plasmonic nanomaterial for biomedical applications.<sup>140,141,260,261</sup> The localized surface plasmon resonance (LSPR) of noble

1  
2  
3 metal NPs has been well studied.<sup>262-264</sup> LSPR arises from collective oscillations of free charge  
4 carriers confined in sub-wavelength structures. Based on this principle, metallic NPs such as  
5 gold nanorods have been studied for photothermal cancer therapy, photoacoustic imaging, and  
6 related applications where strong absorbers are needed. More recently, LSPR in doped copper  
7 chalcogenide QDs with free carrier concentrations about an order of magnitude lower than those  
8 of noble metals has been investigated.<sup>140,172,265-268</sup> In these QDs, free holes oscillate in resonance  
9 with incoming light to produce LSPR. Wang *et al.*<sup>269</sup> studied the plasmonic properties of Cu<sub>2-x</sub>S  
10 QDs prepared from Cu<sub>3</sub>N NPs (NPs) through a one-pot approach. Cu<sub>2-x</sub>S QDs of different sizes  
11 were synthesized by changing the precursor ratios. The highly monodisperse as-synthesized QDs  
12 exhibited very weak LSPR, but slow oxidation by dissolved oxygen over hundreds to thousands  
13 of hours produced strong LSPR that was “pinned” at different wavelengths for QDs of different  
14 sizes (**Figure 19**). The pinned LSPR peak energy increased from 1.09 eV to 1.23 eV, as the QD  
15 diameter increased from 5.4 nm to 11.1 nm. This shift was attributed to reduced carrier scattering  
16 in larger QDs. The authors also investigated ternary Cu<sub>2-x</sub>S<sub>y</sub>Se<sub>1-y</sub> QDs, which exhibited similar  
17 behavior. The pinned LSPR energy after long-term oxidation increased from 0.9 eV to 1 eV as  
18 the Se anion fraction increased from 11% to 66%. This was attributed to a change in the effective  
19 mass of free holes as reported earlier by Liu *et al.*<sup>270</sup>  
20  
21  
22  
23  
24  
25  
26  
27  
28  
29  
30  
31  
32  
33  
34  
35  
36  
37  
38  
39  
40  
41  
42  
43  
44  
45  
46  
47  
48  
49  
50  
51  
52  
53  
54  
55  
56  
57  
58  
59  
60

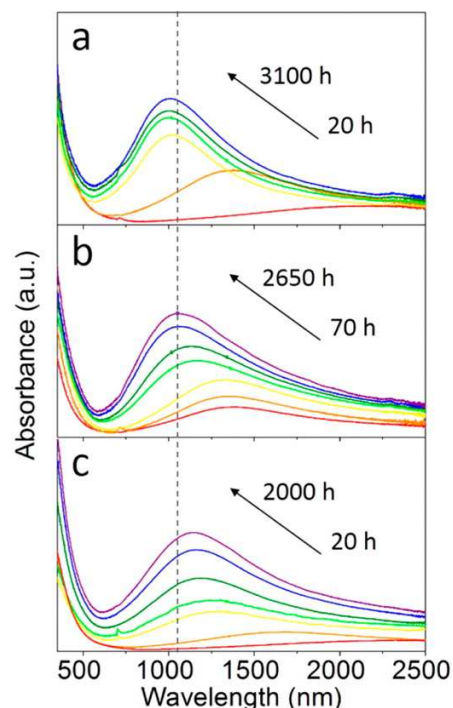
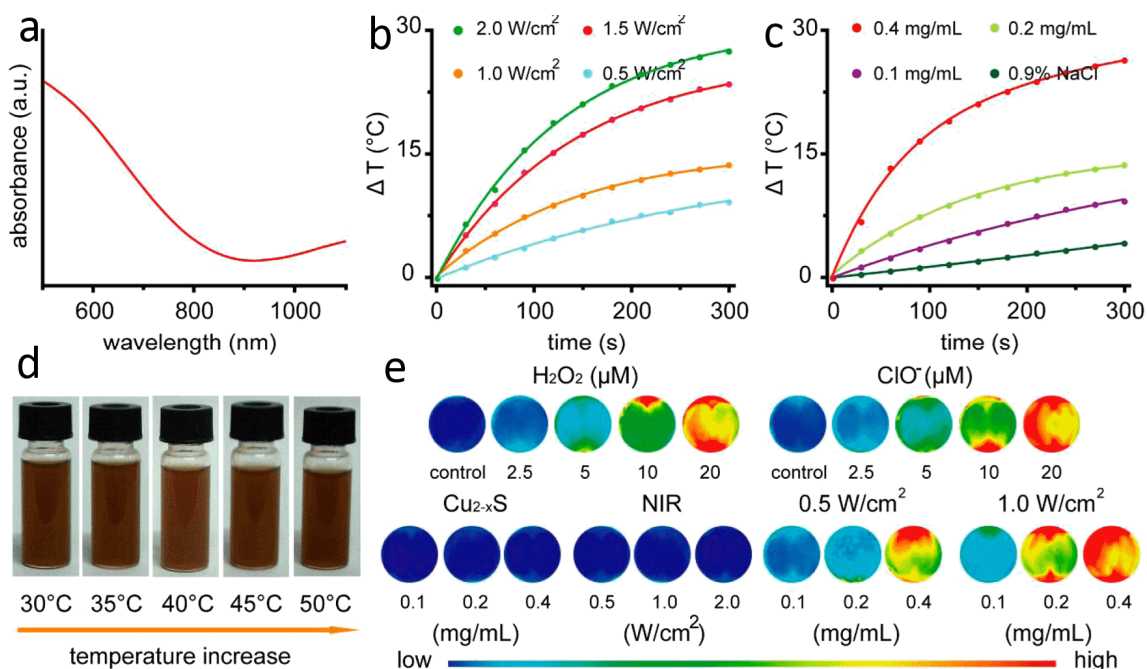


**Figure 19.** Time evolution of LSPR absorbance spectra of  $\text{Cu}_{2-x}\text{S}$  QDs due to oxidation by dissolved  $\text{O}_2$  in  $\text{CCl}_4$ . The  $\text{Cu}_{2-x}\text{S}$  QD diameters are: (a)  $11.0 \pm 0.3$  nm, (b)  $9.2 \pm 0.4$  nm, and (c)  $5.4 \pm 0.3$  nm. All samples show pinning of the LSPR band at long time. Reprinted with permission from Wang *et al.*<sup>269</sup> Copyright 2015 American Chemical Society.

$\text{Cu}_{2-x}\text{S}$  QDs with a broad LSPR absorbance band in the near-IR region (700-1100 nm) were also described by Liu and co-workers (**Figure 20**).<sup>271</sup> They first obtained oleylamine (OAm)-functionalized  $\text{Cu}_{2-x}\text{S}$  QDs in a nonpolar solvent by a thermal decomposition process. The QDs were later transferred to water through ligand exchange reactions. The OAm molecules on the QD surface were replaced by 6-aminocaproic acid. The diameter of the hydrophilic  $\text{Cu}_{2-x}\text{S}$  QDs dispersed in water ranged from 12 nm to 20 nm. The photothermal characteristics of the QDs were investigated under NIR laser illumination (980 nm), showing that the temperature of a 0.2 mg/mL dispersion of QDs in water increased by 15 °C after 5 min illumination ( $1.5 \text{ W/cm}^2$ ). The

1  
2  
3 temperature increase was much greater than the 5 °C change for control samples without QDs.  
4  
5 Photo-induced generation of reactive oxygen species from the Cu<sub>2-x</sub>S QDs was also observed.  
6  
7 The Cu<sup>2+</sup> ions could be reduced to Cu<sup>+</sup> ions by glutathione or ascorbic acid in biological media.  
8  
9  
10  
11 Reactive oxygen species (ROS) were then produced by the Cu<sup>+</sup> ions. Generation of ROS only  
12  
13 occurred under NIR illumination. ROS production was quantified using oxidation-responsive  
14  
15 dichlorofluorescein diacetate, which is oxidized by ROS to fluorescent 2,7-dichlorofluorescein.  
16  
17 In addition to Cu<sub>2-x</sub>S, copper–tin–sulfide (Cu<sub>2</sub>SnS<sub>3</sub>) QDs also exhibit tunable LSPR.<sup>272</sup> The  
18  
19 crystal phase and the size of the Cu<sub>2</sub>SnS<sub>3</sub> QDs were strongly dependent on the Cu and Sn  
20  
21 precursor ratios and the reactivity of the chalcogenide source. Different Cu:Sn elemental ratios  
22  
23 correspond to different doping levels (*i.e.*, different cation vacancy concentrations) in the QDs.  
24  
25 The LSPR peak was red-shifted and damped with increasing Sn content, disappearing  
26  
27 completely at a Cu-Sn ratio of 1:3.  
28  
29  
30  
31  
32  
33

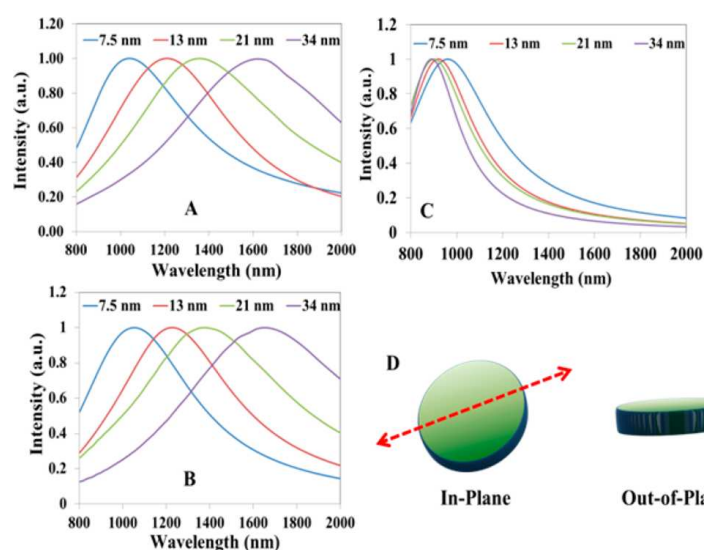


1  
2  
3 **Figure 20.** Photothermal characteristics of plasmonic  $\text{Cu}_{2-x}\text{S}$  QDs. (a) UV–vis–NIR absorbance  
4 spectra of  $\text{Cu}_{2-x}\text{S}$  QDs in water. Temperature change of (b)  $\text{Cu}_{2-x}\text{S}$  QDs at 0.2 mg/mL irradiated  
5 by a NIR laser (980 nm) with different power intensities and (c)  $\text{Cu}_{2-x}\text{S}$  QDs at different  
6 concentrations irradiated at  $1.5 \text{ W/cm}^2$ . (d) Photos of  $\text{Cu}_{2-x}\text{S}$  NCs in a 0.9% NaCl solution  
7 incubated at various temperatures. (e) Fluorescence imaging of ROS generation detected by  
8 DCFH-DA assay. (Upper) Standard  $\text{H}_2\text{O}_2$  and NaClO solutions with different concentrations  
9 treated with DCFH-DA. (Lower) Experimental samples under different intensities of NIR power  
10 intensities and with various concentrations treated with DCFH-DA. Reprinted with permission  
11 from Liu *et al.*<sup>271</sup> Copyright 2015 American Chemical Society.  
12  
13  
14  
15  
16  
17  
18  
19  
20  
21  
22  
23

24 As discussed in Chapter 2.4, the PL and LSPR intensity of copper chalcogenide ( $\text{Cu}_{2-x}\text{S}$ ,  
25  $\text{Cu}_{2-x}\text{Se}$ , or  $\text{Cu}_{2-x}\text{Te}$ ) QDs during oxidation and reduction are inversely correlated.<sup>142</sup> A high  
26 concentration of free charge carriers in these QDs is necessary to observe LSPR. However,  
27 transfer of energy from photogenerated excitons to the LSPR modes quenches PL. Thus,  
28 although these plasmonic QDs can exhibit both excitonic and plasmonic absorbance features,  
29 those with strong LSPR absorbance typically do not exhibit significant PL.  
30  
31  
32  
33  
34  
35  
36  
37  
38

39 The LSPR absorbance spectrum of plasmonic semiconductors can be tuned not only by  
40 changing their composition and crystal structure, which in turn change the free carrier  
41 concentration and effective mass, but also by changing the shape of the nanostructures.<sup>261</sup> Liu *et*  
42 *al.* demonstrated room-temperature synthesis of covellite CuS nanoplatelets with a fixed  
43 thickness of about 4 nm and diameters ranging from  $\sim 4 \text{ nm}$  to  $\sim 33 \text{ nm}$ .<sup>273</sup> Such nanoplatelets  
44 exhibit in-plane and out-of-plane plasmon resonances, but the in-plane resonance dominates.  
45  
46  
47  
48  
49  
50  
51  
52  
53  
54  
55  
56  
57  
58  
59  
60  
With increasing aspect ratio of the nanoplatelets, the LSPR peak wavelength shifted from below  
1000 nm to above 1600 nm, all at a fixed composition, crystal phase, and free carrier

1  
2  
3 concentration. The aspect-ratio dependence of the LSPR peak wavelength was quantitatively  
4 modeled, reproducing the experimental results (**Figure 21**). This aspect-ratio based tuning of the  
5 plasmon resonance is entirely analogous to that observed in gold nanorods.<sup>274</sup> The key difference  
6 is that in plasmonic semiconductors, this shape-based LSPR tuning can be combined with  
7 composition- and phase-based tuning, providing greater flexibility in the combinations of size,  
8 shape, and LSPR energy that can be achieved.  
9  
10  
11  
12  
13  
14  
15  
16



17  
18  
19  
20  
21  
22  
23  
24  
25  
26  
27  
28  
29  
30  
31  
32  
33  
34  
35  
36  
37  
38 **Figure 21.** Comparison of smoothed experimental (A) and simulated (in-plane (B) and out-of-  
39 plane (C)) spectra for CuS nanoplatelets of four different diameters, at fixed thickness of ~4 nm.  
40  
41 (D) Illustration of in-plane and out-of-plane modes. Reproduced with permission from Liu *et*  
42 *al.*<sup>273</sup>, Copyright 2015 American Chemical Society.  
43  
44  
45  
46  
47  
48  
49  
50  
51  
52  
53  
54  
55  
56  
57  
58  
59  
60

## 4.0. Preparation of Biocompatible Cadmium-Free Quantum Dots

Developments in the synthesis and surface functionalization of Cd-free QDs provide the basis for their eventual adoption as efficient nanotags for *in vitro* and *in vivo* applications. Currently, many research groups are developing new techniques for preparing biologically applicable Cd-free QDs. By changing the precursor ratios, reaction temperatures and shell compositions, one can optimize the QD size, quantum yield, and emission wavelength. Moreover, the wide variety of capping molecules that can be used on the surfaces of QDs allow creation of multifunctional nanoprobes that simultaneously serve as drug carriers and imaging probes. In this section, we review recent progress on the synthesis of Cd-free QDs for *in vitro* and *in vivo* applications. This builds on the discussion in the previous section, but focuses on the development of synthetic methods for preparing these Cd-free QDs in forms useful for biological applications.

### 4.1. InP and InP/ZnS Quantum Dots

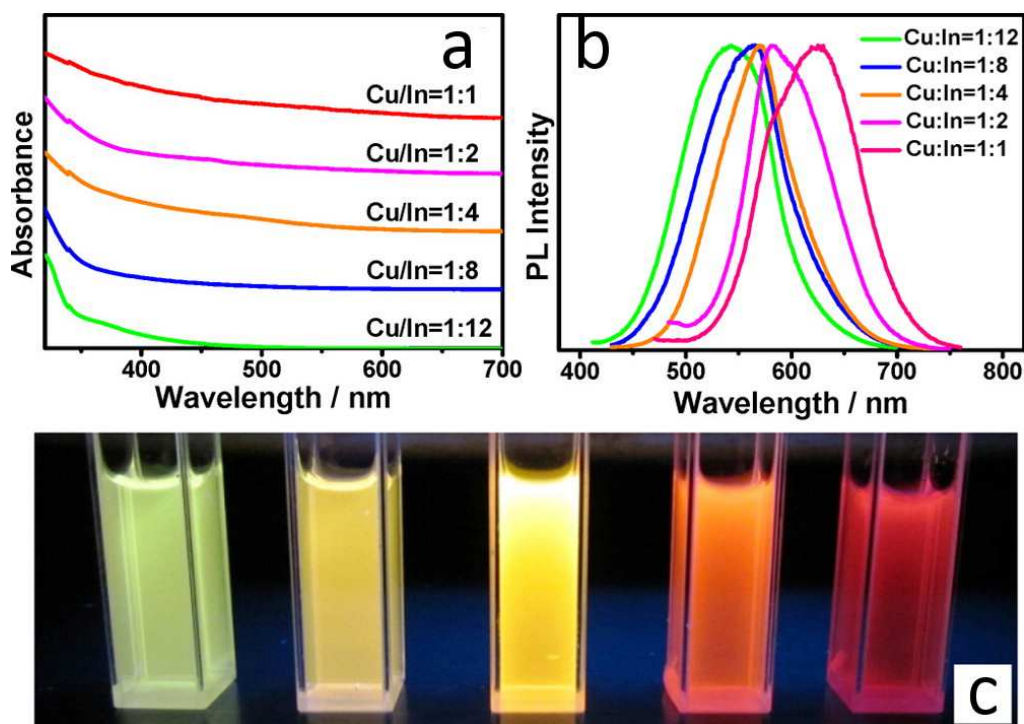
Indium phosphide (InP) QDs are III–V semiconductor nanocrystals with PL properties similar to Cd-based II–VI QDs, but better stability in biological environments due to their more covalent bonding.<sup>275</sup> In part because of their similarity to CdSe QDs, InP QDs have been among the first Cd-free QDs to become commercially available for biological research applications. The intrinsic lower cytotoxicity and long-term *in vivo* biocompatibility of InP QDs have been demonstrated by Brunetti *et al.* and our group.<sup>276,277</sup> The first synthesis of colloidal InP QDs was reported by Micic and co-workers in 1994.<sup>278</sup> Indium precursors were first prepared by reacting  $\text{InCl}_3$  with  $\text{Na}_2\text{C}_2\text{O}_4$  in  $\text{CH}_3\text{CN}$  at a 1:1 molar ratio. The In precursors were added to tris(trimethylsilyl)phosphine ( $\text{P}(\text{SiMe}_3)_3$  or  $\text{P}(\text{TMS})_3$ ) in trioctylphosphine oxide (TOPO), which

1  
2  
3 served as a stabilizing agent. The diameter of the nearly monodisperse InP QDs was  $2.5 \pm 0.19$   
4 nm. Later, Battaglia *et al.*<sup>279</sup> demonstrated a more facile and “greener” synthesis method for InP  
5 QDs that required only 3 to 4 h and used a less toxic solvent (octadecene, ODE) in place of  
6 TOPO, with fatty acids (*e.g.*, palmitic acid and myristic acid) as surface ligands to cap the QDs.  
7 Briefly, the In precursors were obtained by heating indium acetate ( $\text{In}(\text{Ac})_3$ ) in solutions of fatty  
8 acid ligands in ODE at 100-120°C until the solution became clear. Phosphorus precursors  
9 containing  $\text{P}(\text{TMS})_3$  in ODE were added to the In precursors in a molar ratio of 2:1. The  
10 resulting InP QDs were  $3.1 \pm 0.15$  nm in diameter. They were dispersible in nonpolar solvents  
11 and showed clear PL. To reduce the toxicity of InP QDs for *in vitro* and *in vivo* applications, our  
12 group developed a one-pot approach for preparing InP/ZnS core/shell QDs with particle size of  
13 15-20 nm.<sup>42,277</sup> The ZnS shell coating protected the InP core QD from degradation in biological  
14 systems, minimizing the release of  $\text{In}^{3+}$  ions. The InP core QDs were prepared by heating  
15  $\text{In}(\text{Ac})_3$ , myristic acid and ODE, followed by injection of  $\text{P}(\text{TMS})_3$  in ODE. Subsequently, zinc  
16 2-ethylhexanoate and sulfur dissolved in oleylamine were added to the InP cores. The InP/ZnS  
17 core/shell QDs solutions were purified by centrifugation and redispersion. Ligand exchange  
18 using mercaptosuccinic acid made the QDs water dispersible. The emission peak of the QDs was  
19 centered at 650 nm with a QY of 25 to 30%. More recently, Brunetti *et al.*<sup>160,276</sup> synthesized  
20 InP/ZnS core/shell QDs with a QY of 60% by using zinc carboxylate as both the Zn shell  
21 precursor and stabilizing agent. In that study, zinc undecylate, hexadecylamine, stearic acid  
22 and indium chloride were first dissolved in ODE under nitrogen at room temperature. Injection  
23 of  $\text{P}(\text{TMS})_3$  into the heated Zn precursor solution produced the InP core QDs. For ZnS shell  
24 growth, zinc diethyldithiocarbamate was added into the core QD solution. The hydrodynamic  
25 diameter of the dispersed InP/ZnS core/shell QDs was  $11.3 \pm 0.6$  nm.  
26  
27  
28  
29  
30  
31  
32  
33  
34  
35  
36  
37  
38  
39  
40  
41  
42  
43  
44  
45  
46  
47  
48  
49  
50  
51  
52  
53  
54  
55  
56  
57  
58  
59  
60

#### 4.2. $\text{CuInS}_2$ , $\text{CuInS}_2/\text{ZnS}$ and $\text{CuInZnS}/\text{ZnS}$ Quantum Dots

Ternary  $\text{CuInS}_2$  QDs are Cd- and Pb-free alternatives to intrinsically toxic II-VI and IV-VI QDs as PL labels. The  $\text{CuInS}_2$  direct band gap of  $\sim 1.5$  eV allows these QDs to have tunable emission across visible and near-IR wavelengths combined with large molar extinction coefficients.<sup>122,280</sup> Liu *et al.*<sup>162</sup> demonstrated a facile one-pot hydrothermal preparation method for aqueous  $\text{CuInS}_2$  QDs with an average size of 2.2 nm and PL at 660 nm, using mercaptopropionic acid (MPA) as a capping ligand. Briefly, copper chloride ( $\text{CuCl}_2$ ) and indium chloride ( $\text{InCl}_3$ ) were mixed with MPA in water at pH 11.3 and room temperature. Thiourea ( $\text{CS}(\text{NH}_2)_2$ ) was added and the mixture was heated in an autoclave for 21 h to form the  $\text{CuInS}_2$  QDs. Molar ratios of Cu:In:S and Cu:MPA were 1:1:2 and 1:12. Although these QDs initially had a maximum QY of only  $\sim 3\%$ , after adding a ZnS shell the QY increased to 40-60%. The ZnS shell has a large bandgap of 3.7 eV that forms a type I band alignment with the  $\text{CuInS}_2$  cores.<sup>28,281,282</sup> In addition, the lattice mismatch between the ZnS shell and the  $\text{CuInS}_2$  cores is only  $\sim 2.2\%$ , allowing formation of defect-free shells and core/shell interfaces. Li *et al.*<sup>163</sup> prepared  $\text{CuInS}_2/\text{ZnS}$  QDs with PL peaks ranging from 550 to 815 nm and QY of 60% through a two-step approach. They used 1-dodecanethiol (DDT) as both the sulfur precursor and the stabilizing agent during the core QD formation. The  $\text{CuInS}_2$  core QDs were prepared by mixing indium acetate and copper iodide with dodecanethiol and octadecene under argon. QD emission wavelengths redshifted with increasing reaction time. To form the ZnS shell, zinc stearate and zinc ethylxanthate were added to the core QD solutions at the same temperature. The authors transferred the QDs to water for *in vivo* imaging by ligand exchange using dihydrolipoic acid (DHLA). The PL lifetimes of the core/shell QDs reached hundreds of ns.  $\text{CuInS}_2/\text{ZnS}$  QDs with tunable emission from yellow to red and a maximum QY of 65% were prepared by Nam and co-

workers.<sup>283</sup> In their method, copper(I) iodide, indium acetate, 1-dodecanethiol, and 1-octadecene were heated in a sealed autoclave to produce CuInS<sub>2</sub> core QDs with a PL QY up to 8.8%. Zinc ethylxanthate, dimethylformamide (DMF) and toluene were then added to the core QD dispersion and autoclaved. Along with dramatically increased QY, blue shifts of the emission peaks were observed for the core/shell QDs due to the decrease of the core QD size during the shell growth. Later, Chen *et al.*<sup>165</sup> demonstrated a green aqueous-phase synthesis of CuInS<sub>2</sub>/ZnS QDs with a QY of 38% using sodium citrate and L-glutathione as co-stabilizers. Briefly, CuInS<sub>2</sub> core QDs were prepared by mixing CuCl<sub>2</sub> and InCl<sub>3</sub> at a molar ratio of 1:4 with sodium citrate (4:1 to In<sup>3+</sup>) and L-glutathione, followed by injection of Na<sub>2</sub>S. An aqueous mixture of zinc acetate, thiourea and L-glutathione was added to the core QD dispersions. The emission peaks of the QDs could be tuned from 543 to 625 nm by changing the Cu:In precursor ratio (**Figure 22**).



1  
2  
3 **Figure 22.** (a) UV–vis absorbance and (b) PL spectra of Cu–In–S/ZnS QDs with varying Cu:In  
4 ratios. (c) Digital photograph of Cu–In–S/ZnS QDs under UV illumination. Reprinted with  
5 permission from Chen *et al.*<sup>165</sup> Copyright 2013 American Chemical Society.  
6  
7  
8  
9

10  
11  
12  
13 More recently, Xiong *et al.* reported a microwave-assisted synthesis method for preparing  
14 water-dispersible CuInS<sub>2</sub>/ZnS QDs in which glutathione (GSH) was used as a stabilizing agent  
15 (ligand).<sup>166</sup> CuInS<sub>2</sub> core QDs were prepared by mixing aqueous Cu(NO<sub>3</sub>)<sub>2</sub>, InCl<sub>3</sub>, and GSH with  
16 aqueous Na<sub>2</sub>S at pH 8.5, then heating in a Discover (CEM) microwave system. Zinc acetate and  
17 Na<sub>2</sub>S were added to the core QD solution to form the core/shell QDs. The QDs had an average  
18 diameter of 3.3 nm and PL tunable from 540 to 680 nm by varying the Cu:In precursor ratio. The  
19 QD PL showed a long lifetime of 690 ns. Guo *et al.*<sup>91</sup> demonstrated that adding zinc ions in the  
20 CuInS<sub>2</sub> core synthesis before shell coating could reduce the blue shift of the PL during ZnS shell  
21 growth. This is attributed to ion accumulation and inhibition of cation exchange. ZnCuInS core  
22 QDs were prepared by mixing zinc stearate (Zn(SA)<sub>2</sub>), copper iodide (CuI), indium acetate  
23 (In(Ac)<sub>3</sub>) and oleic acid (OA) with 1-dodecanethiol (DDT) and 1-octadecene (ODE) under argon.  
24 The emission wavelength of the ZnCuInS<sub>2</sub> core QDs was tuned from 600 to 815 nm by varying  
25 the Cu:Zn precursor ratio from 2:1 to 1:5. For the ZnS shell coating, the core QDs were reacted  
26 with sulfur powder dissolved in ODE/oleylamine (10:1) and Zn(SA)<sub>2</sub>. The ZnCuInS/ZnS  
27 (ZCIS/ZnS) core/shell QDs were transferred to water using poly(maleic anhydride-alt-1-  
28 octadecene) (PMAO) molecules.  
29  
30  
31  
32  
33  
34  
35  
36  
37  
38  
39  
40  
41  
42  
43  
44  
45  
46  
47  
48  
49

50  
51 Later, the same group<sup>284</sup> developed a direct colloidal preparation method for water-  
52 dispersible ZnCuInS/ZnS QDs without the phase transfer steps that were required in the previous  
53 report. Briefly, hydrophilic ZnCuInS QDs were synthesized by mixing copper iodide (CuI),  
54  
55  
56  
57  
58  
59  
60

1  
2  
3 indium acetate ( $\text{In}(\text{Ac})_3$ ), zinc stearate and 6-sulfanyl-1-hexanol (MPH) with polyethylene glycol  
4  
5 (PEG, 400 Da). ZnS shells were added by injection of zinc stearate dissolved in low molecular  
6  
7 mass PEG. Here, the hydrophilic MPH ligands with mercapto and hydroxyl groups served as  
8  
9 both sulfur precursor and stabilizing agent. The emission wavelength of the ZnCuInS core/shell  
10  
11 QDs was tuned from 580 nm to 710 nm by changing the reaction time from 10 min to 60 min  
12  
13 (Figure 23). With the ZnS shell coating, the QY of the QDs increased from less than 5% to 26%.  
14  
15 In another study, Han *et al.* employed a lipophilic silane to encapsulate hydrophobic  $\text{CuInS}_2/\text{ZnS}$   
16  
17 QDs in silica beads.<sup>199</sup> The  $\text{CuInS}_2/\text{ZnS}@SiO_2$  nanocomplexes maintained a reasonably small  
18  
19 diameter of 17-25 nm. Holo-transferrins (Tf) were then conjugated to these QDs as targeting  
20  
21 molecules. Bright red PL was observed from HeLa cells incubated with  $\text{CuInS}_2/\text{ZnS}@SiO_2@Tf$   
22  
23 NPs.  
24  
25  
26  
27  
28  
29  
30  
31  
32  
33  
34  
35  
36  
37  
38  
39  
40  
41  
42  
43  
44  
45  
46  
47  
48  
49  
50  
51  
52  
53  
54  
55  
56  
57  
58  
59  
60

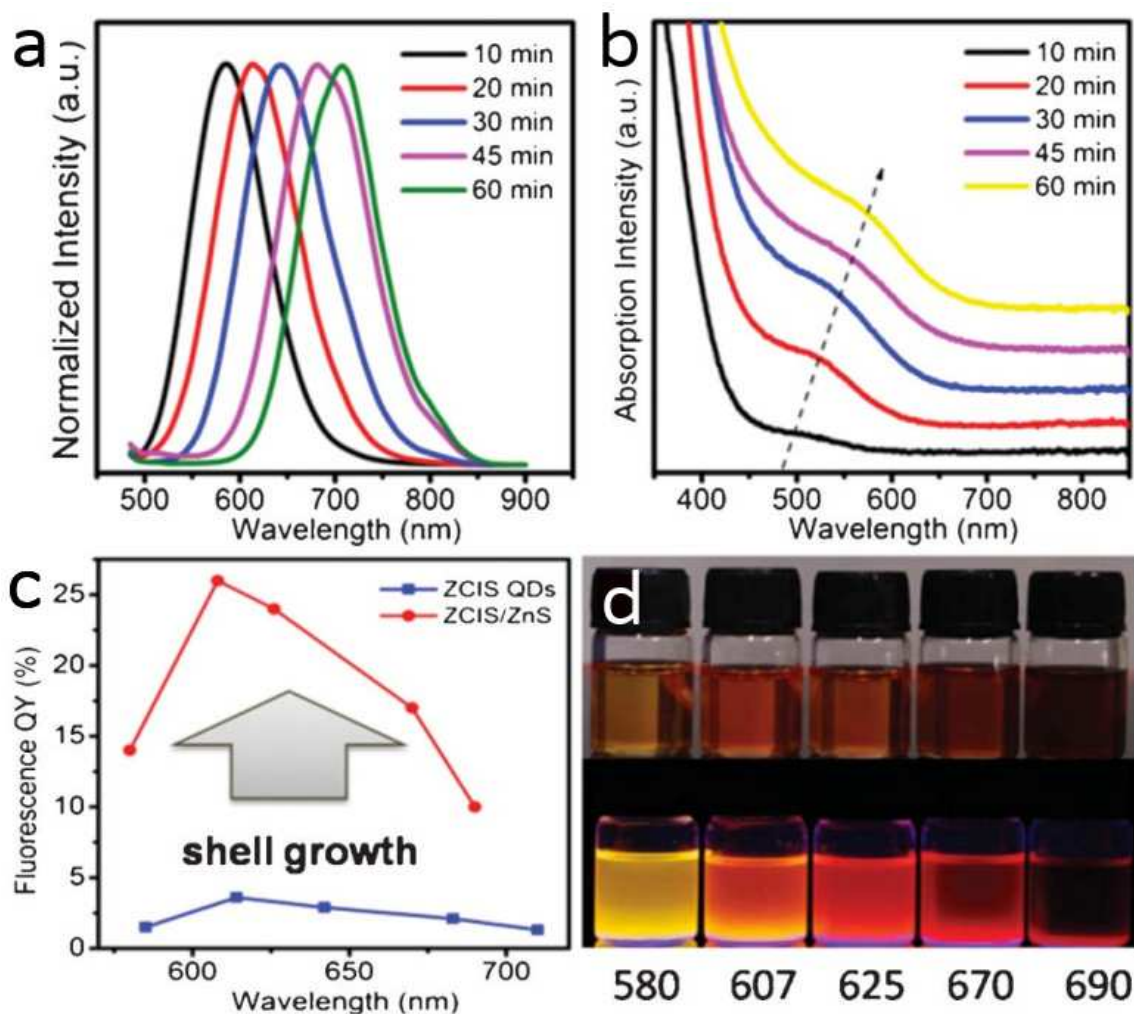


**Figure 23.** Temporal evolution of (a) PL emission spectra and (b) UV-vis absorbance spectra of ZCIS QDs dispersed in water. (c) PL QY and emission peak wavelength of QDs before and after the ZnS shell growth. (d) Digital photograph of the ZCIS/ZnS QDs dispersed in ethanol, taken under a 365 nm UV lamp. Reprinted with permission from Guo *et al.*<sup>284</sup> Copyright 2013 Royal Society of Chemistry.

#### 4.3. Ag<sub>2</sub>S and Ag<sub>2</sub>Se Quantum Dots

Ag<sub>2</sub>S and Ag<sub>2</sub>Se QDs are promising NIR-II nanoprobes for *in vivo* imaging and detection with tunable emission wavelengths ranging from 1000 nm to 1400 nm.<sup>208,285,286</sup> Imaging in the

1  
2  
3 NIR-II window allows one to obtain a maximum penetration depth up to 5 mm with high fidelity  
4 and signal-to-noise ratio because tissue autofluorescence and scattering signals are minimized in  
5 this wavelength range. The first synthesis of Ag<sub>2</sub>S QDs with emission in the NIR II region was  
6 demonstrated by Du and co-workers.<sup>287</sup> In a typical reaction, silver diethyldithiocarbamate  
7 (Ag(DDTC)) was mixed with oleic acid (OA), 1-octadecane (ODE) and octadecylamine (ODA).  
8 The mixture was heated to 100 °C to remove dissolved oxygen, then reacted at 200 °C for 30  
9 min under nitrogen. The QDs had an average diameter of 10 nm with high monodispersity and  
10 peak PL emission at 1058 nm under 785 nm excitation. Later, Jiang *et al.*<sup>138</sup> reported a two-step  
11 seed-mediated growth method for Ag<sub>2</sub>S QDs (1.5 nm - 4.6 nm) with PL emission tunable from  
12 690 to 1227 nm. The PL emission wavelength was tuned by changing the reaction temperature.  
13 Here, Ag<sub>2</sub>S QD seeds were first prepared by mixing silver acetate (AgAc) solutions with 1-  
14 octylamine (OA), 1-octadecene, and myristic acid (MA), followed by rapid injection of  
15 hexamethyldisilathiane ((TMS)<sub>2</sub>S) at a fixed reaction temperature to initiate QD nucleation.  
16 During the seed-mediated growth process, another Ag precursor (silver nitrate and OA in toluene)  
17 and sulfur precursor (S powder dissolved in toluene) were added to the Ag<sub>2</sub>S QD seed solution to  
18 grow the QDs to the desired size (**Figure 24**).  
19  
20  
21  
22  
23  
24  
25  
26  
27  
28  
29  
30  
31  
32  
33  
34  
35  
36  
37  
38  
39  
40  
41  
42  
43  
44  
45  
46  
47  
48  
49  
50  
51  
52  
53  
54  
55  
56  
57  
58  
59  
60

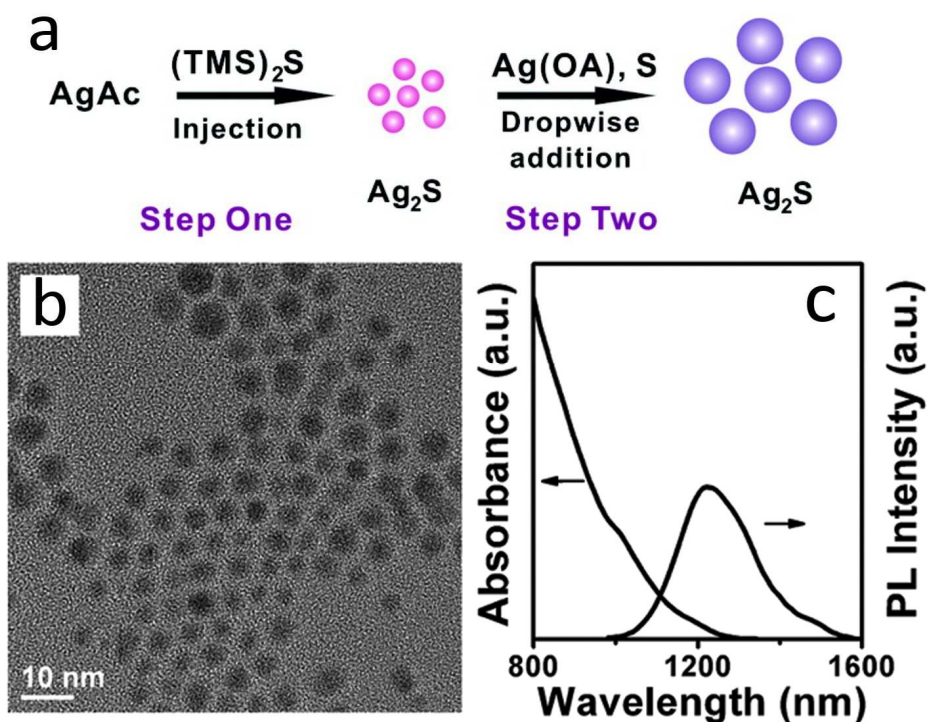


**Figure 24.** (a) Scheme of two-step synthesis of NIR Ag<sub>2</sub>S QDs. (b) TEM image and (c) absorbance and PL spectra of Ag<sub>2</sub>S QDs synthesized in step two. Reprinted with permission from Jiang *et al.*<sup>138</sup> Copyright 2012 American Chemical Society.

Hocaoglu *et al.*<sup>288</sup> demonstrated a one-step aqueous synthesis of Ag<sub>2</sub>S QDs with emission wavelengths from 780 to 950 nm and used them as biocompatible PL labels for *in vitro* imaging. The QDs had a QY of 7 to 39% and showed low cytotoxicity to mouse embryo fibroblast NIH/3T3 cells even at concentrations as high as 600 μg/mL. The emission peak of the QDs was tuned by changing the Ag to S precursor ratio or the MPA to Ag ratio (**Figure 25**).

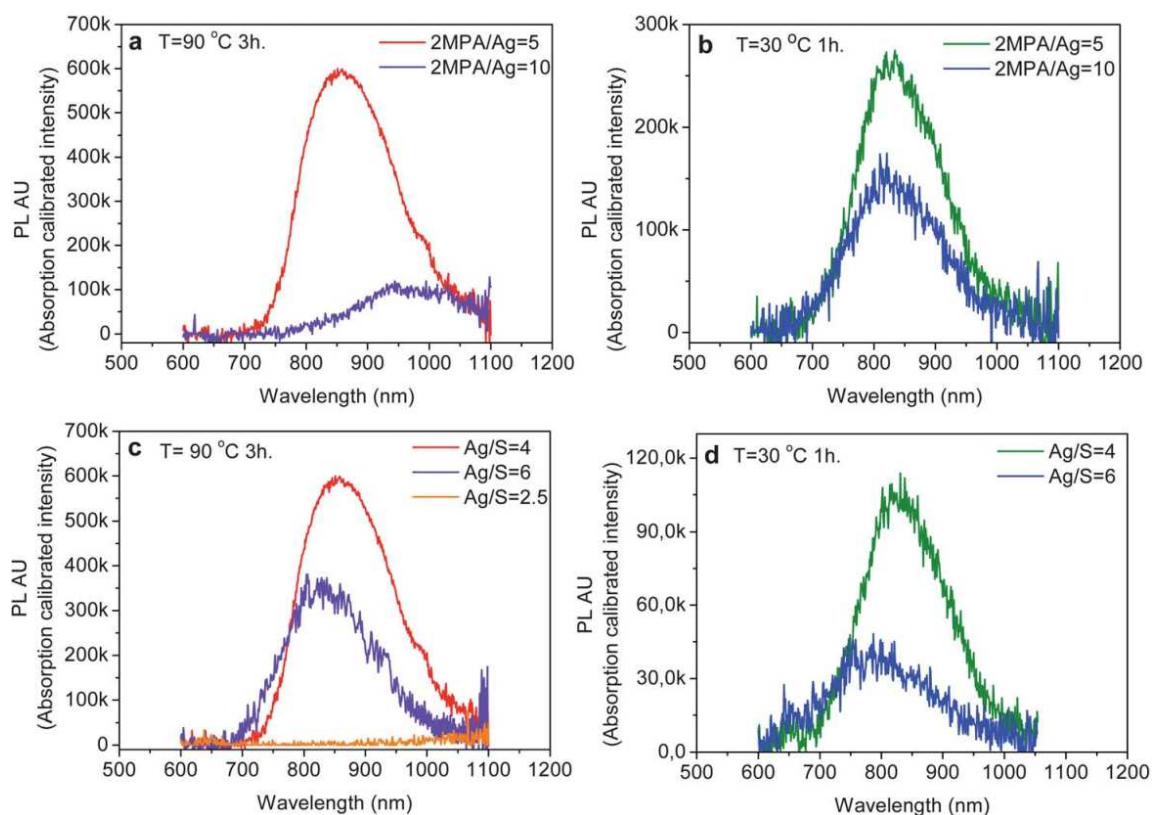


**Figure 25.** PL spectra of Ag<sub>2</sub>S QDs prepared at different 2MPA/Ag ratios at (a) 90 °C and (b) 30 °C, and at different Ag/S ratios at (c) 90 °C and (d) 30 °C. Reprinted with permission from Hocaoglu *et al.*<sup>288</sup> Copyright 2012 Royal Society of Chemistry.

A similar one-step method was reported by Jiang *et al.*<sup>8</sup> using 3-mercaptopropionic acid (3-MPA) and ethylene glycol (EG) rather than 2-MPA. In this case, the QD surface was terminated with carboxyl groups. The QD PL emission wavelength was broadly tunable, from 510 nm to 1221 nm, by varying the growth time. Typically, the precursor solutions of AgNO<sub>3</sub>, MPA and EG were first reacted at 110 °C under argon, then heated to 145 °C for several minutes. During reaction, the white solution became yellowish and then dark brown. Ag<sub>2</sub>S QDs were collected by

1  
2  
3 centrifugation and redispersed in DI water for further use, including *in vivo* small animal  
4  
5  
6 imaging.

7  
8 Zhang *et al.*<sup>289</sup> synthesized PEGylated-Ag<sub>2</sub>S QDs with strong NIR-II luminescence at 1200  
9  
10 nm through a facile thermal decomposition approach based on a single-source precursor.<sup>21,290</sup>  
11  
12 They also evaluated the long-term *in vivo* biodistribution and toxicity of these QDs in mice. They  
13  
14 prepared a single-source precursor, (C<sub>2</sub>H<sub>5</sub>)<sub>2</sub>NCS<sub>2</sub>Ag, by mixing AgNO<sub>3</sub> with  
15  
16 (C<sub>2</sub>H<sub>5</sub>)<sub>2</sub>NCS<sub>2</sub>Na·3H<sub>2</sub>O (Na(DDTC)) then adding 1-dodecanethiol (DDT). A ligand exchange  
17  
18 process was used to replace the DDT with dihydrolipoic acid (DHLA), thereby making the QDs  
19  
20 hydrophilic. The PEG-conjugated Ag<sub>2</sub>S QDs were obtained after 30 min sonication of the  
21  
22 DHLA-capped QDs with a solution of six-armed PEG and EDC/NHS. Wang *et al.*<sup>290</sup>  
23  
24 demonstrated that the emission wavelength of the Ag<sub>2</sub>S QDs prepared by this method was  
25  
26 independent of the particle size. However, the PL intensity decreased with increasing QD  
27  
28 diameter from 5.4 nm to 10 nm. Hong *et al.*<sup>21</sup> studied the photostability of PEGylated-Ag<sub>2</sub>S QDs  
29  
30 under 808 nm excitation at 0.14 W/cm<sup>2</sup>. The PL intensity remained stable for 200 s and was  
31  
32 reduced by only 50% after 30 min continuous irradiation, which was much longer than the  
33  
34 typical illumination time of 2 min for *in vivo* imaging. A one-pot synthesis method for preparing  
35  
36 bovine serum albumin (BSA)-functionalized Ag<sub>2</sub>S QDs with near IR PL was developed by  
37  
38 Wang and co-workers.<sup>291</sup> They further conjugated these QDs with vascular endothelial growth  
39  
40 factor antibodies (antiVEGF) for targeted *in vivo* imaging of VEGF positive U-87 MG human  
41  
42 glioblastoma tumors in mice. The Ag<sub>2</sub>S QDs were synthesized by first mixing AgNO<sub>3</sub> and BSA  
43  
44 solutions. A Na<sub>2</sub>S solution was quickly injected into the BSA-Ag<sup>+</sup> mixture with intense agitation.  
45  
46 The mixture was then incubated at 37 °C for 12 h. The color of the mixture changed from light  
47  
48 yellow to colorless and finally reddish brown. For VEGF bioconjugation, antiVEGF was first  
49  
50  
51  
52  
53  
54  
55  
56  
57  
58  
59  
60

1  
2  
3 processed at room temperature with N-(3-dimethylaminopropyl)-N'-ethylcarbodiimide  
4 hydrochloride (EDC) and N-hydroxysulfosuccinimide sodium salt (Sulfo-NHS) in PBS for 15  
5  
6 min. The antiVEGF mixtures were then added to the BSA-Ag<sub>2</sub>S QD dispersions and reacted at  
7  
8  
9 4 °C for 12 h to obtain antiVEGF-Ag<sub>2</sub>S QDs for biological labeling.

10  
11 To obtain both UV/blue (380-450 nm) and near-IR (1155-1175 nm) PL from a single  
12  
13 nanostructure, Shen *et al.*<sup>292</sup> designed Ag<sub>2</sub>S-ZnS heteronanostructures having a matchstick shape  
14  
15 with Ag<sub>2</sub>S QDs as the heads and ZnS quantum rods as the stems. These hybrid quantum rods  
16  
17 were synthesized by a one-pot thermal decomposition method, and their size could be tuned by  
18  
19 changing the ratio between the silver diethyldithiocarbamate (Ag(DDTC)) and zinc  
20  
21 diethyldithiocarbamate (Zn(DDTC)<sub>2</sub>) precursors. Ag(DDTC) and Zn(DDTC)<sub>2</sub> precursors were  
22  
23 first prepared by mixing silver nitrate/zinc acetate and sodium diethyldithiocarbamate  
24  
25 (Na(DDTC)) for 3 h. Then, Ag(DDTC) and Zn(DDTC)<sub>2</sub> precursors were mixed with oleylamine  
26  
27 and 1-dodecanethiol and heated to 70 °C for 20 min and then to 160 °C for 30 min. The diameter  
28  
29 of the Ag<sub>2</sub>S head in the heterostructures was around 8.5 nm and the stem size was ~7.8×35 nm  
30  
31 when a 1:2 Ag(DDTC):Zn(DDTC)<sub>2</sub> molar ratio was used in the synthesis. With an increased  
32  
33 molar ratio of 2:1, the diameter of the Ag<sub>2</sub>S head in the heterostructures was around 4.5 nm and  
34  
35 the stem size was ~4×48 nm. Both the UV/blue and NIR emission peaks were redshifted with  
36  
37 increasing diameter of the Ag<sub>2</sub>S-ZnS heteronanostructures. Later, the same group<sup>293</sup> modified the  
38  
39 synthesis approach to demonstrate one-pot fabrication of manganese (Mn)-doped Ag<sub>2</sub>S-ZnS  
40  
41 quantum rods with multicolor PL in three wavelength regions including blue, orange and NIR  
42  
43 (Figure 26). The orange emission (580-590 nm) of the heteronanostructures was due to the <sup>4</sup>T<sub>1</sub>-  
44  
45 <sup>6</sup>A<sub>1</sub> transition of Mn ions in the ZnS lattice.; Blue emission resulted from the ZnS stems while  
46  
47 the NIR emission was attributed to the bandgap emission of Ag<sub>2</sub>S QDs (match heads).  
48  
49  
50  
51  
52  
53  
54  
55  
56  
57  
58  
59  
60

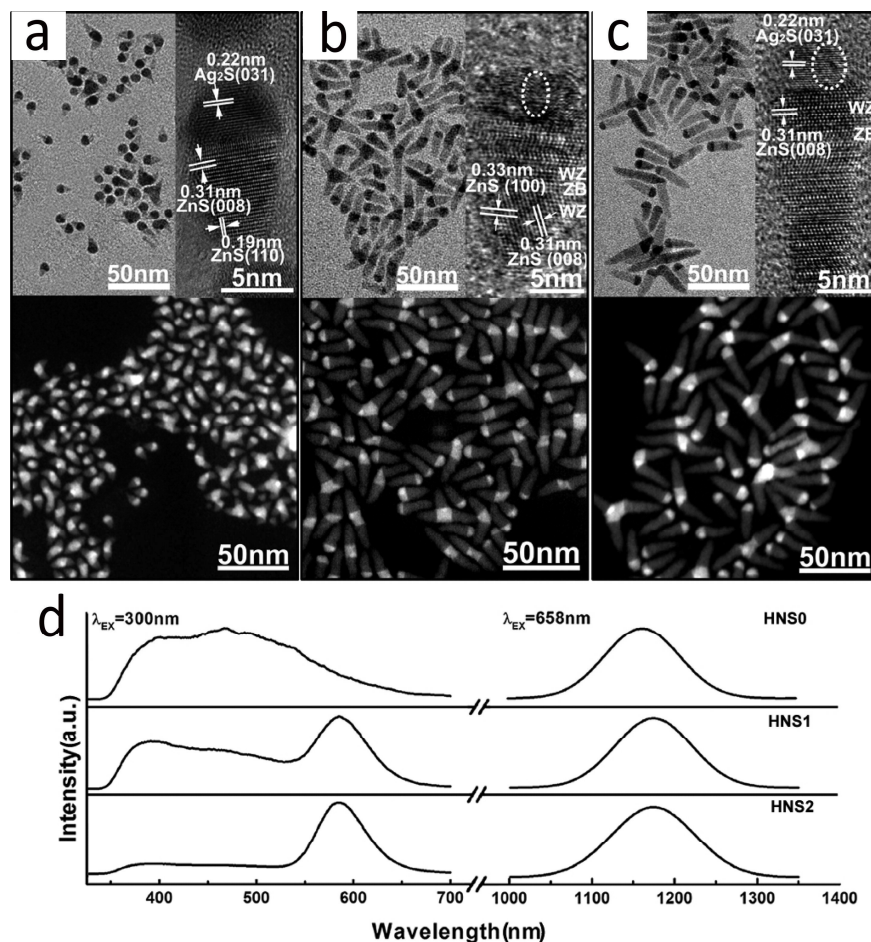


**Figure 26.** TEM, HRTEM, and STEM images of  $\text{Ag}_2\text{S}$ -ZnS heteronanostructures doped with (a) 0%, (b) 2.1% and (c) 5.9%  $\text{Mn}^{2+}$ . (d) Normalized PL and NIR PL spectra of  $\text{Ag}_2\text{S}$ -ZnS heteronanostructures with (upper) 0%, (middle) 2.1% and (lower) 5.9%  $\text{Mn}^{2+}$  dopants. Reproduced with permission from Shen *et al.*<sup>293</sup> Copyright 2012 American Chemical Society.

A biomimetic green synthesis approach was developed by Gu and co-workers<sup>294</sup> for preparing water-dispersible ultrasmall  $\text{Ag}_2\text{Se}$  QDs ranging from  $1.5 \pm 0.4$  to  $2.4 \pm 0.5$  nm diameter, with corresponding PL peaks from 700 to 820 nm (**Figure 27**). The Ag and Se precursors were prepared by processes that mimicked binding of  $\text{Ag}^+$  with alanine and reduction

of selenite from  $\text{SeO}_3^{2-}$  to GSSeH in yeast cells.  $\text{Ag}_2\text{Se}$  QDs were generated by injecting the Se precursor into the  $\text{Ag}^+$ -Ala precursor and reacting at  $90^\circ\text{C}$  for 10 min under nitrogen. The size of the  $\text{Ag}_2\text{Se}$  QDs was tuned by changing the Ag:Se precursor ratio.

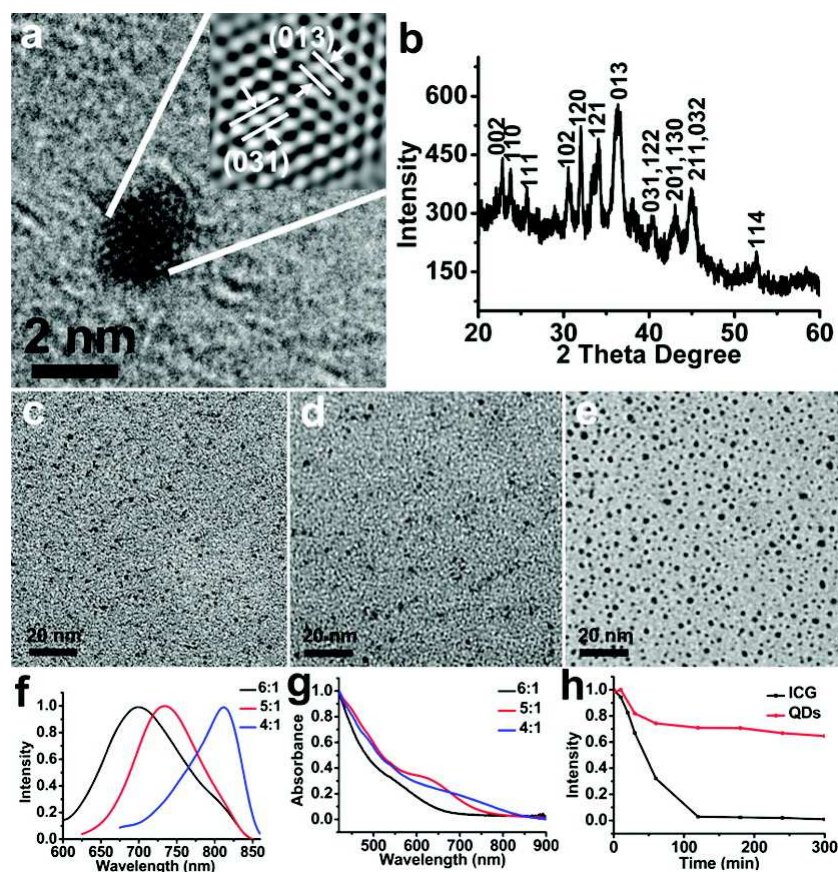
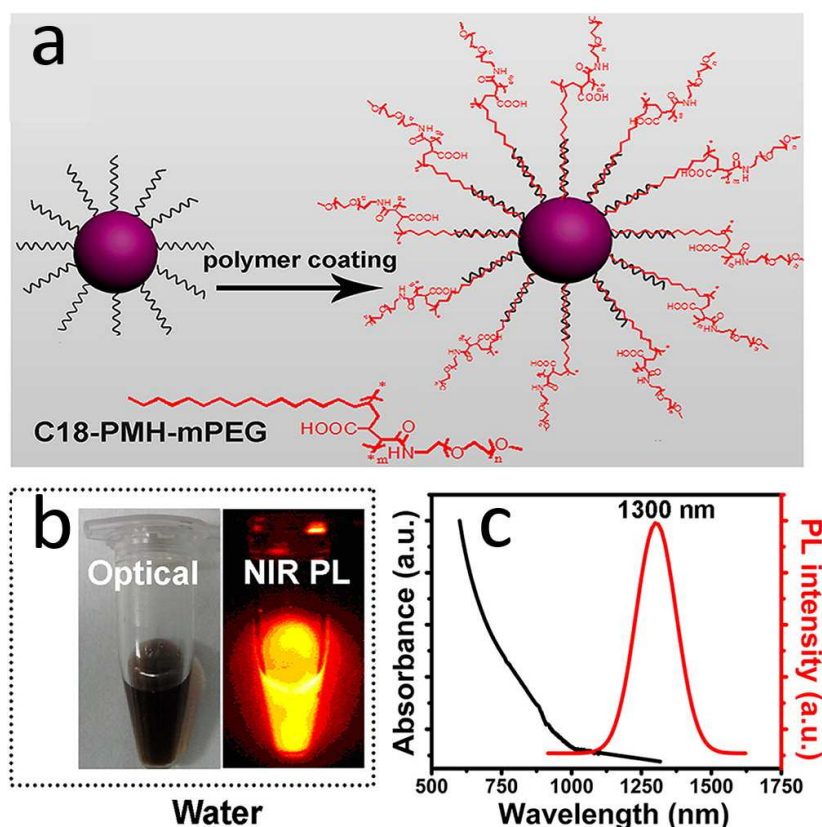


**Figure 27.** Characterization of the  $\text{Ag}_2\text{Se}$  QDs synthesized in water. (a) HRTEM image, (b) XRD pattern and (c–e) TEM images of  $\text{Ag}_2\text{Se}$  QDs synthesized at 6:1 (c), 5:1 (d), and 4:1 (e) Ag:Se precursor ratios, (f) PL emission spectra, (g) absorbance spectra, and (h) photostability curve of  $\text{Ag}_2\text{Se}$  QDs. Reprinted with permission from Gu *et al.*<sup>294</sup> Copyright 2012 American Chemical Society.

1  
2  
3  
4  
5  
6  
7  
8  
9  
10  
11  
12  
13  
14  
15  
16  
17  
18  
19  
20  
21  
22  
23  
24  
25  
26  
27  
28  
29  
30  
31  
32  
33  
34  
35  
36  
37  
38  
39  
40  
41  
42  
43  
44  
45  
46  
47  
48  
49  
50  
51  
52  
53  
54  
55  
56  
57  
58  
59  
60

Dong *et al.* developed a solvothermal approach to fabricate luminescent Ag<sub>2</sub>Se QDs with bright emission at 1300 nm.<sup>139</sup> Silver nitrate was heated in oleylamine (OAm) and toluene until it became transparent. The Ag-OAm solution was then reacted with dodecanethiol (DDT) and NaHSe at 180 °C for one hour, followed by ethanol precipitation and collection by centrifugation. The QY of these QDs reached 70%. Their size and PL were tuned by changing the Ag to Se precursor ratio. A PEG grafted amphiphilic polymer, poly(maleic anhydride-alt-1-octadecene)-methoxy poly(ethylene glycol) (C18-PMH-PEG), was used to transfer the QDs into water for biological applications (**Figure 28**). They used these QDs as PL labels in the first demonstration of *in vivo* imaging using NIR-II emission of Ag<sub>2</sub>Se QDs.



1  
2  
3 **Figure 28.** Optical properties of Ag<sub>2</sub>Se QDs coated with C18-PMH-PEG polymer. (a) The  
4 scheme for C18-PMH-PEG polymer coating on the surface of organic synthesized Ag<sub>2</sub>Se QDs.  
5  
6  
7 (b) A white light optical image and a PL image of the C18-PMH-PEG-Ag<sub>2</sub>Se QDs dispersed in  
8 water. (c) Absorbance and PL spectra of the C18-PMH-PEG-Ag<sub>2</sub>Se QDs in water. Reprinted  
9  
10 with permission from Dong *et al.*<sup>139</sup> Copyright 2013 American Chemical Society.  
11  
12  
13  
14  
15  
16

#### 17 **4.4. ZnS-AgInS<sub>2</sub> (ZAIS) Quantum Dots**

18  
19 Ternary I-III-VI AgInS<sub>2</sub> QDs with a bandgap of 1.8 eV are promising nanoprobes for *in vivo*  
20 imaging because their emission wavelength can fall in the red to NIR range.<sup>295</sup> However,  
21 biological applications of these QDs have been limited due to their low PL QY and relatively  
22 broad emission spectra. Torimoto *et al.*<sup>170</sup> demonstrated a thermal decomposition synthesis of  
23 ZnS-AgInS<sub>2</sub> (ZAIS) QDs with a QY of 24% and PL emission peak tunable from 540 nm to 720  
24 nm. PL tunability arises from the energy gap change with varying ZnS content in the  
25 ZnS-AgInS<sub>2</sub> alloy QDs (**Figure 29**). In this study, precursor solutions containing (AgIn)<sub>x</sub>Zn<sub>2(1-</sub>  
26 <sub>x)</sub>(S<sub>2</sub>CN(C<sub>2</sub>H<sub>5</sub>)<sub>2</sub>)<sub>4</sub> were first prepared by mixing sodium diethyldithiocarbamate with AgNO<sub>3</sub>,  
27  
28 In(NO<sub>3</sub>)<sub>3</sub> and Zn(NO<sub>3</sub>)<sub>2</sub> in a molar ratio of *x*:*x*:2(1-*x*), followed by 30 min heating at 180 °C.  
29  
30 After purification and drying, the brown precursor powder was dissolved in oleylamine then  
31  
32 reacted at 180 °C for 3 min under nitrogen. The highest QY of 24% was obtained with an *x* value  
33  
34 of 0.86. The emission wavelengths of ZAIS QDs red-shifted with increasing *x*.  
35  
36  
37  
38  
39  
40  
41  
42  
43  
44  
45  
46  
47  
48  
49  
50  
51  
52  
53  
54  
55  
56  
57  
58  
59  
60

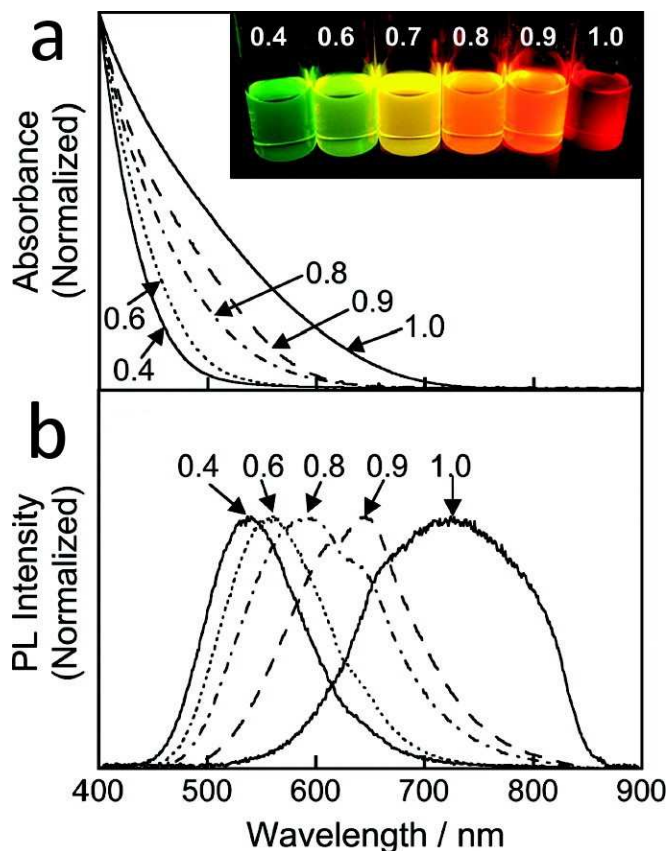


**Figure 29.** (a) Absorbance and (b) PL spectra of ZnS-AgInS<sub>2</sub> (ZAIS) QDs. The value of  $x$  in the (AgIn) <sub>$x$</sub> Zn<sub>2(1-x)</sub>(S<sub>2</sub>CN(C<sub>2</sub>H<sub>5</sub>)<sub>2</sub>)<sub>4</sub> precursor is indicated in the figure. The inset in panel a shows a photograph of ZAIS QDs under UV illumination. Reprinted with permission from Torimoto *et al.*<sup>170</sup> Copyright 2007 American Chemical Society.

Subramaniam *et al.*<sup>171</sup> demonstrated a facile room-temperature sonochemical approach for rapid synthesis of a series of Zn <sub>$x$</sub> S-Ag <sub>$y$</sub> In<sub>1-y</sub>S<sub>2</sub> (ZAIS) QDs of varied composition. The QD PL was tuned from blue to red (480 nm to 700 nm) by changing cation composition ( $x$  and  $y$ ). The PL of these QDs showed less size dependence than that of CdSe or CdTe QDs. Precursor solutions prepared by mixing sodium diethyldithiocarbamate (NaS<sub>2</sub>CN(C<sub>2</sub>H<sub>5</sub>)<sub>2</sub>) with solutions of

1  
2  
3 AgNO<sub>3</sub>, In(NO<sub>3</sub>)<sub>3</sub>·xH<sub>2</sub>O and Zn(NO<sub>3</sub>)<sub>2</sub>·6H<sub>2</sub>O were reacted with dodecylamine by sonication for  
4  
5 5 min at an optimum frequency of 20 kHz and output power of 200W. 3-mercaptopropionic acid  
6  
7 (MPA) was used to modify the dodecylamine-coated ZAIS QDs to make them water dispersible.  
8  
9 The QDs were used for both brain tumor cell and stem cell imaging, and also served as siRNA  
10  
11 nanocarriers for targeting cancer cells. Recently, Hsu's group reported a two-step, one-pot  
12  
13 synthesis of highly luminescent AgInS<sub>2</sub>/ZnS QDs by directly injecting Zn and S precursors into a  
14  
15 dispersion of as-prepared AgInS<sub>2</sub> cores without purification, resulting in a dramatic increase of  
16  
17 QY from 22% to 60%.<sup>46</sup> The core/shell QDs were coated with PMAO polymers and then  
18  
19 conjugated with folic acid (FA) to label HepG2 cells.  
20  
21

22  
23  
24 Gu's group reported the aqueous synthesis of quaternary Zn-Ag-In-S (ZAIS) QDs with PL  
25  
26 emission tunable from 525 to 625 nm and a QY of 15-30%.<sup>296</sup> Then QDs were modified using  
27  
28 DHLA-PEG functionalized with folic acid and RGD peptide. FA receptor-negative and positive  
29  
30 cells, A549 and BEL-7402 cells, were co-incubated with the QD-PEG2000-FA probes. This  
31  
32 study demonstrated enhanced cell penetration and nuclear binding by the folate modified QDs. In  
33  
34 addition, the QD-PEG2000-RGD probes were co-incubated with αvβ3-positive MDA-MB-231  
35  
36 cells and αvβ3-negative MCF-7 cells to investigate their targeting ability. QDs incubated with  
37  
38 MDA-MB-231 cells were internalized through phagocytosis and mainly accumulated in the  
39  
40 cytoplasm.  
41  
42  
43  
44

#### 45 46 **4.5. ZnSe/InP/ZnS Quantum Dots**

47  
48 Kim *et al.*<sup>177</sup> reported the synthesis of type-II QDs with a ZnSe/InP/ZnS core/shell/shell  
49  
50 structure with PL emission tuned from blue to red by tuning the thickness of the inner InP shell  
51  
52 layer. The QY was improved by addition of the outer ZnS shell. In the first step, ZnSe cores  
53  
54 were prepared from diethyl zinc (Et<sub>2</sub>Zn) and tri-*n*-octylphosphine selenide (TOP-Se) by first  
55  
56  
57  
58  
59  
60

1  
2  
3 heating hexadecylamine (HDA) and tri-*n*-octylphosphine oxide (TOPO) under nitrogen at  
4  
5 125 °C for 2.5 h, then increasing the temperature to 320 °C, followed by injection of a solution  
6  
7 containing Et<sub>2</sub>Zn and TOP-Se. The mixture was held at 270 °C for 1 hour. After cooling to room  
8  
9 temperature, zinc acetate powder was added, and the mixture was heated to 230 °C for 3 h to  
10  
11 obtain the ZnSe QDs. The use of zinc acetate eliminated surface traps and improved the QY  
12  
13 from 20% to 43%. InP shells were coated on the ZnSe cores by adding solutions of  
14  
15 tris(trimethylsilyl)phosphine and tributylphosphine-indium followed by reaction at 210 °C. The  
16  
17 outer ZnS shells were coated onto the ZnSe/InP by adding zinc acetate at room temperature  
18  
19 followed by reaction at 230 °C for 4 h and another 1-hour reaction with 1-dodecanethiol. The  
20  
21 ZnSe/InP/ZnS core/shell/shell QDs had an average size of 5.4 nm and a QY of 60%.

#### 22 23 24 25 26 27 **4.6. InAs/InP/ZnSe Quantum Dots**

28  
29 InAs/InP/ZnSe core/shell/shell QDs with NIR emission at 800 nm were also prepared by Gao  
30  
31 *et al.*<sup>297</sup> They functionalized these QDs with mercaptopropionic acid (MPA) and human serum  
32  
33 albumin (HSA) for *in vivo* tumor imaging. Briefly, InAs core QDs were first synthesized, as  
34  
35 described by Xie *et al.*<sup>298</sup>, by heating indium stearate, trioctylphosphine (TOP) and octadecene  
36  
37 (ODE) to 150 °C under argon, followed by addition of As(Si(CH<sub>3</sub>)<sub>3</sub>)<sub>3</sub>. The InAs QDs were  
38  
39 obtained after 75 min reaction at 300 °C. The InAs core QDs were cooled to 110 °C, then stearic  
40  
41 acid in ODE and tris-(trimethylsilyl)phosphine ((TMS)<sub>3</sub>P) in octylamine were added. The  
42  
43 reaction mixture was heated to 178 °C for 45 min to form the InAs/InP core/shell QDs. Finally,  
44  
45 Se dissolved in TOP was injected, followed by zinc undecylenate solution. 30 min reaction at  
46  
47 220 °C produced the outer ZnSe shell on the InAs/InP QDs.<sup>299</sup> The QDs were then transferred to  
48  
49 water using MPA. Finally, human serum albumin (HSA) was attached to the QDs through  
50  
51 electrostatic interactions.  
52  
53  
54  
55  
56  
57  
58  
59  
60

#### 4.7. Silicon Quantum Dots

In this section, we highlight the recent developments on the synthesis of silicon QDs (Si QDs) for biological applications.<sup>300</sup> Erogbogbo *et al.*<sup>38</sup> prepared RGD peptide-conjugated Si QDs and used them for *in vivo* multi-channel bioimaging and sentinel lymph node (SLN) mapping. In that study, nonluminescent Si QDs with diameters of 5-10 nm were first obtained through high-temperature CO<sub>2</sub> laser pyrolysis of SiH<sub>4</sub>. These QDs were dispersed in methanol and etched with hydrofluoric acid and nitric acid for 2-4 min to form hydrogen-terminated Si QDs that exhibited bright PL.<sup>65</sup> Organic molecules were covalently attached to the QD surface via hydrosilylation, yielding stable colloidal dispersions in organic solvents (**Figure 30**). For biological applications, the QDs were encapsulated in PEGylated phospholipid micelles using DSPE-PEG (2000). The mixture was sonicated and evaporated before conjugating with thiolated RGD peptide. Later, the same group<sup>242</sup> demonstrated the preparation of F-127 block copolymer-encapsulated Si QDs and showed that the nanoformulation did not show any adverse impact to monkeys injected with 200 mg/kg of QDs. In this study, the QDs exhibited near-IR emission peaking at 800 nm, and could be imaged using NIR excitation and emission wavelengths.

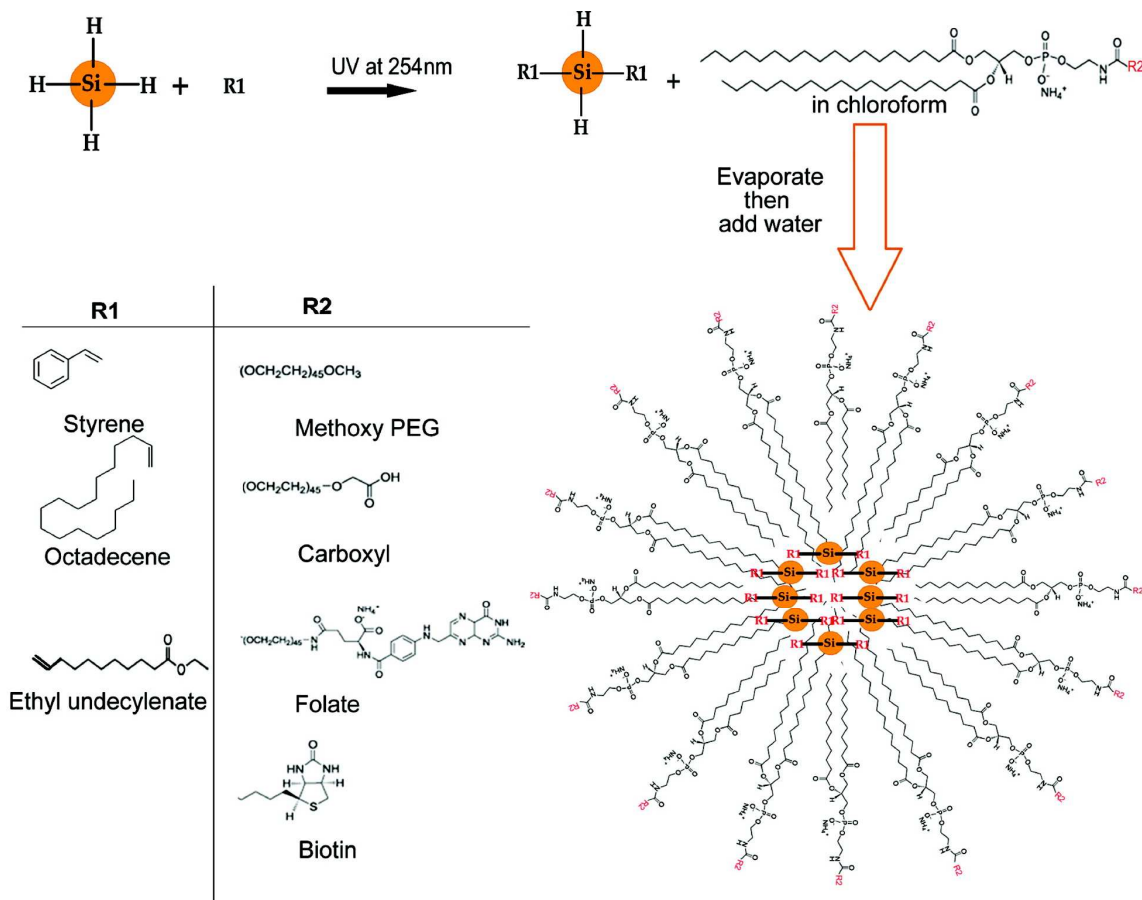


**Figure 30.** Scheme of surface functionalization of Si QDs using organic compounds (R1) followed by micellar encapsulation using phospholipids with different functional groups (R2). Reprinted with permission from Erogbogbo *et al.*<sup>65</sup> Copyright 2008 American Chemical Society.

Water-dispersible Si QDs (20-40 nm) with ultrahigh stability against UV light irradiation were synthesized by Shen *et al.*<sup>301</sup> using a two step approach. The Si QDs were first prepared by 13.56 MHz radio frequency (RF) plasma-assisted decomposition of  $\text{SiBr}_4$ . The QDs were then dispersed in toluene *via* sonication and treated with HF to remove surface oxides. Then, a

1  
2  
3 solution containing a block copolymer (Pluronic F127) was added into the Si-toluene dispersion.  
4  
5 After 10 h reaction, F127-coated Si QDs were formed and showed a higher PL stability in live  
6  
7 cells (> 30 min) compared to endoplasmic reticulum (ER)-tracker red (< 90 secs).  
8  
9

10 Shiohara *et al.*<sup>302</sup> prepared Si QDs of varying size using a microemulsion technique. The  
11  
12 particle size was tuned by changing the hydride reducing agents used in synthesis. The stronger  
13  
14 the hydride reducing agent used, the smaller the size and narrower the size distribution of the  
15  
16 QDs. Typically, hydrogen-terminated Si QDs were first prepared by dissolving SiCl<sub>4</sub> in  
17  
18 anhydrous hexane and pentaethylene glycol monododecyl ether (C<sub>12</sub>E<sub>5</sub>) and then reacting it with  
19  
20 allylamine under 4 h UV-irradiation. The surface-passivated Si QDs were further purified  
21  
22 through size-exclusion chromatography (SEC).  
23  
24  
25

26  
27 A one-step method of producing ssDNA conjugated Si QDs (4 nm) using pulsed laser  
28  
29 ablation in liquid (PLAL) was demonstrated by Intartaglia *et al.*<sup>178</sup> Single stranded DNA was  
30  
31 added to DI water in which bulk Si was then ablated by femtosecond laser pulses. The attached  
32  
33 DNA molecules were not denatured during the ablation process and these bioconjugates could be  
34  
35 applied for labeling.  
36  
37

38 Cheng *et al.*<sup>179</sup> reported a novel colloidal solution method for the synthesis and  
39  
40 functionalization of Si QDs with PL QY of ~5.2% and used them for imaging of HeLa cancer  
41  
42 cells. Si QDs were prepared through a microemulsion process by reducing halogenated silane  
43  
44 precursors. To make the QDs dispersible in both polar and non-polar solvents, the hydrogen-  
45  
46 terminated QDs were functionalized with 1,8-nonadiyne molecules by UV-promoted  
47  
48 hydrosilylation, then purified by size-exclusion chromatography, followed by modifying their  
49  
50 surface with azide molecules through a copper (I)-catalyzed azide alkyne cycloaddition (CuAAC)  
51  
52 “click” reaction. In a typical click reaction, 10 mg nonadiyne-Si QDs were first dispersed in 3  
53  
54  
55  
56  
57  
58  
59  
60

1  
2  
3 mL DI water and 3 mL dimethylformamide (DMF). Then CuSO<sub>4</sub>, L-sodium ascorbate, and  
4  
5 azides (molar ratio of 1:20:100) were added. The mixture was stirred overnight at room  
6  
7 temperature to produce the biocompatible Si QDs. The authors showed that this multi-step  
8  
9 functionalization approach enabled a higher efficiency of attachment of the desired groups than a  
10  
11 conventional single-step method.  
12  
13

#### 14 15 **4.8. ZnO Quantum Dots**

16  
17 A facile sol-gel preparation of biocompatible polymer-coated ZnO QDs with emission  
18  
19 wavelengths in the green (520 nm) and yellow regions (550 nm) was reported by Xiong and co-  
20  
21 workers.<sup>182</sup> They mixed zinc methacrylate in ethanol with poly(ethylene glycol) methyl ether  
22  
23 methacrylate (PEGMEMA) and 2,2'-azobisisobutyronitrile (AIBN) molecules. The mixtures  
24  
25 were reacted at 80 °C for 2 min, followed by the addition of LiOH and AIBN solutions and  
26  
27 refluxing for 1 h. ZnO QDs with green emission and a QY of 50% were obtained after dialysis in  
28  
29 DI water for 3 days. The synthesis protocols for ZnO QDs with yellow emission were similar  
30  
31 except that the LiOH was replaced by NaOH. The QDs were non-toxic and were used for  
32  
33 cytoplasm imaging at concentrations up to 0.2 mg/mL. More recently, Asok *et al.*<sup>181</sup>  
34  
35 demonstrated a room-temperature synthesis method for ZnO QDs based on ethanolic  
36  
37 precipitation. Solutions containing Zn<sup>2+</sup> precursors and LiOH were degassed in an ultrasonic  
38  
39 bath and the reaction vessel was purged with nitrogen. The ZnO QD surface exhibited a high  
40  
41 concentration of oxygen due to the oxygen deficient conditions, leading to bright PL from these  
42  
43 defects, with a QY of 60%. QDs with average diameters from 2.9 nm to 12.2 nm were produced  
44  
45 by varying the [Zn]/[LiOH] precursor ratio from 0.25 to 2. This was attributed to counterion  
46  
47 capping on the hydroxylated QD surface. The emission peak of the ZnO QDs was found to be  
48  
49 size-dependent and could be tuned from ~450 to 550 nm.  
50  
51  
52  
53  
54  
55  
56  
57  
58  
59  
60

#### 4.9. WS<sub>2</sub> Quantum Dots

Two-dimensional transition metal dichalcogenide (TMDC) nanomaterials such as tungsten disulfide (WS<sub>2</sub>) and molybdenum disulfide (MoS<sub>2</sub>) have a structure similar to that of graphene, with atomically-thin layers held together only by van der Waals interactions.<sup>303,304</sup> Recently, Lin *et al.*<sup>183</sup> fabricated luminescent WS<sub>2</sub> QDs by chemical exfoliation, similar to the approach used to exfoliate and cut graphite into graphene QDs. In general, there were three main steps: (i) WS<sub>2</sub> was intercalated by potassium atoms, exploiting the weak van der Waals force between the WS<sub>2</sub> layers; (ii) air exposure at room temperature produced deintercalation of the K-WS<sub>2</sub> mixtures; and (iii) first EtOH then H<sub>2</sub>O was added, and the solution was ultrasonicated for 2 h. After filtration, a WS<sub>2</sub> QD dispersion with yellow color was collected (**Figure 31**). Because the intercalation in the first step expanded the interlayer distance, exfoliation to single layers with reduced sizes was easily achieved by the ultrasonication process. The WS<sub>2</sub> QDs were characterized as monolayer structures with lateral sizes from 8 to 15 nm. UV-vis absorbance spectroscopy showed that the transition energy of WS<sub>2</sub> QDs (3.16 eV) was much larger than that of the pristine WS<sub>2</sub> sheets (2.1 eV), leading to a bright green-blue PL that could not be observed in the WS<sub>2</sub> flakes. WS<sub>2</sub> QDs were used for *in vitro* imaging at a concentration of 50 µg/mL.

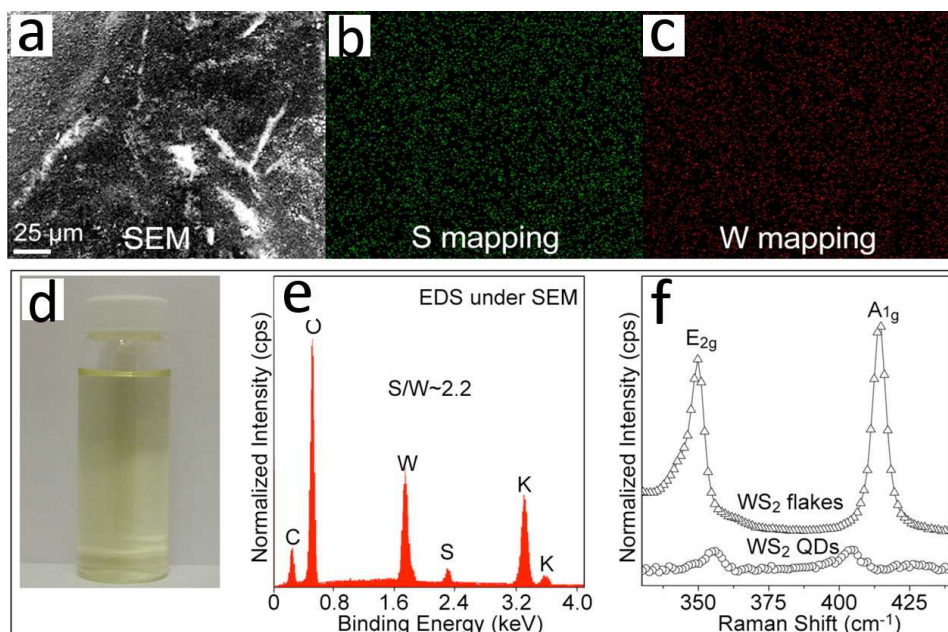


**Figure 31.** Characterization of the exfoliated and disintegrated WS<sub>2</sub> QDs. (a) SEM image and (b and c) EDS elemental mapping of the dried suspension; (d) photograph of the WS<sub>2</sub> QD suspension; (e) EDS analysis and (f) Raman analysis of the dried suspension. Reprinted with permission from Lin *et al.*<sup>183</sup> Copyright 2013 American Chemical Society.

#### 4.10. Graphene Quantum Dots

In general, there are two types of luminescent carbon-based QDs, *i.e.*, carbon nanodots and graphene QDs.<sup>305</sup> Carbon nanodots are quasi-spherical carbon NPs with an average diameter less than 10 nm. Structurally, they are either amorphous or crystalline carbon with sp<sup>2</sup>-bonded clusters. Graphene QDs are similar in size to carbon nanodots but clearly possess the crystalline structure of single- or multiple- graphene layers (usually 3 or fewer layers). In this review, we only consider graphene QDs as they exhibit features similar to other QDs.

1  
2  
3 Luminescent graphene QDs were prepared by Pan *et al.*<sup>306</sup> in 2009 by cutting micron-scale  
4 reduced graphene oxide (rGO) into 9.6 nm graphene QDs via a hydrothermal treatment. The  
5 graphene QDs showed strong blue PL. Such PL is not observed from pristine graphene sheets or  
6 graphene nanoribbons with larger lateral dimensions. The authors attributed the luminescence to  
7 edge effects in the graphene QDs. TEM imaging showed that the (002) interlayer spacings were  
8 3.64 Å and 3.34 Å for reduced GO and bulk graphite, respectively. The first step of the graphene  
9 QD synthesis involves the oxidation of rGOs with strong acid mixtures of HNO<sub>3</sub> and H<sub>2</sub>SO<sub>4</sub>. The  
10 size of the rGOs decreased from several micrometers to 50 nm to 2 μm, while their (002)  
11 interlayer spacing increased to 3.85 Å. After hydrothermal treatment at 200 °C, their size was  
12 reduced below 10 nm and the (002) interlayer spacing decreased to 3.43 Å, close to that of bulk  
13 graphite. The interlayer spacing change confirms the deoxidization of the graphene sheets.  
14  
15  
16  
17  
18  
19  
20  
21  
22  
23  
24  
25  
26  
27  
28

29 Later, a one-pot hydrothermal preparation method for polyethylene glycol (PEG)-  
30 functionalized graphene QDs was reported by Shen *et al.*<sup>184</sup> They first prepared GO via  
31 Hummers method and then oxidized the GO with concentrated HNO<sub>3</sub> at 70 °C for 24 h. The  
32 resulting suspensions were ultrasonicated mildly after cooling to room temperature. In the next  
33 step, PEG10000 was added, and the mixtures were autoclaved at 200 °C for 24 h, followed by  
34 dialysis for 7 days. The emission wavelength of the graphene QDs-PEG was 360 nm and their  
35 QY was ~28%, which was double that of graphene QDs without the PEG surface passivation.  
36  
37  
38  
39  
40  
41  
42  
43  
44  
45

46 Deviating from previous preparation methods for graphene QDs, Peng *et al.*<sup>307</sup> developed a  
47 much simpler approach using low-cost and commercially available carbon fibers. The pitch-  
48 based carbon fibers are resin-rich materials. Graphene QDs were obtained by chemically  
49 exfoliating the carbon fibers (CFs) with strong acids (H<sub>2</sub>SO<sub>4</sub> and HNO<sub>3</sub> in a volume ratio of 3:1).  
50 The mixture of CFs and acids was first sonicated for 2 h and then stirred for 24 h at a fixed  
51  
52  
53  
54  
55  
56  
57  
58  
59  
60

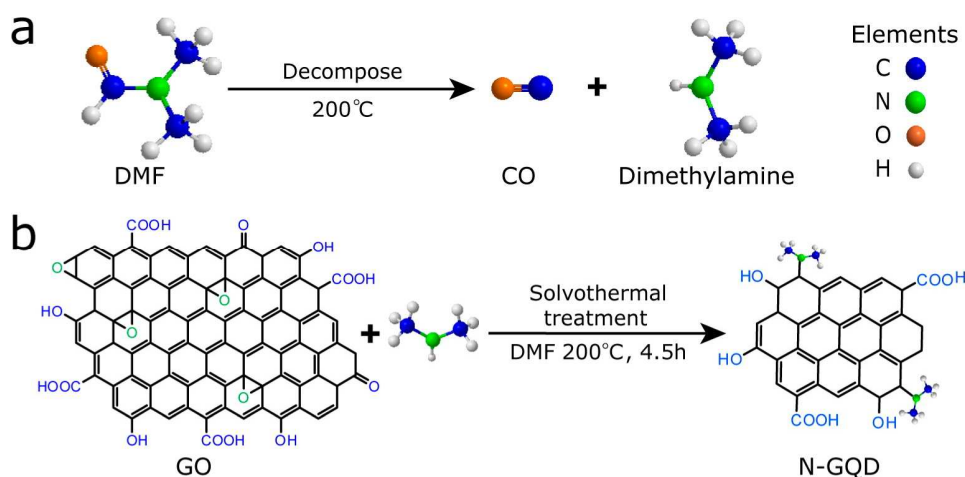
1  
2  
3 reaction temperature. The submicron-scale stacked graphitic planar structures of the carbon  
4  
5 fibers were easily broken down to produce graphene QDs with diameters from 1 to 4 nm. The as-  
6  
7 prepared graphene QDs showed good dispersibility in water and polar solvents like dimethyl  
8  
9 sulfoxide (DMSO) and dimethylformamide (DMF). Their thicknesses ranged from one to three  
10  
11 layers. Their emission wavelength was size dependent and was tuned by changing the reaction  
12  
13 temperature from 80 to 120°C. Dong *et al.*<sup>308</sup> demonstrated a one-step synthesis method for  
14  
15 simultaneous production of single and multilayer graphene QDs. They used CX-72 carbon black  
16  
17 as a precursor to produce large batches of QDs at low cost. The CX-72 carbon black was  
18  
19 chemically oxidized by concentrated HNO<sub>3</sub>. After refluxing for 24 h, the mixture was  
20  
21 centrifuged at 2770 g for 10 min. The supernatant was heated at 200 °C to evaporate water and  
22  
23 residual acids. The graphene QDs from the supernatant were single-layer structures. The  
24  
25 precipitates were purified by hydrochloric acid treatment, dried in vacuum, dispersed in DI water  
26  
27 and filtered through a 100-kDa membrane. The filtrates were multilayer graphene QDs. The  
28  
29 authors suggested that the monolayer graphene QDs are potential candidates for bioimaging, and  
30  
31 multilayer GQDs may serve as building blocks for optical or electronic devices.  
32  
33  
34  
35  
36  
37  
38

39 Protein-functionalized graphene QDs for immunosensing applications were produced by  
40  
41 Shen and co-workers.<sup>309</sup> Briefly, graphene QDs were prepared from powders containing GO  
42  
43 sheets by reaction with N,N-dimethylformamide and dichlorosulfoxide at 80 °C for 72 h. The  
44  
45 mixture was then centrifuged and collected as the precipitate, followed by washing with  
46  
47 anhydrous tetrahydrofuran. After evaporation, the product was mixed with *n*-butylamine and  
48  
49 heated at 60 °C for 96 h to form a yellow solution containing graphene QDs. To functionalize the  
50  
51 graphene QD surface with carboxyl groups, the solution was mixed with sodium hydroxide and  
52  
53 chloroacetic acid and sonicated for 3 h to convert hydroxyl groups to carboxyl groups. Protein  
54  
55  
56  
57  
58  
59  
60

1  
2  
3 molecules like mouse IgG could then be covalently bound to carboxyl groups on the surface of  
4  
5 graphene QDs by a N-(3-dimethylaminopropyl)-N'-ethylcarbodiimide hydrochloride (EDC)/N-  
6  
7 hydroxysuccinimide (NHS) reaction. The antibody-conjugated graphene QDs were further used  
8  
9 in immunoassays for specific biomolecule detection.  
10

11  
12       Zhu *et al.*<sup>310</sup> investigated the luminescence mechanism of graphene QDs with different  
13  
14 surface functionalizations, showing that the structure of the graphene QDs varied when the  
15  
16 nonradiative recombination of electron-hole pairs was suppressed by functionalization. Graphene  
17  
18 QDs with green PL emission were synthesized by a two-step solvothermal approach (**Figure 32**).  
19  
20 GO was first reacted with DMF by 30 min ultrasonication and then autoclaved at 200 °C for 8 h,  
21  
22 followed by purification using column chromatography. The epoxy and carboxyl groups on the  
23  
24 surface of the graphene QDs could be reduced to hydroxyl groups using alkylamine coupling or  
25  
26 reduction by sodium borohydride. The luminescence of the graphene QDs was tuned from green  
27  
28 to blue using this surface modification technique. The authors asserted that the intrinsic state  
29  
30 emission, and not defect state emission, is the dominant source of graphene QD luminescence.  
31  
32 Up-converted luminescence from graphene QDs was also successfully demonstrated by exciting  
33  
34 them with a pulsed NIR laser. Nitrogen-doped graphene QDs (N-GQDs) have recently shown  
35  
36 promise as fluorescent labels for two-photon *in vitro/in vivo* imaging due to their large two-  
37  
38 photon absorption cross-section of up to 48000 Göppert-Mayer (GM) units, which is much larger  
39  
40 than either traditional organic dyes or Cd-based QDs. Liu and co-workers<sup>6</sup> demonstrated a one-  
41  
42 pot synthesis method for making N-GQDs using GO in combination with dimethylformamide  
43  
44 (DMF) as the nitrogen source. The GO precursors were firstly synthesized by Hummer's method  
45  
46 and then dispersed into DMF. Heating decomposed the DMF into dimethylamine and CO.  
47  
48 Doping of GO occurred via ring opening reactions between dimethylamine and epoxy groups on  
49  
50  
51  
52  
53  
54  
55  
56  
57  
58  
59  
60

1  
2  
3 the GO. The two-photon luminescence of the N-GQDs was excited by a femtosecond laser in the  
4 near-IR region. Imaging depths of up to 1800  $\mu\text{m}$  were demonstrated in scattering tissue  
5  
6  
7  
8  
9 phantoms.



31 **Figure 32.** Scheme for the preparation of nitrogen-doped graphene QDs (N-GQDs). (a)  
32 Decomposition of DMF at a high temperature. (b) Reduction of GOs to N-GQDs in the presence  
33 of DMF. Reprinted with permission from Liu *et al.*<sup>6</sup> Copyright 2013 American Chemical Society.  
34  
35  
36  
37  
38  
39

40  
41 Wu and co-workers demonstrated a one-step thermolysis method for preparing luminescent  
42 graphene QDs (GQDs) with a QY of 54.5%.<sup>185</sup> In that study, L-glutamic acid was pyrolyzed at  
43 210 °C. The color of the L-glutamic acid changed from transparent to brown after 45 seconds,  
44 indicating formation of the graphene QDs, which were recovered by centrifugation. These  
45 graphene QDs showed excitation-wavelength-dependent PL from blue to NIR wavelengths.  
46  
47  
48  
49  
50  
51  
52  
53  
54  
55  
56  
57  
58  
59  
60  
60 Their NIR luminescence showed a large 455 nm Stokes shift. This unique property could be used  
to improve the sensitivity of QDs for distinguishing specific biotargets.

#### 4.11. Doped ZnS/ZnSe Quantum Dots

Doped zinc chalcogenide QDs (e.g., ZnS and ZnSe QDs) are another type of Cd-free QDs that show great potential in bioimaging and bioanalysis.<sup>311-313</sup> Currently, doped QDs for biological applications are mainly based on doping with transition metal ions like  $\text{Mn}^{2+}$  and  $\text{Cu}^{2+}$ . The emission lifetimes from these dopants are longer than that of the host QDs and that of typical tissue autofluorescence. The intrinsic toxicities of doped ZnS/ZnSe QDs containing nontoxic metals are significantly lower than those of CdSe and CdTe QDs. Manzoor *et al.*<sup>314</sup> reported a facile synthesis method for producing doped ZnS QDs with different dopants including  $\text{Mn}^{2+}$ ,  $\text{Cu}^{2+}$ - $\text{Al}^{3+}$ ,  $\text{Cu}^{+}$ - $\text{F}^{-}$  and  $\text{Cu}^{+}$ - $\text{Al}^{3+}$ - $\text{Mn}^{2+}$  that exhibited PL ranging 480 to 622 nm.  $\text{Mn}^{2+}$ -doped ZnS QDs with orange-red PL were prepared by mixing aqueous  $\text{ZnSO}_4$  and  $\text{MnSO}_4$  in a nitrogen atmosphere, then injecting  $\text{Na}_2\text{S}$  at pH 6.5.  $\text{Cu}^{2+}$ - $\text{Al}^{3+}$  co-doped ZnS QDs were prepared by mixing  $\text{ZnSO}_4$  and copper acetate under nitrogen, adding  $\text{Na}_2\text{SO}_3$  to reduce Cu(II) ions to Cu(I), then adding aluminum chloride and finally precipitation by  $\text{Na}_2\text{S}$  addition.  $\text{Cu}^{+}$ - $\text{Al}^{3+}$ - $\text{Mn}^{2+}$ -doped ZnS QDs were produced by the same process with manganese sulfate added along with the  $\text{AlCl}_3$ . The doped ZnS QDs were directly functionalized with folic acid (FA) through zinc(II)-carboxylate coordination. The FA-QDs were used to image human nasopharyngeal epidermoid carcinoma (KB) cells with folate receptors.

In addition to FA, mercaptopropionic acid (MPA) was also used as a stabilizing agent for doped ZnS QDs. MPA-functionalized  $\text{Mn}^{2+}$ -doped ZnS QDs were synthesized by Wu and co-workers<sup>253,315,316</sup> and used for phosphorescent sensing after further conjugation with glucose oxidase (GOD). Aqueous  $\text{ZnSO}_4$  and manganese(II) acetate ( $\text{Mn}(\text{Ac})_2$ ) were mixed with MPA and reacted for 30 min under argon. The pH was adjusted to 11 using NaOH.  $\text{Na}_2\text{S}$  was then injected and reacted for 20 min at room temperature and then at 50 °C for 2 h. The MPA-

1  
2  
3 functionalized  $\text{Mn}^{2+}$ -doped ZnS QDs were collected by precipitation and centrifugation, then  
4  
5 redispersed in DI water. GODs were conjugated to the QD surface by an EDC/NHS procedure.  
6  
7 The QY of the MPA-functionalized  $\text{Mn}^{2+}$ -doped ZnS QDs was  $\sim 8.2\%$ .<sup>316</sup> Later, Geszke *et al.*<sup>119</sup>  
8  
9 improved the QY of MPA-functionalized  $\text{Mn}^{2+}$ -doped ZnS QDs to 22% by coating a ZnS shell  
10  
11 onto the doped ZnS core. They used zinc acetate ( $\text{Zn}(\text{OAc})_2 \cdot 2\text{H}_2\text{O}$ ) and MPA as the ZnS shell  
12  
13 precursors. The  $\text{Zn}^{2+}$ -MPA mixtures were reacted at a pH of 10.3 for 30 min under a nitrogen  
14  
15 atmosphere, then injected into dispersions of the MPA-functionalized  $\text{Mn}^{2+}$ -doped ZnS QDs.  
16  
17 ZnS shells were formed on the core QD surface by decomposing the  $\text{Zn}^{2+}$ -MPA precursors at  
18  
19 100 °C for 7 h. The ZnS:Mn/ZnS core/shell QDs were coupled with 2,2'-(ethylenedioxy)-bis-  
20  
21 ethylamine and then conjugated with FA through EDC/NHS chemistry.  
22  
23  
24  
25  
26

27 More recently, Zhou *et al.*<sup>317</sup> demonstrated that deposition of nano fluorine-doped  
28  
29 hydroxyapatite (nanoFap) onto  $\text{Mn}^{2+}$ -doped ZnSe/ZnS core/shell QDs could further reduce their  
30  
31 cytotoxicity. In this study,  $\text{Mn}^{2+}$ -doped ZnSe core QDs were prepared by a nucleation doping  
32  
33 method.<sup>316</sup> Zn and Mn precursors were produced by mixing manganese chloride and zinc stearate  
34  
35 with stearic acid. For the core QD synthesis, selenium powder was first reacted with oleylamine  
36  
37 and octadecene at 100 °C for 30 min and then at 280 °C under argon, followed by the addition of  
38  
39 Mn precursors. MnSe QDs were formed after 2 min reaction at 260 °C. Zinc precursors were  
40  
41 then injected and reacted at 250 °C for 15 min. Subsequently, mixtures containing the second Zn  
42  
43 precursor and oleylamine were added and reacted at 240 °C for another 15 min. The  $\text{Mn}^{2+}$ -doped  
44  
45 ZnSe core QDs were functionalized with MPA and reacted with  $\text{Na}_2\text{S}$  and zinc acetate, first at  
46  
47 50 °C then 70 °C for 40 min. To form the nano-Fap-QDs, the  $\text{Mn}^{2+}$ -doped ZnSe/ZnS core/shell  
48  
49 QDs were conjugated with o-phosphoethanolamine (PEA)-modified nano-Fap in an optimum  
50  
51 weight ratio of 1:2 through covalent binding.  
52  
53  
54  
55  
56  
57  
58  
59  
60

#### 4.12. Plasmonic Copper Chalcogenide Quantum Dots

Plasmonic copper chalcogenide QDs have only recently been introduced into the biomedical field.<sup>141,260,261</sup> These QDs exhibit localized surface plasmon resonance (LSPR) properties like those observed in noble metal NPs. Because they have a much lower free charge carrier density than metallic NPs, their LSPR absorption peak is at much longer wavelength, typically in the NIR region that is optimal for biological applications like photothermal therapy and photoacoustic imaging. Zhao *et al.*<sup>172</sup> synthesized  $\text{Cu}_{2-x}\text{S}$  ( $x = 1, 0.2, 0.03$ ) QDs with stoichiometry-dependent NIR absorbance by three different approaches, including sonoelectrochemical, hydrothermal and solventless thermolysis methods.  $\text{Cu}_{1.97}\text{S}$  QDs exhibited better stability in air than did  $\text{Cu}_2\text{S}$  QDs. With the sonoelectrochemical approach, the composition of the QDs could be changed from covellite ( $\text{CuS}$ ) to djurleite ( $\text{Cu}_{1.97}\text{S}$ ) by varying the reduction potential. More specifically, 33 mM cupric sulfate solution was reacted with 16.5 mM sodium thiosulfate and 87 mM citric acid by ultrasonication at 20 kHz for 1 h and electrodeposition with a fixed potential of 0.0, -0.6 or -1.2 V to produce  $\text{CuS}$ ,  $\text{Cu}_{1.8}\text{S}$ , or  $\text{Cu}_{1.97}\text{S}$  QDs, respectively. The average diameters of  $\text{CuS}$ ,  $\text{Cu}_{1.8}\text{S}$  QDs and  $\text{Cu}_{1.97}\text{S}$  QDs were  $14.9 \pm 7.1$  nm,  $18.1 \pm 7.9$  nm and  $12.1 \pm 4.6$  nm, respectively. Absorbance spectra of  $\text{Cu}_{1.8}\text{S}$  QDs and  $\text{Cu}_{1.97}\text{S}$  QDs had a peak near 400 nm and a valley around 800 nm with increased intensity at longer wavelengths, while that of  $\text{CuS}$  QDs showed a broad absorbance peak around 450 nm and valley at 650 nm with a stronger rise at longer wavelengths. For the hydrothermal approach and solventless thermolysis, QDs of different composition were produced by tuning the pH during the preparation and the precursor pretreatment. In the hydrothermal approach, copper precursors ( $\text{CuSO}_4 \cdot 5\text{H}_2\text{O}$ ) were first reacted with mercaptopropionic acid (MPA) to form a Cu-MPA complex. The pH was tuned by adding 1 M sodium hydroxide (pH 2 for  $\text{CuS}$  QDs and pH 5 for

1  
2  
3 Cu<sub>1.97</sub>S QDs), followed by 7 h reflux with 0.2 M Na<sub>2</sub>S<sub>2</sub>O<sub>3</sub> at 100 °C. Both types of QDs  
4  
5 exhibited an absorbance minimum around 600 nm and increased absorbance from 800 nm to  
6  
7 longer wavelengths. In the solventless thermolysis approach, the Cu-MPA precipitates were (i)  
8  
9 dried in air at room temperature and heated under nitrogen at 200 °C for 1 h to obtain Cu<sub>1.8</sub>S QD  
10  
11 powder, or (ii) dried as a wax-like gel in nitrogen for 30 min before the heating process to form  
12  
13 Cu<sub>1.97</sub>S QD powder. The Cu<sub>1.8</sub> QDs (D = 50 nm) and Cu<sub>1.97</sub>S QDs (D = 70 nm) both showed a  
14  
15 broad absorbance peak from 400 nm to 650 nm, which was respectively 70 nm and 50 nm  
16  
17 redshifted in comparison to those prepared by sonoelectrochemical and hydrothermal approaches.  
18  
19

20  
21  
22 Luther and co-workers<sup>140</sup> prepared highly monodisperse Cu<sub>2-x</sub>S QDs with precise control of  
23  
24 QD size, from 2.5 nm to 6 nm (**Figure 33**). The Cu<sup>2+</sup> precursors were obtained by heating cupric  
25  
26 acetylacetonate (Cu(acac)<sub>2</sub>) in oleic acid at 110 °C. The sulfur precursors were prepared by  
27  
28 heating 1-dodecanethiol, oleic acid and ammonium diethyldithiocarbamate at 180 °C under  
29  
30 nitrogen. Cu<sub>2-x</sub>S QDs were synthesized by injecting 3 mL Cu<sup>2+</sup> precursors into sulfur precursors  
31  
32 dissolved in oleic acid, followed by 3-12 min reaction. The total reaction volume was fixed at 20  
33  
34 mL by tuning the amount of the oleic acid. Size control of the Cu<sub>2-x</sub>S QDs was achieved by  
35  
36 changing the Cu:S precursor ratios and the reaction time. For instance, the 2.5 nm and 6 nm QDs  
37  
38 were prepared using Cu:S ratios of 3:0.63 and 1:1.25 with reaction times of 3 and 12 min,  
39  
40 respectively. The NIR absorbance peaks of the Cu<sub>2-x</sub>S QDs were red-shifted and broadened with  
41  
42 decreasing QD size due to surface scattering of free carriers.  
43  
44  
45  
46  
47  
48  
49  
50  
51  
52  
53  
54  
55  
56  
57  
58  
59  
60

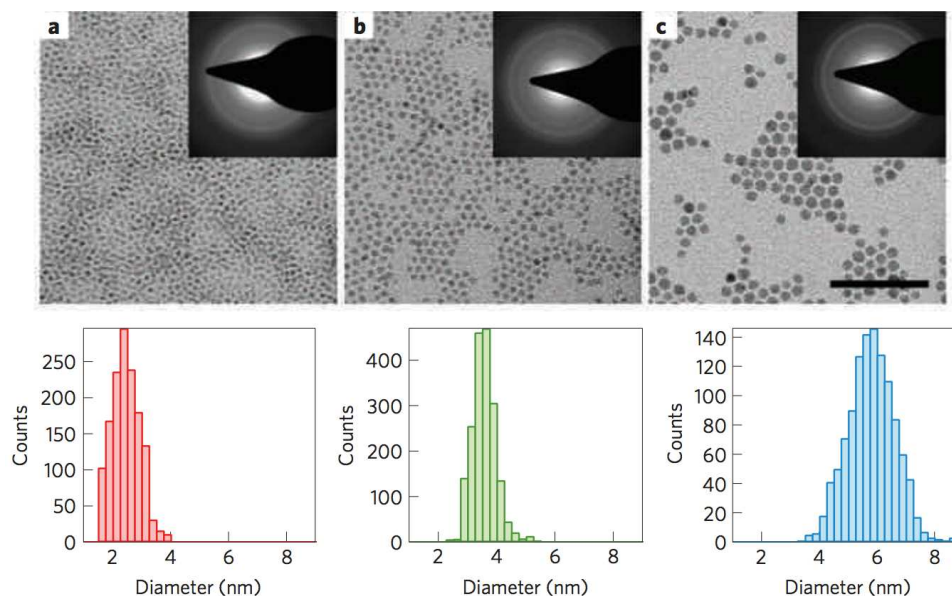


**Figure 33.** TEM images, (inset) SAED patterns and size distribution histograms of three Cu<sub>2-x</sub>S QDs with average size of (a) 2.4±0.5 nm (b) 3.6±0.5 nm, and (c) 5.8±0.8 nm. Scale bar represents 50 nm. Reprinted with permission from Luther *et al.*<sup>140</sup> Copyright 2011 Nature Publishing Group.

Liu *et al.*<sup>273</sup> reported a room temperature synthesis approach for CuS nanoplates with a fixed thickness of 4 nm and tunable diameter from 4 nm to over 30 nm. The peak LSPR absorbance of the CuS nanoplates was tuned by up to 600 nm by changing the aspect ratio (*i.e.*, the ratio between the lateral dimension and the thickness). The reaction precursors for Cu and sulfur were oleylamine-Cu (OAm-Cu) and ammonium sulfide (AS) dissolved in toluene.

Hollow and solid Cu<sub>2-x</sub>Te QDs with high NIR extinction coefficients of  $8.1 \times 10^7 \text{ M}^{-1} \text{ cm}^{-1}$  at 1200 nm for the hollow structure and  $2.6 \times 10^7 \text{ M}^{-1} \text{ cm}^{-1}$  at 1150 nm for the solid structure were recently synthesized by Yang and co-workers.<sup>318</sup> The difference in the preparation of solid and hollow Cu<sub>2-x</sub>Te QDs was the injection time of the trioctylphosphine-Te (TOP-Te) into the Cu<sup>2+</sup> precursors (**Figure 34**). TOP-Te precursors were prepared by dissolving 0.025 g Te powder in 2

1  
2  
3 mL TOP by heating at 150 °C for one hour. In a typical synthesis, 6 mL oleylamine (OAm) was  
4  
5 mixed with 0.078 g Cu(acac)<sub>2</sub> under argon, then heated to 120 °C for one hour, followed by  
6  
7 heating to 220 °C. At this time, 1.5 mL TOP-Te with a concentration of 0.1 M was injected into  
8  
9 the Cu<sup>2+</sup> precursors and reacted for one hour at 220 °C. For the synthesis of hollow Cu<sub>2-x</sub>Te QDs,  
10  
11 the Cu precursors were kept at 220 °C for another one hour after the one-hour at 120 °C. Then,  
12  
13 the Te-TOP precursors were added and reacted for only 30 min rather than one hour. The color  
14  
15 of the mixture changed from dark red to dark green. The average diameters of the solid and  
16  
17 hollow Cu<sub>2-x</sub>Te QDs were 8.8 ± 1.8 nm and 16.5 ± 2.7 nm, respectively. The NIR absorbance  
18  
19 peaks of the solid and hollow Cu<sub>2-x</sub>Te QDs could be tuned by adding a reducing agent  
20  
21 (diisobutylaluminum hydride) that resulted in a decrease of free carrier concentration (*i.e.*, the  
22  
23 number of copper deficiencies). It is also worth noting that the LSPR response to the refractive  
24  
25 index change of the surrounding media was more pronounced for the hollow Cu<sub>2-x</sub>Te QDs than  
26  
27 for the solid ones.  
28  
29  
30  
31  
32

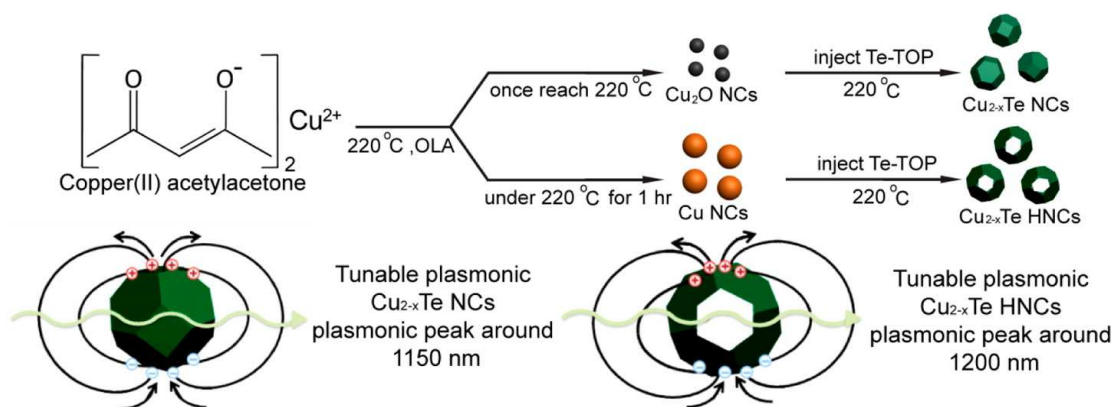


**Figure 34.** Scheme for the formation of solid Cu<sub>2-x</sub>Te QDs and hollow Cu<sub>2-x</sub>Te nanostructures by injecting TOP-Te at different reaction times. Reprinted with permission from Yang *et al.*<sup>318</sup>

Copyright 2013 American Chemical Society.

## 5.0. Biophotonic Applications

QD technology is having tremendous positive impact on biophotonic sensing and imaging. New nanoemitters such as copper indium sulfide (CuInS<sub>2</sub>), silver indium sulfide (AgInS<sub>2</sub>), indium phosphide (InP), doped Zn chalcogenides, silver sulfide (Ag<sub>2</sub>S), silver selenide (Ag<sub>2</sub>Se), silicon (Si) and graphene QDs have been synthesized and used for these applications. The manipulation of QD optical properties can be used to selectively image and monitor a specific biological site as well as to understand local macromolecular interactions such as protein-protein interactions.<sup>319,320</sup> By combining QDs with other contrast agents, one can achieve multimodal imaging of biological structures and processes *in vivo*.<sup>95,321</sup> Such information can be used to study molecular events that are early indicators of an emerging disease state, or to monitor response to a particular stimulus.<sup>322,323</sup> Multiple targeting ligands can be attached to QDs of different emission colors to identify multiple biomarkers of a specific disease through multiplexed imaging.<sup>324,325</sup> Integrating QDs into various optical imaging techniques coupled with localized microspectroscopy can provide detailed molecular imaging with high spatial resolution. More importantly, QD nanoprobe and nanocarriers that are sensitive to pH, temperature, activity of a specific ion, or activity of biomolecules in cells can enable functional imaging.<sup>326-329</sup> Cd-free QDs can be used for both optical and photoacoustic imaging as well as sensing *in vitro*, *ex vivo*, and *in vivo* to create a highly integrated approach for diagnostics.<sup>20,57,330</sup> Section 5 of this review presents a detailed description of the use of QDs in biophotonic applications including optical imaging, photoacoustic imaging, sensing, optical tracking, photothermal therapy, and multimodal imaging (**Figure 35**).

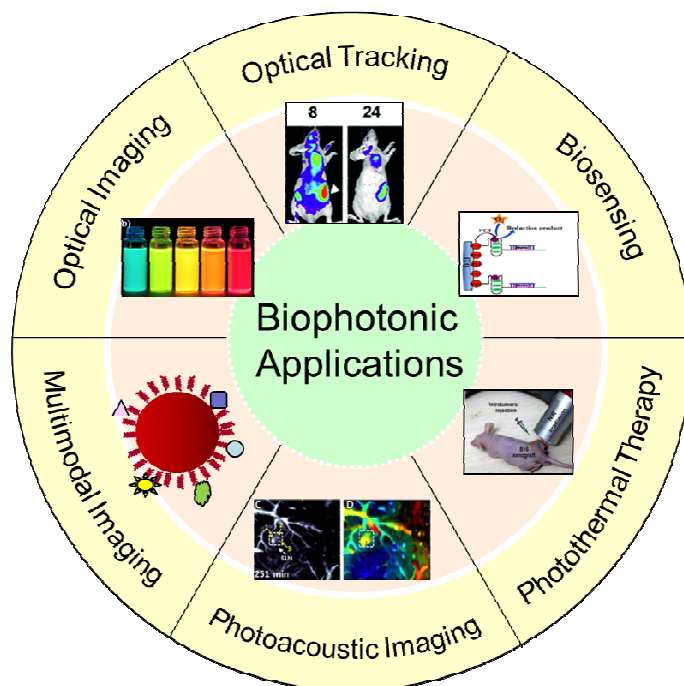


**Figure 35.** Schematic illustration of the biophotonic applications of Cd-free QDs.

The typical biophotonic applications of Cd-free QDs are summarized in **Table 2**.

**Table 2.** Typical biophotonic applications of Cd-free QDs

| Biophotonic Application | QD type                             | Functional group/molecule                 | Feature of the technique                | Model used  | Ref |
|-------------------------|-------------------------------------|---|---|---|-----|
| <b>Optical imaging</b>  |                                     |   |   |   |     |
| <i>In vitro</i> imaging | AgInS <sub>2</sub>                  | Pluronic F127 triblock copolymer micelles | NIR imaging at 800 nm                   | human peripheral blood monocyte-derived macrophages | 331 |
|                         | AgInSe <sub>2</sub> /ZnS core/shell | RGD-PAA                                   | PL QYs 40%, emission peak 700-820 nm    | MDA-MB-231  | 332 |
|                         | CuInS <sub>2</sub> /ZnS core/shell  | ε-PL-g-LA/DMA                             | positive surface charge at low pH       | HeLa cell   | 333 |
|                         | CIZS/ZnS                            | AFP                                       | PL QYs 25-35%, emission peak 465-700 nm | HepG2 cell  | 206 |

|    |                           |   |                   |                       |                   |      |
|----|---------------------------|---|-------------------|-----------------------|-------------------|------|
| 1  |                           |   |                   |                       |                   |      |
| 2  |                           |   |                   |                       |                   |      |
| 3  |                           |   |                   |                       |                   |      |
| 4  |                           | InP/ZnS   | anti-claudin 4 or | cell-targeted imaging | pancreatic cancer | 42,7 |
| 5  |                           | core/shell  | anti-PSCA         |                       | cells             | 6    |
| 6  |                           | GQDs  | polydopamine      | stable PL intensity   | KB cells          | 334  |
| 7  |                           |   |                   |                       |                   |      |
| 8  |                           | Si QDs  | IgG               | PL QYs 25%,           | HeLa cells        | 335  |
| 9  |                           |   |                   | emission peak 470-    |                   |      |
| 10 |                           |   |                   | 560 nm                |                   |      |
| 11 |                           | Mn-doped ZnSe                                       | AMACR             | cell-targeted imaging | LNCaP             | 336  |
| 12 |                           |   |                   |                       |                   |      |
| 13 |                           | ZnS: Mn/ZnS   | folic acid        | cell-targeted imaging | HeLa cells        | 337  |
| 14 |                           | core/shell  |                   |                       |                   |      |
| 15 |                           | ZAIS  | PEG2000-FA-       | emission peak 525-    | MDA-MB-231        | 296  |
| 16 |                           |   | RGD               | 625 nm                |                   |      |
| 17 |                           | (Zn)CuInS <sub>2</sub>                              | anti-Her2 Abs     | time-gated imaging    | human breast      | 338  |
| 18 |                           |   |                   |                       | cancer cells      |      |
| 19 |                           |   |                   |                       |                   |      |
| 20 | <i>In vivo</i> imaging    |   |                   |                       |                   |      |
| 21 |                           |   |                   |                       |                   |      |
| 22 |                           | AgInS <sub>2</sub>                                  | multidentate      | imaged with a 630     | nude mice         | 223  |
| 23 |                           |   | polymer           | nm laser              |                   |      |
| 24 |                           | CuInS <sub>2</sub> /ZnS                             | FA-SOC            | emission peak 720-    | Bel 7402 tumor    | 36   |
| 25 |                           | core/shell  | micelles          | 800 nm                | mice              |      |
| 26 |                           |   |                   |                       |                   |      |
| 27 |                           | Cu <sub>x</sub> In <sub>y</sub> S <sub>2</sub> /ZnS | PMMA              | emission peak of 726  | nude mice         | 280  |
| 28 |                           |   | microspheres      | nm                    |                   |      |
| 29 |                           | CuInSe <sub>2</sub> /ZnS                            | –                 | emission peak 700-    | lymph node in     | 136  |
| 30 |                           | core/shell  |                   | 1000 nm               | nude mice         |      |
| 31 |                           |   |                   |                       |                   |      |
| 32 |                           | GQDs  | –                 | multicolor cell       | BABL/C mice       | 339  |
| 33 |                           |   |                   | imaging               |                   |      |
| 34 |                           |   |                   |                       |                   |      |
| 35 |                           |   |                   |                       |                   |      |
| 36 | <b>Photoacoustic</b>      |   |                   |                       |                   |      |
| 37 | <b>imaging</b>            |   |                   |                       |                   |      |
| 38 |                           |   |                   |                       |                   |      |
| 39 | <i>In vivo</i> imaging    | Cu <sub>2-x</sub> Se                                | –                 | 1.7 pmol/L for PA     | SLN in nude mice  | 340  |
| 40 |                           |   |                   | LOD                   |                   |      |
| 41 |                           |   |                   |                       |                   |      |
| 42 |                           | CuS   | –                 | 800 μm resolution at  | SLN in nude mice  | 341  |
| 43 |                           |   |                   | 0.7 nmol              |                   |      |
| 44 |                           |   |                   |                       |                   |      |
| 45 |                           |   |                   |                       |                   |      |
| 46 | <b>Optical sensing</b>    |   |                   |                       |                   |      |
| 47 |                           |   |                   |                       |                   |      |
| 48 |                           |   |                   |                       |                   |      |
| 49 | <i>In vitro</i> detection | Ag <sub>2</sub> S                                   | Silica NPs &      | LOD of 10 oocysts     | <i>C. parvum</i>  | 342  |
| 50 |                           |   | anti-oocysts      | per mL                |                   |      |
| 51 |                           |   | McAb              |                       |                   |      |
| 52 |                           | Ag <sub>2</sub> Se QDs                              | PEI               | LOD of 2 mM           | dopamine          | 343  |
| 53 |                           |   |                   |                       |                   |      |
| 54 |                           | Ag <sub>2</sub> Se QDs                              | TGA               | LOD of 0.08 μg/ml     | ConA              | 344  |
| 55 |                           |   |                   |                       |                   |      |
| 56 |                           |   |                   |                       |                   |      |
| 57 |                           |   |                   |                       |                   |      |
| 58 |                           |   |                   |                       |                   |      |
| 59 |                           |   |                   |                       |                   |      |
| 60 |                           |   |                   |                       |                   |      |

|                             |                                    |   |  |                           |     |
|-----------------------------|------------------------------------|---|--|---------------------------|-----|
|                             | CuInS <sub>2</sub>                 | 3-APBA  | LOD of 0.2 μmol/L                          | dopamine                  | 345 |
|                             | GQD                                | c-ssDNA   | LOD of 0.4 nM                              | ssDNA                     | 346 |
| <b>Optical tracking</b>     |                                    |   |  |                           |     |
| <i>In vivo</i> tracking     | InAs/InP/ZnSe                      | MPA-HAS   | large fluorescence contrast                | LS174t & 22B tumor mice   | 297 |
|                             | PbS                                | SOC   | PL intensity increased from 24 hr to 48 hr | Bel-7402 tumor mice       | 347 |
|                             | Ag <sub>2</sub> S                  | Tat peptide                                       | 1000 stem cells with 100 ms resolution     | thMSCs in nude mice       | 47  |
| <b>Photothermal therapy</b> |                                    |   |  |                           |     |
| <i>In vitro</i> therapy     | Cu <sub>2-x</sub> Se               | amphiphilic poly(maleic anhydride)                | 22% transduction rate                      | HCT-116                   | 348 |
| <i>In vivo</i> therapy      | CuS                                | cysteine  | 38% transduction rate                      | K7M2 tumor mice           | 349 |
| <b>Multimodal imaging</b>   |                                    |   |  |                           |     |
| MRI/fluorescent             | InP/ZnS                            | 80 Gd(III)  | 900 mM-1s-1 of relaxivity                  | rat brain & ovarian cells | 193 |
|                             | AgInS <sub>2</sub> /ZnS core/shell | folic acid & MnFe <sub>2</sub> O <sub>4</sub> NPs | bright yellow fluorescence                 | HeLa cells                | 350 |
|                             | CuInS <sub>2</sub> @ZnS:Mn         | DHLA-PEG  | multi-target imaging                       | LS180 tumor mice          | 156 |

### 5.1. Optical Imaging

Optical imaging is an extremely useful tool for biological research because it can provide high-resolution *in vitro* and *in vivo* information.<sup>351,352</sup> Key advantages of optical imaging include high sensitivity, low cost, high frame rate, easy portability, and powerful potential for multiplex imaging. The real-time capability of optical imaging allows one to employ this technique during

1  
2  
3 surgery and endoscopic procedures. Optical imaging is useful for early cancer detection and for  
4 image-guided surgical resection of tumors. For both *in vitro* and *in vivo* optical imaging, cells or  
5 tissues are often labeled with organic dyes, and fluorescence from these dyes is collected using  
6 appropriate imaging tools.<sup>174,353,354</sup> Optical probes for these applications should have high QY  
7 and resistance to photobleaching for long-term imaging. QDs combine high QY and excellent  
8 photostability with other attractive features, and can outperform organic dyes in many imaging  
9 applications. In addition, the large surface area and rich surface chemistry of QDs allows them to  
10 be conjugated with biomolecules for targeted imaging. In contrast to most dyes, QDs with  
11 different emission wavelengths can be excited with a single light source, which facilitates  
12 multiplex imaging of QD-labeled samples.<sup>36,38,66,219</sup> In comparison to QDs, organic fluorophores  
13 typically have broader emission spectra and smaller Stokes shifts. The overlap of emission and  
14 absorbance spectra complicates imaging. Here, we survey the use of Cd-free QDs in optical  
15 imaging methods including fluorescence/photoluminescence (PL) imaging, multicolor imaging,  
16 confocal imaging and multi-photon imaging.

17  
18  
19  
20  
21  
22  
23  
24  
25  
26  
27  
28  
29  
30  
31  
32  
33  
34  
35  
36 Liu *et al.* prepared NIR-emitting AgInS<sub>2</sub> QDs (emission peak at ~800 nm) and encapsulated  
37 them within Pluronic F127 triblock copolymer micelles to make them water-dispersible.<sup>331</sup> The  
38 AgInS<sub>2</sub> QDs served as luminescent probes for *in vitro* and *in vivo* tumor-targeted imaging. The *in*  
39 *vitro* study showed that the Pluronic-F127 encapsulated AgInS<sub>2</sub> QDs were taken up by human  
40 peripheral blood monocyte-derived macrophages. For the *in vivo* study, fibrosarcoma cells were  
41 implanted on the shoulder of mice to establish a tumor model. Accumulation of micelle-  
42 encapsulated QDs at the tumor site was observed as early as 15 min after tail vein injection.  
43 After 80 min, the AgInS<sub>2</sub> NCs had accumulated in the liver and spleen, and signal from the  
44 tumor site decreased significantly. These results suggest that tumor tissue accumulation was a  
45  
46  
47  
48  
49  
50  
51  
52  
53  
54  
55  
56  
57  
58  
59  
60

1  
2  
3 passive process driven by the enhanced permeability and retention (EPR) effect. Compared with  
4  
5 AgInS<sub>2</sub> QDs, AgInS<sub>2</sub>/ZnS core/shell QDs exhibit higher optical stability and better  
6  
7 biocompatibility. More recently, our group has synthesized AgInS<sub>2</sub>/ZnS and CuInS<sub>2</sub>/ZnS QDs  
8  
9 and encapsulated them in F127 micelles.<sup>355</sup> Both AgInS<sub>2</sub>/ZnS and CuInS<sub>2</sub>/ZnS QD-micelles were  
10  
11 taken up by macrophages *in vitro* and the cells showed no morphological changes or signs of  
12  
13 damage. *In vivo* imaging showed that the AgInS<sub>2</sub>/ZnS QD-micelles accumulated at the tumor site  
14  
15 after tail vein injection, via the EPR effect. PL from intra-abdominally injected CuInS<sub>2</sub>/ZnS QD-  
16  
17 micelles was easily differentiated from the background autofluorescence.  
18  
19  
20  
21

22 Tan *et al.* used a multidentate polymer (MDP) to encapsulate NIR-emitting AgInS<sub>2</sub> QDs for  
23  
24 *in vivo* optical imaging.<sup>223</sup> The effects of administration route were demonstrated using two  
25  
26 groups of nude mice. One group received QDs *via* subcutaneous injection and were then imaged  
27  
28 under 630 nm laser excitation at successive time points. PL intensity decreased little over time,  
29  
30 suggesting localized accumulation of the QDs at the injection site and reflecting the high PL  
31  
32 stability of the QDs *in vivo*. In the other group, QDs were injected *via* the tail vein and images  
33  
34 were collected 4, 12, and 24 h after injection. Four hours after injection, the QDs were  
35  
36 distributed throughout the bodies of the mice. At later times, the QD PL signal gradually  
37  
38 decreased, reflecting the slow degradation and clearance of QDs (with a half-life of 20.1±3.4 h).  
39  
40 The excellent contrast of the images suggested that such QDs were suitable for deep tissue  
41  
42 imaging *in vivo*. Gu's group prepared AgInSe<sub>2</sub>/ZnS QDs functionalized with an RGD peptide for  
43  
44 targeted *in vivo* imaging.<sup>332</sup> Both αβ3-positive MDA-MB-231 cells and αβ3-negative MCF-7  
45  
46 cells were injected subcutaneously into nude mice, followed by intravenous administration of the  
47  
48 RGD-PAA-QDs. Six hours after administration of QDs, stronger QD PL was observed in the  
49  
50 αβ3-positive tumor-bearing nude mice compared to that in the αβ3-negative tumor-bearing  
51  
52  
53  
54  
55  
56  
57  
58  
59  
60

ones (Figure 36), demonstrating targeting of the RGD-PAA-QDs to tumor cells that overexpress  $\alpha_v\beta_3$  integrin receptors.

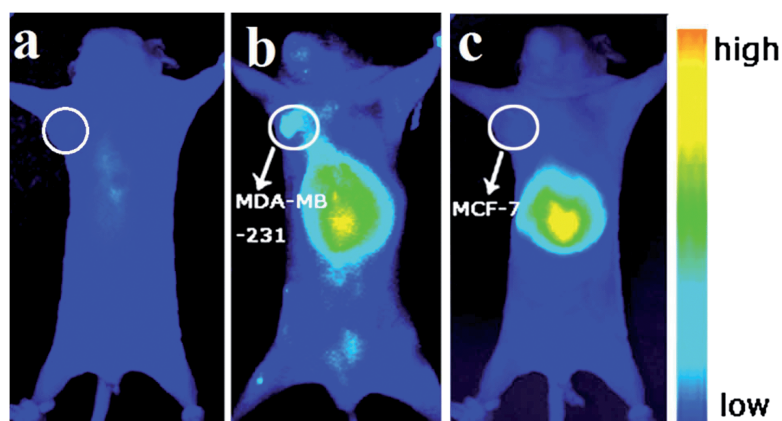


**Figure 36.** NIR PL images of tumor-bearing mice before tail-vein injection (a) and 6 h after intravenous injection with 775 nm-emitting RGD-PAA-QDs: (b)  $\alpha_v\beta_3$ -positive MDA-MB-231 tumor and (c)  $\alpha_v\beta_3$ -negative MCF-7 tumor. Reprinted with permission from Deng *et al.*<sup>332</sup> Copyright 2014 Royal Society of Chemistry.

NIR imaging of  $\text{Ag}_2\text{Se}$  QDs with PL at 1300 nm was also demonstrated in small animals.<sup>139</sup> The  $\text{Ag}_2\text{Se}$  QDs were functionalized with C18-PMH-PEG to obtain a stable aqueous dispersion with bright PL and good photostability. The hydrodynamic diameter of the QDs was  $\sim 43$  nm. The imaging performance of  $\text{Ag}_2\text{Se}$  QDs was compared to ICG. A dose of 37 mg/kg ICG provided a weak signal and fuzzy images of the vasculature due to scattering and absorbance by tissues. On the other hand, C18-PMH-PEG- $\text{Ag}_2\text{Se}$  QDs at a dose of 6 mg/kg produced clear images of the liver, spleen, and vasculature, under 808 nm laser excitation, within a few minutes following injection (Figure 37).

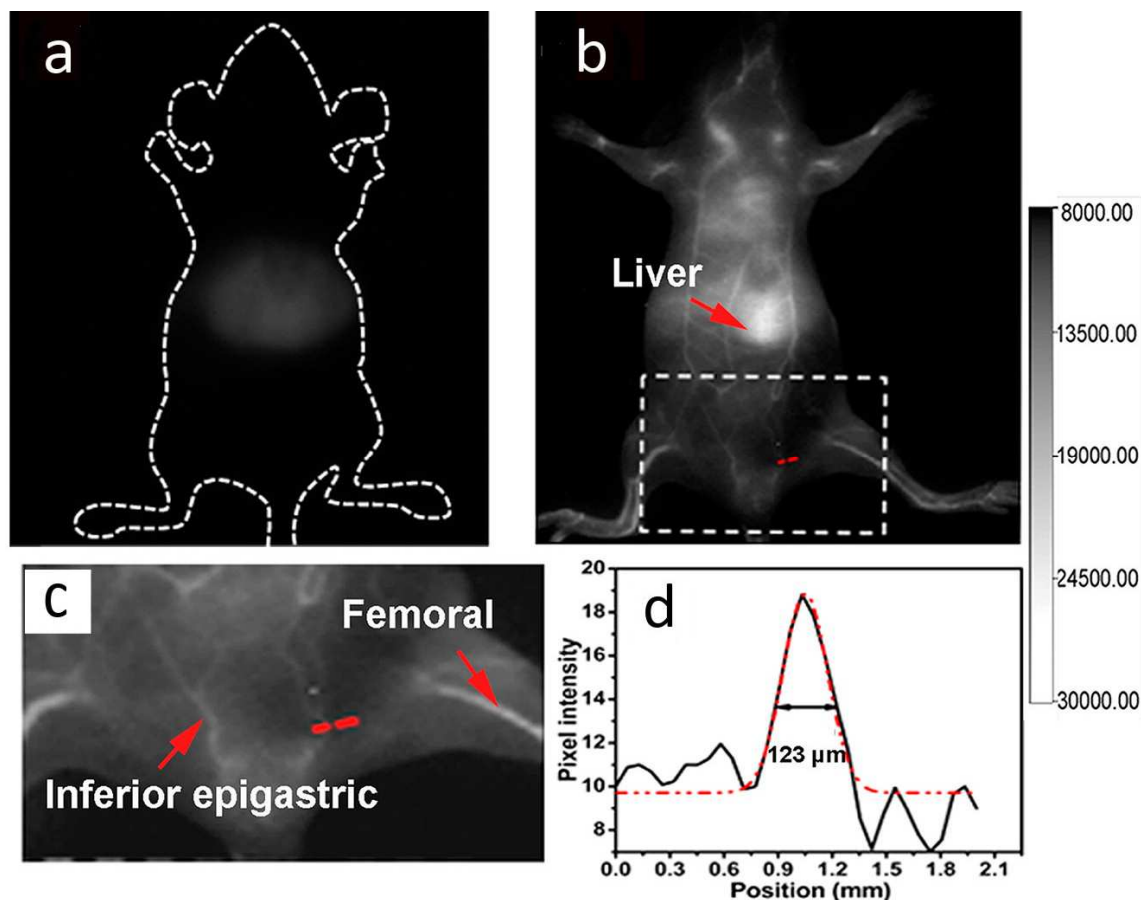


**Figure 37.** *In vivo* imaging using ICG and C18-PMH-PEG-Ag<sub>2</sub>Se QDs. *In vivo* imaging of a live mouse in supine position after tail vein injection of (a) ICG or (b) C18-PMH-PEG-Ag<sub>2</sub>Se QDs. (c) Magnified view of the zone indicated in (b). (d) A cross-sectional intensity profile measured along the red-dashed line in (c) with its peak fitted to a Gaussian function. Reprinted with permission from Dong *et al.*<sup>139</sup> Copyright 2013 American Chemical Society.

CuInS<sub>2</sub> QDs also exhibit strong near-IR PL and show promise in biomedical optical imaging. In the research works from our group mentioned above, the CuInS<sub>2</sub>/ZnS QDs were encapsulated in F127 micelles to make them water-dispersible.<sup>281</sup> They were then conjugated with folic acid (FA) to construct QD-FA probes that target cells which overexpress FA receptors. Pancreatic

1  
2  
3 cancer cells (CRL-1469) that overexpress FA receptors were used to create a tumor model in  
4  
5 nude mice. The QD-FA formulation was systemically administered by intravenous injection  
6  
7 followed by whole-animal PL imaging. Strong QD PL was observed from tumors of mice treated  
8  
9 with FA-conjugated QDs while mice treated with unconjugated QDs exhibited little PL from the  
10  
11 tumor site, demonstrating the tumor-specificity of the QD-FA probes. In addition, CuInS<sub>2</sub> QDs  
12  
13 with two different emission colors were injected subcutaneously at different sites to demonstrate  
14  
15 the potential of these NIR QDs for *in vivo* multiplex imaging. The luminescence from the two  
16  
17 different QDs was easily distinguished. In a separate study, CuInS<sub>2</sub>/ZnS QDs were packaged in  
18  
19 biodegradable folic acid-modified chitosan micelles for cancer imaging.<sup>36</sup> The ability of the QD-  
20  
21 loaded micelles to target tumor cells was evaluated *in vitro* and *in vivo*. FA receptor-positive Bel  
22  
23 7402 cells showed a much higher uptake of the QD-loaded FA-SOC micelles than did FA  
24  
25 receptor-negative A549 cells. For *in vivo* studies, A549 and Bel-7402 cells were injected into  
26  
27 nude mice to generate tumors, and QD-loaded micelles were administered by tail vein injection.  
28  
29 The results confirmed the high targeting efficacy of QD-loaded FA-SOC micelles to FA  
30  
31 receptor-positive tumors. Multiplex NIR PL imaging was performed by administering two types  
32  
33 of QD-loaded micelles (QD720 and QD800) subcutaneously. Again, signals of different QDs  
34  
35 were well separated.  
36  
37  
38  
39  
40  
41  
42

43 Yu *et al.* developed a low-temperature approach for producing CuInS<sub>2</sub>/ZnS QDs with bright  
44  
45 PL and applied them for *in vitro* and *in vivo* imaging.<sup>356</sup> Mercaptoundecanoic acid (MUA) and  
46  
47 dihydrolipoic acid (DHLLA) were each used for phase transfer of the QDs into water. Two single-  
48  
49 domain antibodies (sd Abs), 2A3 and EG2 were used to functionalize QDs for tumor cell  
50  
51 targeting *in vitro* and *in vivo*. The *in vitro* result showed that the 2A3-conjugated CuInS<sub>2</sub>/ZnS  
52  
53 QDs were efficiently taken up by BxPC3 pancreatic cancer cells, yielding images with good  
54  
55  
56  
57  
58  
59  
60

1  
2  
3 contrast. However, the signal from cells treated with unconjugated CuInS<sub>2</sub>/ZnS QDs was barely  
4  
5 detectable. The *in vivo* result showed PL signals from EG2-conjugated CuInS<sub>2</sub>/ZnS QDs in a  
6  
7 brain tumor 4 h after intravenous injection.  
8  
9

10 Because the extracellular microenvironment in a tumor is typically more acidic (pH~6.5-6.8)  
11  
12 than normal tissue, targeting strategies exploiting this pH difference have been studied as a route  
13  
14 to smart and programmable delivery systems. Dong *et al.* designed a charge-reversible pH-  
15  
16 sensitive NIR luminescent nanoprobe that showed enhanced cellular uptake at low extracellular  
17  
18 pH.<sup>333</sup> The CuInS<sub>2</sub>/ZnS QDs were encapsulated within a lauric acid and 2,3-dimethyl maleic  
19  
20 anhydride modified ε-polylysine (ε-PL-g-LA/DMA) shell, which provided a dense protective  
21  
22 layer for the QDs and enhanced charge-mediated endocytosis at low pH. When the negatively-  
23  
24 charged QDs were exposed to low pH, the β-carboxyl amide bond in the polymer shell was  
25  
26 broken, creating positive surface charge on the QDs. *In vitro* experiments showed higher QD  
27  
28 uptake by tumor cells at pH 6.8 than at pH 7.4. The pH-responsive nature of these QDs may  
29  
30 prolong circulation time and enhance QD accumulation in tumor tissue. Such nanoprobe avoid  
31  
32 the limitation of receptor targeting probes associated with the heterogeneity of different cancer  
33  
34 cells and thus provide an attractive general tumor targeting strategy. Using Cu<sub>x</sub>In<sub>y</sub>S<sub>2</sub>/ZnS QDs  
35  
36 with bright NIR PL at 726 nm, Choi *et al.* achieved a detection depth of 9 mm and acquired  
37  
38 strong signals from 2 mm beneath the skin of nude mice.<sup>280</sup> In comparison, Cu<sub>x</sub>In<sub>y</sub>S<sub>2</sub>/ZnS QDs  
39  
40 with 589 nm emission showed negligible signal at the same conditions (**Figure 38**).  
41  
42  
43  
44  
45  
46  
47  
48  
49  
50  
51  
52  
53  
54  
55  
56  
57  
58  
59  
60

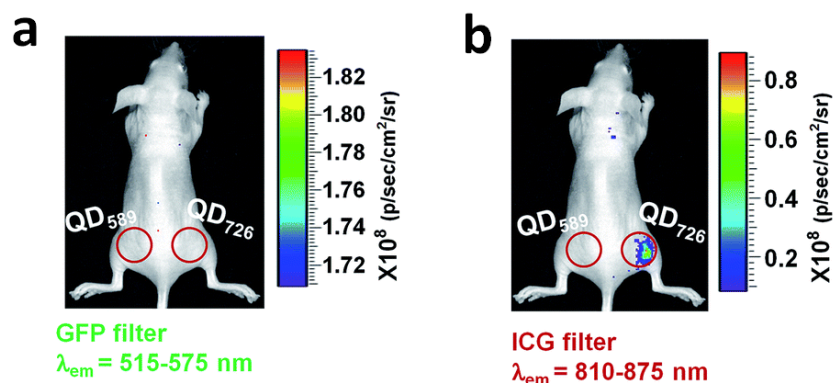


**Figure 38.** PL images of QD-loaded PMMA microspheres implanted into thigh muscles by intramuscular injection. Images taken using a GFP excitation filter (445–490 nm) with a GFP emission filter (515–575 nm) (a) and an ICG emission filter (810–875) (b). Reprinted with permission from Choi *et al.*<sup>280</sup> Copyright 2015 Royal Society of Chemistry.

Cassette *et al.* also prepared NIR (700–1000 nm) Cu-In-Se/ZnS QDs for small animal imaging.<sup>136</sup> The QD formulation was injected subcutaneously in the right anterior paw of healthy mice. PL from the regional lymph node was observed after a few minutes, and the QDs accumulated in the right axillary lymph node after 4 h, as confirmed by ICP-MS measurements. Lymph node imaging can provide useful information for diagnosis and therapy of potentially metastatic tumors. Use of QDs as luminescent contrast agents for imaging lymph nodes *in vivo* can therefore have rapid clinical impact. Similarly, Jiang *et al.* synthesized Cu-doped In-Zn-S QDs (CIZS QDs) by a hydrothermal method and achieved tunable PL emission from 465 to 700 nm.<sup>206</sup> Adding a ZnS shell to the CIZS core improved the PL QY to 25–35%. For imaging, rabbit-anti-alpha-fetoprotein (AFP) was covalently conjugated to the QDs, and the CIZS/ZnS QD-AFP were incubated with Hep-G2 cancer cells. Bright yellow PL was observed in the cytoplasm along with weak PL in the nucleus. The same group synthesized Zn-doped AgIn<sub>5</sub>S<sub>8</sub>

1  
2  
3 (ZAIS) QDs, and performed similar cell-targeted imaging.<sup>295</sup> Again, QDs coated with AFP  
4 antibodies bound specifically to the antigen receptor in the cytoplasm of Hep G2 cells.  
5  
6

7  
8 Fahmi and Chang prepared double layer-encapsulated AgInS<sub>2</sub>/ZnS QDs (DL-QDs) using  
9 alkyl-capping ligands that interact with the hydrophobic ligands on the QDs surface.<sup>357</sup> The  
10 alkyl-capping ligands included carbon chains of varied length with different terminal functional  
11 groups (*e.g.*, thiol, amine, carboxyl and hydroxyl), which can serve as reactive sites for coupling  
12 with biomolecules (*e.g.*, antibodies, DNA/RNA, enzymes). Specifically, DL-QD-COOH were  
13 functionalized with folate to target HeLa cells. Confocal imaging demonstrated that the folate-  
14 conjugated DL-QDs specifically and effectively targeted HeLa cells through a folate receptor-  
15 mediated pathway and showed minimal uptake by breast cancer (MCF-7) cells and liver  
16 carcinoma (HepG2) cells.  
17  
18  
19  
20  
21  
22  
23  
24  
25  
26  
27

28  
29 Generally, the PL lifetimes of QDs are long relative to autofluorescence and typical  
30 fluorescence lifetimes of dyes. Heyes's group reported biocompatible (Zn)CuInS<sub>2</sub> QDs with long  
31 PL lifetime and used them as probes in time-gated imaging.<sup>338</sup> Suppression of autofluorescence  
32 by time gating produced an order-of-magnitude improvement in signal-to-noise ratio. The PL  
33 lifetime of these (Zn)CuInS<sub>2</sub> QDs was 21 ns, significantly longer than the 8 ns lifetime of Cd-  
34 based QDs, which enabled better suppression of cell autofluorescence through time-gated  
35 detection. The (Zn)CuInS<sub>2</sub>/ZnS QDs were used to specifically detect the Her2 receptor on human  
36 breast cancer cells (**Figure 39**). The sensitivity was comparable to, or even superior to, Cd-based  
37 QDs and much higher than molecular probes. The authors asserted that this was the first report of  
38 using Cd-free QDs for labeling breast cancer cells by time-gated imaging.  
39  
40  
41  
42  
43  
44  
45  
46  
47  
48  
49  
50  
51  
52  
53  
54  
55  
56  
57  
58  
59  
60

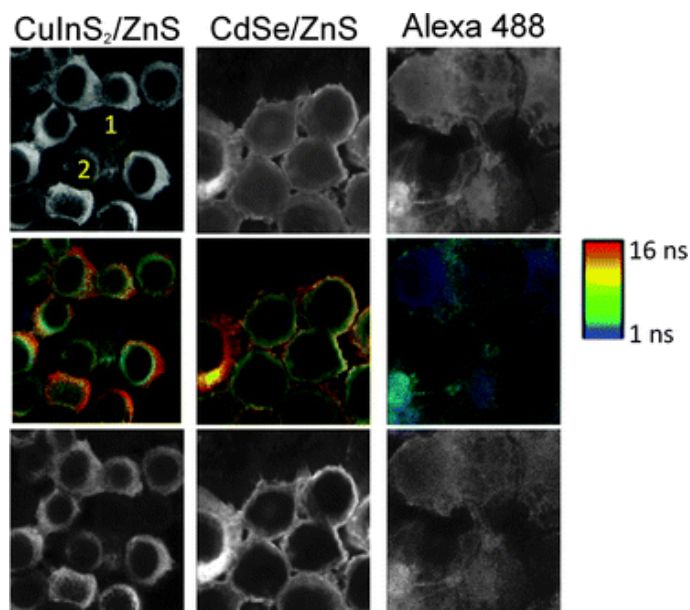


**Figure 39.** Time-gated bioimaging of human breast cancer cell labeled by QDs-anti-Her2. Upper row: PL intensity images of the cancer cells, the cells labeled 1 and 2 are two cancer cells expressing Her2 receptors at different levels; Middle row: FLIM images; ranging from 1 ns (blue) to 16 ns (red); Bottom row: image after time-gating the first 10 ns of photons, which significantly improves contrast, and removes unlabeled cells from the images. Reprinted with permission from Mandal *et al.*<sup>338</sup> Copyright 2014 Royal Society of Chemistry.

Bouccara *et al.* developed Zn-Cu-In-Se/ZnS QDs for cell labeling *via* time-gated imaging.<sup>358</sup> The PL lifetime of their QDs was much longer (150-200 ns) than that of (Zn)CuInS<sub>2</sub>/ZnS QDs, which further facilitates separation of PL from autofluorescence (5-10 ns). To prolong the observation time, they stained the cells with a high concentration of NIR QDs *via* electroporation. The internalized NIR QDs were homogeneously distributed in the cell cytoplasm, and the time-gated imaging effectively eliminated contributions from autofluorescence.

InP and InP/ZnS QDs are also promising optical probes due to their excellent optical features and strong resistance to corrosion in biological systems. Our group has modified water-

1  
2  
3 dispersible InP/ZnS core/shell QDs with mercaptosuccinic acid and functionalized them with  
4 two antibodies (anti-claudin 4 and anti-PSCA) as targeting molecules.<sup>42,76</sup> Receptors for these  
5 antibodies are overexpressed on pancreatic cancer cells. Confocal microscopy revealed that the  
6 QDs were transported into the cytoplasm by a receptor-mediated pathway.  
7  
8  
9

10  
11 In addition to Cu- and In-based QDs, Mn-doped ZnSe QDs were also demonstrated as  
12 nontoxic and effective optical probes for tumor targeting. Su *et al.* conjugated Mn-doped ZnSe  
13 QDs with the anti- $\alpha$ -methylacyl-CoA racemase (AMACR) for specific imaging of prostate  
14 cancer cells.<sup>336</sup> The targeting ability of the QDs was confirmed by comparing their  
15 internalization in AMACR-negative PC3M cancer cells and AMACR-positive LNCaP cancer  
16 cells. ZnS:Mn/ZnS core/shell QDs have also been used for bioimaging.<sup>337</sup> Yu *et al.* synthesized  
17 ZnS:Mn/ZnS QDs using MPA as a stabilizer. The QDs were then functionalized with FA to form  
18 nanocomplexes that specifically bound to FA receptors. The QDs targeted HeLa cells *in vitro*  
19 and accumulated at the HeLa cell tumor site *in vivo*, demonstrating that the Mn-doped QDs could  
20 provide another alternative to Cd-based QDs in biomedical optical imaging.  
21  
22  
23  
24  
25  
26  
27  
28  
29  
30  
31  
32  
33  
34  
35

36 Cellular uptake of NPs generally depends on their size and surface functionalization.<sup>359</sup>  
37 However, Soenen *et al.* suggested that the QD core composition may also affect the cell uptake.  
38 They prepared ZnSe/ZnS QDs and InP/ZnS QDs with the same size and surface ligands and used  
39 them for cellular bioimaging. Confocal microscopy showed highly colocalized QD PL from  
40 endosomal compartments, revealing the intraendosomal accumulation of QDs. Moreover, they  
41 estimated the QD concentration from PL intensity observed in cells and found that ZnSe/ZnS  
42 QDs were internalized by cells slightly more efficiently than the InP/ZnS QDs. This result  
43 suggests that QD core composition may affect cellular uptake, but further evaluation of this  
44 possibility is needed.  
45  
46  
47  
48  
49  
50  
51  
52  
53  
54  
55  
56  
57  
58  
59  
60

1  
2  
3 Silicon QDs (Si QDs), are potential optical probes for *in vivo* imaging due to their nontoxic  
4 properties, small size, high brightness and resistance to photobleaching.<sup>360</sup> Porous silicon NPs  
5  
6 have been shown to degrade in physiological environments and to thereby be eliminated in mice  
7  
8 *via* renal clearance, further reducing toxicity concerns. All these advantages have motivated the  
9  
10 investigation of Si QDs for *in vitro* and *in vivo* bioimaging, biosensing and cancer theranostics.  
11  
12 Gooding *et al.* prepared photostable Si QDs and functionalized their surface using a versatile  
13  
14 click-chemistry approach.<sup>53</sup> To demonstrate the biomedical potential of the functionalized Si  
15  
16 QDs, amine-functionalized Si QDs were used as *in vitro* PL probes for HeLa cells under  
17  
18 continuous laser excitation. After 45 s of irradiation, the cell autofluorescence was bleached  
19  
20 while the PL of Si QDs remained. Such photostable and biocompatible Si QDs have great  
21  
22 potential for long-term cellular imaging. Zhong *et al.* presented a facile and low-cost  
23  
24 photochemical method to obtain highly photoluminescent (QY 25%) Si QDs with PL tunable  
25  
26 from 470 nm to 560 nm.<sup>335</sup> After conjugating with IgG using carbodiimide chemistry, the Si QD-  
27  
28 IgG conjugates served as bioprobes for cellular immunofluorescent imaging. To compare  
29  
30 photobleaching rates, the Si QDs, FITC dye, CdTe QDs, and CdSe/ZnS QDs were all employed  
31  
32 for cellular imaging by laser-scanning confocal luminescence microscopy. All the QDs showed  
33  
34 less photobleaching than the dye, which stopped emitting within 4 min. Long-time UV  
35  
36 irradiation lead to severe PL bleaching of II-VI Cd-based QDs (absolute bleaching within 25 min  
37  
38 for CdTe and within 50 min for CdSe/ZnS). Impressively, the Si QDs exhibited the best  
39  
40 resistance to photobleaching, remaining bright and stable after 2 h of continuous irradiation  
41  
42 (**Figure 40**). The results suggested that the Si QDs are suitable PL probes for long-term  
43  
44 bioimaging and tracking. In that study, the Si QDs were capped with covalently-bound  
45  
46 hydrophobic ligands. For bio-imaging, they were encapsulated in phospholipid-PEG polymer  
47  
48  
49  
50  
51  
52  
53  
54  
55  
56  
57  
58  
59  
60

micelles that were further functionalized with a cyclic RGD peptide for *in vivo* targeting of the tumor vasculature.

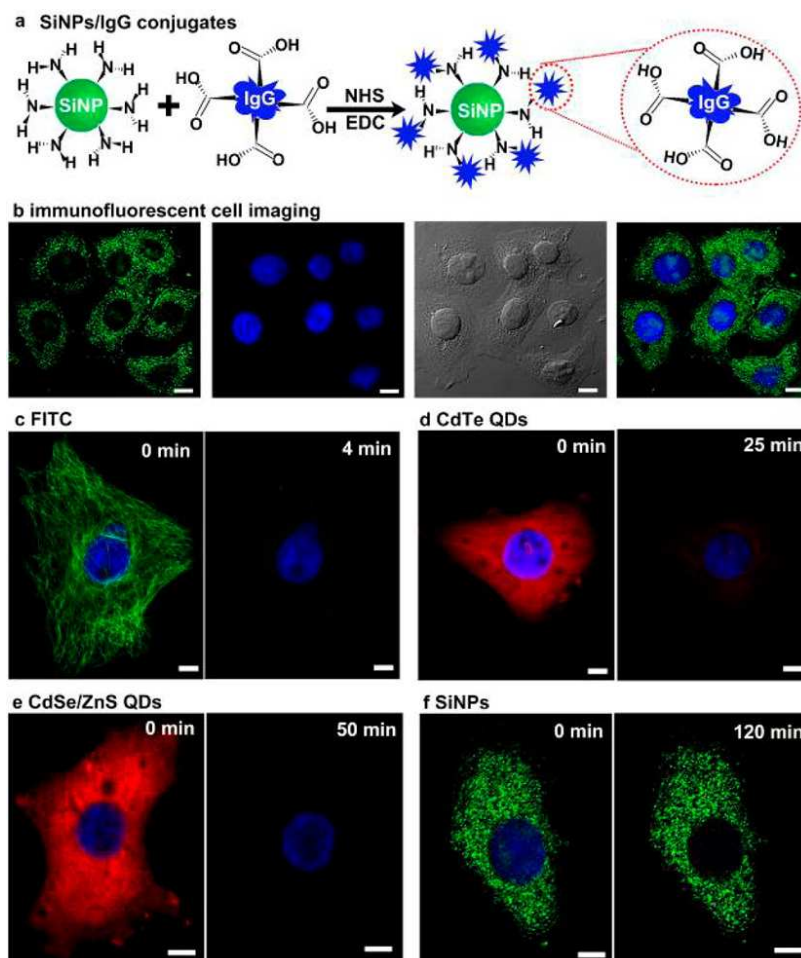


**Figure 40.** The fluorescence images of the cells labeled by different probes and their photobleaching rates. (a) Schematic illustration of conjugation of SiNPs with goat-antimouse IgG. (b) (Left) microtubules are labeled by the IgG-conjugated SiNPs; (middle) cellular nuclei are imaged by Hoechst; (right) overlay of the two fluorescence images. (c–f) Photobleaching of FITC, CdTe QDs, CdSe/ZnS QDs, Hoechst, and SiNPs after the indicated times. Scale bars: 10  $\mu\text{m}$ . Reprinted with permission from Zhong *et al.*<sup>335</sup> Copyright 2015 American Chemical Society.

1  
2  
3 More recently, Cheng *et al.*<sup>361</sup> employed Si QDs for both one- and two-photon cellular  
4 imaging using fluorescence lifetime imaging microscopy (FLIM). The use of FLIM minimized  
5 signal from the biological background, while the two-photon near-IR light excitation avoided the  
6 phototoxicity associated with UV excitation of Si QDs. The authors functionalized the Si QDs  
7 with amine groups and used HeLa cells as target label examples. The PL lifetime of the Si  
8 QDs, > 4 ns, was much longer than that of the cell autofluorescence (< 2.5 ns). Thus, the cellular  
9 autofluorescence could be separated from Si QD PL through deconvolution of the FLIM. Two  
10 excitation wavelengths of 740 nm and 800 nm were tested for the two-photon FLIM imaging, and  
11 800 nm excitation was found to be more effective. Most of the detected PL was distributed  
12 throughout the cytoplasm rather than the nucleus. Förster resonance energy transfer (FRET) from  
13 SiQDs to DY485, a dye that serves as an acceptor, was also demonstrated and allowed tuning of  
14 the emission from blue to yellow. The dye emission was enhanced by 200% after coupling with  
15 the Si QDs.

16  
17  
18  
19  
20  
21  
22  
23  
24  
25  
26  
27  
28  
29  
30  
31  
32  
33  
34 Recently, graphene QDs have emerged as novel optical probes with advantages including  
35 small size, superior stability and good biocompatibility. Zhu *et al.* used the top-down “nano-  
36 cutting” method to create photoluminescent GQDs of ~4 nm diameter.<sup>339</sup> The GQDs were  
37 incubated with rat Schwann cells, and their uptake over time was observed by confocal  
38 microscopy and fluorescence activated cell sorting (FACS). GQDs were distributed in the  
39 cytoplasm and in lysosomes. Multicolor cellular imaging was demonstrated using different  
40 excitation wavelengths. In addition, the GQDs were injected subcutaneously into BABL/C mice.  
41 The Ex/Em=465/620 nm wavelength pair provided the best bioimaging result with minimal  
42 autofluorescence and increased signal-to-noise ratio. Similarly, Lee’s group synthesized low-  
43 toxicity GQDs by a facile exfoliation/oxidation approach and then functionalized them with  
44  
45  
46  
47  
48  
49  
50  
51  
52  
53  
54  
55  
56  
57  
58  
59  
60

1  
2  
3 polydopamine for improved colloidal stability.<sup>334</sup> When dispersed in PBS buffer, the uncoated  
4  
5  
6 GQDs showed a 45% decrease in PL intensity after 14 days, while PL from pDA-coated GQDs  
7  
8 remained stable. *In vitro* imaging showed that GQDs with and without the pDA coating were  
9  
10 taken up by KB cells. However, the biodistribution and clearance profiles observed by *in vivo*  
11  
12 imaging differed between coated and uncoated GQDs.  
13

14  
15 Peng *et al.* reported that different sizes of graphene QDs were produced by acid treatment  
16  
17 and chemical exfoliation of traditional pitch-based carbon fibers.<sup>307</sup> The QDs had diameters of 1  
18  
19 to 4 nm, and thicknesses of 1 to 3 atomic layers (0.4 to 2 nm). The QD PL color was tuned by  
20  
21 varying the synthesis parameters to produce QDs of varying size. Green-emitting graphene QDs  
22  
23 were used to stain T47D cancer cells and the nucleus of the cells was stained with DAPI (blue  
24  
25 color) for comparison. PL imaging clearly showed the high contrast PL signal of green GQDs  
26  
27 near the nucleus. These images suggest that graphene QDs can be used for bioimaging, but their  
28  
29 QY remains relatively low compared to Cd-based QDs. Thus, further engineering is needed to  
30  
31 improve brightness and QY for ultrasensitive imaging of cells.  
32  
33

34  
35 Two-photon PL contrast agents can enable increased imaging depth while reducing  
36  
37 autofluorescence and photodamage, because they are excited in the near IR. One of the earliest  
38  
39 demonstrations of two-photon imaging using Cd-free QDs was presented by Bharali *et al.* in  
40  
41 2005<sup>76</sup> using InP/ZnS core-shell QDs. The large Bohr radius of InP makes these QDs more  
42  
43 polarizable, enhancing nonlinear optical properties. Liu *et al.* employed nitrogen-doped graphene  
44  
45 QDs as two-photon PL contrast agents.<sup>6</sup> The two-photon absorbance cross-section of the QDs  
46  
47 reached 48,000 Göppert-Mayer units, exceeding that of conventional chromophores and  
48  
49 comparable to that of Cd-based QDs. The authors achieved imaging depths of 1800  $\mu\text{m}$  in a  
50  
51 tissue phantom. Moreover, they found that the QDs are biocompatible and possess excellent  
52  
53  
54  
55  
56  
57  
58  
59  
60

1  
2  
3 photostability. This combination of imaging depth, high two-photon absorption cross-section,  
4  
5 and outstanding photostability of the QDs can make them valuable two-photon PL probes for  
6  
7 long term two-photon imaging *in vivo*. He *et al.* demonstrated two- and three-photon excited  
8  
9 upconverted emission from Si QDs<sup>239</sup>, but did not present bioimaging results in that study.  
10  
11  
12 Geszke-Moritz *et al.* demonstrated two-photon excited PL imaging using Mn-doped ZnS QDs.<sup>256</sup>  
13  
14

## 15 **5.2. Photoacoustic Imaging**

16  
17 Recently, photoacoustic (PA) imaging has emerged as a valuable noninvasive biomedical  
18  
19 imaging method combining key advantages of optical imaging and ultrasound imaging. It  
20  
21 acquires images based upon optical absorbance contrast, with a combination of high spatial  
22  
23 resolution and deep imaging depth that cannot be achieved by either optical or ultrasound  
24  
25 imaging alone (**Figure 41**).<sup>78,362-366,340</sup> The use of NIR optical excitation in PA imaging  
26  
27 significantly increases the penetration depth of imaging.<sup>366-368</sup> Our recent work reported the use  
28  
29 of Cu<sub>2-x</sub>Se QDs, a new type of QDs with NIR LSPR absorbance, for lymph node mapping by PA  
30  
31 imaging.<sup>369</sup> The Cu<sub>2-x</sub>Se QDs were used for volumetric *in vivo* mapping of SLNs by injection  
32  
33 into the paw pad of rats, followed by PA imaging of the corresponding axillary region. Results  
34  
35 showed strong NIR LSPR absorbance from the SLN. The PA detection limit of the 7.6 nm Cu<sub>2-</sub>  
36  
37 xSe QDs was 1.7 pmol/L. If compared on the basis of particle volume, rather than number  
38  
39 concentration of particles, this matches the performance of gold nanocages and other top-  
40  
41 performing PA contrast agents. Building on this study, our group presented a heterodimer  
42  
43 nanostructure composed of a semiconductor domain (Cu<sub>2-x</sub>Se) and a metal domain (Au).<sup>369</sup> This  
44  
45 nanostructure exhibits broad LSPR absorbance spanning visible and NIR wavelengths, arising  
46  
47 from interactions between the Cu<sub>2-x</sub>Se and Au domains. A clinically relevant imaging depth of up  
48  
49 to 17 mm was achieved in this study.  
50  
51  
52  
53  
54  
55  
56  
57  
58  
59  
60

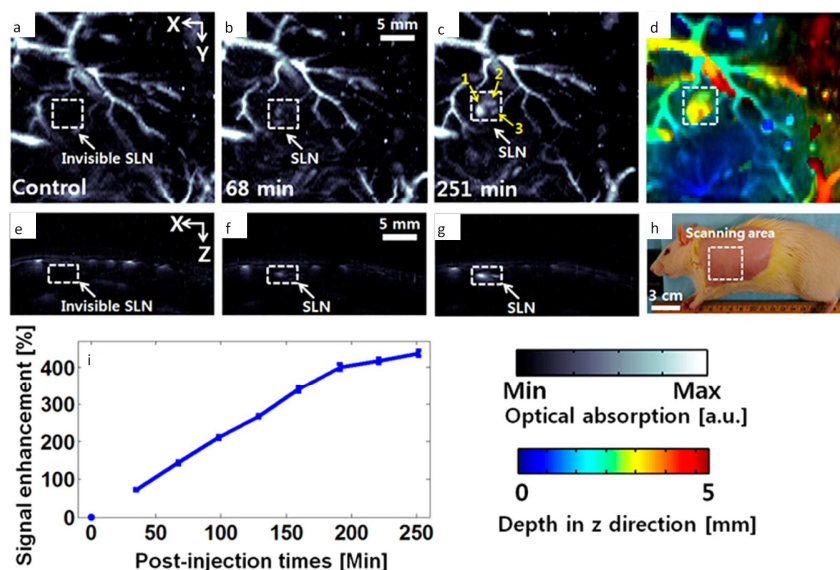


**Figure 41** *In vivo* photoacoustic (PA) coronal maximum amplitude projection (MAP) images. PA images were acquired before (a) and after (b–c) Au–Cu<sub>2–x</sub>Se injection. (d) Depth-encoded PA coronal MAP image of (c). (e–g) Depth-resolved cross-sectional PA B-scan images of a–c. (h) Photograph of the experimental rat. (i) Enhancement of PA signal from a sentinel lymph node (SLN) over time. Reprinted with permission from Liu *et al.*<sup>369</sup> Copyright 2013 American Chemical Society.

In addition to Cu<sub>2–x</sub>Se QDs, 11 nm CuS NPs with absorbance peaking at 990 nm have been engineered as a PA contrast agent for deep tissue imaging using 1064 Nd:YAG laser excitation.<sup>341</sup> The CuS NPs were clearly visualized in the mouse brain 24 h after intracranial injection. Following interstitial injection into the front paw pad, images of lymph nodes located 12 mm beneath the skin were acquired. To further probe the application potential of these CuS NPs, an agarose gel containing CuS NPs was embedded in chicken breast at depth of ~5 cm. Imaging resolution of ~800 μm was achieved with a detection limit of ~0.7 nmol per imaging voxel. Similarly, Ke *et al.* employed PEGylated CuS NPs as PA contrast agents.<sup>370</sup> In their *in*

*in vitro* studies, the contrast enhancement effect of the CuS NPs was proportional to particle size, with higher signal intensity from larger NPs. However, in *in vivo* studies CuS NPs smaller than 5 nm achieved better performance in tumor imaging, especially at the tumor boundary (**Figure 42**). These results provide useful information to support development of precision-engineered PA probes for imaging guided tumor therapy.

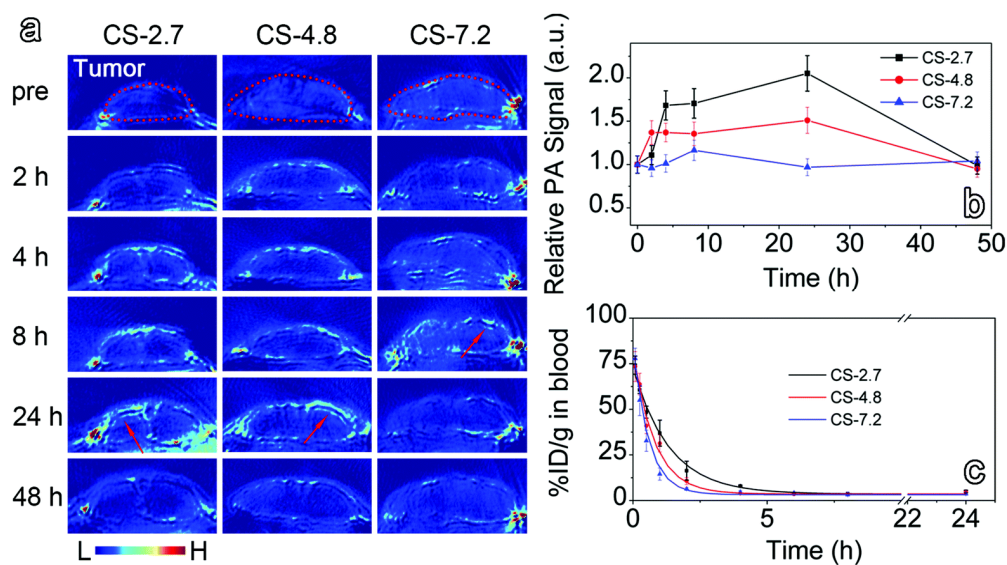


**Figure 42.** *In vivo* photoacoustic images acquired before and at different time points after intravenous injection of CuS QDs of three different sizes into tumor-bearing mice (a), temporal photoacoustic signals recorded from the tumor region (b), and blood clearance profiles of differently sized CuS QDs in rats ( $n = 4$ ) (c). Reprinted with permission from Ding *et al.*<sup>370</sup> Copyright 2015 Royal Society of Chemistry.

Kai *et al.* designed an activatable CuS-based PA imaging nanoprobe to label matrix metalloproteinases (MMPs) *in vivo*.<sup>371</sup> The MMPs play an important role in tumor angiogenesis and are overexpressed in the tumor microenvironment. CuS NPs with NIR absorbance were conjugated with black hole quencher 3 (BHQ3) *via* an MMP-sensitive peptide linker. After

1  
2  
3 conjugation, the absorbance spectra of the CuS-peptide-BHQ3 complexes showed two  
4  
5 distinctive peaks at 630 nm and 930 nm. When exposed to the tumor microenvironment, the  
6  
7 MMP-sensitive peptide was cleaved by the overexpressed MMP and the BHQ3 was released  
8  
9 from the CuS NPs. The BHQ3, which is a small molecule, was rapidly cleared out of the tumor  
10  
11 while CuS NPs were retained. The ratio of PA signal at 680 nm to that at 930 nm provided a  
12  
13 sensitive indicator of MMP activity in the tumor. This simple and straightforward strategy allows  
14  
15 researchers to use PA imaging to monitor specific enzyme activity in deep tissues.  
16  
17

18  
19  
20 Dai's group developed multifunctional CuS NPs capped with doxorubicin (DOX)-conjugated  
21  
22 gelatin, CuS@Gel-DOX and demonstrated their use for photoacoustic imaging and photothermal  
23  
24 therapy.<sup>372</sup> Moreover, the gelatin-DOX was degraded by gelatinase to provide enzyme-  
25  
26 responsive drug release. The potential of CuS@Gel-DOX NPs as PA contrast agents was  
27  
28 investigated both *in vitro* and *in vivo*. The *in vitro* study employed a phantom containing an agar  
29  
30 gel loaded with CuS@Gel-DOX NPs, which was embedded beneath chicken breast tissue. At a  
31  
32 depth of 3.2 cm, five agar objects embedded with CuS NPs were clearly distinguished from the  
33  
34 agar gel background. As an *in vivo* demonstration, the cerebral cortex of a mouse was imaged  
35  
36 using PA imaging before and after the injection of the functionalized CuS NPs. The brain  
37  
38 vasculature began to be clarified 5 min after injecting CuS@Gel-DOX NPs and the PA signal  
39  
40 increased gradually. The analysis of drug release profile revealed a 3-fold increase in drug  
41  
42 release during the 6 h following gelatinase addition, relative to the release without adding  
43  
44 gelatinase. Such CuS@Gel-DOX NPs could potentially be used for imaging cancer tissues and  
45  
46 killing cancer cells by combining PA imaging, photothermal therapy, and chemotherapy. Using  
47  
48 CuS NPs as a PA imaging platform, the same group also constructed a nanoplatform  
49  
50 functionalized with manganese (II) chelate and poly (ethylene glycol) (PEG) for PA/MR dual-  
51  
52  
53  
54  
55  
56  
57  
58  
59  
60

1  
2  
3 modal imaging and imaging-guided photothermal therapy.<sup>373</sup> The CuS NPs exhibited uniform  
4 small size (~9 nm), excellent NIR-absorbance and minimal cytotoxicity. The NPs were injected  
5 into tumor-bearing mice and PA images were collected. The PA signal from the tumor site  
6 gradually increased after intravenous injection, and peaked 5 h after injection. Enhanced PA  
7 signal from the tumor site persisted after 24 h, indicating the CuS NPs remained at the tumor site.  
8 PA results were further confirmed by MRI imaging. Finally, photothermal therapy was  
9 performed on MDA-MB-231 xenograft tumor-bearing mice. The tumor treated with the laser and  
10 CuS NPs disappeared within the first week. Tumor growth was unaffected in mice treated with  
11 the laser or CuS NPs alone. The authors suggested that CuS NPs functionalized with Mn (II)  
12 chelate hold great potential as a theranostic for PA/MR imaging-guided photothermal therapy.  
13 However, the use of a chelator on the NP surface may limit the ability to conjugate other  
14 targeting or therapeutic agents.  
15  
16  
17  
18  
19  
20  
21  
22  
23  
24  
25  
26  
27  
28  
29  
30

31  
32 Gao *et al.* developed a doping method for constructing a Ni-integrated CuS nanostructure as  
33 a new PA/MRI contrast agent.<sup>368</sup> The Ni:CuS NPs exhibited small and uniform size along with  
34 good crystallinity. Their absorbance spectra covered the 700-900 nm range over which tissues  
35 are relatively transparent. Moreover, compared to Ni ions, the doped NPs exhibited a  
36 dramatically enhanced  $T_1$  relaxivity, indicative of promise as MRI contrast agents. To  
37 demonstrate sentinel lymph node mapping, mice were administered Ni:CuS NPs subcutaneously  
38 at the distal part of the right anterior paw. Increased PA signal from the Ni:CuS NPs at the  
39 sentinel lymph node was observed 30 min post-injection. MR imaging demonstrated the same  
40 accumulation, suggesting that the Ni:CuS NPs are promising PA/MRI dual-modal nanoprobes.  
41  
42  
43  
44  
45  
46  
47  
48  
49  
50  
51  
52

53 Song *et al.* constructed a novel nanovesicle based on reduced graphene oxide (rGO) for PA  
54 imaging and chemo/photothermal therapy and tested it *in vitro* and *in vivo*.<sup>374</sup> They designed and  
55  
56  
57  
58  
59  
60

1  
2  
3 synthesized a new type of carbon-metal hybrid nanostructure, rGO-doxorubicin (DOX)-loaded  
4 plasmonic gold nanorod vesicles (rGO-AuNRVe-DOX). The encapsulation of rGO-DOX in the  
5 gold nanorod vesicle protected the rGO-DOX from degradation or damage during circulation and  
6 cellular internalization. The PA signal, photothermal effect and drug release profiles were  
7 measured and evaluated systematically. The rGO-AuNRVe nanocomplexes exhibited better  
8 photothermal effect and higher PA signal compared with AuNR alone or the mixture of rGO and  
9 AuNRVe. This enhancement was attributed to the plasmonic coupling between the encapsulated  
10 rGO and AuNR in the vesicular shell. *In vivo*, the PA signal in the tumor region increased  
11 gradually after injecting rGO-AuNRVe. The maximum PA signal, at 24 h postinjection, was 4  
12 times that obtained using AuNRVe alone. The *in vivo* evaluation on the chem/photothermal  
13 therapeutic effect of rGO-AuNRVe-DOX demonstrated that such nanovesicles had a dual photo-  
14 and acid-responsive DOX release pattern and synergistic chemo/photothermal effects. Their  
15 combination of properties makes the nanovesicles useful for visualization of the shape and size  
16 of a tumor by PA imaging, elimination of the cancer cells through chemo/photothermal effects,  
17 and minimization of side effects to the surrounding tissue.

18  
19 Overall, advances in plasmonic nanotechnology are allowing rapid development of NP-based  
20 PA contrast agents with exceptionally strong absorbance in the NIR spectral range. Several of  
21 these recently-developed materials incorporate QDs, although the absorbance used for PA  
22 contrast is usually associated with plasmonic, rather than excitonic, properties of the QDs.  
23 Rapidly developing PA technology is expected to significantly enhance both pre-clinical and  
24 clinical targeted imaging of tumors and other tissues.

### 5.3. Biosensing

Specific biomarker detection is valuable for early diagnosis and therapy of diseases, as well as for probing complex physiological process. In the past decade, the unique optical properties of QDs and the ability to specifically functionalize their surfaces have been widely applied to the detection of various chemical and biological species.<sup>83,211,375,376</sup> In this section, we discuss some important examples of the use of Cd-free QDs for optical sensing applications in biophotonics.

Dinakaran *et al.* developed an immunosensor for detection of *C. parvum* using NIR-emitting Ag<sub>2</sub>S@silica nanospheres.<sup>342</sup> In a sandwich assay, anti-oocyst McAb were immobilized on functionalized quartz glass, incubated with *C. parvum*, and treated with anti-oocyst McAb immobilized Ag<sub>2</sub>S@silica nanospheres. The PL spectra of the washed glass plates were recorded and used to determine the concentration of *C. parvum*. The PL intensity increased as oocyst number increased and the detection limit was 10 oocysts per mL. They also studied the specificity of binding using five other pathogens, and found that the PL intensity only changed dramatically when the pathogen *C. parvum* was added.

Dopamine (DA) is an important neurotransmitter in the central nervous, renal and hormonal systems. Cui *et al.* reported the use of near-IR electro-generated chemiluminescence (ECL) of Ag<sub>2</sub>Se QDs for detection of dopamine in a pharmaceutical drug formulation (dopamine hydrochloride injection) that contains other chemicals such as sodium bisulfite, edetate disodium and sodium chloride.<sup>343</sup> Immobilized on a glassy carbon electrode, the Ag<sub>2</sub>Se QDs displayed a cathodic ECL signal in the presence of K<sub>2</sub>S<sub>2</sub>O<sub>8</sub> as a coreactant. A peak at 695 nm was observed in the ECL spectrum and this is consistent with the PL emission peak of the Ag<sub>2</sub>Se QDs. Dopamine, with an energy level between the lowest unoccupied molecular orbital (LUMO) and highest occupied molecular orbital (HOMO) of Ag<sub>2</sub>Se QDs, was selected as an analyte model for

1  
2  
3 evaluating the potential of this system as an ECL sensor. Upon increasing the concentration of  
4  
5 dopamine, the ECL signal intensity decreased linearly due to energy transfer between Ag<sub>2</sub>Se  
6  
7 QDs and dopamine. The authors reported that even after 10000-fold dilution, dopamine was still  
8  
9 detected in the drug formulation at the level of  $0.055 \pm 0.002$  M using ECL sensing. This  
10  
11 obtained value was consistent with the reference value of 0.054 M.  
12  
13  
14

15 The interactions between sugar-chains and proteins play an important role in biological  
16  
17 processes. Shinchi *et al.* developed sugar-chain-functionalized photoluminescent NPs (SFNPs)  
18  
19 based upon Zn-Ag-In-S (ZAIS) QDs and applied them to probe lectin-sugar interactions.<sup>222</sup>  
20  
21 Cellular imaging and flow cytometry analysis were performed to detect binding between SFNPs  
22  
23 and lectins. Binding profiles differed between cell types, reflecting differing expression levels of  
24  
25 sugar chain-binding receptor proteins in cells. These functionalized NPs can be applied for cell  
26  
27 profiling based on sugar chain-protein interactions.  
28  
29  
30

31 Concanavalin A (ConA) is a legume lectin harvested from Jack bean which can bind to the  
32  
33 glucose moiety of cell membrane glycoproteins. This binding can initiate cell mitogenesis,  
34  
35 agglutination, T-cell activation, and apoptosis. Various detection methods have been engineered  
36  
37 to sense ConA because this biomolecule is a useful probe for studying carbohydrate-protein  
38  
39 interactions. Thus, development of a simple approach for detecting ConA would be quite  
40  
41 valuable. Yan *et al.* prepared ultrasmall water-dispersible Ag<sub>2</sub>Se QDs by reduction of selenium  
42  
43 powder along with binding of thioglycollic acid (TGA) and silver ions.<sup>344</sup> Glycine was used to  
44  
45 passivate the QD surface. This method does not require the use of high temperature, high  
46  
47 pressure, or organic solvents. Conjugating ConA to TGA-modified Ag<sub>2</sub>Se QDs produced  
48  
49 structures whose aggregation was detectable by resonance Rayleigh scattering (RRS). The RRS  
50  
51 signals from the QDs were used to detect ConA with a detection limit of 0.08 μg/mL. This  
52  
53  
54  
55  
56  
57  
58  
59  
60

1  
2  
3 method provides a relatively low limit of detection and can be adapted for sensing other complex  
4  
5 biomolecules in blood samples.  
6

7  
8 Water-dispersible AgInS<sub>2</sub>/ZnS QDs prepared by a microwave-assisted method were used to  
9  
10 determine intracellular copper (II) levels.<sup>377</sup> Briefly, HeLa cells were incubated with AgInS<sub>2</sub>/ZnS  
11  
12 QDs, then Cu(NO<sub>3</sub>)<sub>2</sub> was used to manipulate the intracellular copper(II) level. In this experiment,  
13  
14 the PL intensity was found to decrease due to quenching by intracellular Cu<sup>2+</sup> ions. The  
15  
16 introduced Cu<sup>+</sup> could displace Zn<sup>2+</sup> on the QD surface and form a CuS shell, thereby facilitating  
17  
18 non-radiative recombination of excitons. In addition, confocal laser scanning microscopy (CLSM)  
19  
20 was employed to investigate the PL quenching process in HeLa cells. The authors highlighted  
21  
22 that AgInS<sub>2</sub>/ZnS QDs can be used as intracellular Cu<sup>2+</sup> imaging probes for imaging the dynamic  
23  
24 interaction between copper ions and cell components.  
25  
26  
27

28  
29 Liu *et al.* created a PL detection system for sensing lysozyme using CuInS<sub>2</sub> QDs as optical  
30  
31 probes.<sup>378</sup> Poly(dimethyl diallyl ammonium chloride) (PDAD), a cationic polyelectrolyte, was  
32  
33 applied to quench the PL of CuInS<sub>2</sub> QDs *via* electrostatic interactions and subsequent electron  
34  
35 transfer between PDAD and the QDs. When a negatively-charged lysozyme aptamer was added,  
36  
37 it bound PDAD and disrupted the interaction between QDs and PDAD, producing PL recovery.  
38  
39 When lysozyme was also introduced into the system, it bound its aptamer and released the  
40  
41 PDAD which then quenched the QD PL (**Figure 43**). The concentration of lysozyme was  
42  
43 determined by measurement of PL intensity changes.  
44  
45  
46  
47  
48  
49  
50  
51  
52  
53  
54  
55  
56  
57  
58  
59  
60

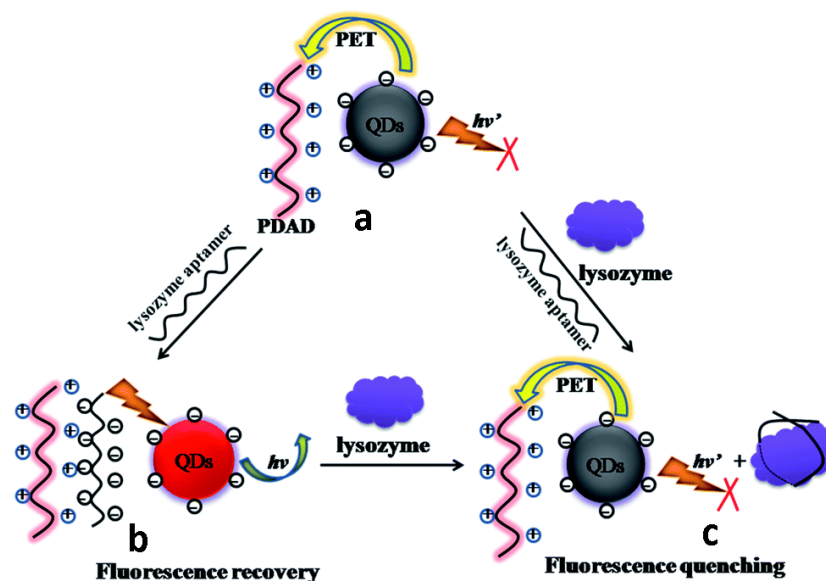


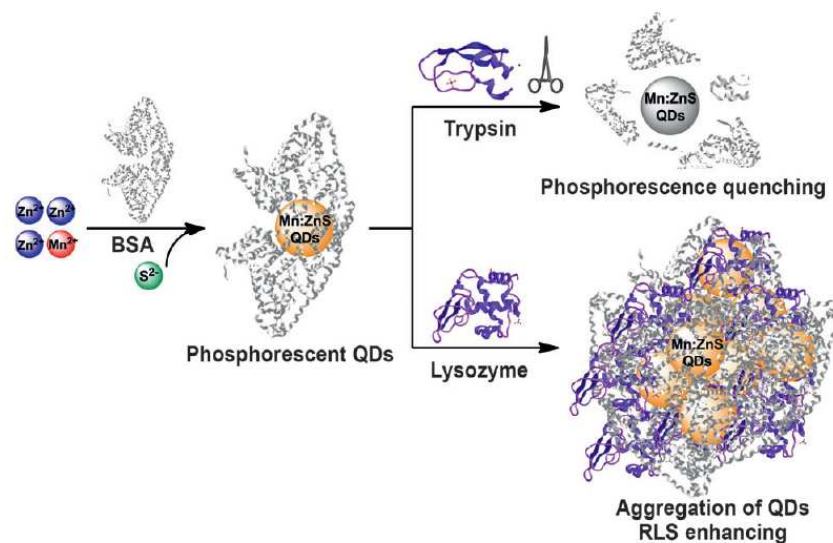
**Figure 43.** Schematic design for lysozyme sensing. (a) Coexistence of the MPA-capped CuInS<sub>2</sub> QDs and cationic polyelectrolyte PDAD. (b) Electrostatic bonding of the lysozyme aptamer and PDAD. (c) Bonding of the lysozyme aptamer and lysozyme. Reprinted with permission from Liu *et al.*<sup>378</sup> Copyright 2014 Royal Society of Chemistry.

CuInS<sub>2</sub> QDs have been modified with 3-aminophenyl boronic acid and used as PL probes for the detection of benzene-based organic compounds.<sup>345</sup> The bioconjugated CuInS<sub>2</sub> QDs displayed PL peaking at 736 nm. The boronic acid functional groups were reactive towards vicinal diols. Their reaction formed five- or six-member cyclic esters in an alkaline buffer and caused PL quenching of the QDs. Thus, one can use these QDs for monitoring of dopamine and vicinal diols such as catechol, pyrogallol, and gallate. This assay is unaffected by other phenolic compounds such as phenol, resorcinol, and hydroquinone. The QDs were also used to detect dopamine in human serum samples with reasonable accuracy. Using the same strategy, the same group reported a method for sensing dicyandiamide based on PL quenching of surface-modified

1  
2  
3 CuInS<sub>2</sub> QDs.<sup>379</sup> Based on cyclization of the guanidine group of dicyandiamide with 2,3-  
4 butanedione and 3-aminophenylboronic acids, the PL of the 3-aminophenylboronic acid-  
5 functionalized CuInS<sub>2</sub> QDs was quenched by dicyandiamide in the presence of 2,3-butanedione.  
6  
7 This approach can be used to differentiate dicyandiamide from other amino acids and nitrogen  
8 pollutants such as melamine in milk samples. A linear correlation between the luminescence  
9 intensity of surface modified QDs and the dicyandiamide concentration, from  $2.0 \times 10^{-6}$  to  $2.0 \times 10^{-3}$   
10 mol L<sup>-1</sup> was reported for this detection scheme. A sensitivity of 0.6 μmol L<sup>-1</sup> was achieved in  
11 this system. Later, they demonstrated a urea-biosensing system using dopamine-modified CuInS<sub>2</sub>  
12 QDs as the luminescence probe.<sup>376</sup> When the pH of the dopamine-capped CuInS<sub>2</sub> QD dispersion  
13 was changed from neutral to basic, the dopamine on the QD surface was converted to quinone,  
14 which quenched the PL of the bioconjugated QDs. This was mainly due to charge transfer  
15 interactions between QDs and the proximal quinone molecules. Because the hydrolysis of urea in  
16 the presence of urease will release OH<sup>-</sup> and raise the pH, the fluorescence intensity of dopamine-  
17 capped QDs can be used to evaluate the enzymatic degradation of urea. The proposed urea-  
18 biosensing scheme can be used to determine urea concentrations ranging from 0.2 to 6 mM.  
19  
20  
21  
22  
23  
24  
25  
26  
27  
28  
29  
30  
31  
32  
33  
34  
35  
36  
37  
38

39 Many proteins have both nanosize dimensions and sites that bind inorganic ions. These  
40 features allow them to be used for the synthesis of NP-protein hybrids with specific functionality  
41 and excellent water dispersibility. Wu *et al.* reported protein-templated fabrication of Mn-doped  
42 ZnS QDs using bovine serum albumin (BSA) as a template.<sup>380</sup> The QDs exhibited  
43 phosphorescence at 590 nm with a decay lifetime of 1.9 ms. Two sensing approaches for the  
44 detection of trypsin and lysozyme with dBSA-templated Mn-doped Zn SQDs were developed.  
45 Phosphorescence quenching was used to detect trypsin molecules, while enhancement of  
46 resonant light scattering (RLS) and phosphorescence were applied for sensing lysozyme. Trypsin  
47  
48  
49  
50  
51  
52  
53  
54  
55  
56  
57  
58  
59  
60

1  
2  
3 could digest the BSA on the QD surface and quenched the phosphorescence, while lysozyme  
4 was hypothesized to assemble with the BSA and induce aggregation of QDs, leading to an  
5 enhanced RLS signal (**Figure 44**). The detection limits for trypsin and lysozyme were 40 and 3  
6 nM, respectively.  
7  
8  
9  
10  
11  
12  
13  
14  
15  
16  
17  
18  
19  
20  
21  
22  
23  
24  
25  
26  
27  
28  
29  
30  
31  
32



33  
34 **Figure 44.** Schematic diagram of Mn-doped ZnS QDs for dual-functional sensing:  
35 phosphorescent sensing for trypsin and RLS sensing for lysozyme. Reprinted with permission  
36 from Wu *et al.*<sup>380</sup> Copyright 2013 John Wiley and Sons.  
37  
38  
39

40  
41 The ability to sense intracellular Zn<sup>2+</sup> is important due to its significances in various  
42 biological processes. Ren *et al.* reported the synthesis of silica-coated S<sup>2-</sup>-enriched Mn-doped  
43 ZnS QDs for imaging of intracellular Zn<sup>2+</sup> ions.<sup>381</sup> The excited states in S<sup>2-</sup> enriched QDs are  
44 prone to non-radiative recombination because of the abundant S<sup>2-</sup> dangling bonds. As a result,  
45 the S<sup>2-</sup>-enriched QDs exhibited weak PL. Exposure to Zn<sup>2+</sup> ions could eliminate the S<sup>2-</sup> dangling  
46 bonds and suppress non-radiative recombination, thereby enhancing the PL of the QDs. The  
47 probes provided a good linear correlation between the recovered PL intensity of the QDs and the  
48  
49  
50  
51  
52  
53  
54  
55  
56  
57  
58  
59  
60

1  
2  
3 concentration of  $\text{Zn}^{2+}$  from 0.3 to 15.0  $\mu\text{M}$ , good reproducibility, and a detection limit of 80 nM  
4  
5  $\text{Zn}^{2+}$ . Furthermore, the QDs displayed low cytotoxicity.  
6  
7

8 Wen *et al.* reported a phosphorescence nanosensing system based on L-cysteine-capped Mn-  
9 doped ZnS QDs.<sup>382</sup> Sanguinarine was attached to the QD surface to form nanoconjugates with  
10 quenched phosphorescence. When G-quadruplex sequences combined with the sanguinarine of  
11 the nanoconjugates, the QD phosphorescence was recovered. The interactions between  
12 sanguinarine and six G-quadruplex DNAs with various sequences (tel24-1, tel24-2, tel22, k-ras,  
13 HIF-1 $\alpha$  and c-kit1) were examined using this method and were found to depend on the number  
14 of bases and conformation of the DNA. The developed method is simple, rapid, and insensitive  
15 to fluorescence interferences of the system. These features can make it a valuable tool for  
16 studying the interaction of drugs with different G-quadruplexes.  
17  
18  
19  
20  
21  
22  
23  
24  
25  
26  
27  
28

29 QDs are commonly employed for PL sensing. However, their use in time-resolved  
30 fluorometry could be more effective if they had longer-lived emission. Zhu *et al.* prepared  
31 aqueous Mn-doped ZnSe QDs using a microwave synthesis approach.<sup>383</sup> The PL lifetime of the  
32 QDs was 400  $\mu\text{s}$ , roughly 10,000 times that of CdS, CdSe, and CdTe QDs. The QDs displayed  
33 good photostability over 35 hours under continuous irradiation at 260 nm. The Mn-doped  
34 mercaptopropionic acid-capped ZnSe QDs were used for time-resolved PL sensing of 5-  
35 fluorouracil (5-FU), and provided a detection limit of 128 nM. These results suggest that the Mn-  
36 doped ZnSe QDs can be used for highly sensitive time-resolved fluorometry in the detection of  
37 other drugs.  
38  
39  
40  
41  
42  
43  
44  
45  
46  
47  
48  
49

50 Graphene QDs (GQDs) are of interest for biomedical imaging and sensing owing to their  
51 distinct optical properties, resistance to photobleaching, and excellent biocompatibility. Qian *et*  
52 *al.* designed a DNA nanosensor that combined GQDs with carbon nanotubes (CNTs).<sup>346</sup> Single-  
53  
54  
55  
56  
57  
58  
59  
60

1  
2  
3 stranded DNA probes, ssDNA-rGQDs, were obtained by linking DNA with reduced GQDs.  
4  
5 Multi-walled CNTs were modified to be water dispersible by oxidation in nitric and sulfuric acid.  
6  
7 The ssDNA-rGQDs were then adsorbed on the oxidized CNTs through  $\pi$ - $\pi$  stacking and  
8 electrostatic interactions to form ssDNA-rGQD/CNT complexes. The PL of the ssDNA-rGQD  
9  
10 was almost completely quenched when assembled with CNTs, due to energy transfer to the  
11  
12 CNTs. When complementary DNA was added, it bound to ssDNA-rGQDs with a high affinity  
13  
14 and separated the ssDNA-rGQDs from the CNTs, producing PL recovery. With a detection limit  
15  
16 of 0.4 nM, this method shows promise for distinguishing complementary and mismatched DNA  
17  
18 sequences with high sensitivity and good reproducibility. In a subsequent study, CNTs were  
19  
20 replaced with graphene oxide (GO) to construct a dual-color GQD/GO sensor.<sup>384</sup> GO, 1,2-  
21  
22 ethylenediamine functionalized graphene QDs (eGQDs) and different-colored reduced graphene  
23  
24 QDs, rGQDs were prepared separately. ssDNA was connected to the eGQDs and a thrombin  
25  
26 aptamer was linked with the rGQDs. The ssDNA-eGQDs and TA-rGQDs were mixed with GO  
27  
28 to form an assembly, and fast electron transfer between them caused PL quenching of the GQDs.  
29  
30 Addition of complementary DNA or thrombin could recover the PL due to comparatively  
31  
32 stronger affinity to ssDNA and TA, respectively. The result demonstrated that, as dual-color  
33  
34 probes, the developed GQDs/GO assemblies allow the simultaneous detection of DNA and  
35  
36 thrombin.

37  
38 Zhao *et al.* reported a GQD/graphene probe for sensing human immunoglobulin G (IgG).<sup>309</sup>  
39  
40 In their work, the FRET pair was fabricated using mouse anti-human immunoglobulin G  
41  
42 (mIgG)-conjugated GQDs as donor and graphene as an acceptor. In the graphene dispersion, the  
43  
44 functionalized GQDs had their PL quenched as a combined result of the  $\pi$ - $\pi$  stacking interaction  
45  
46 between graphene and GQDs and nonspecific binding of the mIgG to the graphene surface.  
47  
48  
49  
50  
51  
52  
53  
54  
55  
56  
57  
58  
59  
60

1  
2  
3 When human IgG, which binds mIgG through a specific antibody–antigen interaction, was added,  
4  
5 the mIgG–QDs separated from the graphene surface, leading to recovery of the QD PL.  
6  
7

8 Zhang *et al.* developed another graphene-based nanosensor for selective glucose detection.<sup>385</sup>  
9  
10 They produced boron-doped graphene QDs (BGQDs) by hydrothermal cutting of boron-doped  
11  
12 graphene (BG). Boronic acid groups on the BGQD surface allowed them to serve as optical  
13  
14 probes for label-free glucose sensing. In the sensing process, the reaction between the boronic  
15  
16 acid groups on the BGQD surfaces and the cis-diol units in glucose formed BGQD–glucose  
17  
18 aggregates, which surprisingly resulted in greatly enhanced PL. The authors suggested that the  
19  
20 aggregation of the BGQDs could stiffen their structure, limiting interactions of neighboring  
21  
22 luminescence centers, which reduced non-radiative recombination and therefore enhanced the PL.  
23  
24  
25  
26  
27

#### 28 29 **5.4. Optical Tracking** 30

31  
32 Scattering, absorbance and endogenous autofluorescence of living tissues produce significant  
33  
34 challenges to improving tissue penetration depth and 3D spatial resolution of fluorescence- and  
35  
36 PL-based imaging using exogenous optical nanoprobe. Near-IR-emitting Cd-free QDs open up  
37  
38 new capabilities for *in vivo* imaging to achieve precise optical tracking.<sup>47,174,386</sup> Li *et al.*  
39  
40 synthesized CuInS<sub>2</sub>/ZnS QDs with PL QY up to 60% and used them for an *in vivo*  
41  
42 biodistribution study.<sup>163</sup> QDs with emission wavelengths from 650 to 750 nm were transferred  
43  
44 into water by ligand exchange using DHLA. The biodistribution of the QDs was visualized by  
45  
46 PL imaging after tail vein injection in nude mice. Fifteen min after injection, the QDs had  
47  
48 accumulated mainly in the spleen, lungs, and liver. Twenty-four hours after injection, the mice  
49  
50 were dissected and their organs were analyzed, confirming the noninvasive *in vivo* observations.  
51  
52 The lungs are among the blood first-pass organs and functioned as a filter immediately after QD  
53  
54  
55  
56  
57  
58  
59  
60

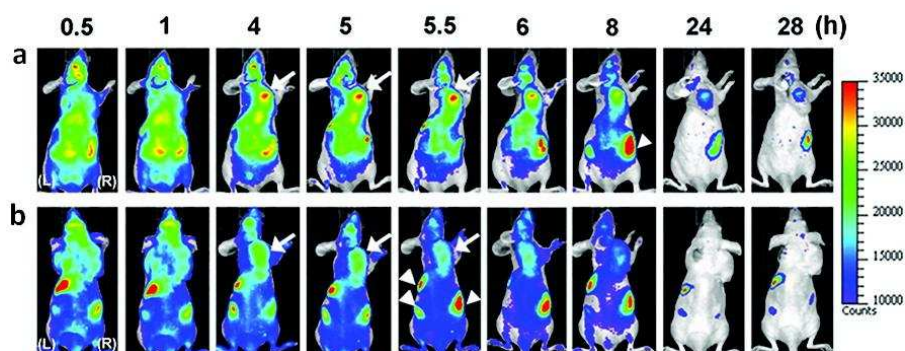
1  
2  
3 injection. The liver and spleen take up QDs in their functional roles as part of the reticulo-  
4  
5 endothelial system (RES). Aggregation of QDs within the organs was attributed to opsonin  
6  
7 binding. The biodistribution of these non-targeted QDs in non-tumor-bearing mice provides  
8  
9 general information on the fate of such QDs upon tail vein injection.  
10  
11

12  
13 NIR InAs/InP/ZnSe QDs coated with MPA, with hydrodynamic diameter below 10 nm and  
14  
15 PL near 800 nm (QD800-MPA) were also used for *in vivo* imaging.<sup>297</sup> Two murine tumor models,  
16  
17 22B and LS174T, were employed. One hour after tail-vein injection, PL from QD800-MPA was  
18  
19 observed in both tumor models. PL from other organs was much lower. After 4 h, the tumors  
20  
21 were easily distinguished from other tissues by PL, indicating high uptake efficiency. The PL  
22  
23 intensity of QD800-MPA in the tumor gradually increased from 0.5 to 4 hours after injection,  
24  
25 then decreased slowly after 6 hours due to renal clearance, and finally remained low after 18  
26  
27 hours. To assess the dependence of uptake by enhanced permeation and retention (EPR) effects  
28  
29 on size, they conducted a parallel experiment using QD800-COOH with hydrodynamic diameter  
30  
31 of 25 nm as a control sample to target 22B tumors. In contrast to the results with smaller QDs,  
32  
33 there was no obvious PL from QD800-COOH at the tumor site, and the PL intensity from the  
34  
35 liver, spleen, and bone marrow became brighter from 30 min to 6 hours after injection. Human  
36  
37 serum albumin (HSA) protein, a major soluble protein of the circulatory system, was used to  
38  
39 modify QD800-MPA to reduce uptake in the RES system. The results showed increased QD800-  
40  
41 MPA-HSA uptake by the tumor, compared with QD800-MPA, accompanied by reduced uptake  
42  
43 by the RES organs. Later, the same group coupled QD800-PEG with arginylglycylaspartic acid  
44  
45 (RGD) and arginine-alanine-aspartic acid (RAD) peptides to visualize tumors.<sup>387</sup> Due to the PEG  
46  
47 coating, these QDs had larger hydrodynamic diameter than QD800-MPA. Size measurements by  
48  
49 DLS gave hydrodynamic diameters of 16.5 nm, 20.1 nm and 19.6 nm for QD800-PEG, QD800-  
50  
51  
52  
53  
54  
55  
56  
57  
58  
59  
60

1  
2  
3 RAD and QD800-RGD, respectively. The three types of QDs were administered intravenously  
4 into nude mice with subcutaneous human glioma (U87MG) tumors. PL from the tumors of mice  
5 injected with either QD800-RAD or QD800-RGD was detected at 30 min postinjection. After  
6 one hour, the tumors of mice treated with QD800-RGD showed bright PL, while the PL signal  
7 from tumors of mice treated with QD800-RAD had decreased. This indicated that the QD800-  
8 RGD had higher specificity for U87MG tumor. No significant PL contrast was observed in  
9 tumors of mice treated with QD800-PEG. Moreover, PL contrast remained pronounced even  
10 after 24 hours in the mice treated with QD800-RGD. All these results confirmed that specific  
11 tumor targeting by QD800-RGD led to longer retention of QDs in the tumor.  
12  
13  
14  
15  
16  
17  
18  
19  
20  
21  
22  
23

24 In another study, the same group used anti-HER2 antibodies with a cysteine added at their N-  
25 terminus to functionalize maleimide-terminated QD800-PEG.<sup>388</sup> Two tumor models with varied  
26 HER2 expression levels, SKOV3 (high HER2 level) from human ovarian cancer and PC-3 (low  
27 HER2 level) from human prostate carcinoma were used to study HER2 based targeting. PL  
28 images were collected at multiple time points from 30 min to 24 h after injection into tumor-  
29 bearing mice. Already at 30 min post-injection, PL from the QD800-affibody was observed in  
30 the SKOV3 tumor models. Within 4 h, the PL intensity of the tumor provided high contrast with  
31 other tissues in SKOV3 tumor-bearing mice, while no tumor contrast was observed in the control  
32 groups of PC-3 tumor-bearing mice or SKOV3 tumor-bearing mice treated with QD800-PEG. In  
33 the SKOV3 tumor-bearing mice treated with the QD800-HER2, tumor PL contrast remained  
34 distinguishable even after 24 hours, due to the enhanced tumor retention of the QDs induced by  
35 the high targeting efficiency of HER2. This study showed that the QD800-HER2 could serve as  
36 excellent labels for imaging and tracking of HER2 expressing tumors.  
37  
38  
39  
40  
41  
42  
43  
44  
45  
46  
47  
48  
49  
50  
51  
52  
53  
54  
55  
56  
57  
58  
59  
60

1  
2  
3  
4 Gao *et al.* prepared dendron-functionalized InP/ZnS core/shell QDs for molecular tracking,  
5  
6 with PL emission peaking at 710 nm.<sup>389</sup> The QDs were conjugated with RGD peptide dimers  
7  
8 (RGD2) to form QD710-Dendron-RGD2. *In vivo* PL images were collected at successive time  
9  
10 points, while ICP-MS was used to quantify the QD content of urine and feces. Acute tumor  
11  
12 uptake of QD710-Dendron provided high contrast between the tumor and surrounding tissues,  
13  
14 suggesting that passive targeting by the EPR effect was significant. However, the specific  
15  
16 interaction of QD710-Dendron-RGD2 with integrin  $\alpha_v\beta_3$ -positive tumor cells (SKOV3) led to  
17  
18 greater tumor uptake and longer retention (>24 h) of the QDs at tumor sites (**Figure 45**). ICP  
19  
20 measurements demonstrated that the QD710-Dendron was cleared renally, with 60% of the  
21  
22 initial dose cleared after one day, nearly all cleared after one week, and reaching undetectable  
23  
24 levels ten weeks after the injection.  
25  
26  
27  
28



43 **Figure 45.** *In vivo* NIR PL images of tumor-bearing mice, at different time points, post injection  
44 with QD710-Dendron-RGD<sub>2</sub> (a) and QD710-Dendron (b) (arrows, tumor; L, left side; R, right  
45 side). Reprinted with permission from Gao *et al.*<sup>389</sup> Copyright 2012 American Chemical Society.  
46  
47  
48  
49

50 Lymph nodes (LN) play an essential role in immune response to exogenous substances.  
51  
52 Dubertret *et al.* prepared CuInS<sub>2</sub>/ZnS core/shell QDs with PL near 800 nm and high QY and  
53  
54 stability in both organic and aqueous media.<sup>390</sup> They administered CuInS<sub>2</sub>/ZnS QD-loaded  
55  
56 phospholipid micelle dispersions subcutaneously in the right anterior paw of mice. Two regional  
57  
58  
59  
60

1  
2  
3 lymph nodes, *i.e.*, right axillary LNs (RALNs), could be clearly visualized a few minutes after  
4 injection. No obvious inflammation was found 7 days after injection. Later, the same group used  
5 these CuInS<sub>2</sub>/ZnS QDs to visualize the sentinel lymph node (SLN) in a murine metastatic breast  
6 tumor model using a NIR imaging system.<sup>391</sup> Indium content of selected organs was then  
7 analyzed by ICP-MS. Metastasis was assessed through molecular techniques and  
8 immunohistology. SLN metastasis is an important predictor of recurrence/survival and guides the  
9 therapy modality for tumor patients. Thus, real-time localization and evaluation of the SLN plays  
10 a key role in the clinic. Imaging showed that QD PL appeared in the SLN 5 min after injection  
11 and increased up to 8 hours after subcutaneous injection. ICP-MS analysis showed that the QD  
12 levels significantly decreased at the administration point and increased in the LNs within one  
13 hour after injection. In addition, 3.5% of the injected indium content was excreted through feces  
14 after 96 hours. The immunoassay revealed a maximum of 36% metastatic invasion to the SLN.

15  
16  
17  
18  
19  
20  
21  
22  
23  
24  
25  
26  
27  
28  
29  
30  
31  
32 CuInSe<sub>x</sub>S<sub>2-x</sub>/ZnS core/shell QDs have also been used as probes for tracking the fate of oral  
33 vaccines administered to mice.<sup>392</sup> The QDs were loaded into poly(lactic-co-glycolic acid) to form  
34 microparticles 500 nm to 2 μm in diameter. QDs conjugated with non-binding variant D911A or  
35 wild-type invasin were used as control. The QD-PLGA-invasin microparticles were orally  
36 gavaged to mice. A noninvasive Caliper Life Sciences IVIS Spectrum System was employed for  
37 *in vivo* tracking of PL retention in the gastrointestinal tract from 15 min to 45 h. After 15 min,  
38 the QD PL appeared in the stomach. After 18 h and 45 h, QD PL was only visible in the cecums  
39 and the colons of the mice treated with QDs-PLGA-invasin. In mice treated with QDs-PLGA-  
40 D911A, no PL was observed after 18 h and 45 h.

41  
42  
43  
44  
45  
46  
47  
48  
49  
50  
51  
52  
53 For *in vivo* imaging, probes with emission in the second near-IR region (NIR-II, 1000-1350  
54 nm) are often more desirable than visible or even NIR-I probes (700-950 nm). Both tissue  
55  
56  
57  
58  
59  
60

1  
2  
3 autofluorescence and noise associated with absorbance and scattering from tissues are  
4 significantly reduced in the NIR-II window. Li *et al.* prepared PEGylated Ag<sub>2</sub>S QDs with PL  
5 emission peaking at 1200 nm.<sup>174</sup> They explored *in vivo* dynamic imaging using Ag<sub>2</sub>S QDs as  
6 labels for monitoring lymph flow, blood flow, and angiogenesis in mice with subcutaneous  
7 xenograft tumors (**Figure 46**). Upon subcutaneous injection, the Ag<sub>2</sub>S QDs were first located in  
8 the lymphatics and transferred to the popliteal and lumbar lymph nodes within two minutes.  
9  
10 Lymphatic vessels with an average diameter of 100 μm were unambiguously visualized. The  
11 video-rate PL images showed that the QDs returned to the heart after intravenous injection and  
12 then entered the pulmonary circulation before being distributed throughout the mouse body.  
13  
14 Real-time visualization of tumor-induced angiogenesis showed that vascular structures were  
15 recruited to feed the tumor, with PL clearly observed on the 15<sup>th</sup> day after tumor xenografting.  
16  
17 The NIR-II QD labels could improve diagnostic efficiency through tracking pathological and  
18 physiological processes in the lymphatic and circulatory systems.  
19  
20  
21  
22  
23  
24  
25  
26  
27  
28  
29  
30  
31  
32  
33  
34  
35  
36  
37  
38  
39  
40  
41  
42  
43  
44  
45  
46  
47  
48  
49  
50  
51  
52  
53  
54  
55  
56  
57  
58  
59  
60

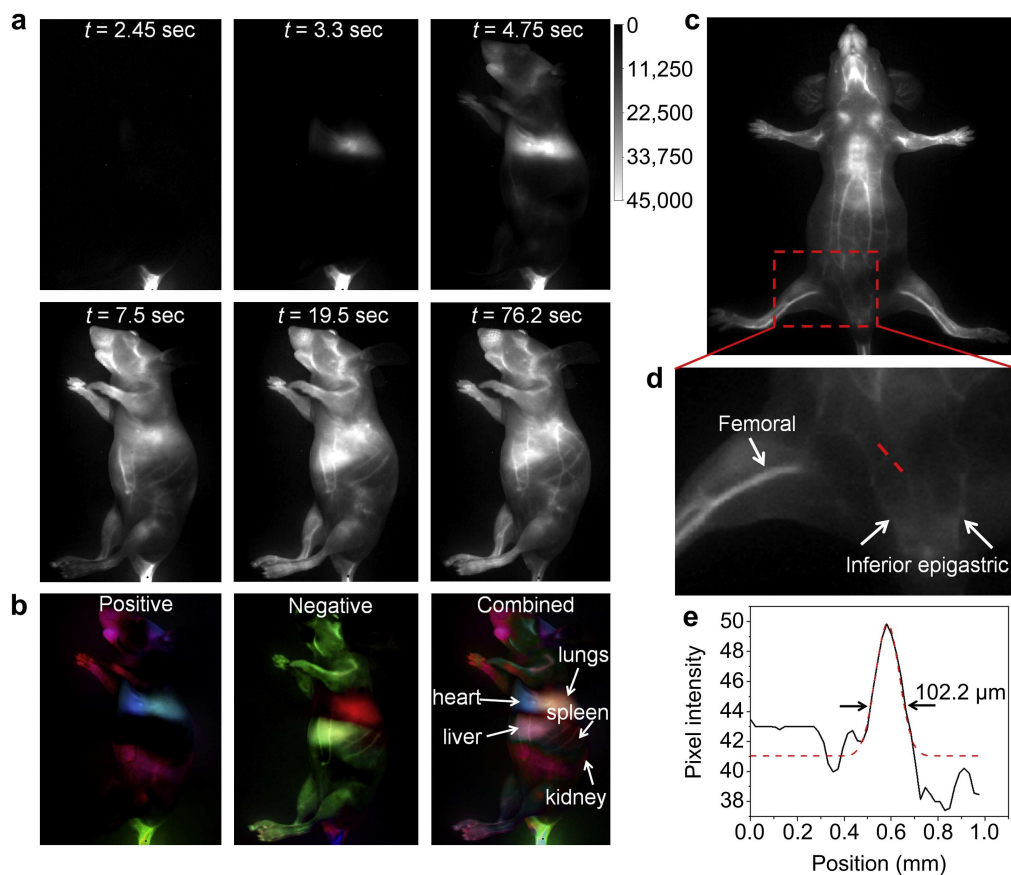


**Figure 46.** Blood pool PL imaging of a nude mouse. (a) Time-lapse images of blood flow in the nude mouse after injection of PEGylated  $\text{Ag}_2\text{S}$  QDs. (b) Dynamic contrast-enhanced images with PEGylated  $\text{Ag}_2\text{S}$  QDs based on PCA analysis. Deep organs such as heart, lungs, liver, spleen, and kidney were observed. (c) Intravital image of the nude mouse in supine position. (d) Amplified fluorescent image of vasculature in the nude mouse. (e) A cross-sectional intensity profile measured along the red-dashed line in (d) with its peak fitted to a Gaussian function. Reprinted with permission from Li *et al.*<sup>174</sup> Copyright 2014 Elsevier.

Recently, stem cell-based therapies have shown increasing potential for applications including liver disease treatment, bone regeneration and even cardiac repair. However,

1  
2  
3 development of this field is impeded by a lack of precise data on aspects such as the *in vivo*  
4  
5 engraftment efficiency of transplanted stem cells, and consistent interpretation of therapeutic  
6  
7 effects and migration behaviors. High-resolution imaging labels and techniques to visualize the  
8  
9 fate of the stem cells in living animal models remain urgently needed.<sup>393</sup> Tamaki *et al.* employed  
10  
11 NIR QDs to label bone marrow stromal cells and visualize cell delivery in mice with cerebral  
12  
13 infarct over a 4 week period after transplantation.<sup>394</sup> This work demonstrated a novel strategy to  
14  
15 observe stem cell function for therapy, showing that NIR QDs could be an excellent probe to  
16  
17 track the migration and transport of stem cells. Using a similar strategy, Chen *et al.* developed  
18  
19 Cd-free NIR QDs for stem cell tracking. They conjugated Ag<sub>2</sub>S QDs (NIR-II, 1.0-1.4 μm) with  
20  
21 Tat peptide.<sup>47</sup> The peptide-functionalized QDs were then used as probes to label and track  
22  
23 transplanted human mesenchymal stem cells (thMSCs) in mice. *In vivo* imaging of organ-  
24  
25 specific accumulation and translocation of QD-labeled thMSCs in mice with liver failure tracked  
26  
27 1000 Ag<sub>2</sub>S QD-labeled thMSCs. The distribution of thMSCs in the liver and lung was tracked  
28  
29 for 14 days, showing heparin-facilitated transfer of thMSCs from lung to liver and the long  
30  
31 retention of thMSCs in the liver (**Figure 47**). The NIR-II Ag<sub>2</sub>S QDs provided the ability to track  
32  
33 stem cells in living animals with high temporal and spatial resolution, which can potentially  
34  
35 accelerate clinical application of stem cell therapies.  
36  
37  
38  
39  
40  
41  
42  
43  
44  
45  
46  
47  
48  
49  
50  
51  
52  
53  
54  
55  
56  
57  
58  
59  
60

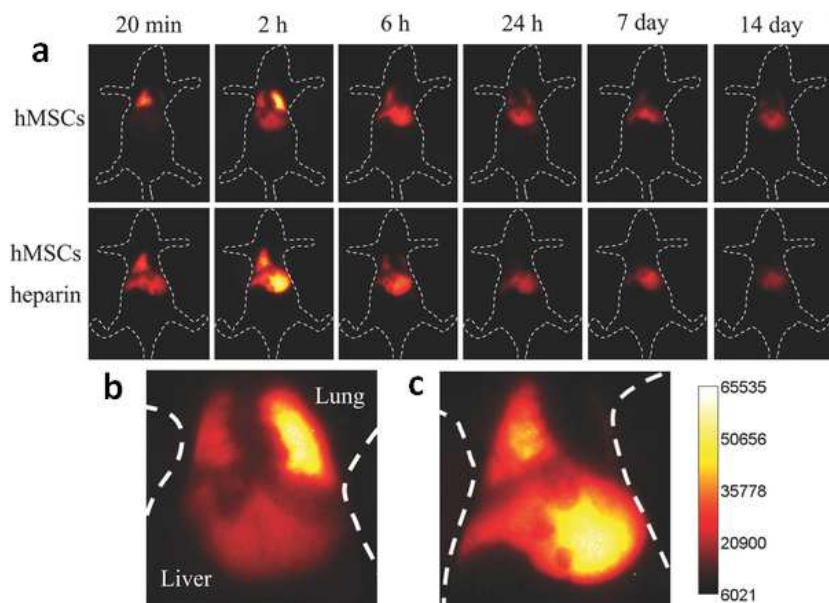


**Figure 47.** *In vivo* tracking of intravenously injected  $\text{Ag}_2\text{S}$  QD-labeled hMSCs in mice. a) Time-lapse *in vivo* NIR PL images of a healthy mouse after transplantation of  $\text{Ag}_2\text{S}$  QD-labeled hMSCs (upper) and a mouse with acute liver failure after transplantation of QD-labeled hMSCs (lower) in combination with heparin at different times (20 min-14 days). b) Higher magnification PL image of a mouse transplanted with hMSCs after 2 h. c) Higher magnification PL image of a mouse with liver failure transplanted with hMSCs in combination with heparin after 2 h. Reprinted with permission from Chen *et al.*<sup>47</sup> Copyright 2014 John Wiley and Sons.

### 5.5. Photothermal Therapy

Photothermal therapy (PTT) of tumors combines nanomaterial delivery with optically-driven heat generation at the tumor site. PTT can significantly reduce tumor size with minimal damage to surrounding healthy tissues. NPs for PTT are usually designed to generate heat upon absorbance of near-IR light from 650 nm to 900 nm.<sup>395-398</sup> *In vivo* PTT effectiveness is determined by accumulation of NPs, light intensity, and the efficiency of conversion of light to heat.<sup>399-402</sup> For example, Hu *et al.* prepared hydrophilic plate-shaped  $\text{Cu}_9\text{S}_5$  NPs with an average

1  
2  
3 size of 13 nm×70 nm and used them as photothermal agents.<sup>403</sup> These NPs showed strong NIR  
4  
5 LSPR absorbance with an extinction coefficient of  $1.2\times 10^9 \text{ M}^{-1} \text{ cm}^{-1}$  at 980 nm. Their light-to-  
6  
7 heat conversion efficiency was up to 25.7%. *Ex vivo* tumors were exposed to 980 nm light for 10  
8  
9 min. Subsequent histological results indicated that most of the cancer cells were killed due to  
10  
11 photothermal heating mediated by the  $\text{Cu}_9\text{S}_5$  NPs.  
12  
13

14  
15 Gold nanoshells have been used as PTT agents in research labs since 1990, and were  
16  
17 commercialized by AuroShell® (Nanospectra Biosciences, TX, USA) in 2008.<sup>404</sup> However, their  
18  
19 therapeutic efficacy can still be improved to treat deeper tumors, and their relatively large size  
20  
21 may be an impediment to achieving desirable biodistribution. Thus, additional PTT agents are  
22  
23 still of interest. In 2011, Korgel's group synthesized ligand-functionalized  $\text{Cu}_{2-x}\text{Se}$  NPs with an  
24  
25 average diameter of 16 nm and used them in PTT experiments.<sup>348</sup> The NP were obtained through  
26  
27 a hot injection technique followed by coating with amphiphilic polymer layers. They showed  
28  
29 strong NIR absorbance with an extinction coefficient up to  $7.7\times 10^7 \text{ M}^{-1} \text{ cm}^{-1}$  at 980 nm. Even  
30  
31 under 800 nm light, the  $\text{Cu}_{2-x}\text{Se}$  nanocrystals showed a photothermal transduction efficiency of  
32  
33 22%, which was higher than that of gold nanorods and gold nanoshells under the same  
34  
35 conditions. *In vitro* photothermal heating of cancer cells (HCT-116) loaded with the  $\text{Cu}_{2-x}\text{Se}$  QDs  
36  
37 resulted in cell destruction after 5 min irradiation at a power density of  $33 \text{ W/cm}^2$ . Likewise, Liu  
38  
39 *et al.* synthesized cysteine-functionalized CuS QDs (Cys-CuS QDs) as PTT agents with high  
40  
41 therapeutic efficacy.<sup>349</sup> The QDs exhibited high stability in the biological environment due to the  
42  
43 biocompatible cysteine coating. They also showed strong absorbance in the NIR with a high  
44  
45 photothermal conversion efficiency of 38%. This value is higher than that of the recently  
46  
47 reported  $\text{Cu}_9\text{S}_5$  and even  $\text{Cu}_{2-x}\text{Se}$  nanocrystals. *In vivo* experiments demonstrated that such QDs  
48  
49 could efficiently inhibit the tumor growth with an 18.5 °C temperature increase in 300 s under  
50  
51  
52  
53  
54  
55  
56  
57  
58  
59  
60

0.72 W cm<sup>-2</sup> excitation at 980 nm for solutions with a concentration of 50 ppm (Figure 48). The high conversion efficiency, photostability and biocompatibility of these NPs show great promise for use in PTT.

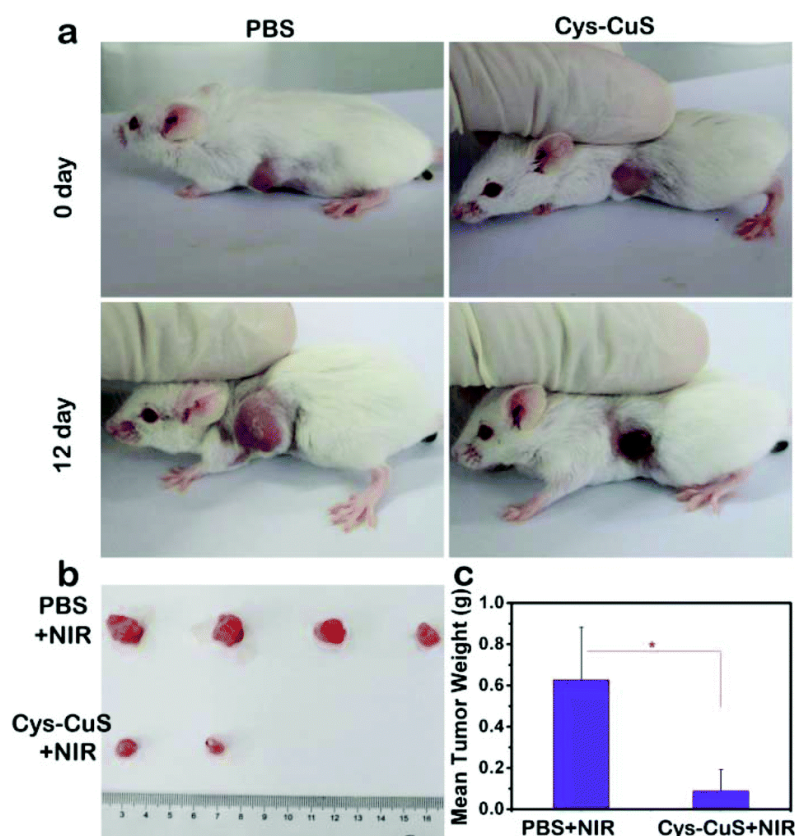


**Figure 48.** Inhibitory effect of Cys-CuS QDs on tumor growth. (a) Representative photos of mice bearing osteosarcoma tumors before and after treatment with PBS or Cys-CuS. (b) Photos of the tumors collected from the mice at the end of treatment (day 12). (c) Mean weights of tumors in (c). Reprinted with permission from Liu *et al.*<sup>349</sup> Copyright 2014 Royal Society of Chemistry.

Surface functionalization of NPs with therapeutic drugs can create bimodal chemo-PTT agents. For example, Hu *et al.* designed and prepared Cu<sub>2-x</sub>Se@mSiO<sub>2</sub>-PEG core/shell QDs. The

1  
2  
3 core of the  $\text{Cu}_{2-x}\text{Se}$  QDs served as a PTT agent, while the  $\text{mSiO}_2$  nanoshells were loaded with  
4 doxorubicin, an anticancer drug. Drug release from the QD conjugates could be triggered by pH  
5 changes and/or illumination. Both chemotherapy and photothermal therapy were triggered by  
6  
7  
8  
9  
10  
11  
12  
13  
14  
15  
16  
17  
18  
19  
20  
21  
22  
23  
24  
25  
26  
27  
28  
29  
30  
31  
32  
33  
34  
35  
36  
37  
38  
39  
40  
41  
42  
43  
44  
45  
46  
47  
48  
49  
50  
51  
52  
53  
54  
55  
56  
57  
58  
59  
60  
irradiation at a safe power density. This significantly improved the therapeutic efficacy  
compared to single modality therapy. The same group also demonstrated similar  $\text{CuS@mSiO}_2$ -  
PEG NPs as a NIR light-dependent drug release system.<sup>405</sup>

Mou *et al.* produced monodisperse and ultrasmall (<5 nm)  $\text{Cu}_{2-x}\text{S}$  QDs (u- $\text{Cu}_{2-x}\text{S}$  QDs) with  
high NIR absorbance and conversion efficiency for PA imaging-guided *in vivo* photothermal  
therapy.<sup>366</sup> Such QDs provide long circulation time and good passive tumor targeting via the  
EPR effect. Advantages of these QDs include not only their small diameter but also their water-  
dispersibility and long-term stability. *In vivo* experiments showed a significant decrease in tumor  
volume after 48 hours for the groups injected with QDs and exposed to laser illumination.  
Tumors were eliminated in 48 hours and had not reoccurred after 16 days. No obvious side  
effects or toxicity of QDs to blood or normal tissue were found after three months. Metabolic  
pathway studies showed that the QDs could be thoroughly cleared through feces and urine within  
5 days. This efficient excretion bodes well for future clinical translation.

Wang *et al.* also examined PTT effectiveness of  $\text{Cu}_{2-x}\text{S}$  QDs.<sup>406</sup> B16 tumor bearing BALB/c  
nude mice were intratumorally injected with  $\text{Cu}_{2-x}\text{S}$  QDs in PBS and photothermal conversion  
efficiency was measured. After 100 s exposure to laser irradiation, the temperature of  
experimental group increased from 32.9 °C to 47.1°C (**Figure 49**). This temperature was high  
enough to kill the tumor cells in tumor-bearing mice. Interestingly, they also found that these  
QDs generated high levels of reactive oxygen species. Thus the  $\text{Cu}_{2-x}\text{S}$  QDs could be used for  
dual mode therapy, *i.e.*, NIR PTT and photodynamic therapy.

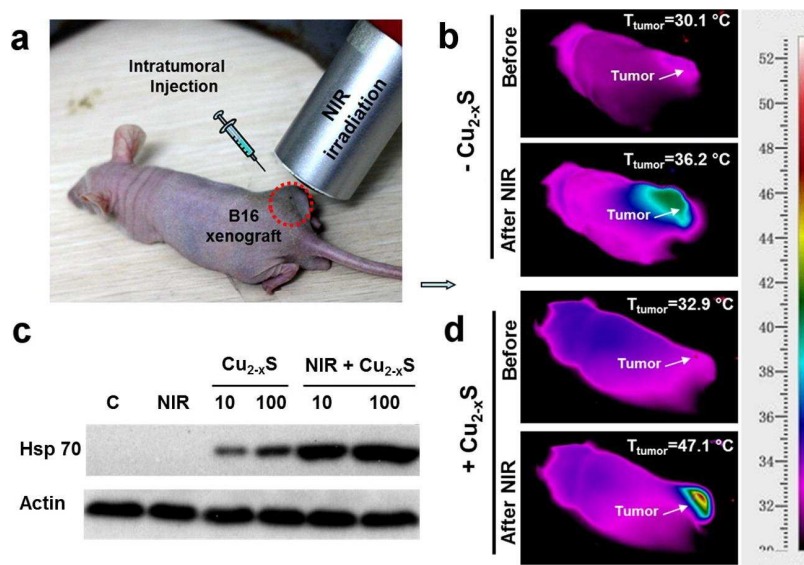


**Figure 49.** IR thermal images of BALB/c mice bearing B16 tumors after 100 s NIR laser irradiation and *in vitro* results for heat shock protein (hsp) expression. (a) B16 tumor-bearing BALB/c nude mouse. The NCs were injected intratumorally, followed by NIR irradiation. (b) IR thermal images taken in the nontreated mice before and after NIR irradiation. (c) Hsp70 expression of B16 cells after treatment with Cu<sub>2-x</sub>S NCs and NIR irradiation. NIR alone was used as a control. (d) IR thermal images of the tumor site post injection of Cu<sub>2-x</sub>S NCs before and after NIR laser irradiation. Reprinted with permission from Wang *et al.*<sup>406</sup> Copyright 2015 American Chemical Society.

Zhu *et al.* developed a facile one-pot synthesis of PEGylated functionalized mesoporous silica coated CuS QDs (CuS@mSiO<sub>2</sub>-PEG) for chemo/photothermal co-therapy.<sup>407</sup> The QDs were colloiddally stable and highly monodisperse. The anti-tumor drug, doxorubicin, was loaded in the mesoporous silica shell of the QDs to provide both pH-dependent drug release and high photothermal efficiency. *In vitro* experiments showed obvious cell death under 980 nm laser diode illumination. However, negligible cell death was observed in control groups treated with either laser exposure or QDs alone. Compared to gold NPs, these Cd-free CuS@mSiO<sub>2</sub>-PEG

1  
2  
3 QDs have two key advantages. First, fabrication costs are reduced because all the elements are  
4 earth-abundant and the preparation procedures are relatively simple, using a one-step reaction.  
5  
6 Second, the absorbance peak of the obtained QD composites was around 980 nm. The  
7 penetration depth at 980 nm is much deeper than at 808 nm, the wavelength often used with  
8 metallic NPs. The safe power density at 980 nm is also higher than at 808 nm.  
9

10  
11 To improve therapeutic efficiency and minimize toxicity to healthy organs, localized  
12 treatment is preferred over systemic chemotherapy. Lin *et al.* designed an anticancer drug carrier  
13 nanoplatfrom, in which doxorubicin was encapsulated within core/shell  $\text{Cu}_9\text{S}_5@\text{mSiO}_2$  QDs.<sup>408</sup>  
14  
15 These QD composites were further integrated with gelatin and poly( $\epsilon$ -caprolactone) to form  
16 nanofibrous fabrics through electrospinning. The fabric pieces were then directly attached at the  
17 surface of the exposed tumor site of mice. The pieces loaded with QDs showed a high light-heat  
18 transfer rate and could ablate tumor cells under 980 nm illumination. At the same time, DOX  
19 was released from the spun pieces and diffused to the tumor site. The results showed that the  
20 synergistic therapy of DOX loaded  $\text{Cu}_9\text{S}_5@\text{mSiO}_2$  composite fibers under 980 nm laser  
21 irradiation provided better tumor inhibition, compared with pure photothermal treatment using  
22  $\text{Cu}_9\text{S}_5@\text{mSiO}_2$  composite fibers.  
23  
24

25  
26 Jiang *et al.* designed a dual plasmonic Au- $\text{Cu}_9\text{S}_5$  nanostructure for photothermal therapy in  
27 the second near IR window (NIR-II: 1000-1350 nm).<sup>81</sup> Larger penetration depth and higher  
28 maximum permissible exposure are possible in this window. 50% enhanced absorbance at 1064  
29 nm was observed for QD conjugates compared to pure  $\text{Cu}_9\text{S}_5$  QDs prepared under similar  
30 conditions. This enhanced absorbance improved the photothermal performance. Moreover, Au-  
31  $\text{Cu}_9\text{S}_5$  QDs exhibited excellent colloidal and photo stability. The NPs had a high photothermal  
32 transduction efficiency of 37% and a tissue penetration depth up to 5 mm at 1064 nm.  
33  
34  
35  
36  
37  
38  
39  
40  
41  
42  
43  
44  
45  
46  
47  
48  
49  
50  
51  
52  
53  
54  
55  
56  
57  
58  
59  
60

1  
2  
3 To ensure a safe and efficient PTT process, precise determination of the tumor size, location  
4 and morphology together with the PTT agent distribution are essential. These aspects could be  
5 enhanced through contrast-enhanced imaging combined with PTT to achieve imaging-guided  
6 PTT. PTT and its integration with traditional chemotherapy are another promising research area,  
7 since most QDs and their nanocomposites that are explored as PTT agents can also function as  
8 PA imaging agents and can exhibit the above-mentioned synergistic effects for  
9 thermoradiotherapy and thermochemotherapy.  
10  
11  
12  
13  
14  
15  
16  
17  
18

### 19 **5.6. Multimodal Imaging**

20 Over the past few decades, cancer has become an increasingly important cause of human  
21 mortality and morbidity worldwide. New diagnostic and imaging technologies are continuously  
22 being developed for early diagnosis and for monitoring of therapies. However, to date, no single  
23 imaging modality can provide both precise and comprehensive information about complex tumor  
24 systems. Multimodal-imaging strategies have attracted attention from the research community  
25 for their potential to address these challenges.<sup>409-411</sup> Currently, MRI is widely used for cancer  
26 diagnosis, based upon its ability to achieve high contrast in soft tissues. However, MRI has key  
27 limitations, such as relatively slow imaging speed, high cost, and limited compatibility with  
28 intra-operative use. Other imaging modalities such as IR thermal imaging and newly developed  
29 PA imaging techniques have been combined with MRI to complement its weaknesses. The  
30 integration of MR/IR-thermal/PA/PL multimodal imaging provides new opportunities for cancer  
31 detection and monitoring.<sup>81,321</sup>  
32  
33  
34  
35  
36  
37  
38  
39  
40  
41  
42  
43  
44  
45  
46  
47  
48  
49  
50

51 Stasiuk *et al.* developed photoluminescent/magnetic dual-mode QDs via covalent binding of  
52 Gd(III) chelates to InP/ZnS QDs.<sup>193</sup> The conjugated QDs exhibited a large relaxivity up to 900  
53  $\text{mM}^{-1}\text{s}^{-1}$  ( $13 \text{ mM}^{-1}\text{s}^{-1}$  per Gd ion) at 298 K and 35 MHz (0.81 T). Bright PL from the InP/ZnS  
54  
55  
56  
57  
58  
59  
60

1  
2  
3 QDs was also demonstrated. Tb (III) and Eu (III) chelates were also successfully conjugated to  
4 the surface of InP/ZnS QDs. There was no energy transfer between the lanthanide ions and the  
5 QDs. Thus, multicolor composites could be formed. Different target-specific ligands were used  
6 to functionalize the QD surface through a direct graft method. For instance, peptides that could  
7 permeate through cell membranes were grafted in a facile one-pot synthesis reaction. QD PL was  
8 used to locate the cells. The QDs also showed longer tissue retention compared to traditional  
9 contrast agents.

10  
11 To obtain both strong MRI signal enhancement and NIR optical absorbance, Mou *et al.*  
12 prepared a novel contrast agent based on Cu<sub>2-x</sub>S nanoprobles for T<sub>1</sub>-weighted MRI/IR thermal/PA  
13 multimodal imaging.<sup>411</sup> These Cu<sub>2-x</sub>S NPs were prepared through thermal decomposition,  
14 followed by biomimetic phospholipid modification. The QDs exhibited high stability in the  
15 physiological environment, prolonged circulation, and effective passive accumulation within  
16 tumors through the EPR effect. Their low cost and one-step synthesis increase their potential for  
17 mass production and future clinical translation. More importantly, the Cu<sub>2-x</sub>S QDs were found to  
18 enhance MRI contrast both *in vitro* and *in vivo*. In addition, the Cu<sub>2-x</sub>S NPs exhibit strong NIR  
19 optical absorbance due to their LSPR properties. This enables them to serve as an excellent  
20 candidate contrast agent for IR thermal/PA imaging. The use of pure single component Cu<sub>2-x</sub>S  
21 NPs for enhanced MR/IR thermal/PA multimodal imaging may bring new possibilities for better  
22 diagnosis and therapy of cancer.

23  
24 Recently, AgInS<sub>2</sub>-ZnS QDs aggregated with MnFe<sub>2</sub>O<sub>4</sub> magnetic NPs (MNPs) through  
25 ultrasonication were prepared and employed for multimodal imaging (**Figure 50**).<sup>350</sup> Bovine  
26 serum albumin (BSA) molecules were used as functional groups for phase transfer into water and  
27 clustering of the QDs. The QD composites worked as both MRI and PL imaging agents. After  
28  
29  
30  
31  
32  
33  
34  
35  
36  
37  
38  
39  
40  
41  
42  
43  
44  
45  
46  
47  
48  
49  
50  
51  
52  
53  
54  
55  
56  
57  
58  
59  
60

further functionalizing them with folic acid and DOX, the hybrid nanostructures could also deliver DOX to HeLa cells. Yellow PL indicated the localization of AgInS<sub>2</sub>-ZnS QDs in the cell cytoplasm and red fluorescence showed the release of DOX in the cell nucleus. The QD-MNP composite NPs showed strong MRI contrast in *in vitro* T<sub>2</sub>-weighted analyses, demonstrating their potential as contrast agents for PL/MR dual-mode imaging.

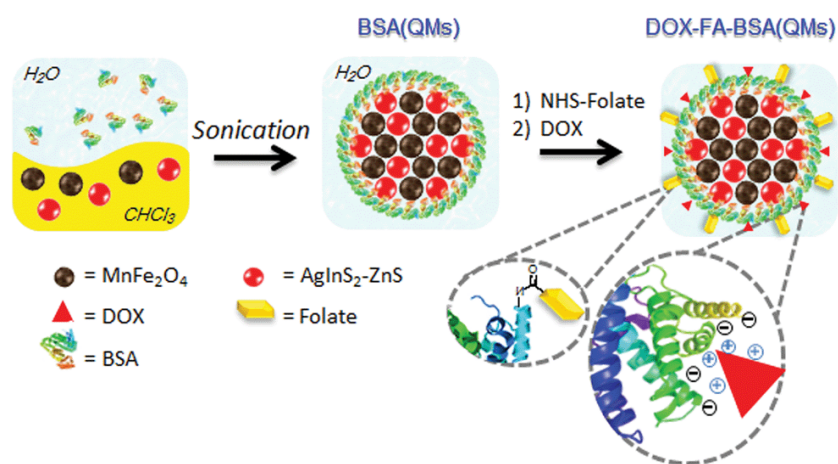


**Figure 50.** Schematic diagram for preparing multi-functional nanoparticles. Reprinted with permission from Fahmi *et al.*<sup>350</sup> Copyright 2014 Royal Society of Chemistry.

Our group has also developed InP/ZnS QDs for multimodal MRI imaging and chemotherapy applications.<sup>412</sup> The InP/ZnS QDs and DOX were coencapsulated in PEGylated phospholipid micelles. The micelles were further conjugated with chelated Gd<sup>3+</sup>. Conjugation with transferrin or anti-claudin-4 was used to enhance the specificity of the multimodal probes. These functional molecules could bind with claudin-4 and transferrin receptors overexpressed by cancer cells. The Gd-conjugated InP/ZnS QDs provided both PL and MRI contrast simultaneously. T<sub>1</sub>-weighted and T<sub>2</sub>-weighted MR imaging showed that the QDs with different formulation ratios exhibited increased or decreased MRI signal. The *in vivo* optical imaging of mice bearing pancreatic

1  
2  
3 cancer xenograft tumors showed that the QD probes could specifically target the tumors to  
4  
5 provide high contrast.  
6

7  
8 QD-based probes can also be prepared with both NIR PL and ultrasound contrast.<sup>413</sup> To do so,  
9  
10 CuInS<sub>2</sub>/ZnS (ZCIS) QDs were modified with plasmid DNA and polyethyleneimine (PEI). PEI is  
11  
12 commonly employed to decorate NPs for electrostatic binding of negatively charged DNA. The  
13  
14 QDs were then adsorbed onto the surface of microbubbles to form MB@QD@PEI/pDNA  
15  
16 conjugates that provided contrast in both PL and ultrasound imaging. *In vitro* cell viability  
17  
18 experiments demonstrated that pDNA molecules were controllably released from the QD  
19  
20 conjugates and could be internalized by cancer cells (HeLa) upon destruction of the  
21  
22 microbubbles. The assays showed a high transfection efficiency and low toxicity to the cells.  
23  
24  
25

26  
27 Ding *et al.* engineered magnetic CuInS<sub>2</sub>@ZnS:Mn QDs as bi-modal nanoprobe for *in vivo*  
28  
29 MRI and PL tumor imaging.<sup>81</sup> The CuInS<sub>2</sub>@ZnS:Mn QDs were transferred into water via ligand  
30  
31 exchange to be used for *in vivo* imaging. Dodecanethiol ligands on the QD surface were replaced  
32  
33 by hydrophilic dihydrolipoic acid-poly(ethylene glycol). PL and MRI images were collected at  
34  
35 successive time points after injection of PEGylated CuInS<sub>2</sub>@ZnS:Mn QDs into tumor-bearing  
36  
37 mice. PL signals appeared in the tumor region by 10 min post-injection and rapidly increased,  
38  
39 reaching maximum intensity after 6 hours. Meanwhile, in *T*<sub>1</sub>-weighted MRI, the *T*<sub>1</sub> value of the  
40  
41 tumor decreased and reached a minimum at 8 h post-injection. The kidneys showed a similar  
42  
43 variation in *T*<sub>1</sub>, suggesting that these QD probes were being cleared via a renal pathway,  
44  
45 consistent with their small size.  
46  
47  
48  
49

50  
51 Bismuth-based nanomaterials have a high X-ray attenuation coefficient and have been used  
52  
53 as X-ray computed tomography (CT) contrast agents. Yang *et al.* synthesized Cu<sub>3</sub>BiS<sub>3</sub> NPs  
54  
55 coated with amphiphilic polyvinylpyrrolidone (PVP) for multimodal imaging and therapy of  
56  
57  
58  
59  
60

1  
2  
3 cancer.<sup>414</sup> The NPs showed strong NIR absorbance, high photostability and photothermal  
4 conversion efficiency. Their cytotoxicity was evaluated, followed by CT imaging and both *in*  
5  
6  
7 *vitro* and *in vivo* experiments on photothermal ablation of cancer cells. The results demonstrated  
8  
9 that the CT value at the tumor site after the NP administration significantly increased from 151.1  
10  
11  $\pm 10$  HU to 741.8  $\pm 10$  HU. Moreover, tumors targeted by the NPs were effectively inhibited  
12  
13 under NIR laser irradiation. Thus, these nanoprobe are good candidates as multifunctional  
14  
15 agents for CT imaging, photothermal imaging and photothermal therapy.  
16  
17

18  
19  
20 Poulouse *et al.* developed multifunctional theranostic QDs that can be used as tri-modal  
21 contrast agents for PL, PA and X-ray micro CT imaging.<sup>415</sup> They prepared Cu<sub>2</sub>S QDs by a hot  
22 injection colloidal approach and then functionalized them with 1,2-distearoyl-sn-glycero-3-  
23 phosphoethanolamine-N-[folate(polyethylene glycol)-2000] (DSPE-PEG-Fol). The functional  
24 molecules were used here both to make the QDs water-dispersible and to provide targeting of  
25 tumors that overexpress folate receptors. The resulting QDs exhibited a blue-green emission  
26 centered at 420 nm under 365 nm light excitation and also broad NIR absorbance due to the  
27 localized surface plasmon resonance from minority carriers, leading to a high absorbance  
28 coefficient as PL and PA contrast agents. In addition, the attenuation coefficient of Cu for the  
29 QDs was demonstrated to be high enough to allow them to serve as contrast agents for X-ray  
30 imaging. The QD surface was further conjugated with DOX. The resulting multimodal PEG-  
31 Cu<sub>2</sub>S-Fol-DOX QDs exhibited excellent biocompatibility and show promise for use in  
32 personalized cancer treatment.  
33  
34  
35  
36  
37  
38  
39  
40  
41  
42  
43  
44  
45  
46  
47  
48  
49

50 Although numerous QD-based strategies have been proposed for cancer treatment, specific  
51 targeting remains a challenge in the design of biocompatible and efficient theranostic QDs. Chen  
52  
53 *et al.* recently reported QD nanoprobe with high specificity for the vasculature in targeted *in*  
54  
55  
56  
57  
58  
59  
60

1  
2  
3 *in vivo* imaging.<sup>416</sup> The QDs could be used for both photothermal imaging and positron emission  
4 tomography (PET) imaging. Photothermally responsive copper sulfide (CuS) NPs were loaded  
5 into biocompatible mesoporous silica nanoshells (CuS@MSN). The surface of the QD  
6 conjugates was then further modified with TRC105 antibodies for targeting and with <sup>64</sup>Cu  
7 positron emitters. *In vitro* targeting, a long-term (60 day) toxicity study, *in vivo* vasculature-  
8 targeted photothermal imaging, and PET imaging were performed systematically. The NPs  
9 exhibited low *in vivo* toxicity even at high doses. The TRC105 antibody on the QD surface could  
10 specifically target both human and murine CD105 in the tumor neovasculature. This significantly  
11 enhanced the tumor vasculature targeting of <sup>64</sup>Cu-CuS@MSN-TRC105 during the *in vivo*  
12 photothermal imaging and PET imaging.  
13  
14  
15  
16  
17  
18  
19  
20  
21  
22  
23  
24  
25  
26

27 Song *et al.* reported the synthesis of biocompatible polyacrylic-acid-functionalized Co<sub>9</sub>Se<sub>8</sub>  
28 nanoplates (PAA-Co<sub>9</sub>Se<sub>8</sub>) and investigated their theranostic properties through both *in vitro* and  
29 *in vivo* experiments.<sup>417</sup> The PAA-Co<sub>9</sub>Se<sub>8</sub> NPs exhibited strong absorbance in the NIR and low  
30 cytotoxicity without light excitation. An 808 nm laser diode was used to excite the NPs for  
31 targeted PA and photothermal therapy. The PAA-Co<sub>9</sub>Se<sub>8</sub> NPs could also serve as T<sub>2</sub>-MRI  
32 contrast agents (**Figure 51**). After encapsulation of DOX drugs, pH-dependent chemotherapy  
33 was observed for the DOX-PAA-Co<sub>9</sub>Se<sub>8</sub> QDs. Thus, this theranostic nanoplatform is promising  
34 for PA/MR dual-modal-imaging and chemo-photothermal co-therapy.  
35  
36  
37  
38  
39  
40  
41  
42  
43  
44  
45  
46  
47  
48  
49  
50  
51  
52  
53  
54  
55  
56  
57  
58  
59  
60

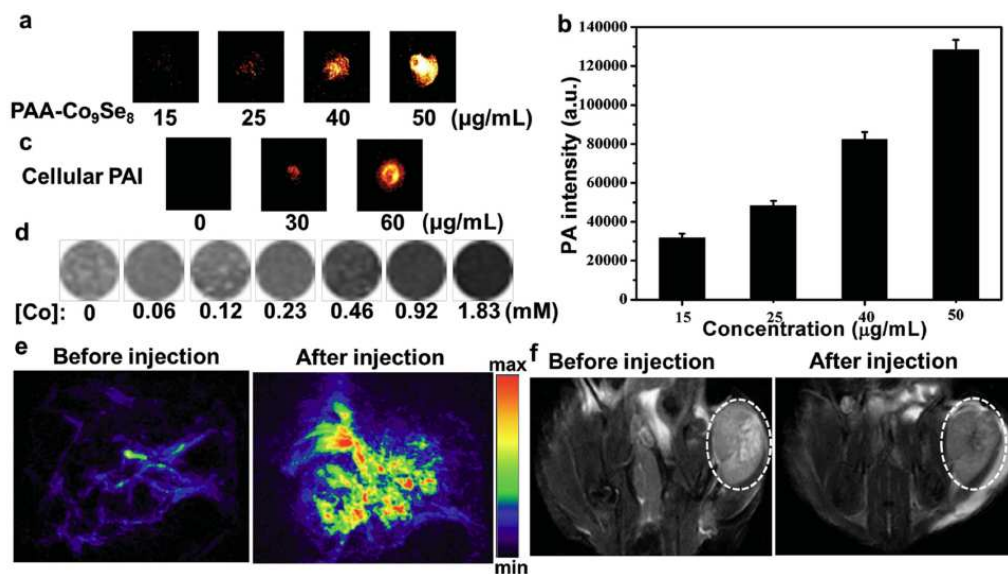


**Figure 51.** Multimodal imaging using PAA-Co<sub>9</sub>Se<sub>8</sub> nanoplates. (a) PA images and (b) PA intensity of PAA-Co<sub>9</sub>Se<sub>8</sub> nanoplates at different concentrations. (c) PA images of HepG2 cells incubated with PAA-Co<sub>9</sub>Se<sub>8</sub> nanoplates. (d) *T*<sub>2</sub>-weighted MR images of the PAA-Co<sub>9</sub>Se<sub>8</sub> nanoplates in aqueous solution at different Co concentrations. (e) PA images of a tumor before and after injection with PAA-Co<sub>9</sub>Se<sub>8</sub> nanoplates. (f) *T*<sub>2</sub>-weighted MRI scans of mice before and after injection with PAA-Co<sub>9</sub>Se<sub>8</sub> nanoplates (white circle: tumor). Reprinted with permission from Song *et al.*<sup>417</sup> Copyright 2015 John Wiley and Sons.

## 6.0. Nanomedicine Applications

Nanomedicine is the application of nanotechnology to disease prevention, detection, diagnosis, imaging, and therapy.<sup>3,84,418-421</sup> A key aim of this field is to engineer targetable diagnostic and therapeutic probes at the nanoscale. These probes can be engineered to respond to stimuli such as light, heat, pH, and magnetic fields, and can combine diagnostic and therapeutic effects, to create theranostics.<sup>422-424</sup> Nanomedicine approaches can overcome challenges faced by existing molecular imaging and delivery methods. For instance, using a nanomedicine approach, one can design formulations for enhanced drug protection to prevent degradation *in vivo*, prolong blood circulation time, reduce side effects, and improve targeting specificity to label and treat diseased cells or tissues.<sup>425,426</sup> Over the past two decades, numerous inorganic nanomaterials have been engineered with unique physiochemical properties for nanomedicine applications.<sup>427-431</sup> This chapter provides a description of nanomedicine applications of Cd-free QDs, including drug delivery, gene delivery, protein and peptide delivery, cancer nanotechnology, imaging guided surgery, *in vitro* diagnostics, drug screening, and infectious disease studies (**Figure 52**). Nanomedical applications discussed in this chapter are listed in **Table 3**.

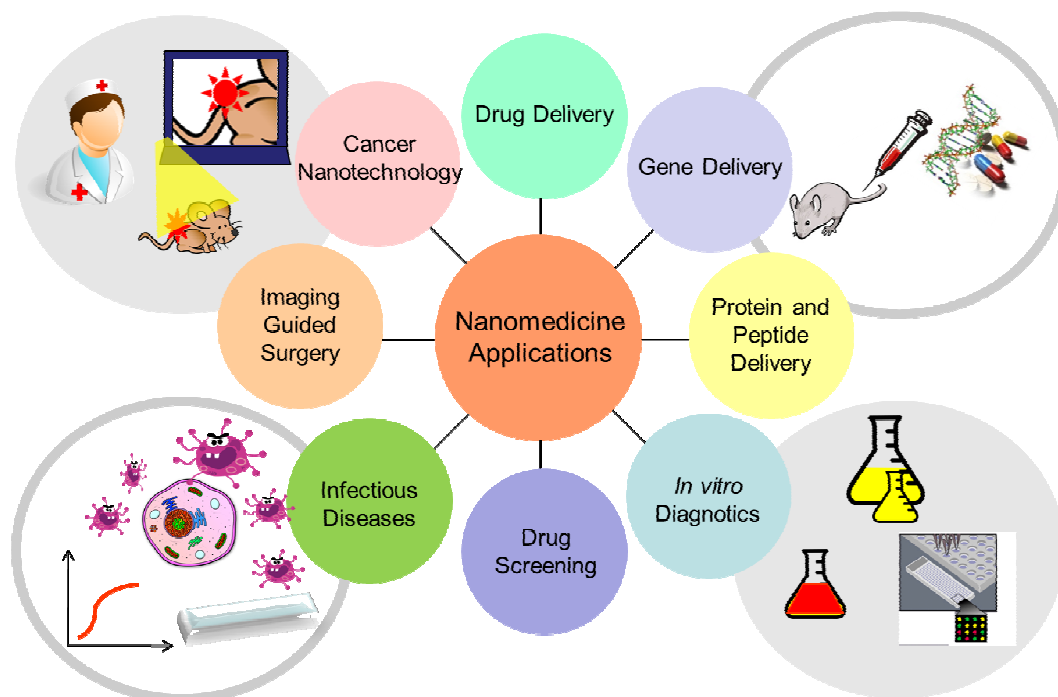


Figure 52. Visual summary of nanomedicine applications of Cd-free QDs.

Table 3. Nanomedicine applications of Cd-free QDs

| Nanomedicine Application | QD type                             | Functional group/molecule | Feature of the technique                              | Model used          | Ref |
|--------------------------|-------------------------------------|---------------------------|---|---------------------|-----|
| <b>Drug delivery</b>     |                                     |                           |   |                     |     |
| <i>In vitro</i>          | InP/ZnS QDs                         | DOX-PEGylated micelles    | 80% inhibition rate at a dose of 80 $\mu\text{g/ml}$  | Panc-1 cancer cells | 412 |
|                          | Ag <sub>2</sub> S QDs               | DOX-cyclic RGD peptide    | 50% inhibition rate at a dose of 2.5 $\mu\text{g/ml}$ | U87 tumor cells     | 209 |
|                          | AgInSe <sub>2</sub> /ZnS core/shell | MTX-PMAO                  | 75% inhibition rate at a dose of 200 $\mu\text{g/ml}$ | HeLa cell           | 432 |
|                          | Mn-doped ZnS                        | IBU-glycopolyptide        | 50% inhibition rate at a dose of 85 $\mu\text{g/ml}$  | HEK293T             | 433 |
|                          | Si QDs                              | Quercetin-PEG-PLA         | drug loading (4%)                                     | HepG2               | 225 |

|    |                                       |  |                            |   |                                       |     |
|----|---------------------------------------|--|----------------------------|---|---------------------------------------|-----|
| 1  |                                       |  |                            |   |                                       |     |
| 2  |                                       |  |                            |   |                                       |     |
| 3  |                                       |  |                            |   |                                       |     |
| 4  |                                       |  |                            |   |                                       |     |
| 5  | <i>In vivo</i>                        | Ag <sub>2</sub> S QDs                  | DOX-cyclic RGD peptide     | 100% survival rate after 16 days              | tumor-bearing mice models MDA-MB-2311 | 209 |
| 6  |                                       |  |                            |   |                                       |     |
| 7  |                                       |  |                            |   |                                       |     |
| 8  | <b>Gene delivery</b>                  |  |                            |   |                                       |     |
| 9  |                                       |  |                            |   |                                       |     |
| 10 | <i>In vitro</i>                       | CuInS <sub>2</sub> /ZnS core/shell     | PEI-pDNA                   | 7.85% transfection rate at a dose < 300 μM    | HeLa cell                             | 413 |
| 11 |                                       |  |                            |   |                                       |     |
| 12 |                                       |  |                            |   |                                       |     |
| 13 |                                       | Mn-doped ZnS                           | chitosan-pCD-UPRT          | DNA binding up to 5.2 μg                      | –                                     | 434 |
| 14 |                                       |  |                            |   |                                       |     |
| 15 |                                       |  |                            |   |                                       |     |
| 16 |                                       | Si QDs                                 | 2-vinylpyridine siRNA      | 50% transfection rate at a dose of 75 μg/ml   | Caco-2 cells                          | 435 |
| 17 |                                       |  |                            |   |                                       |     |
| 18 |                                       |  |                            |   |                                       |     |
| 19 | <b>Protein &amp; peptide delivery</b> |  |                            |   |                                       |     |
| 20 |                                       |  |                            |   |                                       |     |
| 21 |                                       |  |                            |   |                                       |     |
| 22 | <i>In vitro</i>                       | InP/ZnS QDs                            | CPPs & DSPE-PEG2000        | 2% transduction rate at a dose of 150 nM      | A549 cells                            | 41  |
| 23 |                                       |  |                            |   |                                       |     |
| 24 |                                       |  |                            |   |                                       |     |
| 25 |                                       | CuInS <sub>2</sub>                     | BSA                        | monitor catalyzed reaction                    | lactate dehydrogenase                 | 436 |
| 26 |                                       |  |                            |   |                                       |     |
| 27 |                                       |  |                            |   |                                       |     |
| 28 |                                       | Si QDs                                 | anti-IgG                   | monitor antibodies-conjugation                | HRP                                   | 437 |
| 29 |                                       |  |                            |   |                                       |     |
| 30 |                                       |  |                            |   |                                       |     |
| 31 | <b>Cancer nanotechnology</b>          |  |                            |   |                                       |     |
| 32 |                                       |  |                            |   |                                       |     |
| 33 |                                       |  |                            |   |                                       |     |
| 34 | <i>In vitro</i>                       | CuInS <sub>2</sub>                     | silica NPs & anti-PSCA Abs | as a NIR PL tracer                            | PC-3M                                 | 203 |
| 35 |                                       |  |                            |   |                                       |     |
| 36 |                                       |  |                            |   |                                       |     |
| 37 |                                       | InP/ZnS                                | chlorin e6                 | photosensitizer of PDT                        | MDA-MB-231                            | 438 |
| 38 |                                       |  |                            |   |                                       |     |
| 39 |                                       |  |                            |   |                                       |     |
| 40 |                                       | Mn-doped ZnS                           | folic acid & thioglycerol  | two-photon target imaging                     | T47D                                  | 256 |
| 41 |                                       |  |                            |   |                                       |     |
| 42 |                                       |  |                            |   |                                       |     |
| 43 | <b>Imaging-guided surgery</b>         |  |                            |   |                                       |     |
| 44 |                                       |  |                            |   |                                       |     |
| 45 |                                       |  |                            |   |                                       |     |
| 46 |                                       |  |                            |   |                                       |     |
| 47 | <i>In vivo</i>                        | InAs <sub>x</sub> P <sub>1-x</sub> QDs | oligomeric phosphines      | SLN mapping                                   | nude mice                             | 439 |
| 48 |                                       |  |                            |   |                                       |     |
| 49 |                                       | Si QDs                                 | phospholipid-PEG micelle   | tumor vasculature & SLN imaging               | Panc1 tumor mice                      | 38  |
| 50 |                                       |  |                            |   |                                       |     |
| 51 |                                       |  |                            |   |                                       |     |
| 52 |                                       |  |                            |   |                                       |     |
| 53 | <b><i>In vitro</i> diagnostics</b>    |  |                            |   |                                       |     |
| 54 |                                       |  |                            |   |                                       |     |
| 55 |                                       |  |                            |   |                                       |     |
| 56 | <i>In vitro</i>                       | Ag <sub>2</sub> S QDs                  | 3-APBA                     | LOD of 3.2 x 10 <sup>-5</sup> M & 98 cells/ml | glucose & MCF-7 cell                  | 211 |
| 57 |                                       |  |                            |   |                                       |     |
| 58 |                                       |  |                            |   |                                       |     |
| 59 |                                       |  |                            |   |                                       |     |
| 60 |                                       |  |                            |   |                                       |     |

|                 |   |                      |                                      |                                  |     |
|-----------------|---|----------------------|--------------------------------------|----------------------------------|-----|
|                 | CuInS <sub>2</sub>                        | fibrinogen           | LOD of 8.7 x 10 <sup>-12</sup> mol/L | thrombin                         | 440 |
|                 | CuInZn <sub>x</sub> S <sub>2+x</sub> /ZnS | Anti-CRP             | LOD of 1 ng/mL                       | CRP                              | 441 |
|                 | Mn-doped ZnS                              | cysteine - anti-EGFR | 86% specificity & 88% accuracy       | A431 cells                       | 442 |
|                 | <b>Infectious diseases</b>                |                      |                                      |                                  |     |
| <i>In vitro</i> | ZnS                                       | oligonucleotides     | pulse anodic stripping voltammetry   | H5N1, H1N1 & H3N2 influenza      | 443 |
|                 | PbS                                       | 12 (+5 adenine) bp   | target efficiency > 60%              | H5N1 chains                      | 444 |
|                 | GQDs                                      | –                    | induction of oxidative stress        | <i>E.coli</i> & <i>S. aureus</i> | 445 |
|                 | Mn-doped ZnS                              | chitosan             | emission peak at 590 nm              | <i>E.coli</i>                    | 446 |
|                 | Si QDs                                    | FGK45                | enhance immune activation            | CD40 Abs in B cells              | 447 |

The versatility of using bioconjugated QDs for targeted delivery *in vitro* and *in vivo* has led researchers to employ them in many new nanodrug and nanoprobe designs.<sup>448,449</sup> Much current research on applications of QDs in nanomedicine is concentrated in two areas. The first is creation of QDs with multiple functionalities for disease detection and therapy.<sup>203,291,337</sup> A single QD can be linked with multiple biomolecules on its surface to produce multivalent binding and thereby improve specificity in the targeted delivery of the nanoprobe to the disease site. Bioconjugated QDs can be applied to detect and quantify biomarkers on cells and tissues with high sensitivity and specificity. The second key application area of QDs in nanomedicine is in imaging-guided drug and gene delivery.<sup>90,305,450</sup> With sensitive multimodal imaging methods engineered into a cross-evaluation platform for biomolecule screening and investigation, we may soon achieve real time

1  
2  
3 monitoring of distribution, transport, drug release, and pharmacodynamics of QD nanoprobe *in*  
4  
5  
6 *vivo*.

7  
8 The mechanism of delivering a formulation containing both QDs and drugs to a targeted site  
9  
10 such as a tumor is dictated by the overall formulation. Several key principles must be carefully  
11  
12 implemented in QD/drug formulations for targeted delivery:<sup>451-453</sup> (i) the nanoprobe surface must  
13  
14 be conjugated with biomolecules for targeted delivery; (ii) the nanoprobe should degrade into  
15  
16 components below 6 nm in diameter, after performing their function, for rapid renal clearance;  
17  
18 (iii) drugs must be tightly linked to the nanoprobe to minimize off-target effects, but must be  
19  
20 released or activated at target sites in response to external triggers or local microenvironmental  
21  
22 factors; (iv) QDs must be coated with a biocompatible polymer to avoid aggregation and  
23  
24 premature breakdown of the nanoprobe in biological fluids.  
25  
26  
27

28  
29 Two general approaches are used to create nanoprobe that contain both QDs and  
30  
31 drugs.<sup>354,454-456</sup> (i) conjugating drugs to the QDs for delivery to target sites, with release of the  
32  
33 drugs triggered by a change of pH or the presence of enzymes; or (ii) co-encapsulating the drug  
34  
35 molecules and QDs in a biocompatible polymer, delivering these nanocapsules to the specific  
36  
37 sites, and releasing drugs by simple diffusion out of the encapsulating polymer or when the  
38  
39 polymer NP is broken down at a lower pH or in the presence of enzymes. Some groups are  
40  
41 employing the second method for drug delivery, because the preparation process does not require  
42  
43 conjugating the drug to the QD surface and purifying the conjugates. Additional stimuli-response  
44  
45 characteristics, such as light- or field-induced drug release are also possible. Specific examples  
46  
47 are given in subsequent sections of this chapter. In addition to traditional small molecule drugs,  
48  
49 QDs can be employed for delivery of short interfering RNA (siRNA),<sup>151,457</sup> to inhibit the  
50  
51 expression of disease-causing genes. Free siRNA is negatively charged and rapidly degrades in a  
52  
53  
54  
55  
56  
57  
58  
59  
60

1  
2  
3 physiological environment, which impedes its application for *in vivo* and *in vitro* biomedical  
4 studies and applications. Therefore, siRNA is usually modified with or electrostatically bound to  
5 cationic moieties to provide physiological stability and target specificity.  
6  
7  
8  
9

### 10 **6.1. Drug Delivery**

11  
12 Over the past two decades, significant efforts have been made to prepare drugs in  
13 nanoparticulate forms to alter their pharmacokinetics and biodistribution. Nanodrugs can be  
14 fabricated with the drugs loaded into or onto nanosize carriers such as liposomes, micelles,  
15 biodegradable polymer NPs, and inorganic NPs (*e.g.* QDs, gold NPs, iron oxide, etc.).<sup>419,458-462</sup>  
16  
17 Nanocrystals loaded with a drug formulation can provide pharmacokinetic advantages such as  
18 targeted delivery, improved uptake by cells, and long circulation lifetime. The physicochemical  
19 properties of QD-drug formulations can be controlled by tuning the size, surface charge, and  
20 hydrophobicity of the QDs to enhance cellular uptake. Generally, QDs can enter cells through  
21 endocytotic processes such as clathrin-mediated endocytosis, potocytosis, pinocytosis, and  
22 patocytosis.<sup>463-465</sup> Larger particles, >200-300 nm in diameter, are opsonized and removed from  
23 the bloodstream via the reticuloendothelial (RES) system. In designing QDs functionalized with  
24 drug molecules, one must reduce opsonization to extend the blood circulation time. This is most  
25 often achieved by coating the QDs with biocompatible polymers such as polyethylene glycol  
26 (PEG).<sup>466,467</sup> In addition, functionalizing the drug-loaded QDs with targeting ligands can  
27 significantly improve drug delivery to disease sites.<sup>468,469</sup> Oral delivery, transdermal delivery,  
28 intravenous or subcutaneous injection, and pulmonary administration can be used to introduce  
29 QD-drug formulations. Overall, using QDs as drug carriers can enhance the therapeutic potential  
30 of the loaded drugs and contribute to specific targeted therapy. Nanomedicine platforms that  
31 integrate molecular imaging and therapy into one nanosystem are being explored as a means to  
32  
33  
34  
35  
36  
37  
38  
39  
40  
41  
42  
43  
44  
45  
46  
47  
48  
49  
50  
51  
52  
53  
54  
55  
56  
57  
58  
59  
60

1  
2  
3 meet many current challenges in human disease detection and therapy. The ability to link drug  
4 molecules to Cd-free QDs provides new possibilities for advanced diagnosis and treatment of  
5  
6 human diseases. In the following paragraphs, we discuss recent progress toward using Cd-free  
7  
8 QDs as drug carriers.  
9  
10

11  
12 Ag<sub>2</sub>S QDs functionalized with cyclic RGD peptide (cRGD) and doxorubicin (DOX) were  
13 used for combined *in vivo* targeted imaging and drug delivery.<sup>209</sup> Specifically, these  
14 nanoconjugates targeted the  $\alpha_v\beta_3$  integrins overexpressed by U87 tumor cells and MDA-MB-231  
15 xenograft tumors in mice. The DOX-functionalized QDs inhibited tumor cell growth. A 16-day  
16 survival rate of 100% was reported for Ehrlich ascites carcinoma (EAC) tumor-bearing mice  
17 treated with these nanoconjugates (**Figure 53**). These results demonstrate the potential of Ag<sub>2</sub>S  
18 QDs as multifunctional probes for achieving targeted imaging and therapy.  
19  
20  
21  
22  
23  
24  
25  
26  
27  
28  
29  
30  
31  
32  
33  
34  
35  
36  
37  
38  
39  
40  
41  
42  
43  
44  
45  
46  
47  
48  
49  
50  
51  
52  
53  
54  
55  
56  
57  
58  
59  
60

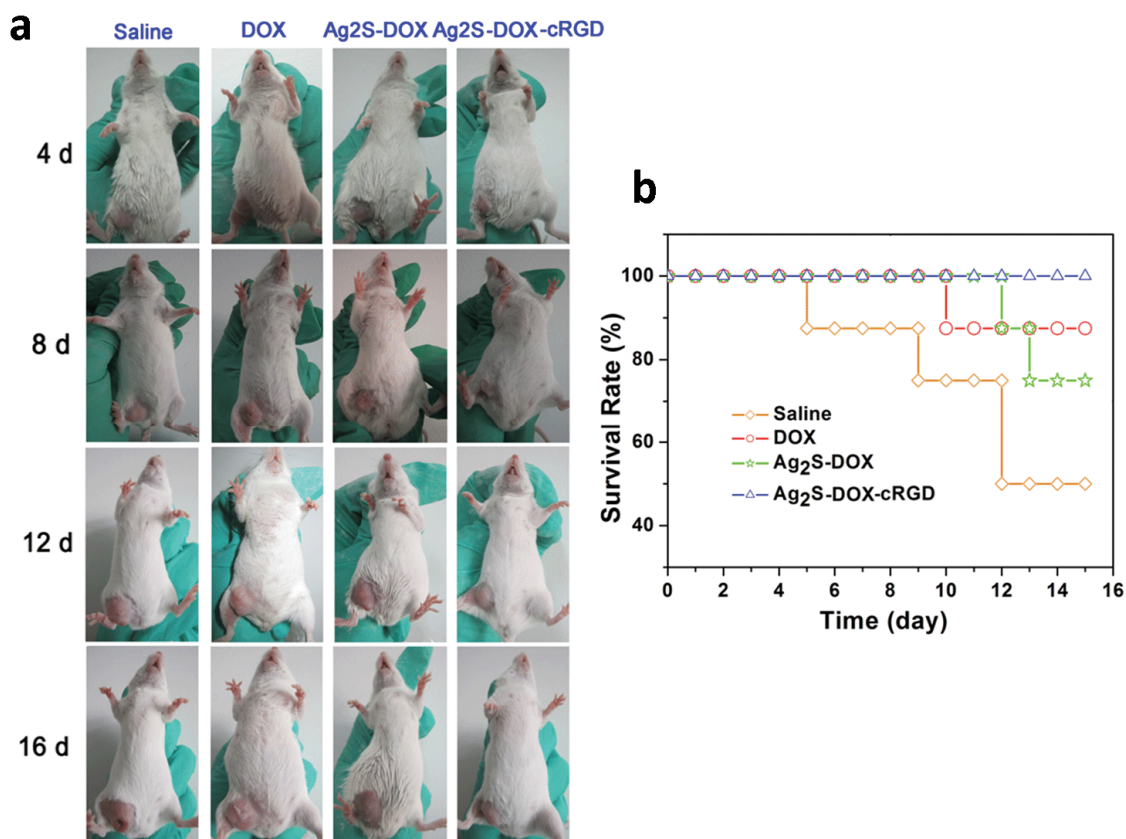


**Figure 53.** Evaluation of therapeutic outcomes of the EAC tumor-bearing mice. (a) Photographs of tumor-bearing mice in the four groups after the indicated duration of treatment. (b) Survival rate of mice from the four groups over 16 days of treatment. Reprinted with permission from Chen *et al.*<sup>209</sup> Copyright 2014 Royal Society of Chemistry.

A similar study employed AgInS<sub>2</sub>/ZnS QDs conjugated with methotrexate (MTX), for cancer treatment.<sup>432</sup> Water-dispersible AgInS<sub>2</sub>/ZnS QDs were prepared by an ultrasonication method, then MTX was covalently linked to their surface using carbodiimide chemistry. An MTT assay indicated that the AgInS<sub>2</sub>/ZnS QDs coated with poly (maleic anhydride-alt-1-octadecene) were highly biocompatible without MTX conjugation. Confocal laser scanning microscopy showed that the MTX-conjugated AgInS<sub>2</sub>/ZnS QDs were effectively taken up by HeLa cells. An MTT assay revealed a strong antiproliferative effect in HeLa cells at a dose of 300 µg/mL. This

1  
2  
3 finding suggests that MTX-conjugated AgInS<sub>2</sub>/ZnS QDs can be further tailored for effective  
4  
5 cancer theranostics.  
6

7  
8 Rather than directly modifying the QD surface for drug delivery, QDs can be encapsulated in  
9  
10 larger particles. For instance, theranostic silica (SiO<sub>2</sub>) nanohybrids loaded with CuInS<sub>2</sub>/ZnS QDs  
11  
12 and Fe<sub>3</sub>O<sub>4</sub> magnetic NPs were prepared and used as drug delivery vehicles and imaging probes  
13  
14 for dual mode PL and MR imaging.<sup>470</sup> These nanohybrids were stably dispersed in water with  
15  
16 hydrodynamic diameter below 30 nm. The nanohybrids were taken up by MCF-7 human breast  
17  
18 cancer cells within one hour and were located within the cytoplasm and near the nucleus. In MRI,  
19  
20 the particles displayed a high spin–spin ( $T_2$ ) relaxivity ( $r_2 = 214 \text{ mM}^{-1} \text{ s}^{-1}$ ). A Pt(IV)-based  
21  
22 anticancer drug was conjugated to the NPs and their theranostic potential was assessed. The  
23  
24 cytotoxicity of drug-conjugated nanohybrids was higher than that of the free drug. This indicates  
25  
26 that the fabricated nanohybrids can be employed as a multifunctional probe for simultaneous  
27  
28 tumor imaging and chemotherapy.  
29  
30  
31  
32

33  
34 Su's group reported a nanodrug delivery system created by electrostatic complexation of  
35  
36 CuInS<sub>2</sub> QDs with poly(l-glutamic acid) (PGA) conjugated with DOX molecules.<sup>200</sup> They first  
37  
38 prepared water-dispersible cysteine-capped CuInS<sub>2</sub> QDs by a hydrothermal method. DOX can  
39  
40 quench the PL of QDs via a photo-induced electron transfer. Thus, the conjugated QDs do not  
41  
42 exhibit PL. After the nanocomplexes were taken up by cancer cells, PGA was hydrolysed,  
43  
44 releasing DOX, and restoring the PL of the CuInS<sub>2</sub> QDs. The nanocomplexes delivered DOX to  
45  
46 PC-3M cancer cells and released DOX to kill the cells (**Figure 54**). DOX release was monitored  
47  
48 by recording the PL intensity from the CuInS<sub>2</sub> QDs. The multifunctional nanocomplex has  
49  
50 potential for use in molecular imaging studies of drug distribution.  
51  
52  
53  
54  
55  
56  
57  
58  
59  
60

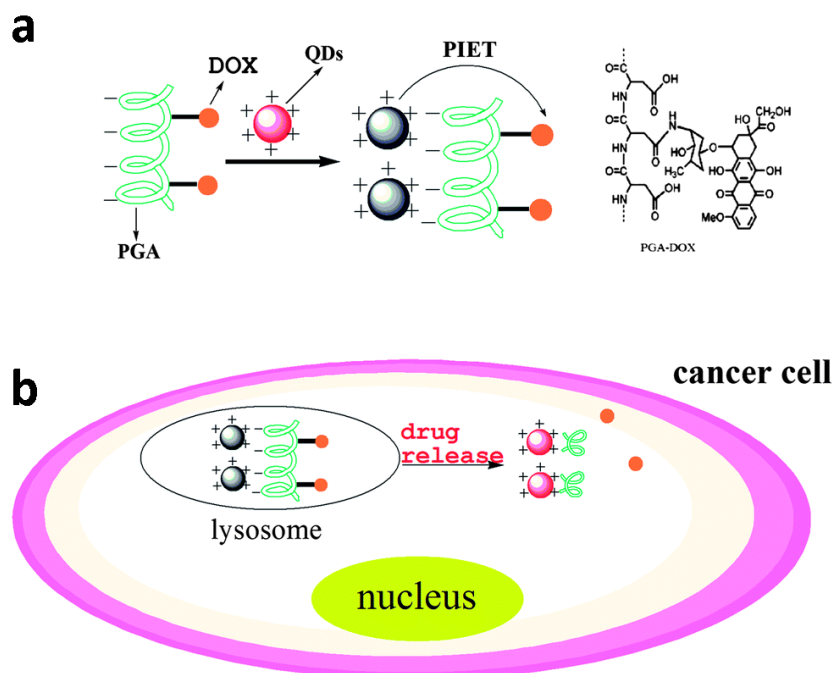


**Figure 54.** Schematic design of a  $\text{CuInS}_2$  QD/PGA–DOX complex and its cellular delivery. (a) construction of the nanocomplex, in which the PL of  $\text{CuInS}_2$  QDs was quenched by DOX through a photoinduced electron-transfer (PIET) process; (b) The nanocomplex was taken up by cancer cells and the DOX was released by hydrolase in lysosomes, restoring  $\text{CuInS}_2$  QD PL and leading to cell death. Reprinted with permission from Gao *et al.*<sup>200</sup> Copyright 2014 Royal Society of Chemistry.

Later, the same group demonstrated the synthesis of MUC1 aptamer functionalized near-IR  $\text{CuInS}_2$  QDs and loaded those QDs with daunorubicin for targeted cancer therapy.<sup>198</sup> More specifically, the  $\text{CuInS}_2$  QDs were conjugated with MUC1 aptamer-(CGA)<sub>7</sub> which allowed daunorubicin to intercalate between the double-stranded CG sequence of the MUC1-functionalized QDs. The aptamer-functionalized QDs effectively delivered daunorubicin to the targeted prostate cancer cells. More importantly, they could be used to detect the concentration

1  
2  
3 of daunorubicin by monitoring the PL intensity of CuInS<sub>2</sub> QDs, which was proportional to the  
4  
5 drug concentration. The detection limit for daunorubicin was about 19 nM.  
6  
7

8 Using similar concepts, other research groups have prepared various types of QD/drug  
9  
10 formulations and have examined their anticancer efficacy in comparison with free drugs.  
11  
12 Mathew *et al.* prepared folic acid-conjugated carboxymethyl chitosan coordinated to Mn-doped  
13  
14 ZnS QDs and used them for targeted imaging and controlled drug delivery to cancer cells.<sup>471</sup>  
15  
16 Fluorouracil drug molecules were encapsulated within the folic acid-conjugated carboxymethyl  
17  
18 chitosan NPs. The drug loaded NPs were 130 to 150 nm in diameter. MCF-7 breast cancer cells  
19  
20 were used to assess imaging, targeted delivery and cytotoxicity of the NPs. MTT assays showed  
21  
22 a sharp reduction in cell viability with increasing NP dose. The stable luminescence of the Mn-  
23  
24 doped ZnS QDs could be employed for imaging the drug carrier in cancer cells, without causing  
25  
26 any adverse effects to the metabolic activity or morphology of the examined cells.  
27  
28  
29  
30

31 Our group engineered multifunctional InP/ZnS QDs for multimodal cancer imaging and  
32  
33 therapy.<sup>412</sup> We co-encapsulated luminescent InP/ZnS QDs and DOX within PEGylated micelles,  
34  
35 then covalently attached DOTA-chelated Gd<sup>3+</sup> to the micelle surface to provide MRI contrast.  
36  
37 Cell viability assays were performed to evaluate the therapeutic efficiency of the nanoprobe.  
38  
39 The viability of cells treated with the DOX-QD micelle NPs decreased to less than 20% at a  
40  
41 concentration of 80 µg/mL, confirming the cytotoxicity of the QD theranostic nanoprobe.  
42  
43 Anticlaudin-4 conjugated QD NPs were delivered to tumor sites *in vivo* in a mouse model,  
44  
45 providing high contrast tumor imaging.  
46  
47  
48  
49

50 Xu *et al.* showed that glycopolypeptide can be used to encapsulate Mn-doped ZnS QDs to  
51  
52 make the QDs suitable for biological applications.<sup>433</sup> They studied the loading capacity and  
53  
54 release of the anti-inflammatory drug, ibuprofen, on the glycopolypeptide coated QDs,  
55  
56  
57  
58  
59  
60

demonstrating high loading efficiency and controllable release (**Figure 55**). Compared with the drug-loaded QDs or with the free drug, the QDs alone had lower cytotoxicity when co-cultured with HEK293T cells.

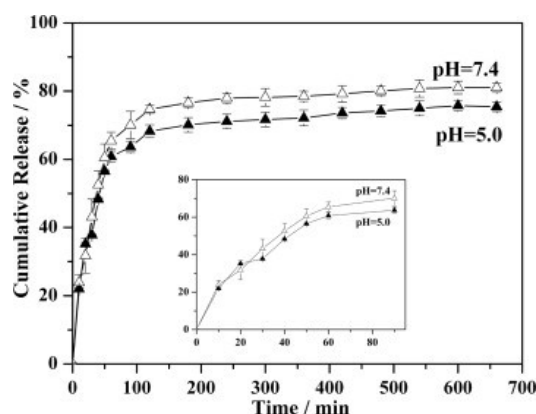


**Figure 55.** Release profiles of ibuprofen from glycopolyptide-coated Mn-doped ZnS QDs in PBS solutions of different pH at 37 °C (mean  $\pm$  SD,  $n = 3$ ). Reprinted with permission from Xu *et al.*<sup>433</sup> Copyright 2011 Elsevier.

Silicon QDs have recently garnered tremendous attention for biological applications ranging from imaging to drug delivery. Si has very low elemental toxicity, and is potentially biodegradable. Moreover, the Si QD surface can be modified by covalent attachment of organic molecules. Although significant efforts have been made to promote the targeting of NPs, many injected NPs are inevitably captured and cleared by mononuclear phagocytes leading to accumulation in the RES organs. This increases the risks of acute or chronic toxicity of the NPs. To date, few studies report self-destruction of NPs into nontoxic and excretable byproducts. A good example was demonstrated by Park *et al.* They demonstrated the preparation of luminescent porous silicon NPs with near-IR PL, which could be loaded with drug molecules for cancer therapy and imaging.<sup>472</sup> The biodistribution and degradation of the particles was monitored based on the location and intensity of PL from NPs. The luminescent porous Si NPs

1  
2  
3 were able to self-degrade *in vivo* and their byproducts were renally cleared over a relatively short  
4 period of time. For drug loading, positively charged DOX was electrostatically attached to the  
5 negatively charged porous Si NPs. DOX was released slowly at physiological pH and  
6 temperature, reaching a plateau within 8 hours. Free silicic acid was detected in solution,  
7 demonstrating the degradation of the NPs, and its appearance correlated well with the DOX  
8 release profile. This study was among the first to demonstrate biodegradable inorganic NPs with  
9 drug loading ability for *in vivo* applications such as targeted therapy and sensing of circulating  
10 tumor cells.  
11  
12

13  
14  
15  
16  
17  
18  
19  
20  
21  
22 Another interesting study was reported by Xu *et al.* They synthesized silicon/polymer  
23 core/shell water-dispersible NPs as carriers for DOX.<sup>473</sup> The size of the nanoprobe ranged from  
24 40 to 110 nm. Their drug loading efficiency was estimated to be 6.1-7.4 wt % for NPs, and the  
25 drug release profile depended upon the pH of the environment. Cytotoxicity studies showed that  
26 DOX-loaded Si QDs exhibited strong anticancer activity against HeLa cells. The authors also  
27 performed a hemolysis study in this work and determined the hemolysis percentages of polymer-  
28 coated Si QDs were less than 2%, which was within the range of safe values. These nanocarriers  
29 were also used as an optical tracker for PL imaging at the cellular level. Hanada *et al.* prepared  
30 water-dispersible alminoprofen-conjugated Si QDs for drug delivery.<sup>474</sup> Alminoprofen is an anti-  
31 inflammatory drug that is commonly used as an analgesic for rheumatism. The authors  
32 demonstrated that these nanoconjugates are less toxic than unconjugated Si QDs or the free-  
33 standing drug. Nonetheless, the nanoconjugates preserved the medicinal effect of the free drug.  
34  
35  
36  
37  
38  
39  
40  
41  
42  
43  
44  
45  
46  
47  
48  
49

50  
51 In addition to direct attachment of drug molecules to the Si QD surface, one can also  
52 coencapsulate drugs and Si QDs in polymeric NPs to produce multifunctional probes. Si QDs  
53 and a hydrophobic anticancer drug, quercetin, were co-encapsulated within poly (ethylene  
54  
55  
56  
57  
58  
59  
60

glycol)-block-poly lactide (PEG-PLA) NPs for cell staining and to promote the solubility of quercetin in biological buffers.<sup>225</sup> The NPs were prepared by a double emulsion method and their cytotoxicity toward HepG2 cells was studied. The drug-loaded NPs suppressed hepatoma HepG2 cells more effectively than free quercetin. Moreover, the nanoformulation was effective in inhibiting DNA damage induced by hydrogen peroxide in cells. These findings demonstrated that the co-encapsulation of quercetin and QDs into one nanosystem could improve aqueous availability of the drug, and enhance biocompatibility of the overall NP formulation while providing the ability to monitor drug delivery and uptake.

Targeted cancer therapy has long been a major focus in the clinical research community, aiming to improve the effectiveness of therapy while reducing systemic exposure of normal tissues to toxic chemotherapeutic agents. Bioconjugated polymeric NPs are often used to carry QDs and drugs for *in vivo* applications because they provide tunable particle size and controllable drug release behavior. Deepagan *et al.* prepared multifunctional NPs composed of Mn-doped ZnS QDs and camptothecin in a poly(lactic-co-glycolic acid) matrix. The NPs, 180 to 200 nm in diameter, targeted EGF receptors, overexpressed on 30% of cancer cells, using the cetuximab antibody.<sup>475</sup> Drug release measurements demonstrated a slow release profile in PBS at pH 7.4. The authors observed high camptothecin activity and uptake of particles in A549 and KB cell lines, which overexpress the EGF receptor. These results indicate that anti-EGF antibody-conjugated NPs embedded with QDs and camptothecin can be used as a theranostic probe to locate and kill tumor cells.

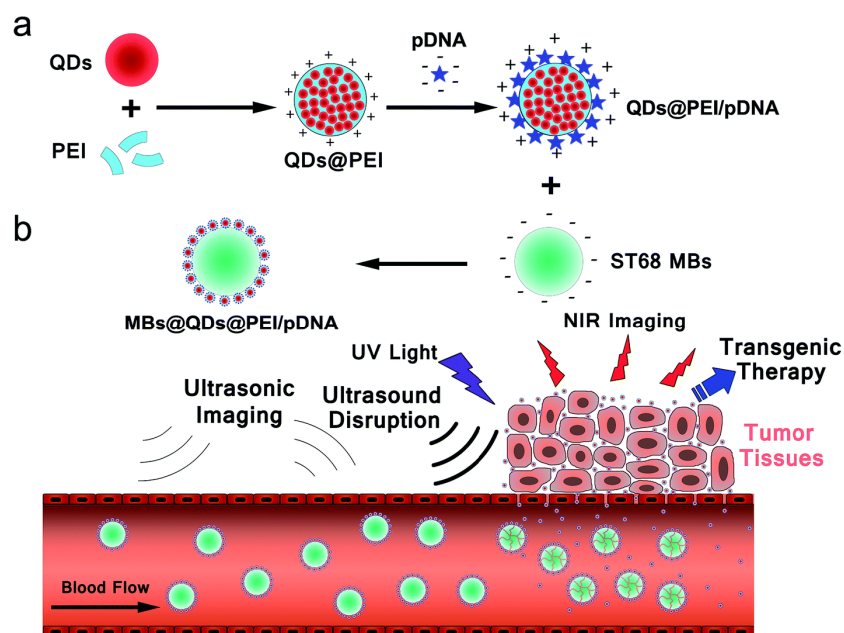
## 6.2. Gene Delivery

Nanoparticle-based gene delivery is a major research area in nanomedicine.<sup>84,476</sup> Gene therapy can address healthcare issues ranging from genetically inherited or acquired diseases, to

1  
2  
3 cancer at a fundamental (genetic) level, to drug or alcohol addiction. The two principal types of  
4 gene therapy with a direct action on genetic activity are: 1) gene augmentation therapy,  
5 enhancing expression of a specific missing/malfunctioning gene by the delivery of an appropriate  
6 plasmid DNA, and 2) gene silencing by RNA interference using a double-stranded RNA, short  
7 interfering RNA (siRNA), aimed at targeting and impairing the post-transcriptional expression of  
8 undesirable genes. Another type of gene therapy that is receiving increasing attention is an  
9 indirect approach, again involving RNA interference, for (a) genetically-induced triggering of  
10 the “neurogenesis” pathway for combating various neurodegenerative diseases and (b)  
11 genetically triggered boosting of innate immune response. Detailed discussion of these  
12 modalities of gene therapy are provided by Prasad<sup>3</sup> and recent advances in clinical trials of gene  
13 therapy were reviewed by Naldini.<sup>477</sup>  
14  
15  
16  
17  
18  
19  
20  
21  
22  
23  
24  
25  
26  
27  
28  
29  
30  
31

32 Early work on gene therapy mainly used engineered viruses (viral vectors) as very efficient  
33 gene delivery vectors. However, their translation for human applications involved many risks  
34 associated with the mutagenicity and immunogenicity of viruses. As a result, nanoparticles  
35 emerged as a class of “nonviral” gene carriers. In general, nonviral vector-mediated methods  
36 have lower transfection efficiency compared to viral methods. However, recent advances have  
37 made nonviral vectors relatively easy to prepare, they are less immunogenic and oncogenic than  
38 viral vectors, and they do not have recombination potential. Integrating genetic substances, such  
39 as plasmid DNA, RNA, and small interfering RNA (siRNA) into nanocomplexes for targeted  
40 gene delivery to tissues and cells is a growing pharmacotherapy research area.<sup>151,478</sup> We describe  
41 here nonviral vector-mediated gene delivery using functionalized Cd-free QDs.  
42  
43  
44  
45  
46  
47  
48  
49  
50  
51  
52  
53  
54  
55  
56  
57  
58  
59  
60

1  
 2  
 3 Yang *et al.* prepared CuInS<sub>2</sub>/ZnS QDs and used them for multimodal imaging and gene  
 4 delivery *in vitro*.<sup>413</sup> The QDs were functionalized with polyethyleneamine (PEI) to allow them to  
 5 form complexes with plasmid DNA (pDNA). These nanocomplexes were then attached to the  
 6 surface of microbubbles and delivered to the tumor site (**Figure 56**). The microbubble  
 7 formulation provided contrast in both ultrasound and PL imaging. *In vitro* cell experiments  
 8 demonstrated that pDNA was released from the microbubbles after they were taken up by HeLa  
 9 cells. High transfection efficiency was achieved by using ultrasound to destroy the microbubbles.  
 10 Cytotoxicity, immunotoxicity, and histological analysis suggested that the formulation is suitable  
 11 for translational medical research. Similarly, chitosan-coated Mn-doped ZnS QDs were proposed  
 12 for gene delivery.<sup>434</sup> Nanocomplexes were prepared by binding pDNA containing the  
 13 bifunctional cytosine deaminase-uracilphosphoribosyl transferase (pCD-UPRT) gene to the  
 14 chitosan-stabilized QDs.  
 15  
 16  
 17  
 18  
 19  
 20  
 21  
 22  
 23  
 24  
 25  
 26  
 27  
 28  
 29  
 30



55  
 56  
 57  
 58  
 59  
 60

**Figure 56.** Schematic illustration of gene delivery based on QDs: (a) formation of MBs@QDs@PEI/pDNA complex; (b) NIR PL/ultrasonic bimodal imaging and targeted delivery

1  
2  
3 of pDNA through ultrasound-targeted microbubble destruction. Reprinted with permission from  
4  
5 Yang *et al.*<sup>413</sup> Copyright 2015 Royal Society of Chemistry.  
6  
7

8 Klein *et al.* employed luminescent Si QDs as a traceable transfection tool for silencing the  
9  
10 ABCB1 gene in Caco-2 cells by RNA interference (RNAi).<sup>435</sup> The QDs were 2-3 nm in diameter,  
11  
12 with green PL. They were capped with 2-vinylpyridine to enable electrostatic binding of siRNA.  
13  
14 Real-time PCR analysis showed a substantial decrease in ABCB1 mRNA level, confirming  
15  
16 release of siRNA from QDs to the cytosol. *In situ* fluorescence spectroscopy was used to monitor  
17  
18 the Pgp efflux dynamics of transfected Caco-2 cells. Reduced transport efficiency for  
19  
20 Rhodamine 123 further demonstrated the successful transfection.  
21  
22

23  
24 Using a similar approach, Chinnathambi *et al.* modified Si QDs with allylamine and then  
25  
26 electrostatically bound cytosine-phosphate-guanine oligodeoxynucleotides (CpG ODN) to  
27  
28 them.<sup>479</sup> The binding mode affected the bifurcation of cytokine induction. The authors also  
29  
30 compared the simultaneous induction of IFN- $\alpha$  and IL-6 using CpG ODN2006x3-PD as free  
31  
32 molecules, electrostatically bound to Si QDs, or covalently linked to the Si QDs.  
33  
34

### 35 36 **6.3. Protein and Peptide Delivery**

37  
38 QDs have also been studied as nanocarriers for therapeutic proteins and peptides with  
39  
40 varying degrees of effectiveness.<sup>219,480-483</sup> In the following paragraphs, we discuss the recent  
41  
42 trend of using QDs as a loading platform for protein and peptide delivery applications. Cell-  
43  
44 penetrating peptides (CPPs) are small peptides that are able to penetrate cell membranes and  
45  
46 deliver cargo into cells. A recent study used CPPs to deliver QDs into cells with minimal toxic  
47  
48 effect. Liu *et al.* prepared carboxyl-terminated InP/ZnS QDs decorated with polyethylene glycol  
49  
50 lipids for peptide delivery *in vitro*.<sup>41</sup> CPPs were noncovalently bound to the functionalized QDs  
51  
52 to form stable nanocomplexes, which were used for delivery of QDs into human A549 cells.  
53  
54  
55  
56  
57  
58  
59  
60

1  
2  
3 For protein delivery and sensing applications, Liu *et al.* prepared water-dispersible CuInS<sub>2</sub>  
4 QDs and functionalized them with bovine serum albumin.<sup>436</sup> The QD PL was quenched by 1,4-  
5 dihydro-nicotinamide adenine dinucleotide (NADH), but not by 1,4-nicotinamide adenine  
6 dinucleotide (NAD<sup>+</sup>). The QDs were used to track the lactate dehydrogenase-catalyzed reaction  
7 of pyruvate by sensing the presence of NADH through QD PL quenching. The protein-coated  
8 QDs were employed for detecting pyruvate molecules, with a detection limit of 25 nM.  
9

10  
11 Tu *et al.* prepared porous silicon NP probes by electrochemical etching.<sup>437</sup> The luminescent  
12 Si QDs within the porous silicon were functionalized with carboxyl-terminated ligands. Their PL  
13 QY reached 50%. The Si QDs were conjugated with goat anti-human IgG antibody which was  
14 modified with horeseradish peroxidase (HRP). Although the authors did not perform biological  
15 studies with the porous silicon NPs, the development of antibody-conjugated silicon-based QDs  
16 paves the way for future *in vivo* delivery and sensing experiments.  
17

18  
19 Chatterjee *et al.* studied the interaction of bovine serum albumin- and allylamine-capped Si  
20 QDs, using fluorescence intensity, quenching, and lifetime measurements, circular dichroism  
21 spectroscopy, and FTIR spectroscopy to monitor changes in the secondary structure of BSA  
22 adsorbed on the Si QDs.<sup>484</sup> BSA fluorescence was quenched by Si QDs, due to ground-state  
23 complex formation. The association process was driven by a favorable negative enthalpy change  
24 and an unfavorable negative entropy change. This result was explained by considering the  
25 specific hydrogen bond between amine groups on the NPs and carboxylate groups of glutamate  
26 and aspartate residues of BSA.  
27  
28  
29  
30  
31

#### 32 **6.4. Cancer Nanotechnology**

33  
34 Cancer nanotechnology is a multidisciplinary research area that employs nanotechnology  
35 solutions to solve challenges faced by the cancer research community. Broadly speaking, this  
36  
37  
38  
39  
40  
41  
42  
43  
44  
45  
46  
47  
48  
49  
50  
51  
52  
53  
54  
55  
56  
57  
58  
59  
60

1  
2  
3 field covers research themes ranging from molecular imaging to targeted therapy. When QDs are  
4 linked to antibodies, proteins, peptides, or other small biomolecules, they can be used to target  
5  
6 tumor antigens, receptors overexpressed on cancer cells, or tumor angiogenesis with high  
7  
8 specificity.<sup>73,485-487</sup> More importantly, multimodal diagnostic (*e.g.*, optical, photoacoustic, or  
9  
10 magnetic) and therapeutic (*e.g.*, photothermal, photodynamic or chemoradiotherapeutic) agents  
11  
12 can be integrated with QDs for advanced theranostic applications. Recent reports have shown  
13  
14 that these QD bioprobes can be used for cellular labeling and targeted drug delivery for cancer  
15  
16 therapy and can be incorporated into nanoscale or microscale devices for early cancer sensing  
17  
18 and screening of biological samples.<sup>488-490</sup> The application of QDs in cancer nanotechnology  
19  
20 provides new opportunities for personalized medicine in which biomarkers are attached to the  
21  
22 QDs and used for diagnosing and treating cancer based on the individual patient's genetic profile.  
23  
24  
25  
26  
27  
28

29  
30 Tan *et al.* demonstrated intracellular synthesis of near-IR (NIR) luminescent Ag<sub>2</sub>S QDs in  
31  
32 HepG2 cancer cells.<sup>491</sup> Treating cultured hepatoma carcinoma cells (HepG2 cells) with silver and  
33  
34 sulfur precursors led them to produce Ag<sub>2</sub>S with reasonable emission efficiency in the presence  
35  
36 of glutathione in the cells. These intracellularly-prepared Ag<sub>2</sub>S QDs were administered into  
37  
38 nude mice by subcutaneous injection, and the mice were imaged under 758 nm laser excitation.  
39  
40 PL of the Ag<sub>2</sub>S QDs was clearly detected from the treated animals. This *in situ* preparation of  
41  
42 Ag<sub>2</sub>S QDs in HepG2 cells was a unique method of making QDs that could potentially be  
43  
44 extended for *in situ* formation of QDs in tumors *in vivo*, which would reduce the need for making,  
45  
46 characterizing, and delivering water-dispersible QDs.  
47  
48  
49

50  
51 Deng *et al.* used a one-pot synthesis method to produce hydrophobic luminescent Zn-Ag-In-  
52  
53 Se QDs<sup>137</sup> and tuned their PL from 660 to 800 nm by tailoring the Ag/Zn ratio. After optimizing  
54  
55 the synthesis, the PL QY reached 50% in some cases. RGD peptide (arginine-glycine-aspartic  
56  
57  
58  
59  
60

acid)-modified N-succinyl-N'-octyl-chitosan (RGD-SOC) was used to make the QDs water-dispersible. For *in vitro* optical imaging,  $\alpha_v\beta_3$  integrin receptor-positive MDA-MB-231 cells and  $\alpha_v\beta_3$  integrin receptor-negative MCF-7 cells were treated with QD-loaded RGD-SOC NPs. PL imaging showed that a large fraction of QD-loaded RGD-SOC NPs entered the cytoplasm via phagocytosis in MDA-MB-231 cells. On the other hand, minimal PL was observed from the  $\alpha_v\beta_3$ -negative MCF-7 cells. Subsequently, these QDs were used for tumor imaging *in vivo* and much greater accumulation of QD-loaded RGD-SOC micelles was found in MDA-MB-231 tumors than in MCF-7 tumors (**Figure 57**).

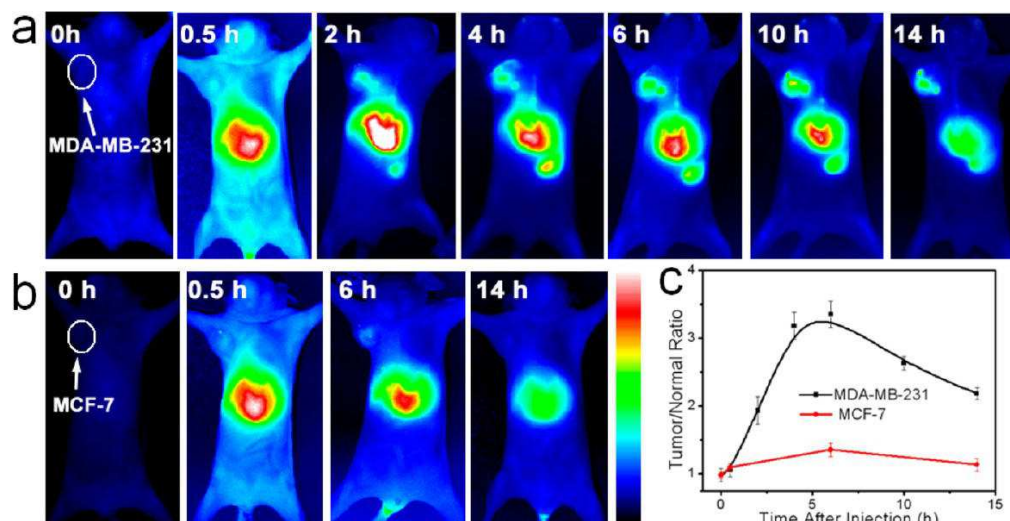
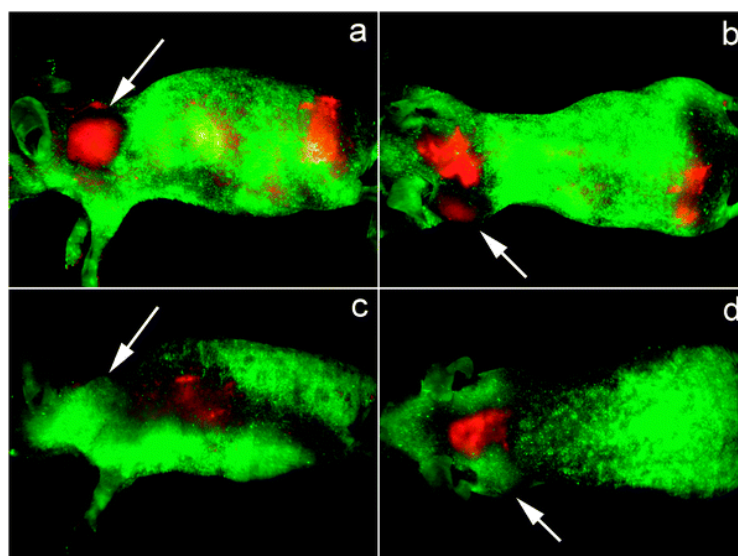


**Figure 57.** Biodistribution of NIR QD-loaded RGD-SOC micelles in nude mice bearing (a) MDA-MB-231 tumor or (b) MCF-7 tumor. (c) Corresponding temporal evolution curves of tumor-to-normal tissue PL ratios in the two groups. Reprinted with permission from Deng *et al.*<sup>137</sup> Copyright 2013 American Chemical Society.

Recently, our group has demonstrated the use of CuInS<sub>2</sub> QDs for targeted multi-color optical imaging *in vivo*.<sup>281</sup> The CuInS<sub>2</sub>/ZnS QDs were made water dispersible by encapsulating them in

1  
2  
3 functional phospholipid micelles, and folic acid was conjugated to the micelle surface for  
4 targeted delivery. For *in vivo* tumor imaging, the NPs were intravenously injected into tumor-  
5 bearing mice. Thirty minutes after injection, intense PL was detected from the tumor site.  
6  
7 However, very weak QD PL was observed from the tumor site in mice treated with unconjugated  
8 QDs (**Figure 58**). More importantly, *in vivo* two-photon imaging of tumors was also  
9  
10 demonstrated. Helle *et al.* used CuInS<sub>2</sub>/ZnS QDs to visualize lymph nodes *in vivo*, showing that  
11 QD PL was maintained for as long as 8 hours.<sup>391</sup> They used immunohistology and molecular  
12 techniques to evaluate the metastatic status of sentinel lymph nodes. Overall, the authors  
13 highlighted that these near-IR emitting Cd-free QDs were excellent sentinel lymph node tracing  
14 markers.



47  
48 **Figure 58.** *In vivo* luminescence imaging of Panc-1 tumor-bearing mice (arrows: tumor) injected  
49 with folic acid-conjugated QDs (a & b) and non-bioconjugated QDs (c & d). The fluorescence  
50 from QDs was coded red and the autofluorescence was coded green. Reprinted with permission  
51 from Yong *et al.*<sup>281</sup> Copyright 2010 Royal Society of Chemistry.  
52  
53  
54  
55  
56  
57  
58  
59  
60

1  
2  
3 Multimodal NP platforms are desirable for cancer diagnosis and therapy. Mathew *et al.*<sup>471</sup>  
4 prepared folic acid-conjugated carboxymethyl chitosan coordinated to Mn-doped zinc sulfide  
5 QDs (FA-CMC-ZnS:Mn) and loaded with 5-Fluorouracil (5-Fu), an anticancer drug that inhibits  
6 growth of breast cancer.<sup>471</sup> The NP functions included cancer targeting, controllable drug  
7 delivery, and tumor imaging. *In vitro* drug release studies showed that the 5-FU was released in a  
8 sustained manner through slow degradation of CMC. An MTT assay was performed to compare  
9 cytotoxicity of FA-CMC-ZnS:Mn alone and loaded with 5-FU. The results demonstrated that  
10 the FA-CMC-ZnS:Mn alone was nontoxic to L929 cells, but increased MCF-7 cell death was  
11 observed when 5-FU was encapsulated in FA-CMC-ZnS:Mn. *In vitro* imaging proved that such  
12 nanoparticles could be used for tracking the path of drug delivery and for targeted imaging of  
13 cancer cells.  
14  
15  
16  
17  
18  
19  
20  
21  
22  
23  
24  
25  
26  
27  
28

29 Silicon, an inherently non-toxic element, has been widely used in food processing and  
30 cosmetic applications. By employing Si QDs in cancer nanotechnology, we can create nontoxic  
31 nanoprobes that are useful for targeting and visualizing tumor cells. Erogbogbo *et al.*  
32 demonstrated preparation of folic acid conjugated Si QDs for targeted imaging of pancreatic  
33 cancer cells.<sup>492</sup> The attachment of folic acid onto the polymer micelles in which the Si QDs were  
34 encapsulated enhanced the specificity of the optical probes and decreased nonspecific uptake of  
35 the particles. In a separate study, they also reported bioconjugated Si QDs covalently linked to  
36 lysine, antimesothelin, and transferrin for bioimaging.<sup>492</sup> Folate- and antimesothelin-conjugated  
37 QDs were able to target Panc-1 cells.  
38  
39  
40  
41  
42  
43  
44  
45  
46  
47  
48  
49

50 Creating a single nanosystem incorporating both plasmonic and PL features can advance  
51 applications in photothermal therapy and drug delivery monitoring *in vivo*. Erogbogbo *et al.*  
52 prepared multimodal NPs by encapsulating Si QDs in polymer micelles and then depositing gold  
53  
54  
55  
56  
57  
58  
59  
60

1  
2  
3 onto the micelle surface to create gold nanoshells.<sup>493</sup> The gold nanoshells displayed plasmonic  
4 light scattering that was used for dark field imaging, while the Si QDs were employed for PL  
5  
6  
7  
8  
9  
10  
11  
12 luminescence and light scattering from the QDs and gold nanoshells, respectively.

13  
14 Recently, Shiohara *et al.* described size-controlled fabrication of Si QDs by a microemulsion  
15 technique. The Si QDs were coated with allylamine and employed for imaging of cancer cells.<sup>302</sup>  
16  
17 The authors found that the amine terminated Si QDs mostly accumulated in lysosomes, but not in  
18 the nuclei. Such QDs may be used as two-photon optical tracers to monitor the activity of cancer  
19 cells over long timescales. Also, Wang *et al.* reported a facile microwave-assisted  
20 hydrosilylation process for fabricating Si QDs.<sup>494</sup> Capping agents with various terminal  
21 functional groups, such as alcohol, alkyl, and carboxylic acid groups, were attached onto the QD  
22 surface. The Si QDs are biocompatible and useful for long-term intracellular PL imaging.  
23  
24 Separately, Cheng *et al.* described another method for preparing colloidal Si QDs for imaging of  
25 cancer cells,<sup>179</sup> by reduction of halogenated silane precursors in a microemulsion synthesis  
26 environment. 1,8-nonadiyne molecules were grafted onto the hydrogen-terminated Si QDs.  
27 Subsequently, different azide molecules were conjugated to the nonadiyne-functionalized QDs,  
28 rendering them dispersible in biological buffers. These Si QDs were used for cell labeling and  
29  
30  
31  
32  
33  
34  
35  
36  
37  
38  
39  
40  
41  
42  
43  
44  
45  
46  
47  
48  
49  
50  
51  
52  
53  
54  
55  
56  
57  
58  
59  
60  
61  
62  
63  
64  
65  
66  
67  
68  
69  
70  
71  
72  
73  
74  
75  
76  
77  
78  
79  
80  
81  
82  
83  
84  
85  
86  
87  
88  
89  
90  
91  
92  
93  
94  
95  
96  
97  
98  
99  
100  
101  
102  
103  
104  
105  
106  
107  
108  
109  
110  
111  
112  
113  
114  
115  
116  
117  
118  
119  
120  
121  
122  
123  
124  
125  
126  
127  
128  
129  
130  
131  
132  
133  
134  
135  
136  
137  
138  
139  
140  
141  
142  
143  
144  
145  
146  
147  
148  
149  
150  
151  
152  
153  
154  
155  
156  
157  
158  
159  
160  
161  
162  
163  
164  
165  
166  
167  
168  
169  
170  
171  
172  
173  
174  
175  
176  
177  
178  
179  
180  
181  
182  
183  
184  
185  
186  
187  
188  
189  
190  
191  
192  
193  
194  
195  
196  
197  
198  
199  
200  
201  
202  
203  
204  
205  
206  
207  
208  
209  
210  
211  
212  
213  
214  
215  
216  
217  
218  
219  
220  
221  
222  
223  
224  
225  
226  
227  
228  
229  
230  
231  
232  
233  
234  
235  
236  
237  
238  
239  
240  
241  
242  
243  
244  
245  
246  
247  
248  
249  
250  
251  
252  
253  
254  
255  
256  
257  
258  
259  
260  
261  
262  
263  
264  
265  
266  
267  
268  
269  
270  
271  
272  
273  
274  
275  
276  
277  
278  
279  
280  
281  
282  
283  
284  
285  
286  
287  
288  
289  
290  
291  
292  
293  
294  
295  
296  
297  
298  
299  
300  
301  
302  
303  
304  
305  
306  
307  
308  
309  
310  
311  
312  
313  
314  
315  
316  
317  
318  
319  
320  
321  
322  
323  
324  
325  
326  
327  
328  
329  
330  
331  
332  
333  
334  
335  
336  
337  
338  
339  
340  
341  
342  
343  
344  
345  
346  
347  
348  
349  
350  
351  
352  
353  
354  
355  
356  
357  
358  
359  
360  
361  
362  
363  
364  
365  
366  
367  
368  
369  
370  
371  
372  
373  
374  
375  
376  
377  
378  
379  
380  
381  
382  
383  
384  
385  
386  
387  
388  
389  
390  
391  
392  
393  
394  
395  
396  
397  
398  
399  
400  
401  
402  
403  
404  
405  
406  
407  
408  
409  
410  
411  
412  
413  
414  
415  
416  
417  
418  
419  
420  
421  
422  
423  
424  
425  
426  
427  
428  
429  
430  
431  
432  
433  
434  
435  
436  
437  
438  
439  
440  
441  
442  
443  
444  
445  
446  
447  
448  
449  
450  
451  
452  
453  
454  
455  
456  
457  
458  
459  
460  
461  
462  
463  
464  
465  
466  
467  
468  
469  
470  
471  
472  
473  
474  
475  
476  
477  
478  
479  
480  
481  
482  
483  
484  
485  
486  
487  
488  
489  
490  
491  
492  
493  
494  
495  
496  
497  
498  
499  
500  
501  
502  
503  
504  
505  
506  
507  
508  
509  
510  
511  
512  
513  
514  
515  
516  
517  
518  
519  
520  
521  
522  
523  
524  
525  
526  
527  
528  
529  
530  
531  
532  
533  
534  
535  
536  
537  
538  
539  
540  
541  
542  
543  
544  
545  
546  
547  
548  
549  
550  
551  
552  
553  
554  
555  
556  
557  
558  
559  
560  
561  
562  
563  
564  
565  
566  
567  
568  
569  
570  
571  
572  
573  
574  
575  
576  
577  
578  
579  
580  
581  
582  
583  
584  
585  
586  
587  
588  
589  
590  
591  
592  
593  
594  
595  
596  
597  
598  
599  
600  
601  
602  
603  
604  
605  
606  
607  
608  
609  
610  
611  
612  
613  
614  
615  
616  
617  
618  
619  
620  
621  
622  
623  
624  
625  
626  
627  
628  
629  
630  
631  
632  
633  
634  
635  
636  
637  
638  
639  
640  
641  
642  
643  
644  
645  
646  
647  
648  
649  
650  
651  
652  
653  
654  
655  
656  
657  
658  
659  
660  
661  
662  
663  
664  
665  
666  
667  
668  
669  
670  
671  
672  
673  
674  
675  
676  
677  
678  
679  
680  
681  
682  
683  
684  
685  
686  
687  
688  
689  
690  
691  
692  
693  
694  
695  
696  
697  
698  
699  
700  
701  
702  
703  
704  
705  
706  
707  
708  
709  
710  
711  
712  
713  
714  
715  
716  
717  
718  
719  
720  
721  
722  
723  
724  
725  
726  
727  
728  
729  
730  
731  
732  
733  
734  
735  
736  
737  
738  
739  
740  
741  
742  
743  
744  
745  
746  
747  
748  
749  
750  
751  
752  
753  
754  
755  
756  
757  
758  
759  
760  
761  
762  
763  
764  
765  
766  
767  
768  
769  
770  
771  
772  
773  
774  
775  
776  
777  
778  
779  
780  
781  
782  
783  
784  
785  
786  
787  
788  
789  
790  
791  
792  
793  
794  
795  
796  
797  
798  
799  
800  
801  
802  
803  
804  
805  
806  
807  
808  
809  
810  
811  
812  
813  
814  
815  
816  
817  
818  
819  
820  
821  
822  
823  
824  
825  
826  
827  
828  
829  
830  
831  
832  
833  
834  
835  
836  
837  
838  
839  
840  
841  
842  
843  
844  
845  
846  
847  
848  
849  
850  
851  
852  
853  
854  
855  
856  
857  
858  
859  
860  
861  
862  
863  
864  
865  
866  
867  
868  
869  
870  
871  
872  
873  
874  
875  
876  
877  
878  
879  
880  
881  
882  
883  
884  
885  
886  
887  
888  
889  
890  
891  
892  
893  
894  
895  
896  
897  
898  
899  
900  
901  
902  
903  
904  
905  
906  
907  
908  
909  
910  
911  
912  
913  
914  
915  
916  
917  
918  
919  
920  
921  
922  
923  
924  
925  
926  
927  
928  
929  
930  
931  
932  
933  
934  
935  
936  
937  
938  
939  
940  
941  
942  
943  
944  
945  
946  
947  
948  
949  
950  
951  
952  
953  
954  
955  
956  
957  
958  
959  
960  
961  
962  
963  
964  
965  
966  
967  
968  
969  
970  
971  
972  
973  
974  
975  
976  
977  
978  
979  
980  
981  
982  
983  
984  
985  
986  
987  
988  
989  
990  
991  
992  
993  
994  
995  
996  
997  
998  
999  
1000

Overall, the current trend of using QDs for cancer nanotechnology relies heavily on conjugating the QDs with specific biomolecules for targeted delivery and imaging. For *in vitro* applications, the NPs reported above will be useful tools for understanding and investigating the transport or interaction mechanisms between biomolecules and the tumor cells. However, if the NPs are intended to be translated for *in vivo* applications, many aspects must be further

1  
2  
3 considered. For example, attaching biomolecules on the surface of QDs will likely increase the  
4  
5 overall hydrodynamic size of the QDs promoting uptake by the RES system rather than renal  
6  
7 clearance. This can lead to accumulation of QDs in the body, which may cause harmful side  
8  
9 effects or be a cause of concern about long-term impacts, even when the QDs do not contain Cd,  
10  
11 Pb or similar heavy metals.  
12  
13  
14  
15  
16

### 17 **6.5. Imaging Guided Surgery**

18  
19  
20 Surgery remains one of the most common modes of cancer treatment.<sup>495-497</sup> Intraoperative  
21  
22 assessment of surgical margins currently depends heavily on surgeons' experience in  
23  
24 subjectively determining the appearance and palpation of the tumor. Tumor recurrence is likely if  
25  
26 the tumor surgical margins are not properly determined, but unnecessarily large margins cause  
27  
28 additional pain and complications for the patient. To improve outcomes, surgeons need enhanced  
29  
30 visualization of the tumor to maximize tumor resection and minimize damage or injury to normal  
31  
32 tissues. Advances in optical imaging are allowing its use for real-time tumor monitoring and  
33  
34 imaging-guided surgery.<sup>488-490,498</sup> Dyes such as indocyanine green are generally employed for  
35  
36 imaging guided surgery, but have drawbacks including aggregation, limited solubility,  
37  
38 nonspecific *in vivo* uptake, and lack of specific tissue targeting. Thus, the clinical research  
39  
40 community has shown strong interest in development of QDs for surgical imaging  
41  
42 applications.<sup>498-500</sup> In the last few years, QDs have increasingly been studied for surgical use,  
43  
44 especially for tumor detection, tumor resection, and sentinel lymph node (SLN) mapping. Many  
45  
46 research articles have argued that QDs will be a useful tool for *in vivo* intraoperative  
47  
48 imaging.<sup>501,502</sup> In the next few paragraphs, we discuss and highlight recent developments in QDs  
49  
50 for possible use during surgery.  
51  
52  
53  
54  
55  
56  
57  
58  
59  
60

1  
2  
3 Zimmer *et al.* produced water-dispersible InAs/ZnSe core/shell QDs that emit in the near-IR,  
4 and used these QDs as contrast agents for multiple sequential lymph node mapping.<sup>503</sup>  
5  
6 Specifically, the InAs/ZnSe QDs were transferred into water using dihydrolipoic acid (DHLA) or  
7 DHLA linked to a short poly(ethylene glycol) chain through carbodiimide coupling chemistry.  
8  
9 Using DHLA alone, the hydrodynamic size of the QDs in PBS buffer was 5.3 nm, but in fetal  
10 bovine serum it increased to 13.8 nm. DHLA-PEG functionalized QDs had an 8.7 nm  
11 hydrodynamic diameter. When the QDs were injected into the paw of a mouse, the QDs travelled  
12 throughout the body and could be detected in the SLN. In addition, the authors reported that they  
13 observed PL from QDs in interstitial fluid after intravenous injection. They deduced that such  
14 QDs were able to extravasate from blood vessels into the interstitial fluid. This shows promise  
15 for use of QDs as efficient and specific intravenously administered tracers, since the first barrier  
16 to tissue penetration is extravasation.  
17  
18  
19  
20  
21  
22  
23  
24  
25  
26  
27  
28  
29  
30

31  
32 Improving tissue penetration depth and spatial resolution of imaging probes is essential for  
33 enhanced surgical imaging. However, scattering and absorbance of tissues *in vivo* present  
34 substantial barriers to these improvements. Li *et al.* demonstrated that Ag<sub>2</sub>S QDs can be used as  
35 NIR luminescent probes for *in vivo* monitoring of lymphatic and vascular networks with deep  
36 penetration.<sup>174</sup> They reported that Ag<sub>2</sub>S QDs can provide spatial resolution of 40 μm during *in*  
37 *in vivo* PL imaging, and this allowed them to monitor the angiogenesis process. The authors suggest  
38 that Ag<sub>2</sub>S QDs will be useful for dissection of sentinel lymph nodes and evaluation of blood  
39 supply in organs.  
40  
41  
42  
43  
44  
45  
46  
47  
48  
49

50  
51 Dong *et al.* reported the synthesis of luminescent Ag<sub>2</sub>Se QDs with emission at 1300 nm for  
52 *in vivo* surgical use<sup>174</sup>. After surface modification with C18-PMH-PEG, the Ag<sub>2</sub>Se QDs  
53 displayed bright PL, high colloidal stability and enhanced biocompatibility. Subsequently, these  
54  
55  
56  
57  
58  
59  
60

1  
2  
3 NPs were used for deep imaging of organs and vascular structures with high spatial resolution.  
4  
5 Such QDs will certainly create new opportunities for imaging-guided surgery applications. Ding  
6  
7 *et al.* demonstrated the preparation of CuInS<sub>2</sub>@ZnS:Mn QDs as multimodal imaging probes for  
8  
9 PL and MR imaging of tumors in mice.<sup>81</sup> For *in vivo* imaging experiments, water-dispersible  
10  
11 CuInS<sub>2</sub>@ZnS:Mn QDs were prepared by functionalizing the QDs with dihydrolipoic acid-poly  
12  
13 (ethylene glycol) ligand. *In vivo* PL and MR imaging experiments showed that the  
14  
15 CuInS<sub>2</sub>@ZnS:Mn QDs were able to target both subcutaneous and intraperitoneal tumors in mice.  
16  
17

18  
19 In another study, core/shell/shell InAs<sub>x</sub>P<sub>1-x</sub> QDs were synthesized with emission wavelengths  
20  
21 from 750 to 850 nm.<sup>439</sup> The InAs<sub>x</sub>P<sub>1-x</sub> core had a graded composition in which the arsenic  
22  
23 concentration increased from the center to the periphery of the QDs. The QDs displayed tunable  
24  
25 NIR emission, and growth of an InP shell on the core resulted in a red-shift and increased QY.  
26  
27 Deposition of an additional ZnSe shell further improved the stability of the NPs for biomedical  
28  
29 imaging. These NIR-emitting core/shell/shell QDs were employed for sentinel lymph node  
30  
31 imaging and mapping *in vivo*. The hydrodynamic diameter of the QDs is critical for precision  
32  
33 SLN mapping, because NPs of 5 to 10 nm diameter can bypass the SLN and travel to other nodes  
34  
35 in the chain. At the other extreme, if the NP diameter is greater than 280 nm, they can hardly  
36  
37 move from the injection site. Thus, the NP formulation must have the right size for effective  
38  
39 delivery to the SLN. In this study, alloyed core/shell/shell QDs coated with oligomeric  
40  
41 phosphines displayed a hydrodynamic size of 12 nm. The authors employed an intraoperative  
42  
43 video imaging system that superimposes the PL signals on a visible-light image of the underlying  
44  
45 anatomy. When the QD formulation was injected into the paw of a mouse, the PL image showed  
46  
47 the lymphatic flow of QDs from the injection site to the SLN. The authors reported that the  
48  
49 introduced QDs travelled to the lymphatics and moved to the sentinel node within 1 minute.  
50  
51  
52  
53  
54  
55  
56  
57  
58  
59  
60

1  
2  
3  
4  
5  
6  
7  
8  
9  
10  
11  
12  
13  
14  
15  
16  
17  
18  
19  
20  
21  
22  
23  
24  
25  
26  
27  
28  
29  
30  
31  
32  
33  
34  
35  
36  
37  
38  
39  
40  
41  
42  
43  
44  
45  
46  
47  
48  
49  
50  
51  
52  
53  
54  
55  
56  
57  
58  
59  
60

Erogbogbo *et al.* demonstrated that micelle-encapsulated Si QDs can be employed for tumor vasculature imaging and sentinel lymph node (SLN) mapping in live mice<sup>38</sup>. Their nanoformulation possessed stable luminescence and long tumor accumulation time *in vivo* (>40 h). This study used Si QDs with hydrodynamic size of 20 nm for SLN imaging. When the QDs were injected subcutaneously into the paw of a mouse, the QDs migrated through the lymphatics and moved to an axillary location. The accumulation spot of QDs showed the position of the SLN (**Figure 59**). Recently, CuInS<sub>2</sub> QDs have been employed for SLN imaging, however these QDs still contain Cu and In metals that may cause some concerns from a clinical perspective.

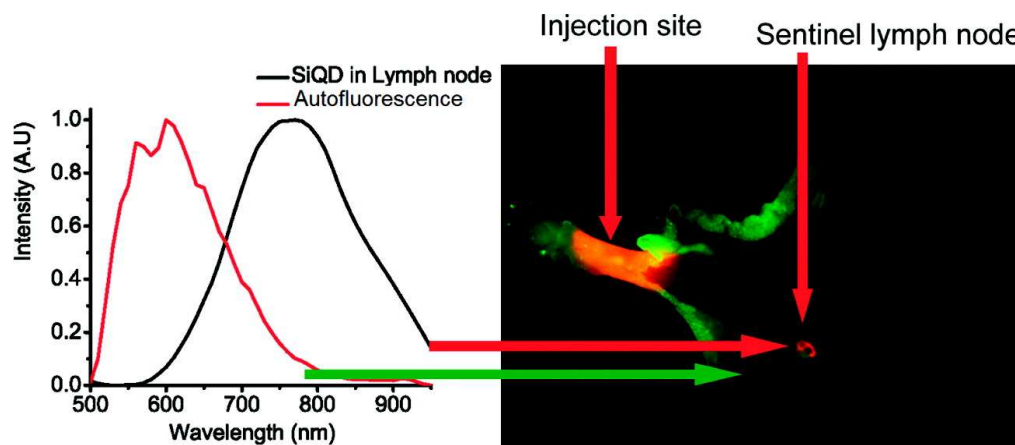


**Figure 59.** Sentinel lymph node PL imaging using micelle-encapsulated silicon QDs. Autofluorescence was coded green, and the unmixed SiQD signal was coded red. Reprinted with permission from Erogbogbo *et al.*<sup>38</sup> Copyright 2011 American Chemical Society.

In summary, the QD community has started to develop various Cd-free QDs, with emission peaks ranging from visible to near-IR, for *in vivo* surgical applications. There are two important factors to be considered for using QDs in surgery: (i) the overall hydrodynamic size of QDs will determine the transport and biodistribution of QDs; and (ii) the type of surface passivation, along with size, will determine the lifespan of the QDs *in vivo*. By carefully controlling and tailoring

1  
2  
3 these two factors, one can engineer specific QD formulations for advanced *in vivo* surgical  
4 applications.  
5  
6

### 7 **6.6. *In vitro* Diagnostics**

8  
9  
10 QDs can be employed in clinical laboratory diagnostics that are used to ascertain disease  
11 information at the genetic or even protein level.<sup>247,504</sup> Depending on the constructed QD  
12 bioconjugates, these NPs can display functional properties such as sensing of chemicals and  
13 biomolecules. These QDs can be incorporated into devices for advanced healthcare applications.  
14  
15 In this section, we discuss available and emerging QD-related diagnostic methods and devices  
16 integrated with QDs that take advantage of the electronic and optical properties of QDs for  
17 detection of biochemical molecules.  
18  
19

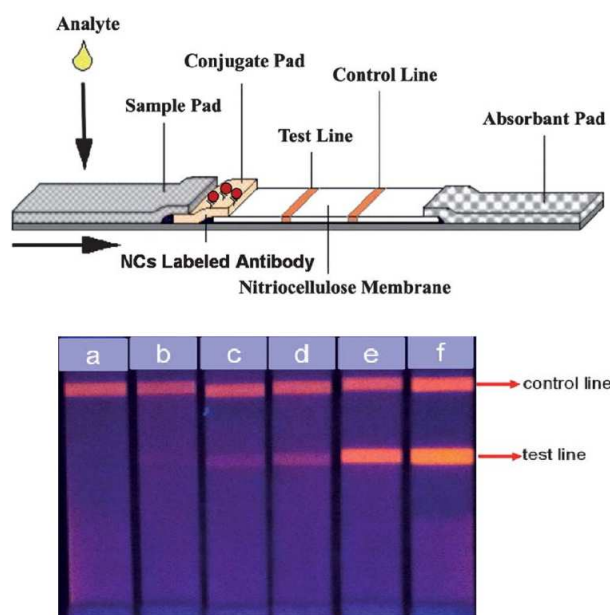
20  
21  
22  
23  
24  
25  
26  
27 Zhang *et al.* used biocompatible Ag<sub>2</sub>S QDs to detect photoelectrochemically active species  
28 such as glucose and cancer cells.<sup>211</sup> Ag<sub>2</sub>S and Ag<sub>2</sub>Se QDs were synthesized and assembled on  
29 SnO<sub>2</sub> modified ITO electrodes. The Ag<sub>2</sub>S/SnO<sub>2</sub>/ITO electrode showed 10 times higher  
30 photocurrent compared to Ag<sub>2</sub>Se/SnO<sub>2</sub>/ITO. Then the Ag<sub>2</sub>S/SnO<sub>2</sub>/ITO electrode was  
31 functionalized with glucose oxidase (GOx) for glucose detection or modified with the 3-  
32 aminophenylboronic acid (3-APBA) for MCF-7 cancer cell detection. When the GOx modified  
33 electrode was exposed to a glucose solution, the conversion of glucose into gluconic acid and  
34 hydrogen peroxide consumed dissolved oxygen, which caused a photocurrent decrease. When  
35 the 3-APBA modified electrode was exposed to MCF-7 cells that overexpress sialic acid (SA),  
36 the strong binding of 3-APBA with SA also resulted in decreased photocurrent. A specificity test  
37 further confirmed that the photocurrent decrease was a result of the specific recognition between  
38 3-APBA ligands and cellular surface SA. The detection limit was  $3.2 \times 10^{-5}$  M for glucose and 98  
39 cells/mL for MCF-7 cells.  
40  
41  
42  
43  
44  
45  
46  
47  
48  
49  
50  
51  
52  
53  
54  
55  
56  
57  
58  
59  
60

1  
2  
3 The long-lived room-temperature phosphorescence (RTP) of Mn-doped ZnS QDs is easily  
4 distinguished from autofluorescence and scattered light, which facilitates its use for detecting  
5 analytes in complex matrixes. Ertas and Kara used L-cysteine capped Mn-doped ZnS QDs with  
6 the anticancer drug Idarubicin (IDA) to detect the interaction between double stranded DNA and  
7 IDA.<sup>258</sup> The RTP emission of the Mn-doped ZnS QDs was quickly quenched upon addition of  
8 IDA, which serves as an electron acceptor. The addition of ds-DNA caused formation of a  
9 DNA/IDA complex, removing IDA from the QD surface and restoring the RTP signal of the  
10 QDs. The linear detection range of this method was 1.2~6.0  $\mu\text{M}$ .  
11  
12  
13  
14  
15  
16  
17  
18  
19  
20  
21

22 Recently, a simple method for the detection of thrombin using  $\text{CuInS}_2$  QDs and fibrinogen  
23 (Fib) was presented.<sup>440</sup> Water-dispersible near-IR  $\text{CuInS}_2$  QDs were prepared by a hydrothermal  
24 method and capped with mercaptopropionic acid. The introduction of fibrinogen to the  $\text{CuInS}_2$   
25 QD dispersion produced a Fib- $\text{CuInS}_2$ QD complex through electrostatic binding and hydrogen  
26 bonding. This binding was accompanied by enhancement of PL intensity and a red-shift of the  
27 PL peak. Addition of thrombin to the Fib- $\text{CuInS}_2$  QD system promoted polymerization of  
28 conjugated and free fibrinogen to produce fibrillar fibrin-QD aggregates. Upon centrifuging the  
29 sample, the PL intensity from the supernatant decreased with increasing thrombin concentration.  
30 In this manner, Fib-QD nanoprobes can be used to detect thrombin at concentrations from  
31  $6.7 \times 10^{-11}$  to  $3.9 \times 10^{-7}$   $\text{mol L}^{-1}$  with a limit of detection of  $8.7 \times 10^{-12}$   $\text{mol L}^{-1}$ . Thrombin detection  
32 was also demonstrated using human serum samples directly. Compared with methods using other  
33 NPs and aptamer-based sensing approaches, this method gave a much lower detection limit for  
34 thrombin.  
35  
36  
37  
38  
39  
40  
41  
42  
43  
44  
45  
46  
47  
48  
49  
50  
51  
52

53 Shen *et al.* developed a lateral flow immunoassay (LFIA) system for sensing of C-reactive  
54 protein using  $\text{CuInZn}_x\text{S}_{1+x}/\text{ZnS}$  QDs as PL labels and a nitrocellulose filter as the substrate.<sup>505</sup>  
55  
56  
57  
58  
59  
60

1  
2  
3 For this purpose, they fabricated the  $\text{CuInZn}_x\text{S}_{1+x}/\text{ZnS}$  core/shell QDs and transferred them into  
4 water using an amphiphilic oligomer (polymaleic acid n-hexadecanol ester). Then the water-  
5 dispersible QDs were conjugated to the mouse anti-C-reactive protein (anti-CRP) monoclonal  
6 antibody. Another anti-CRP monoclonal antibody was attached to the nitrocellulose membrane  
7 of the test line. The C-reactive protein in the analyte facilitated binding of the antibody on the  
8 nitrocellulose membrane with the functionalized QDs, leading to fluorescence enhancement at  
9 the test line in the LFIA system (**Figure 60**). The detection limit was  $1 \text{ ng mL}^{-1}$ , 100 times more  
10 sensitive than a commercial kit.  
11  
12  
13  
14  
15  
16  
17  
18  
19  
20  
21  
22  
23  
24  
25  
26  
27  
28  
29  
30  
31  
32  
33  
34  
35  
36



37  
38  
39  
40  
41  
42  
43  
44  
45  
46  
47  
48 **Figure 60.**(Upper) Schematic representation of the lateral flow immunoassay (LFIA) strip and  
49 (lower) images of LFIA strips at different concentrations of C-reactive protein. Reprinted with  
50 permission from Shen *et al.*<sup>505</sup> Copyright 2012 Royal Society of Chemistry.  
51  
52  
53  
54  
55  
56  
57  
58  
59  
60

1  
2  
3 Interleukin 6 (IL-6), a proinflammatory and anti-inflammatory cytokine, is often used as a  
4 biomarker for cancer or other diseases. Xiong *et al.* reported a facile microwave-assisted method  
5 of making water-dispersible CuInS<sub>2</sub>/ZnS QDs with glutathione as the capping agent for IL-6  
6 detection.<sup>166</sup> Their CuInS<sub>2</sub>/ZnS QDs had an average size of 3.3 nm, long PL lifetime, and  
7 emission wavelengths tunable from the visible to the near-IR by manipulating the initial  
8 precursor ratio. The fabricated CuInS<sub>2</sub>/ZnS QDs were conjugated with a secondary antibody of  
9 IL-6 and applied as optical labels in a fluoroimmunoassay. The primary antibody of IL-6 was  
10 immobilized on the object slide chip, which was treated with IL-6 samples then incubated with  
11 the functionalized QDs. Sandwiched antibody-antigen-antibody complexes formed in the  
12 presence of IL-6 and generated fluorescence on the chip. The results suggested that these QDs  
13 can be used as point-of-care diagnostic tools for detecting biomarkers of cancer and other  
14 diseases.

15  
16  
17  
18  
19  
20  
21  
22  
23  
24  
25  
26  
27  
28  
29  
30  
31  
32 Su's research group has been very active in using CuInS<sub>2</sub> QDs for various biosensing  
33 applications. For example, Liu *et al.* demonstrated the use of a sensitive fluorescence turn-on  
34 assay for detecting biothiols, histidine and threonine.<sup>506</sup> Water-dispersible CuInS<sub>2</sub> QDs  
35 functionalized with mercaptopropionic acid were modified with tyrosine. The PL of tyrosine-  
36 CuInS<sub>2</sub> QDs was found to decrease in the presence of Cu<sup>2+</sup> ions due to the coordination effect of  
37 phenolic hydroxyls of the tyrosine molecules. Afterwards, the addition of glutathione, L-cysteine,  
38 histidine or threonine molecules was found to switch on the PL of the T-CuInS<sub>2</sub> QD-Cu<sup>2+</sup>  
39 system, because these molecules possessed strong affinity towards Cu<sup>2+</sup> ions. The proposed  
40 method was used for sensing L-cysteine, glutathione, threonine, and histidine in human serum  
41 samples with high sensitivity.

1  
2  
3 Correlating protein levels with disease states is important for disease detection and diagnosis.  
4  
5 Tan *et al.* created phosphorescent molecularly-imprinted polymers for sensing target proteins.<sup>507</sup>  
6  
7 They employed an aqueous surface graft imprinting process using methacrylic acid and  
8 acrylamide as functional monomers, vinyl-modified Mn-doped ZnS QDs as supports, and bovine  
9 hemoglobin as the template. The QDs provided signal amplification and an optical readout. The  
10 molecularly imprinted polymer shell provided analyte selectivity and protected the QDs from  
11 non-target molecules, thereby minimizing false signals. The dopant-related emission gradually  
12 decreased with increasing concentration of bovine hemoglobin. The authors demonstrated a good  
13 linear relationship for detection of bovine hemoglobin over a concentration range from  $1.0 \times 10^{-7}$   
14 to  $5.0 \times 10^{-6}$  mol L<sup>-1</sup> with recoveries of 96.7 to 103.8% and 92.6 to 94.2% for urine and serum  
15 samples, respectively. The long phosphorescence lifetime of the molecularly imprinted polymer-  
16 QDs prevents interference due to scattering and autofluorescence of the biomatrix. Subsequently,  
17 the same group reported a method for generating hybrid organic-inorganic imprinted Mn-doped  
18 ZnS QDs for sensing of bovine hemoglobin.<sup>508</sup> Using molecularly imprinted polymer-QD  
19 composites as a PL sensing material, the authors were able to detect relatively low  
20 concentrations of bovine hemoglobin with excellent selectivity by tracking the emission intensity  
21 changes of QDs implanted in the imprinted polymers.  
22  
23  
24  
25  
26  
27  
28  
29  
30  
31  
32  
33  
34  
35  
36  
37  
38  
39  
40  
41  
42

43 Mn-doped ZnS QDs exhibited enhanced light scattering signals and phosphorescence upon  
44 aggregation. Based on this phenomenon, Yan and Wang developed a phosphorescence turn-on  
45 assay for heparin using target-induced aggregation of PEI-functionalized Mn-doped ZnS QDs.<sup>509</sup>  
46 The functionalized QDs possessed highly positive surface charge due to the abundant amino  
47 groups on PEI. Aggregation of the PEI-capped QDs upon addition of negatively-charged heparin  
48 increased their phosphorescence intensity (**Figure 61**). Varying the PEI loading provided linear  
49  
50  
51  
52  
53  
54  
55  
56  
57  
58  
59  
60

detection over different concentration ranges relevant to post-operative care, long-term therapy, and cardiovascular surgery. This method can also be used to determine the concentration of heparin in a diluted blood serum sample.

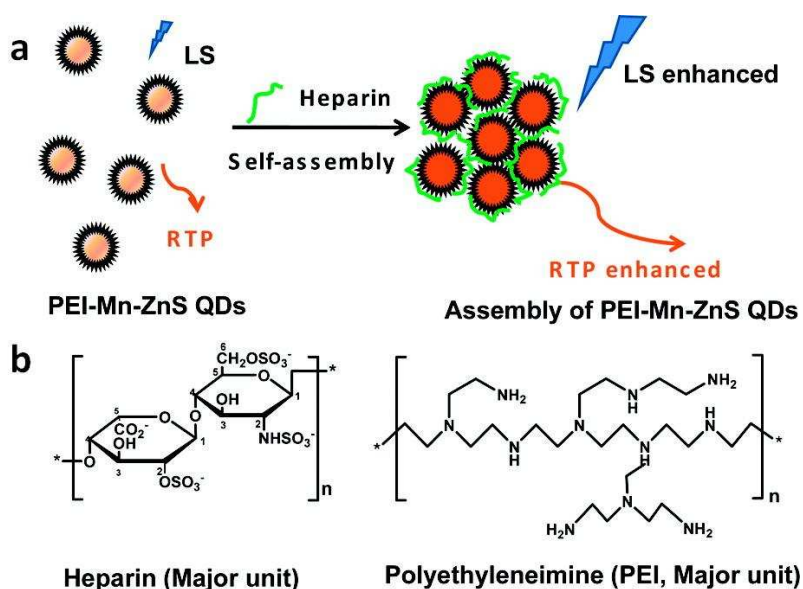


**Figure 61.** (a) Schematic of phosphorescence turn-on assay. (b) Chemical structures of heparin and PEI. Reprinted with permission from Yan *et al.*<sup>509</sup> Copyright 2011 American Chemical Society.

Manganese-doped ZnS QDs have also been applied for probing the overexpression of epidermal growth factor receptor (EGFR) in clinical tumor tissues.<sup>442</sup> The cysteine-capped QDs were bioconjugated to streptavidin and then attached to biotinylated EGFR antibodies using the streptavidin-biotin interaction. They were used for specific staining of EGF receptors on EGFR(+ve) A431 cells in a co-culture with EGFR(-ve) NIH3T3 cells. In addition, the antibody conjugated QD formulation was used to identify EGFR over-expressing cells from clinical tumor tissues with specificity of 86% and accuracy of 88%, compared to immunohistochemistry techniques. Tissues stained with EGFR-modified ZnS:Mn nanocrystals displayed good

1  
2  
3 luminescence even after 15 months of storage, suggesting their usefulness for long term  
4 immunofluorescent labeling and sensing of antigens on *ex vivo* samples.  
5  
6  
7  
8  
9

## 10 **6.7. Infectious Diseases**

11  
12  
13 Despite enormous improvements in sanitation, vaccines, antibiotics, and antiviral drugs,  
14 infectious diseases remain a major source of illness and death worldwide. A large fraction of  
15 infection-related mortalities occurs in developing countries, often due to poor hygiene conditions,  
16 inadequate healthcare facilities, drug costs, and co-morbidities that can impair the immune  
17 system, due to malnutrition and/or immune-deficiency-causing infections such as HIV, MERS  
18 and Ebola. The list of pathogens and the diseases caused by them is diverse and provides the  
19 basis for an entire sub-discipline of microbiology. It is also a growing list due to the evolution of  
20 new strains of pathogens. QD technology is poised to play a role in the detection, prevention, and  
21 multidrug treatment of infectious diseases,<sup>510,511</sup> as described in this section.  
22  
23  
24  
25  
26  
27  
28  
29  
30  
31  
32  
33

34 Influenza is a contagious respiratory disease that causes significant morbidity and mortality.  
35 A crucial tool for fighting influenza pandemics is timely and speedy diagnosis. Krejcová *et al.*  
36 reported QD-oligonucleotide complexes using influenza-derived oligonucleotides.<sup>443</sup>  
37 Electrochemical methods can detect the target oligonucleotide as well as metallic components of  
38 the QDs. The authors studied the electrochemical behavior of Zn(II), Pb(II), Cu(II) and Cd(II)  
39 ions by differential pulse anodic stripping voltammetry and they compared the results to the  
40 behavior of ZnS, PbS, CuS and CdS QDs. The authors analyzed the complexes between  
41 oligonucleotides (ODNs) derived from influenza and the fabricated QDs by differential pulse  
42 anodic stripping voltammetry and square wave voltammetry to detect peaks of nucleic bases. The  
43 authors showed that voltammetry could be used to discriminate QD-oligonucleotide complexes.  
44  
45  
46  
47  
48  
49  
50  
51  
52  
53  
54  
55  
56  
57  
58  
59  
60

1  
2  
3 Later, Fialova *et al.* developed an effective method for sensing influenza protein hemagglutinin  
4 (HA) by labeling them with CuS, PbS or CdS QDs.<sup>512</sup> The influenza protein was identified by  
5  
6 analyzing the concentration of Cu(II), Pb(II) or Cd(II) ions contained in the QDs. The  
7  
8 streptavidin-coated particles were surface-modified with biotinylated glycan for sensing  
9  
10 influenza proteins. The functionalized QDs served as electrochemical signal amplification tags  
11  
12 for detection of the influenza virus at concentrations of the H5N1 proteins as low as 0.0444  
13  
14  $\mu\text{g}/\mu\text{L}$ . Although CdS QDs showed the best sensing results due to a strong interaction between  
15  
16 the cadmium ions and protein molecules, the toxicity concern associated with these QDs still  
17  
18 limits their potential for the clinical applications. The cadmium-free QDs could, after proper  
19  
20 surface functionalization and size-optimization, be alternative candidates for the next generation  
21  
22 of electrochemical nanotags.  
23  
24  
25  
26  
27  
28

29  
30 Antibacterial agents are important for microbiology due to emerging antibiotic resistance.  
31  
32 Ristic *et al.* reported the use of graphene QDs prepared by an electrochemical method to generate  
33  
34 reactive oxygen species (ROS) under photoexcitation (470 nm, 1 W) and kill two strains of  
35  
36 pathogenic bacteria, *Escherichia coli* and methicillin-resistant *Staphylococcus aureus*.<sup>445</sup>  
37  
38 Bacterial killing was observed through the reduction in number of bacterial colonies in a  
39  
40 standard plate count method. In addition, increased propidium iodide uptake indicated cell  
41  
42 membrane damage, and morphological defects were detected using atomic force microscopy.  
43  
44 The induction of oxidative stress in bacteria treated with photoexcited QDs was confirmed by  
45  
46 staining with redox-sensitive fluorochrome dihydrorhodamine 123 (**Figure 62**). Exposure to  
47  
48 QDs or light alone did not generate ROS or decrease the viability of bacteria.  
49  
50  
51  
52  
53  
54  
55  
56  
57  
58  
59  
60

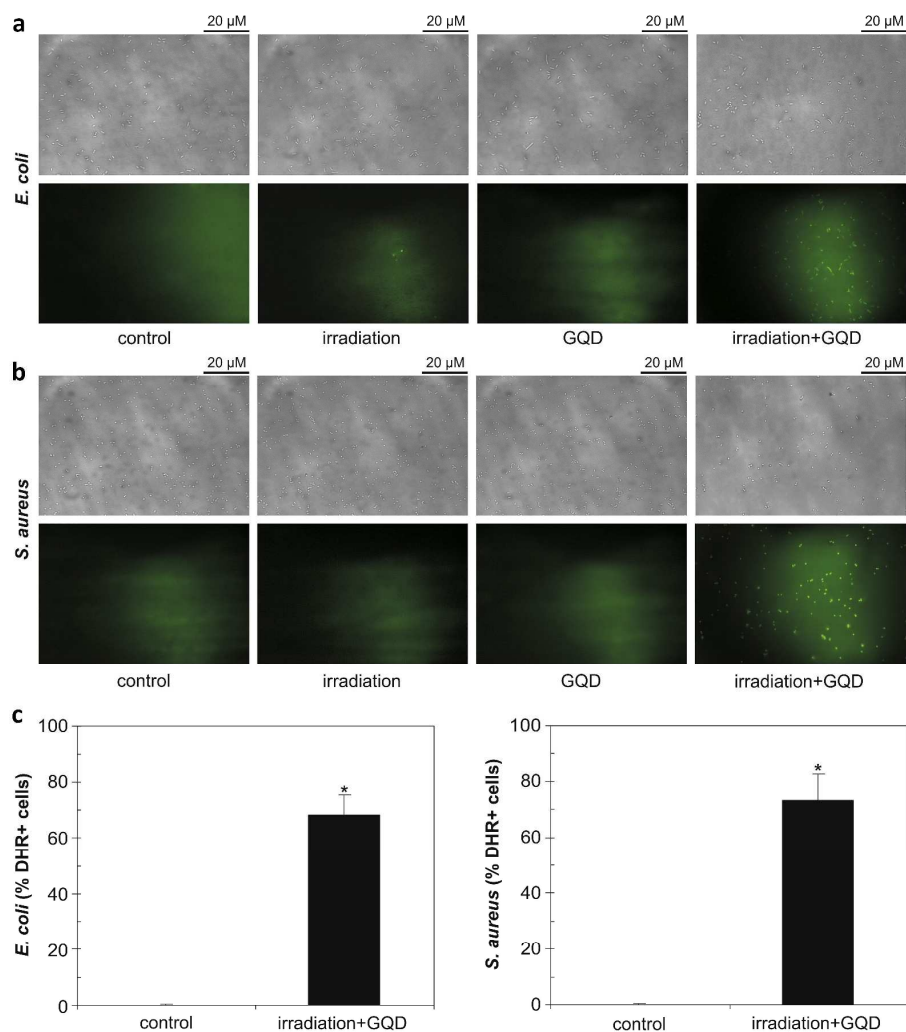


**Figure 62.** Photoexcited GQDs induce oxidative stress in bacterial cells. Suspensions of *E. coli* (a) and *S. aureus* (b) were treated under various conditions. After staining with dihydrorhodamine 123, bacterial cells were visualized. (c) Counts of ROS-producing bacterial cells are shown as mean  $\pm$  SD values (\* $p < 0.05$ ). Reprinted with permission from Ristic *et al.*<sup>445</sup> Copyright 2014 Elsevier.

Pathogenic *E. coli* infections account for thousands of hospitalizations in the United States every year. Early detection of *E. coli* infections could reduce their impact. Baruah *et al.* used chitosan-functionalized Mn-doped ZnS QDs.<sup>446</sup> with PL emission at 590 nm for fluorescent

1  
2  
3 labeling and long term imaging of *E. coli* cells through a fluorescence *in situ* hybridization (FISH)  
4 method. The positively charged chitosan allows the QDs to bind to the carboxyl and phosphoryl  
5 groups on the *E. coli* cell walls via electrostatic interaction. Translocation studies of the cells  
6 incubated with QDs showed that the QDs entered the cells. The fluorescence of the QDs was  
7 maintained well at the translocation temperature of 65 degrees. The QDs were found to be  
8 biocompatible, and no harmful effects on the stained cells were observed.  
9

10  
11 The immune system safeguards an organism by discriminating and removing foreign  
12 substances from the body. Gu *et al.* reported the preparation of NPs for triggering the immune  
13 system and thereby improving the intended activation of antigen presenting cells.<sup>447</sup> Luminescent  
14 porous silicon NPs, each functionalized with multiple copies of an agonistic antibody (FGK45)  
15 to the APC receptor CD40, significantly promoted the activation of B cells. The cellular  
16 responses to the silicon NP-based stimulators were 30 to 40 fold higher than that of free FGK45.  
17 The PL signals of silicon NPs were used to track the biodistribution of NPs in the antigen  
18 presenting cells.  
19

20  
21 The highly pathogenic H5N1 avian influenza virus has caused outbreaks in birds in more  
22 than 60 countries since its discovery in China in 1996. The main challenge in treating H5N1 is to  
23 create effective antiviral drugs. Krejcova *et al.* engineered a magnetic electrochemical bar code  
24 array for detecting single point mutations (mismatches in up to four nucleotides) in the H5N1  
25 neuraminidase gene, which aids in overcoming the drug resistance induced by point mutations.<sup>444</sup>  
26 Paramagnetic Dynabeads® coated with oligo (dT)25 were used to isolate complementary H5N1  
27 chains. Followed by the magnetic isolation, oligonucleotide chains of 12 (+5 adenine) or 28 (+5  
28 adenine) bp were linked to ZnS or PbS QDs for electrochemical detection of the target gene. Cd-  
29 free QDs served as signal amplification tags. No signals were collected for the oligonucleotides  
30  
31  
32  
33  
34  
35  
36  
37  
38  
39  
40  
41  
42  
43  
44  
45  
46  
47  
48  
49  
50  
51  
52  
53  
54  
55  
56  
57  
58  
59  
60

1  
2  
3 without QD labeling. Each probe was hybridized for targeting a specific molecule, with more  
4  
5 than 60% efficiency. The measured signals mapped out the mutations present in the sequence.  
6  
7 The biosensor could detect sub-nanogram quantities of the target nucleic acids, demonstrating  
8  
9 potential for future development of an influenza nanosensor based on Cd-free QDs.  
10  
11  
12  
13  
14  
15  
16  
17  
18  
19  
20  
21  
22  
23  
24  
25  
26  
27  
28  
29  
30  
31  
32  
33  
34  
35  
36  
37  
38  
39  
40  
41  
42  
43  
44  
45  
46  
47  
48  
49  
50  
51  
52  
53  
54  
55  
56  
57  
58  
59  
60

## 7.0. Pharmacokinetics and Biodistribution of Cadmium-Free Quantum Dots

Pharmacokinetics addresses the time-dependent biodistribution of drugs or other entities from the vascular space into tissues and organs, and their clearance through metabolism and excretion.<sup>3</sup> In general, mathematical models are used to describe the time course of drug absorption into the plasma after systemic delivery, drug distribution, and drug elimination from the body by metabolism and excretion.<sup>3,513,514</sup> Thus, pharmacokinetics addresses the relationship between (i) the drug input defined by dosage form, dose, frequency, and administration route and (ii) the drug concentration in the plasma and other body tissues over time.

Serial collection and analysis of blood samples over time is required for pharmacokinetics studies. Radioactive labeling has often been used to provide sensitive detection of drugs in blood.<sup>515</sup> Some drugs, such as photosensitizers for photodynamic therapy, are fluorescent and can be detected optically without additional labeling.<sup>516,517</sup> Labeling with QDs can allow PL-based detection of non-fluorescent drugs, especially when the PL is in the near-IR window of biological optical transparency. The use of NPs for drug delivery can dramatically influence drug fate, often resulting in highly favorable pharmacokinetics. The size and surface characteristics of NPs have a major influence on the performance of NPs as drug carriers. Encapsulation of hydrophobic drugs in a NP formulation can provide improved absorption and systemic availability. In addition, liver metabolism is significantly reduced, thus leading to prolonged circulation and increased half-life. Functionalization of QDs with polyethylene glycol (PEG) also prolongs circulation of NPs by reducing hydrophobic and electrostatic interactions with proteins and cells.<sup>518,519</sup> Other uncharged hydrophilic molecules can provide a similar effect, but PEG is

1  
2  
3 by far the most popular. The surface charge of NPs plays an important role in avoiding RES  
4 uptake, minimizing opsonization, and prolonging circulation time.<sup>520</sup>  
5  
6

7  
8 Biodegradation and excretion are key considerations for the *in vivo* use of any nanomaterial.  
9  
10 The maximum size for renal clearance is around 5.5 nm.<sup>521,522</sup> Thus, NPs greater than ~5.5 nm in  
11 hydrodynamic diameter show dramatically reduced renal excretion rates. While this extends their  
12 circulation times, it also usually leads to capture of NPs by the RES. Thus, nanostructures that  
13 break down into components small enough to be cleared renally are often desirable. Real-time *in*  
14 *vivo* monitoring of QD PL allows detailed investigation of their biodistribution, degradation, and  
15 excretion. For example, our group has optically tracked near-IR emitting QDs delivered through  
16 the tail vein of a mouse.<sup>523</sup>  
17  
18  
19  
20  
21  
22  
23  
24  
25  
26

27 Biodistribution studies aim to measure the presence of NPs in tissues throughout the body.  
28 They provide very useful information on localization of a drug or NP at a targeted disease site as  
29 well as in other organs and tissues. Various factors affect NP biodistribution including plasma  
30 protein binding, hydrophobicity, and intentional functionalization of a nanoformulation to  
31 influence cellular uptake and efflux.<sup>524,525</sup> A detailed study of the biodistribution of a NP  
32 formulation can allow one to determine its potential for success in a targeted therapy strategy.  
33  
34 Biodistribution profiles are most often obtained using a radioactively or fluorescently labeled  
35 nanoformulation that is injected into a small animal model (e.g. mouse, rat, or rabbit).<sup>526,527</sup> The  
36 treated animal is then sacrificed and the organs are removed and analyzed. Nanoparticle-based  
37 delivery can produce favorable biodistribution profiles through both active and passive targeting  
38 approaches. Nanoparticles that act as contrast agents for multimodal imaging can allow one to  
39 monitor biodistribution in live animals, reducing the number of animals required and improving  
40 the data by reducing animal-to-animal variation between time points.<sup>528,529</sup> This section describes  
41  
42  
43  
44  
45  
46  
47  
48  
49  
50  
51  
52  
53  
54  
55  
56  
57  
58  
59  
60

1  
2  
3 recent studies of pharmacokinetics and biodistribution of Cd-free QDs (**Table 4**) and discusses  
4  
5 how functionalized QDs provide benefits in targeted delivery and therapeutic efficiency of  
6  
7 payloads, while minimizing adverse side effects.  
8  
9  
10  
11  
12  
13  
14  
15  
16  
17  
18  
19  
20  
21  
22  
23  
24  
25  
26  
27  
28  
29  
30  
31  
32  
33  
34  
35  
36  
37  
38  
39  
40  
41  
42  
43  
44  
45  
46  
47  
48  
49  
50  
51  
52  
53  
54  
55  
56  
57  
58  
59  
60

Table 4. Pharmacokinetics and Biodistribution of Cd-free QDs

| QD type                      | TEM Size (nm) | Functional groups                       | Targeting molecules | Injection              | Methods  | Model  | Major accumulation          | Post-injection | Ref |
|------------------------------|---------------|---|---------------------|------------------------|--|--|-----------------------------|----------------|-----|
| <b>Ag<sub>2</sub>S</b>       | 5.4           | DHLA and 6PEG                           | -                   | tail-vein injection    | PL imaging, ICP-MS   | BALB/c mouse bearing 4T1 tumor                             | tumor, liver, spleen        | 72 h           | 21  |
| <b>Ag<sub>2</sub>S</b>       | 5.4           | DHLA and 6PEG                           | -                   | tail-vein injection    | PL imaging, ICP-MS   | BALB/c mouse   | liver, spleen               | 7 days         | 21  |
| <b>Ag<sub>2</sub>S</b>       | 5.4           | 6PEG and COOH                           | -                   | tail-vein injection    | blood biochemistry, hematological analysis and histological examinations | BALB/c mouse   | liver, spleen               | 60 days        | 289 |
| <b>Ag<sub>2</sub>Se</b>      | 21.5(HD)      | C18-PMH-PEG                             | -                   | tail-vein injection    | PL imaging   | nude mouse   | vasculature                 | a few min      | 139 |
| <b>CuInS<sub>2</sub>/ZnS</b> | ~20           | PEG2000-COOH and PEG2000 lipid micelles | -                   | subcutaneous injection | PL imaging, ICP-MS, RT-PCR   | BALB/c OlaAnN mouse bearing murine metastatic breast tumor | lymph nodes, liver, spleen  | 3 months       | 391 |
| <b>CuInS<sub>2</sub>/ZnS</b> | ~7            | dihydrolipoic acids                     | -                   | tail-vein injection    | PL reflectance imaging   | nude mouse   | lung, spleen, liver         | 24 h           | 163 |
| <b>Cu-In-Se/ZnS</b>          | 2~5           | DHLA-Sulfobetaine                       | -                   | subcutaneous injection | PL imaging, ICP-MS   | BALB/c OlaHsd mouse  | lymph nodes                 | 4 h            | 136 |
| <b>Zn-Cu-In-S/ZnS</b>        | 5.6           | MPH and PEG-400                         | -                   | tail-vein injection    | PL imaging   | nude mouse   | liver                       | 6 h            | 284 |
| <b>InAs/ZnS</b>              | 3.2           | DHLA and DHLA-PEGn                      | -                   | intravenous injection  | PL imaging   | Sprague-Dawley rat   | depending on the No. of PEG | 4 h            | 530 |



### 7.1 Biodistribution of Non-targeted Cadmium-Free Quantum Dots

Ag<sub>2</sub>S QDs are promising near-IR II (1000-1400 nm) emitters for *in vivo* imaging. Hong *et al.* prepared six-arm branched PEG-functionalized Ag<sub>2</sub>S QDs (~5.4 nm diameter) with 1200 nm PL for *in vivo* imaging<sup>21</sup> and studied their biodistribution. NIR-II emission was monitored to analyze the biodistribution of the QDs over 24 h post-injection (**Figure 63a–e**). From 30 min to 24 h, PL intensity steadily increased at the tumor site and decreased in the skin and other organs, due to the EPR effect. As a result, the tumor-to-background (TBR) ratio gradually increased to a value above the Rose criterion (TBR>5, **Figure 63g**). The organs were harvested 72 h after injection and inductively coupled plasma-mass spectrometry (ICP-MS) was used to quantify QD content in organs (**Figure 63i**). The QDs mainly accumulated in the spleen and liver. Tumor uptake of PEG modified-Ag<sub>2</sub>S QDs formulation was 10% ID/g, which resulted from the long circulation half-life of 4 h. Excretion of the QDs was mainly through biliary transport and not through renal clearance.

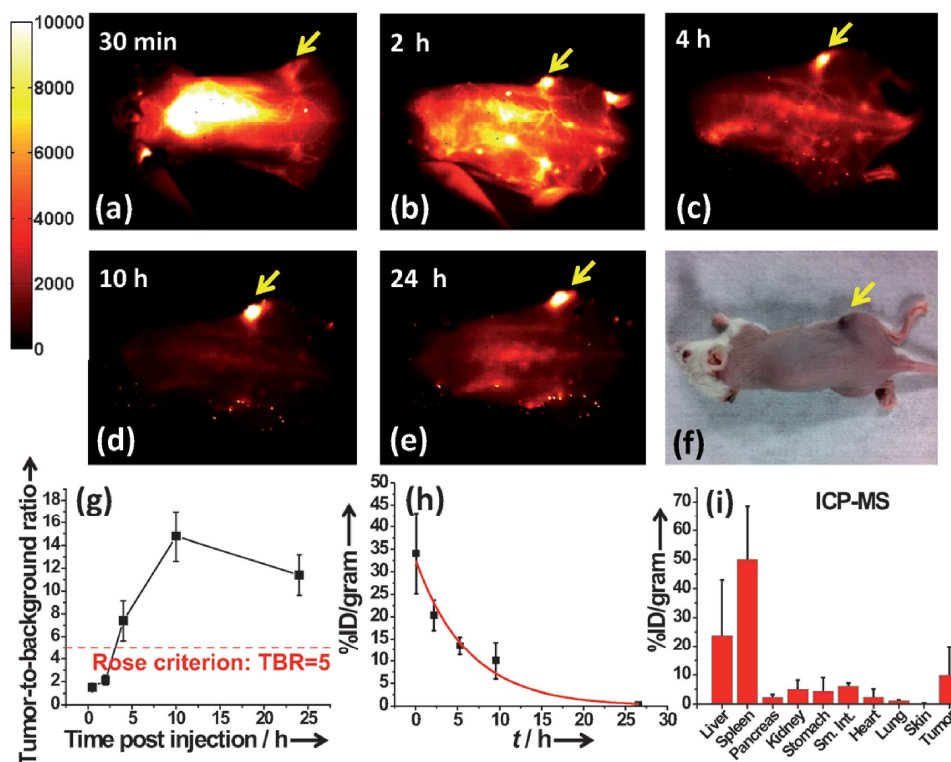


**Figure 63.** PL images of a 4T1 tumor-bearing mouse injected with 6PEG-Ag<sub>2</sub>S QDs. (a–e) Time-lapse images of the mouse. f) A white-light optical image of the mouse at 24 h. g) The tumor-to-background ratio plotted as a function of injection time. h) A representative plot of the % ID/gram of the 6PEG-Ag<sub>2</sub>S QDs in the blood versus time after injection. i) Quantitative biodistribution of 6PEG-Ag<sub>2</sub>S QDs in various organs and the tumor 72 h after injection, based on ICP-MS analysis. Reprinted with permission from Hong *et al.*<sup>21</sup> Copyright 2012 John Wiley and Sons.

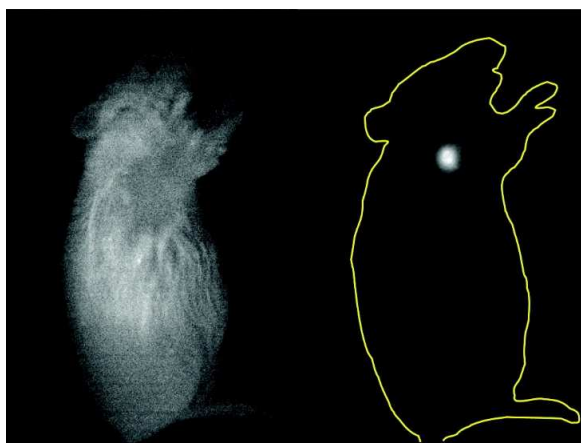
The long-term biodistribution of PEG-functionalized Ag<sub>2</sub>S QDs in mice was also investigated recently.<sup>289</sup> Randomly-selected mice were sacrificed at fixed time points over a

1  
2  
3 period of 60 days post-injection, and the retention of Ag<sub>2</sub>S in organs and tissues was analyzed by  
4 ICP-MS. After 1 day, QDs were widely distributed among many organs and tissues. During the  
5  
6 1st week, the concentrations of the QDs gradually decreased in most organs and tissues but  
7  
8 increased in RES organs. Over a period of 2 months, QDs were slowly removed from body. The  
9  
10 main clearance pathway was found to be fecal excretion. After 60 days, most of the QDs were  
11  
12 cleared from the body and the rest of the QDs mainly remained in the liver, spleen, bone, and  
13  
14 intestine.  
15  
16  
17  
18  
19

20 In another study, the biodistribution of CuInS<sub>2</sub>/ZnS QDs was investigated in mice bearing a  
21  
22 metastatic breast cancer model.<sup>391</sup> The mice were subcutaneously injected with QDs in the right  
23  
24 anterior paw. QD PL was detected in the sentinel lymph node a few minutes after injection and  
25  
26 reached a maximum in intensity after 8 h. Indium content of organs and tissues was quantified  
27  
28 using ICP-MS. The right lymph nodes and injection site had similar In concentrations 1 h after  
29  
30 injection (40 mg In/g tissue), while In was not detected in the liver and spleen. After 4 h, the In  
31  
32 concentration decreased at the injection site (14.16 mg In/g tissue), while the In concentration in  
33  
34 the right lymph nodes considerably increased, and In was present in both the liver (2.46 mg In/g  
35  
36 tissue) and spleen (3.36 mg In/g tissue). The clearance of QDs was determined by measuring In  
37  
38 content of collected urine and feces for 4 days post-injection. The authors found that 3.5% of the  
39  
40 injected In was excreted in feces and only a trace quantity was detected in the urine within the  
41  
42 first 4 days. In this study, the QD PL and ICP-MS measurements complement one another, with  
43  
44 the PL imaging allowing real-time biodistribution studies in the live animal, while the *ex vivo*  
45  
46  
47  
48  
49  
50  
51  
52  
53

1  
2  
3 ICP-MS measurements provide more precise quantification and allow detection of any In  
4 released by QD degradation, in addition to the In present in intact QDs.  
5  
6

7  
8 Migration of photoluminescent Cu-In-Se/ZnS core/shell QDs from the regional lymph nodes  
9 has also been studied recently.<sup>136</sup> Aqueous Cu-In-Se/ZnS QDs were prepared by using  
10 hydrophilic ligands with a dithiol anchor group and a compact sulfobetaine zwitterionic group.  
11 QDs with 800 nm emission were subcutaneously injected into the right anterior paw of mice.  
12 Their near-IR PL was detected in the regional lymph node a few minutes after injection and  
13 persisted for several hours after injection (**Figure 64**). The QD accumulation in the right axillary  
14 lymph node after 4 h corresponded to 1.42% of the injected dose, as measured by ICP-MS  
15 analysis.  
16  
17  
18  
19  
20  
21  
22  
23  
24  
25  
26



43 **Figure 64.** *In vivo* PL imaging of a mouse before (left) and 4 h after (right) subcutaneous  
44 injection of QDs. The injection point is hidden to improve the visualization of the lymph node.  
45  
46

47 Reprinted with permission from Cassette *et al.*<sup>136</sup> Copyright 2010 American Chemical Society.  
48  
49

1  
2  
3 Guo *et al.* recently characterized the biodistribution of Zn–Cu–In–S/ZnS (ZCIS/ZnS) QDs  
4 with PL emission at 690 nm in 6-week-old female nude mice.<sup>284</sup> The QDs were intravenously  
5 injected into mice that were then monitored for 6 h. The PL of the QDs was observed in the liver  
6 and lung. At 6 h post-injection, major organs were harvested to evaluate the QD biodistribution.  
7 Strong PL was observed in the liver, indicating accumulation of the QDs in the RES. The authors  
8 suggest that the first-pass hepatic removal was due to the size of the QDs (~49 nm). The QDs  
9 were slowly removed from the liver through hepatobiliary processing, as shown by the gradual  
10 decrease of PL signal from the liver.  
11  
12

13 A 2009 study observed organ- and tissue-selective distribution and excretion routes of NIR  
14 InAs/ZnS QDs based upon the overall size of functionalized QDs with a fixed inorganic core  
15 size.<sup>530</sup> The QDs were not functionalized with any targeting ligands. The QD cores were ~3.2 nm  
16 in diameter. Dihydrolipoic acid (DHLA) and DHLA-PEG<sub>n</sub> (where  $n = 2, 3, 4, 8, 14, \text{ or } 22$ ) were  
17 used as surface coating agents to prepare water-dispersible NIR QDs of varied size. The QDs  
18 dispersed in PBS at pH 7.4 had hydrodynamic diameters ranging from 4.5 to 16 nm as the  
19 number of PEG repeating units increased from 0 to 22. The QDs were intravenously injected into  
20 Sprague-Dawley rats, and their distribution and excretion were analyzed (**Figure 65**). The QDs  
21 coated with DHLA PEG2 were located mainly in the liver. Those coated with DHLA-PEG3  
22 accumulated in the kidneys and bladder. QDs coated with DHLA-PEG4 were more rapidly  
23 excreted through the liver and kidneys. QDs coated with DHLA-PEG8 were observed in the  
24 pancreas. QDs coated with DHLA-PEG14 were removed quickly through the liver to the  
25 intestine. QDs with DHLA PEG22 were found mainly in the vasculature at 4 h post-injection. To  
26  
27  
28  
29  
30  
31  
32  
33  
34  
35  
36  
37  
38  
39  
40  
41  
42  
43  
44  
45  
46  
47  
48  
49  
50  
51  
52

1  
2  
3  
4  
5  
6  
7  
8  
9  
10  
11  
12  
13  
14  
15  
16  
17  
18  
19  
20  
21  
22  
23  
24  
25  
26  
27  
28  
29  
30  
31  
32  
33  
34  
35  
36  
37  
38  
39  
40  
41  
42  
43  
44  
45  
46  
47  
48  
49  
50  
51  
52  
53  
54  
55  
56  
57  
58  
59  
60

verify that the QDs were indeed removed through renal clearance, the kidney was harvested at 4 h post-injection, and cross-sectional images were taken and analyzed. QDs with DHLA-PEG4, with a diameter of 5.6 nm, could pass through the glomerular filters, and PL of QDs could be found in the medulla and cortex. QDs coated with DHLA-PEG2 were not found in the kidney, but mainly accumulated in the liver.

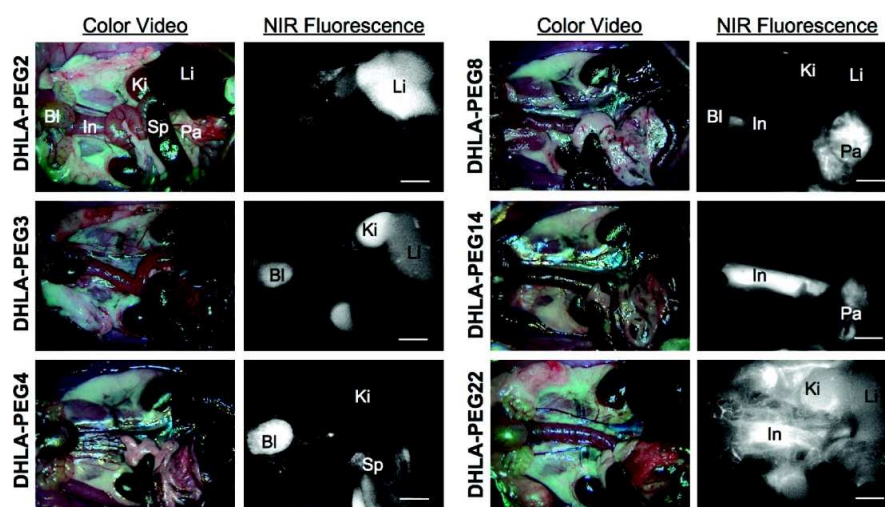


**Figure 65.** PL imaging of InAs(ZnS) QDs in Sprague–Dawley rats 4 h postinjection. The QDs were coated with DHLA-PEG2, DHLA-PEG3, DHLA-PEG4, DHLA-PEG8, DHLA-PEG14, and DHLA-PEG22. (Ki, kidneys; Bl, bladder; Li, liver; Pa, pancreas; Sp, spleen; and In, intestine). Scale bar = 500  $\mu\text{m}$ . Reprinted with permission from Choi *et al.*<sup>530</sup> Copyright 2009 American Chemical Society.

Dextran-coated Si QDs with a hydrodynamic diameter of 15.1 nm were attached to a macrocyclic ligand- $^{64}\text{Cu}^{2+}$  complex for multimodal imaging of clearance and distribution patterns.<sup>96</sup> The QD biodistribution in mice was determined by *in vivo* positron emission

1  
2  
3 tomography (PET) and *ex vivo* gamma counting. A short burst of fast clearance was followed by  
4  
5 a long slow clearance of QDs from the blood. Two minutes after tail-vein injection, 95.7%ID/g  
6  
7 of QDs had been removed from the blood. After 10 min, only 2.5%ID/g remained in the blood.  
8  
9 Then, the clearance slowed and 1.5%ID/g remained in the blood after 120 min. The fast  
10  
11 clearance of Si QDs was similar to that of PEG-coated CdSe QDs (12 or 21 nm). Five min and 1  
12  
13 h post-injection, the QDs mainly accumulated in the urinary bladder and the liver. After 4 h, 24 h,  
14  
15 and 48 h, the QDs were mainly in the liver. A weak PL signal was still detected in the bladder 4  
16  
17 h post-injection. Based on *ex vivo* gamma counting analysis of major organs, the liver took up  
18  
19 about 12.4% ID/g, and the kidneys took up 3.0-4.0% ID/g of the QDs. Other organs, such as  
20  
21 heart, intestine, spleen and lung also displayed accumulation of QDs. A small amount of QDs  
22  
23 were located in the bladder and brain. The authors explained that when the QDs were dispersed  
24  
25 into the blood, they were rapidly opsonized, which accelerated the phagocytosis process.  
26  
27 Ultrasmall NPs with size less than 7 nm were rapidly removed through renal filtration and larger  
28  
29 particles were captured by the RES system.  
30  
31

32  
33  
34  
35  
36 Li *et al.* studied the biodistribution of CuInS<sub>2</sub>/ZnS QDs in healthy nude mice.<sup>163</sup> The  
37  
38 core/shell QDs had PL tunable from 550 to 815 nm with a maximum PL QY of 60%. These  
39  
40 QD's PL lifetimes of hundreds of nanoseconds allowed use of time-resolved imaging to remove  
41  
42 background autofluorescence. The QDs were transferred to the aqueous phase using DHLA. The  
43  
44 QDs were intravenously injected into nude mice and the distribution of the QDs was monitored  
45  
46 for 24 hours using a fluorescence reflectance imaging system (**Figure 66**). 15 min post-injection,  
47  
48 the QDs accumulated in the spleen, liver and lung. The liver and spleen are RES organs and  
49  
50  
51  
52

known for removing foreign particles from the body, especially when the particles are covered with circulating plasma opsonins. The results suggest that the negatively charged DHLA-coated QDs favored opsonin binding and aggregation *in vivo*, promoting RES uptake.

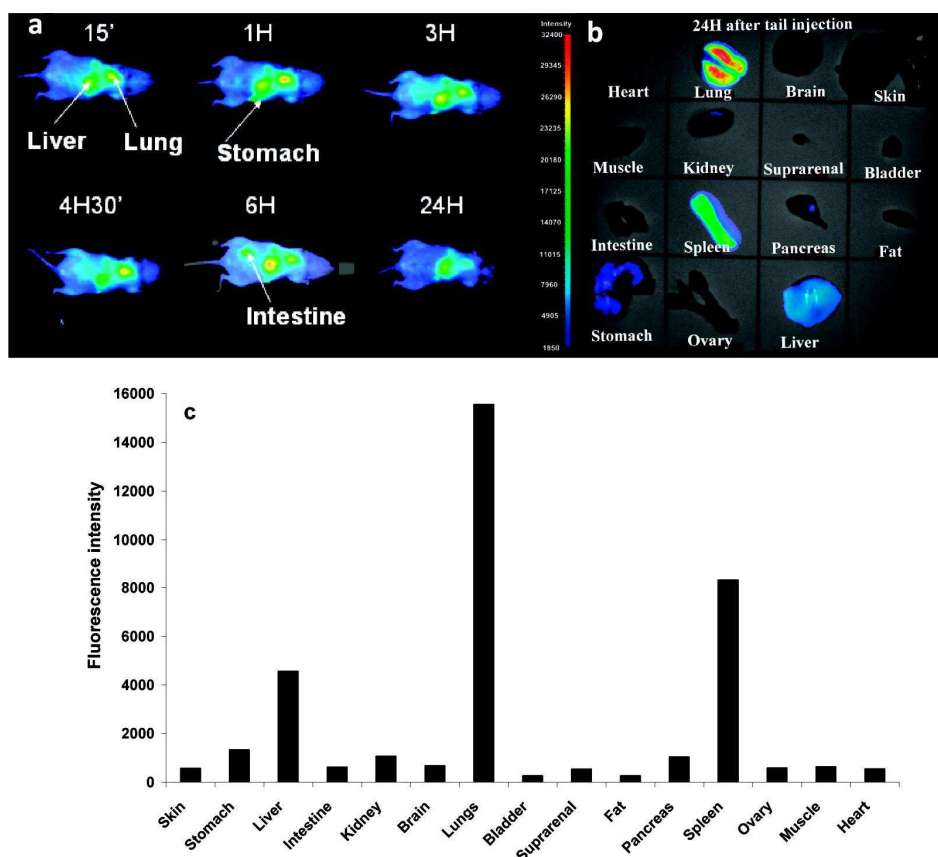


**Figure 66.** The biodistribution of CuInS<sub>2</sub>/ZnS QDs in healthy nude mice. (a) PL images showing the temporal evolution of the biodistribution of QDs injected into the tail of a healthy nude mouse. (b) PL images of the different parts of the mouse after dissection. (c) Biodistribution and tissue PL of the QDs, 24 h after tail vein administration. Reprinted with permission from Li *et al.*<sup>163</sup> Copyright 2009 American Chemical Society.

## 7.2 Biodistribution of Targeted Cadmium-Free Quantum Dots

Ag<sub>2</sub>S QDs bioconjugated with antiVEGF were employed for *in vivo* cancer targeted imaging.<sup>291</sup> In this study, 0.02 mmol of the bioconjugated QDs in PBS was intravenously injected into U87MG tumor-bearing mice with volume of 500  $\mu$ L per mouse. PL from antiVEGF-Ag<sub>2</sub>S QDs was detected in the tumors 0.5 h after injection and remained detectable 24 h after injection. In contrast, the antiVEGF-Ag<sub>2</sub>S QDs were mostly cleared from the body of normal mice 12 hours after injection, and PL signals disappeared completely after 24 hours. Thus, the excretion rate of antiVEGF-Ag<sub>2</sub>S QDs in the tumor-bearing mice was much slower than in healthy mice. This may be due to the high affinity of the antiVEGF to tumors, which lead to retention of the antiVEGF-Ag<sub>2</sub>S QDs at the tumor site.

The pharmacokinetics and biodistribution of hydrophobic luminescent Zn-Ag-In-Se (ZAISE) QDs discussed in section 6.4, were also analyzed in Deng's work.<sup>137</sup> Nude mice bearing MDA-MB-231 or MCF-7 tumors were treated with NIR QD-loaded RGD-SOC NPs. Four hours after treatment, strong PL was detected at the tumor site for MDA-MB-231 tumor bearing mice but not for MCF-7 tumor bearing mice. Unfortunately, no further biodistribution analysis was reported. Later, the same group employed quaternary Zn-Ag-In-Se QD loaded into folate-modified N-succinyl-N'-octyl-chitosan NPs for imaging tumor *in vivo*.<sup>531</sup> Strong PL was observed from the tumors of folic acid receptor-positive Bel-7402 tumor-bearing mice, indicating that a significant fraction of the QDs were located in the tumor matrix. This group has also reported another method to produce water-dispersible quaternary Zn-Ag-In-S QDs modified with DHLA-PEG-based ligands.<sup>296</sup> The QDs were further conjugated with targeting ligands

1  
2  
3 such as folate and RGD peptide for imaging of tumor cells such as MDA-MB-231 cells and Bel-  
4  
5  
6 7402 cells.

7  
8 The biodistribution of CuInS<sub>2</sub>/ZnS QDs in tumors and major organs has also been studied  
9  
10 over a period of few hours.<sup>36</sup> The QDs, with PL from 550 to 800 nm and QY up to 80%, were  
11  
12 packaged within folate-modified N-succinyl-N'-octyl chitosan (FA-SOC) micelles for targeted  
13  
14 delivery and imaging. They were intravenously injected into Bel-7402 tumor-bearing nude mice  
15  
16 (FA receptor-positive model) and A549 tumor-bearing nude mice (FA receptor-negative model).  
17  
18 At 4 h post-injection, PL was detected in the liver and the tumor area in the Bel-7402 tumor-  
19  
20 bearing nude mice, but no QD PL was detected at the tumor site for the nude mice bearing A549  
21  
22 tumors. This result demonstrated specific uptake of FA-conjugated nanomicelles to FA receptor-  
23  
24 positive tumors.  
25  
26  
27  
28

29  
30 Recently, our group used CuInS<sub>2</sub>/ZnS QDs for targeted *in vivo* tumor imaging.<sup>281</sup> The  
31  
32 CuInS<sub>2</sub>/ZnS QDs were encapsulated in phospholipid micelles, which were further conjugated  
33  
34 with folic acid (FA). Thirty minutes after intravenous injection, QD PL was detected from the  
35  
36 tumor sites of mice treated with the FA-conjugated QDs, but not from the tumors of mice treated  
37  
38 with non-bioconjugated QDs, demonstrating the specificity of folic acid conjugation for tumor  
39  
40 targeting. After 60 min, the mice were sacrificed and analyzed with a small animal luminescence  
41  
42 imaging system. QDs had mainly accumulated in the spleen and the liver, indicating clearance by  
43  
44 the RES. QD PL was detected in the lung and kidneys, but the signals were much weaker than  
45  
46 those from the liver and the spleen.  
47  
48  
49  
50  
51  
52  
53  
54  
55  
56  
57  
58  
59  
60

1  
2  
3  
4  
5  
6  
7  
8  
9  
10  
11  
12  
13  
14  
15  
16  
17  
18  
19  
20  
21  
22  
23  
24  
25  
26  
27  
28  
29  
30  
31  
32  
33  
34  
35  
36  
37  
38  
39  
40  
41  
42  
43  
44  
45  
46  
47  
48  
49  
50  
51  
52  
53  
54  
55  
56  
57  
58  
59  
60

CuInSe<sub>x</sub>S<sub>2-x</sub>/ZnS QDs have also been used as a contrast agent for tracking a microparticle-based oral vaccine in mice.<sup>392</sup> The CuInSe<sub>x</sub>Se<sub>2-x</sub>/ZnS QDs were encapsulated with poly(lactic co-glycolic acid) (PLGA) to form microparticles that were then conjugated with invasin or D911A. The invasin-functionalized PLGA microparticles (15 mg) encapsulating the CuInSe<sub>x</sub>Se<sub>2-x</sub> QDs were orally introduced into mice and tracked. The mice were imaged at 15 min, 18 h, and 2 d after treatment. At 15 min, QD PL was primarily found in the stomach. At 18 and 45 h, most ingested microparticles had been excreted, and QD PL was restricted to the colon and the cecum.

Tumor uptake and the biodistribution of peptide-conjugated, PEG-passivated, near-IR InAs/InP/ZnSe QDs were studied *in vivo*.<sup>387</sup> The hydrodynamic diameter of QDs was 15.9 nm, and their circulation half-life was about 29 min. After conjugating the QDs with RGD or RAD peptides, the authors administered them to tumor-bearing nude mice. Tumor uptake of QD-RGD conjugates was much higher than that of QD-PEG and QD-RAD conjugates. Semiquantitative analysis of tumor uptake was performed using an IVIS Imaging System and living imaging software. The results showed a tumor uptake of 10.7% ID/g in mice treated with QD-RGD. At 4 h post injection, the mice were sacrificed and their organs were harvested to study the biodistribution of all the QD formulations (**Figure 67**). The QD PL of the liver was highest among the harvested organs, followed by the spleen and lung. Detectable but small PL signal was observed from the kidney, intestine and bone.

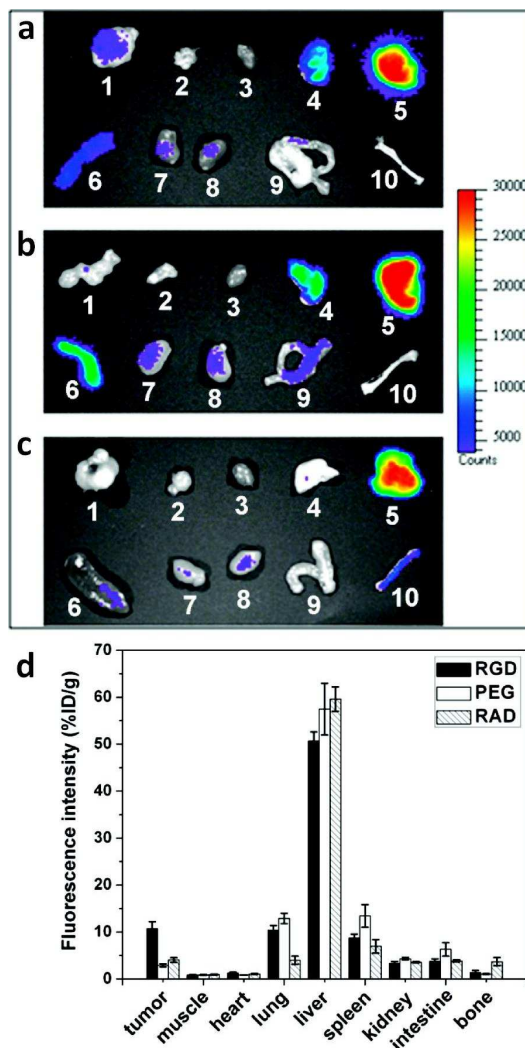


**Figure 67.** PL imaging of major organs of mice injected with (a) QD800-RGD, (b) QD800-PEG, and (c) QD800-RAD and sacrificed after 4 hr. 1, U87MG tumor; 2, muscle; 3, heart; 4, lung; 5, liver; 6, spleen; 7, kidney (left); 8, kidney (right); 9, intestine; and 10, bone. (d) ROI analysis of major organs in *ex vivo* PL imaging. Reprinted with permission from Gao *et al.*<sup>387</sup> Copyright 2010 American Chemical Society.

1  
2  
3 The pharmacokinetics and distribution of dendron-coated InP/ZnS QDs were also examined  
4 in a tumor-bearing nude mouse model and healthy mice.<sup>389</sup> The dendron-coated QDs were  
5  
6 functionalized with arginine-glycine-aspartic acid peptide dimers (RGD<sub>2</sub>) for tumor targeting and  
7 labeling, and then injected intravenously into SKOV3 tumor-bearing nude mice. The PL from  
8 both QD-dendron-RGD<sub>2</sub> and QD-dendron were detected in tumors at 1 h post injection, and  
9 stained tumors were easily distinguishable from tissues 4 h post-injection. In mice treated with  
10 QD-Dendron-RGD<sub>2</sub>, the QDs remained in the tumor even after 24 h, but PL was not detected at  
11 this time point for mice treated with the QD-dendron formulation. This demonstrated the specific  
12 targeting ability of the QD-dendron-RGD<sub>2</sub> to integrin  $\alpha_v\beta_3$ -positive SKOV3 tumors. To further  
13 quantify the biodistribution of the QD-Dendron, ICP-MS analysis was performed in BALB/c  
14 mice. 1 nmol of QD-dendron dispersion was injected intravenously into the mice and the blood  
15 and organs were analyzed. 24 h after injection, ~60% of the QD-dendron was removed from the  
16 body. Some QDs accumulated in the liver, spleen, and kidney. QD-dendron NPs accumulated in  
17 all organs, were excreted within a week, and were almost completely cleared at 10 weeks post-  
18 injection. The authors also investigated whether the QD-dendron could be removed through the  
19 renal system (**Figure 68**). QD PL was observed from the urinary bladder 30 min post-injection,  
20 and PL was also detected in the collected urine 90 min post-injection. The authors highlighted  
21 that QDs with larger hydrodynamic sizes (*e.g.* 20 nm) were generally located in the RES system  
22 where they may induce higher risk for long-term toxicity. Smaller QDs were more likely to be  
23 cleared through renal filtration, thereby reducing their potential toxicity.  
24  
25  
26  
27  
28  
29  
30  
31  
32  
33  
34  
35  
36  
37  
38  
39  
40  
41  
42  
43  
44  
45  
46  
47  
48  
49  
50  
51  
52  
53  
54  
55  
56  
57  
58  
59  
60

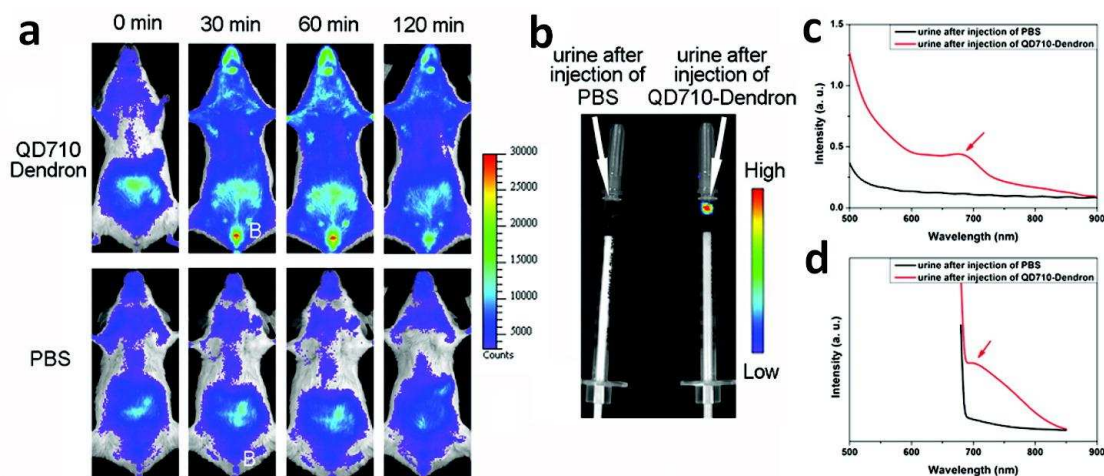


**Figure 68.** Renal clearance of QD710-Dendron. (a) PL imaging of BALB/c mice before and after tail-vein injection of QD710-Dendron or PBS. The PL signal originating from QD710-Dendron in the bladder (labeled as B) was clearly visible. (b) PL imaging of urine samples collected 90 min p.i. of QD710-Dendron or PBS. (c) UV-vis absorbance and (d) PL emission spectra of the urine samples collected 90 min p.i. of QD710-Dendron or PBS show absorbance and emission from QD710-Dendron. Reprinted with permission from Gao *et al.*<sup>389</sup> Copyright 2012 American Chemical Society.

## 8.0. *In vitro* and *in vivo* Toxicity of Cadmium-Free Quantum Dots

The toxicity of QDs must be addressed if they are to achieve their potential to positively impact healthcare. Substantial concern about the possible toxicity of QDs has been voiced by the press, biomedical researchers, bioengineers, and practicing physicians.<sup>533,534</sup> Detailed risk-benefit analyses of the use of engineered QDs for nanomedicine are crucial for their translation into specific diagnostic and therapeutic applications. The toxicity of QDs depends upon those

1  
2  
3 physicochemical properties that determine QD behavior *in vitro* and *in vivo*,<sup>3,31</sup> as well as the  
4 elemental composition of the QDs themselves. Studies of QD toxicology aim to understand how  
5 QDs might interact with biological systems to produce toxic effects. Risk factors associated with  
6 unintentional environmental exposure to QDs are also of great interest. Such unintentional  
7 exposure could result from handling of QDs or commercial products containing QDs, including  
8 inhalation of airborne QDs.<sup>535-538</sup> In general, the toxic effects generated by intentional and  
9 unintentional exposures to QDs are of same types, but the exposure routes and doses can be very  
10 different. The chemical components, physical characteristics (*e.g.*, size, shape and stability) and  
11 surface properties (*e.g.*, surface charge, surface coating) of the QDs play major roles in  
12 determining their toxicity.<sup>277,539,540</sup> Because of the high surface-to-volume ratio of QDs, surface-  
13 initiated processes are particularly important. Thus, size and shape of QDs clearly have an  
14 important role to play in determining overall toxicity. A key source of QD toxicity can be the  
15 release of heavy metal ions. For example, the release of highly toxic Cd<sup>2+</sup>, Pb<sup>2+</sup>, or Hg<sup>2+</sup> ions  
16 from CdSe, CdTe, PbSe, PbS or HgTe QDs has been of great concern to the biomedical  
17 community, and has prompted the development of the Cd-free QDs discussed in this  
18 review.<sup>56,541-543</sup> Clearly, the toxicity of QDs is dependent on a wide range of their  
19 physicochemical properties. This makes consistent, reproducible toxicological studies of QDs  
20 that produce generalizable results very challenging compared to toxicology studies of standard  
21 chemicals, *i.e.* well-defined molecules. As a result, many contradicting toxicological results on  
22 the same type of QDs have been reported. These discrepancies often originate from subtle  
23 differences in the QD's physicochemical characteristics.<sup>31</sup> This demonstrates the urgent need for

1  
2  
3 the QD research community to create a set of characterization protocols to standardize important  
4 tests and assays for accurate assessment of QD toxicity *in vitro* and *in vivo*, accompanied by  
5 standardized means of characterizing the QD's physicochemical properties. This section  
6 describes recent findings on *in vitro* and *in vivo* toxicity of Cd-free QDs and discusses how these  
7 functionalized QDs may interact with biological systems to generate adverse responses. The  
8 studies of QD toxicity discussed in this section are summarized in **Table 5**.  
9  
10  
11  
12  
13  
14  
15  
16  
17  
18  
19  
20  
21  
22  
23  
24  
25  
26  
27  
28  
29  
30  
31  
32  
33  
34  
35  
36  
37  
38  
39  
40  
41  
42  
43  
44  
45  
46  
47  
48  
49  
50  
51  
52  
53  
54  
55  
56  
57  
58  
59  
60

Table 5 Toxicity of Cd-free QDs

| QD type                                   | Surface modification | Dose                     | Time | Assay methods                     | Model                    | Toxic effects                     | Ref |
|---|----------------------|--------------------------|------|-----------------------------------|--------------------------|-----------------------------------|-----|
| Ag <sub>2</sub> Se                        | C18-PMH-PEG          | 0 ~ 100 µg/mL            | 24 h | MTT, apoptosis and necrosis assay | hMSCs and L929 cells     | >50 µg/mL, apoptosis and necrosis | 139 |
| CuInS <sub>2</sub> and AgInS <sub>2</sub> | F127                 | 0-300 mg/mL              | 48 h | cell viability study              | human macrophages        | cell viability >85% at 300 mg/mL  | 355 |
| ZnS-AgInS <sub>2</sub> /ZnS               | sugar-Chain          | 5-50 µg/mL               | 24 h | MTT                               | HepG2 cells              | nontoxic                          | 222 |
| CuInS <sub>2</sub> @SiO <sub>2</sub>      | amine-functionalized | 0~150 mg/mL              | 24 h | MTT                               | PC-3M cells              | nontoxic                          | 317 |
| CuInS <sub>2</sub> /ZnS                   | PEG                  | 100~950 µg/mL            | 24 h | MTT                               | Panc-1 cells             | cell viability >80% at 195 µg/mL  | 281 |
| CuInS <sub>2</sub> /ZnS                   | TTAB                 | 0-500 µM                 | 6 h  | Cell Counting Kit-8, hoechst33258 | MCF-7, HeLa, HepG2 cells | cell viability >80% at 500 µM     | 544 |
| Zn-Cu-In-S/ZnS                            | MPH,PEG-400          | 0~1µM of Cu <sup>+</sup> | 24 h | MTT                               | NIH/3T3 cell             | nontoxic                          | 284 |
| InAs/InP/ZnSe                             | MPA                  | 10~100 nmol/L            | 48 h | MTT                               | RAW 264.7 cells          | less toxic than CdTe/ZnTe         | 299 |
| zwitterion-like CuInS <sub>2</sub> /ZnS   | PMAO-DMAPA           | 0~100 nmol/L             | 72 h | MTT, FDA/PI staining              | U87MG, HEK-293 cells     | minimally toxic                   | 545 |
| CuInS <sub>2</sub> /ZnS                   | PEI,pDNA,ST68MBs     | 0~1 mM                   | 48 h | MTT                               | HeLa, HUVEC              | cell viability >90% even at       | 413 |

211



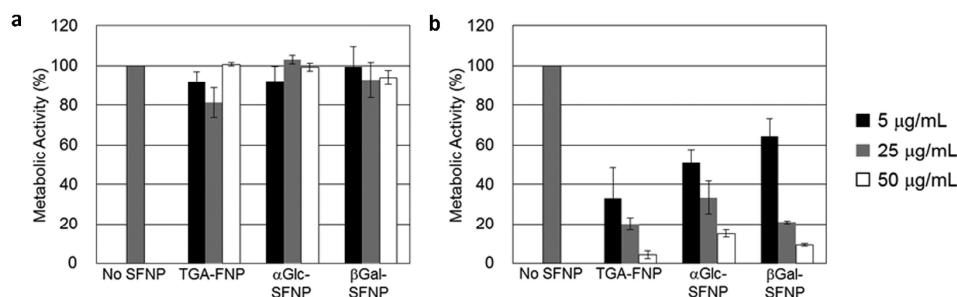


### 8.1 *In vitro* Toxicity

The biocompatibility of polymer-coated Ag<sub>2</sub>Se QDs (C18-PMH-PEG-Ag<sub>2</sub>Se QDs) was evaluated using standard MTT and apoptosis/necrosis assays.<sup>139</sup> Human mesenchymal stem cells (hMSCs) and mouse fibroblast L929 cells were used for the cytotoxicity evaluation. The authors used both normal cells and stem cells to examine the cytotoxicity of Ag<sub>2</sub>Se QDs more holistically, based on the fact that hMSCs are very sensitive to their environment. The two cell lines were exposed to Ag<sub>2</sub>Se QDs at concentrations ranging from 0 to 100 µg/mL for 24 h. Cell viability determined by MTT assay demonstrated that the L929 cells and hMSCs maintained their viability even at 100 µg/mL. Flow cytometry was used to analyze apoptosis/necrosis events of L929 cells and hMSCs treated with polymer-coated Ag<sub>2</sub>Se QDs for 24 h. For both cell lines, when exposed to Ag<sub>2</sub>Se QDs at 50 and 100 µg/mL, the population of cells that underwent apoptosis and necrosis was the same as in control experiments without exposure to Ag<sub>2</sub>Se QDs.

Cytotoxicity studies have also been carried out to assess the biocompatibility of Pluronic F127 micelle-encapsulated CuInS<sub>2</sub>/ZnS and AgInS<sub>2</sub>/ZnS QDs.<sup>355</sup> For the cell viability study, human macrophages were treated with varying concentrations (0-300 µg/mL) of QDs for 48 h. Cell viability remained above 85% throughout this concentration range, indicating that the cytotoxicity of the QDs was minimal. Recently, hybrid CuInS<sub>2</sub> QD@SiO<sub>2</sub> nanobeads and anti-PSCA conjugated CuInS<sub>2</sub> QD@SiO<sub>2</sub> nanobeads were evaluated using the MTT assay for their toxicity to PC-3M cells.<sup>317</sup> Both were nontoxic at concentrations up to 150 µg/mL. Similarly, the MTT assay and morphological analysis were used to evaluate the cytotoxicity of ZnS-AgInS<sub>2</sub> (ZAIS)/ZnS QDs and CdTe/CdS QDs toward HepG2 cells.<sup>222</sup> The MTT assay was carried out

1  
2  
3 after 24 h incubation; metabolic activity of cells was similar to that of the control group (**Figure**  
4  
5  
6 **69**). No morphological changes were observed in the cells treated with ZAIS/ZnS QDs, further  
7  
8 demonstrating that these QDs were nontoxic over the concentration range of 5–50  $\mu\text{g/mL}$ . In  
9  
10 contrast, exposure to CdTe/CdS QDs decreased metabolic activity of the cells significantly.



11  
12  
13  
14  
15  
16  
17  
18  
19  
20  
21  
22  
23  
24 **Figure 69.** MTT assay comparison for HepG2 cells treated with ZAIS/ZnS QDs (a) or  
25 CdTe/CdS QDs (b) for 24h. Reprinted with permission from Shinchi *et al.*<sup>222</sup> Copyright 2014  
26 American Chemical Society.  
27  
28

29  
30  
31 Our group reported cytotoxicity evaluation of PEGylated phospholipid micelle-encapsulated  
32 CuInS<sub>2</sub>/ZnS QDs using the MTT assay.<sup>281</sup> Cells maintained 80% viability when treated with 195  
33  $\mu\text{g/mL}$  of micelle-encapsulated QDs for 24 h, suggesting the QDs have minimal cytotoxicity.  
34  
35 Cysteine-capped CdTe QDs were also studied, for comparison. The concentration corresponding  
36 to 50% cell viability ( $\text{IC}_{50}$ ) was estimated to be 100  $\mu\text{g/mL}$  for CdTe QDs and 300  $\mu\text{g/mL}$  for  
37 CuInS<sub>2</sub>/ZnS QDs in Panc-1 cells. This indicates that the CuInS<sub>2</sub>/ZnS QDs can be loaded into  
38 cells at a higher dosage for bioimaging studies. The difference in toxicity between Cd-containing  
39 and Cd-free QDs is, in this case, notable, but the Cd-free QDs still exhibit significant toxicity at  
40 high doses. In another study, Wang *et al.* performed cytotoxicity assays of CuInS<sub>2</sub>/ZnS QDs  
41  
42  
43  
44  
45  
46  
47  
48  
49  
50  
51  
52  
53

1  
2  
3 modified with the cationic surfactant (1-tetradecyl) trimethylammonium bromide (TTAB).<sup>544</sup>  
4  
5 The cell counting kit-8 assay study showed that CIS–ZnS–TTAB QDs had little impact on the  
6  
7 cell viability of the MCF-7 cells treated with QDs; 80% of the cells survived the QD treatment.  
8  
9 The cytotoxicity test for hydrophilic Zn–Cu–In–S/ZnS (ZCIS/ZnS) QDs<sup>284</sup> was also performed  
10  
11 on NIH/3T3 cells for 24 h and showed no significant signs of toxicity at doses up to 1 mM of Cu  
12  
13 ions. The *in vitro* cytotoxicity of InAs/InP/ZnSe core/shell/shell QDs with near-IR PL was also  
14  
15 studied.<sup>299</sup> The MTT assay showed that InAs/InP/ZnSe core/shell/shell QDs at 10 nmol/L are  
16  
17 significantly less cytotoxic compared to CdTe/ZnS core/shell QDs.  
18  
19

20  
21 In a more recent study, the cytotoxicity of zwitterion-like CuInS<sub>2</sub>/ZnS QDs (ZWL-QDs)  
22  
23 toward human primary glioblastoma (U-87 MG) cells and human embryonic kidney 293 (HEK-  
24  
25 293) cells was assessed.<sup>545</sup> The cell viability was determined by staining the cells with FDA/PI to  
26  
27 differentiate between live and dead cells. Both U-87MG and HEK-293 cells were treated with 20  
28  
29 nM of the ZWL-QDs, and untreated cells were used as controls. The toxicity of the ZWL-QDs  
30  
31 was insignificant compared to the controls. Relative cell viability for both cells after 72 hours of  
32  
33 incubation with different ZWL-QD concentrations was determined. The onset of ZWL-QD  
34  
35 toxicity was at ~100 nM.  
36  
37  
38  
39

40  
41 The potential toxicity of a CuInS<sub>2</sub>/ZnS alloy QD-based multifunctional contrast agent was  
42  
43 also investigated using the MTT assay.<sup>413</sup> Specifically, the QDs were passivated with  
44  
45 polyethyleneimine (PEI), allowing them to complex with plasmid DNA (pDNA). The DNA  
46  
47 conjugated QDs adsorbed onto the surface of microbubbles (MBs) formed in a mixed surfactant  
48  
49 system containing Tween 80 and Span 60, creating MB@QD@PEI/pDNA complexes. The  
50  
51  
52

1  
2  
3 biocompatibility of these nanocomplexes was evaluated in HeLa cells and human umbilical vein  
4 endothelial (HUVEC) cells. Both cell types were treated with varying doses of the  
5  
6 MB@QD@PEI/pDNA formulation for 48 h and the viability of the treated cells was evaluated  
7  
8 by a MTT assay. The viability of HeLa and HUVEC cells remained above 90% up to a  
9  
10 concentration equivalent to 1 mM PEI. To further evaluate the biocompatibility of the  
11  
12 nanocomplex formulation, bone marrow dendritic cells (BMDC) and T cells were treated with  
13  
14 the formulation for 24 h. The viable cells were stained green using calcein acetoxymethyl ester  
15  
16 and the dead cells were stained red using propidium iodide (PI). Fluorescence microscopy of the  
17  
18 live/dead stained cells revealed no adverse effects to either BMDC or T cells after treatment with  
19  
20 the MB@QD@PEI/pDNA formulation (**Figure 70**).  
21  
22  
23  
24  
25  
26  
27  
28  
29  
30  
31  
32  
33  
34  
35  
36  
37  
38  
39  
40  
41  
42  
43  
44  
45  
46  
47  
48  
49  
50  
51  
52  
53  
54  
55  
56  
57  
58  
59  
60

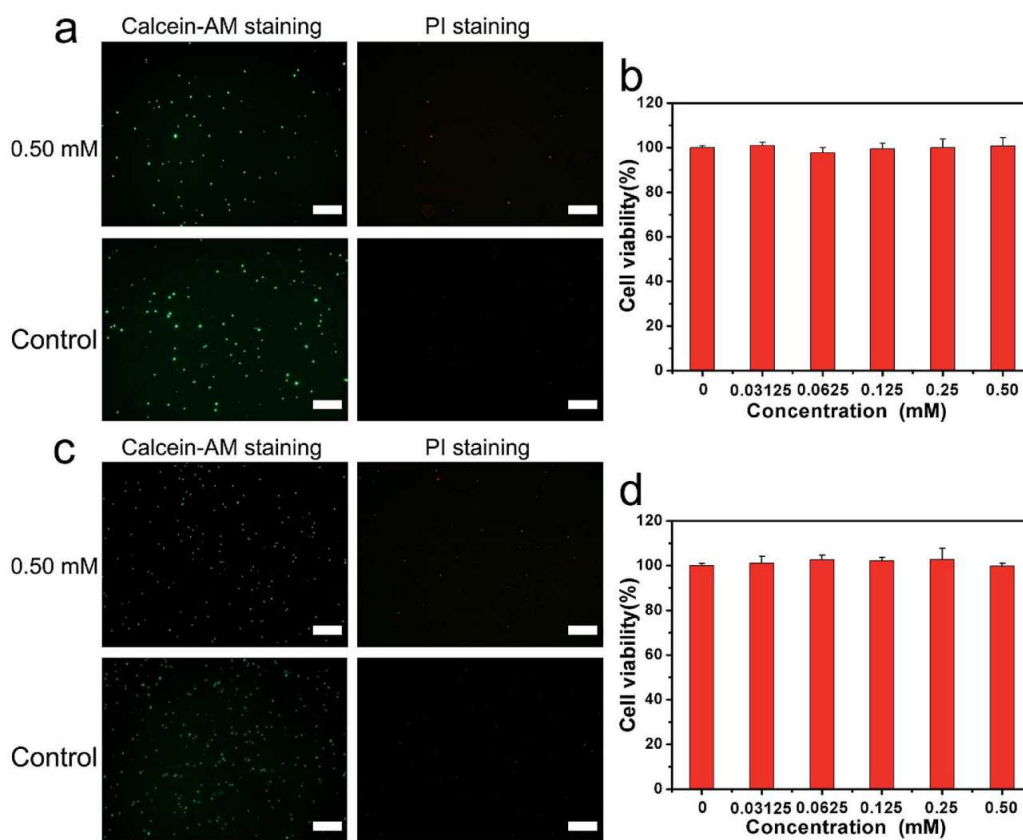


**Figure 70.** Fluorescence microscopy images of BMDC cells (a) and T cells (c) treated with MB@QD@PEI/pDNA and live/dead staining with calcein AM and PI. Scale bars are 500 μm. The cell viability of BMDC cells (b) and T cells (d) treated with MB@QD@PEI/pDNA for 24 h. Reprinted with permission from Yang *et al.*<sup>413</sup> Copyright 2015 Royal Society of Chemistry.

The *in vitro* cytotoxicity of different graphene QDs was tested using the MTT assay,<sup>310</sup> demonstrating that graphene QDs and r-graphene QDs (graphene QDs reduced with NaBH<sub>4</sub>) had low toxicity toward MC3T3 cells. The cell viability remained near 80% in the presence of 400 μg/mL graphene QDs or r-graphene QDs. On the other hand, m-graphene QDs (alkyl-amine

1  
2  
3 modified graphene QDs) showed a clear dose-dependent impact on cell viability. The cell  
4  
5 viability dropped below 60% in the presence of 400  $\mu\text{g}/\text{mL}$  m-graphene QDs. The authors  
6  
7 attributed the cytotoxicity to the presence of alkyl-amines, in which both alkyl chains and  
8  
9 nitrogen adversely impacted the cells.  
10

11  
12 Stern *et al.* investigated cytotoxicity mechanisms of lipid-coated and PEGylated CdSe/ZnS  
13  
14 and InGaP/ZnS QDs with core sizes of 5.1 and 3.7 nm.<sup>546</sup> Based on MTT assay results, the  
15  
16 CdSe/ZnS QDs ( $\text{IC}_{50}$   $\sim 10$  nM) were determined to be 10-fold more toxic to porcine renal  
17  
18 proximal tubule (LLC-PK1) cells compared to the InGaP/ZnS QDs ( $\text{IC}_{50}$   $\sim 100$  nM). Using  
19  
20 reduced glutathione content and lipid peroxide analysis, the authors found that neither type of  
21  
22 QDs induced oxidative stress, suggesting that the toxicity was not associated with the QD metals.  
23  
24 The cells treated with CdSe QDs were not linked with any changes in Cd-related caspase-3  
25  
26 enzyme activation or metallothionein-IA gene expression. On the other hand, treating LLC-PK1  
27  
28 cells with InGaP QDs caused a significant increase in MT-IA expression during the first 24 h  
29  
30 post-treatment. More importantly, the authors found the evidence of extensive autophagy for  
31  
32 QD-treated cells. This was determined by analyzing LysoTracker dye uptake, cell morphology  
33  
34 from TEM images (**Figure 71**), and LC3 immunoblotting. Autophagy is a process involving  
35  
36 recycling and degrading of long-lived proteins and organelles by lysosomes. It is also viewed as  
37  
38 a general pathway of programmed cell death which has a similar homeostatic function as  
39  
40 apoptosis.  
41  
42  
43  
44  
45  
46  
47  
48  
49  
50  
51  
52  
53

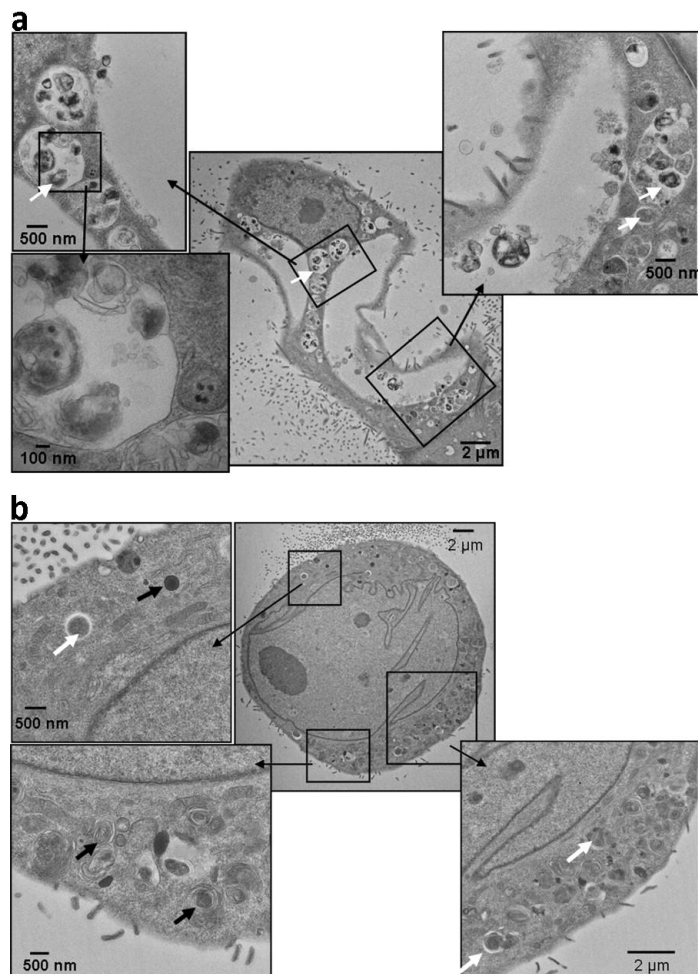


**Figure 71.** TEM ultrastructures of LLC-PK1 cells treated for 24 h with 10 nM CdSe QD (a) or 100nM InGaP QD (b). White arrows: autophagic vacuoles; black arrows: lysosomal remnants.

Reprinted with permission from Stern *et al.*<sup>546</sup> Copyright 2008 Oxford University Press.

## 8.2 *In vivo* Toxicity

Some detailed studies of *in vivo* toxicity of Cd-free quantum dots have also been reported. The toxicology of NIR Ag<sub>2</sub>S QDs was studied in mice.<sup>289</sup> The effect of PEGylated-Ag<sub>2</sub>S QDs on

1  
2  
3 the body weight of mice was examined by comparing treated and untreated mice for two months  
4 after injection. The control group and experimental groups receiving injected doses of 15 and 30  
5 mg/kg showed similar weight gain. In addition, blood biochemistry analysis was carried out,  
6 evaluating the ratio of albumin to globulin, glucose, globulin, total protein, total cholesterol,  
7 aspartate aminotransferase, alkaline phosphatase, alanine aminotransferase, blood urea nitrogen  
8 and albumin. Mice were sacrificed for blood sample collection at intervals during the 60 days  
9 following treatment. All biochemistry parameters remained in the normal range compared to the  
10 control group of mice, for both 15 and 30 mg/kg doses. Hematological toxicity was assessed by  
11 white blood cell count, red blood cell count, mean corpuscular volume, mean corpuscular  
12 hemoglobin, mean corpuscular hemoglobin concentration, hematocrit, hemoglobin, platelet  
13 count and red blood cell volume distribution width (**Figure 72**). Except for platelet and white  
14 blood cell counts, all these hematological indicators were in the normal range. The platelet and  
15 white blood cell levels in the experimental groups dropped significantly during the first few days  
16 after the injection of the NPs. The authors speculated that this drop was caused by macrophage  
17 inhibition and platelet damage associated with the acute immune response to the injected Ag<sub>2</sub>S  
18 QDs. For mice receiving 30 mg/kg QDs, necropsies were performed on animals sacrificed at 3, 7,  
19 14, 21, 28, and 60 days post-injection. Tissue sections from the liver, spleen, and kidney were  
20 analyzed by H&E staining and no obvious lesions or signs of hydropic damage were found.  
21  
22  
23  
24  
25  
26  
27  
28  
29  
30  
31  
32  
33  
34  
35  
36  
37  
38  
39  
40  
41  
42  
43  
44  
45  
46  
47  
48  
49  
50  
51  
52  
53  
54  
55  
56  
57  
58  
59  
60

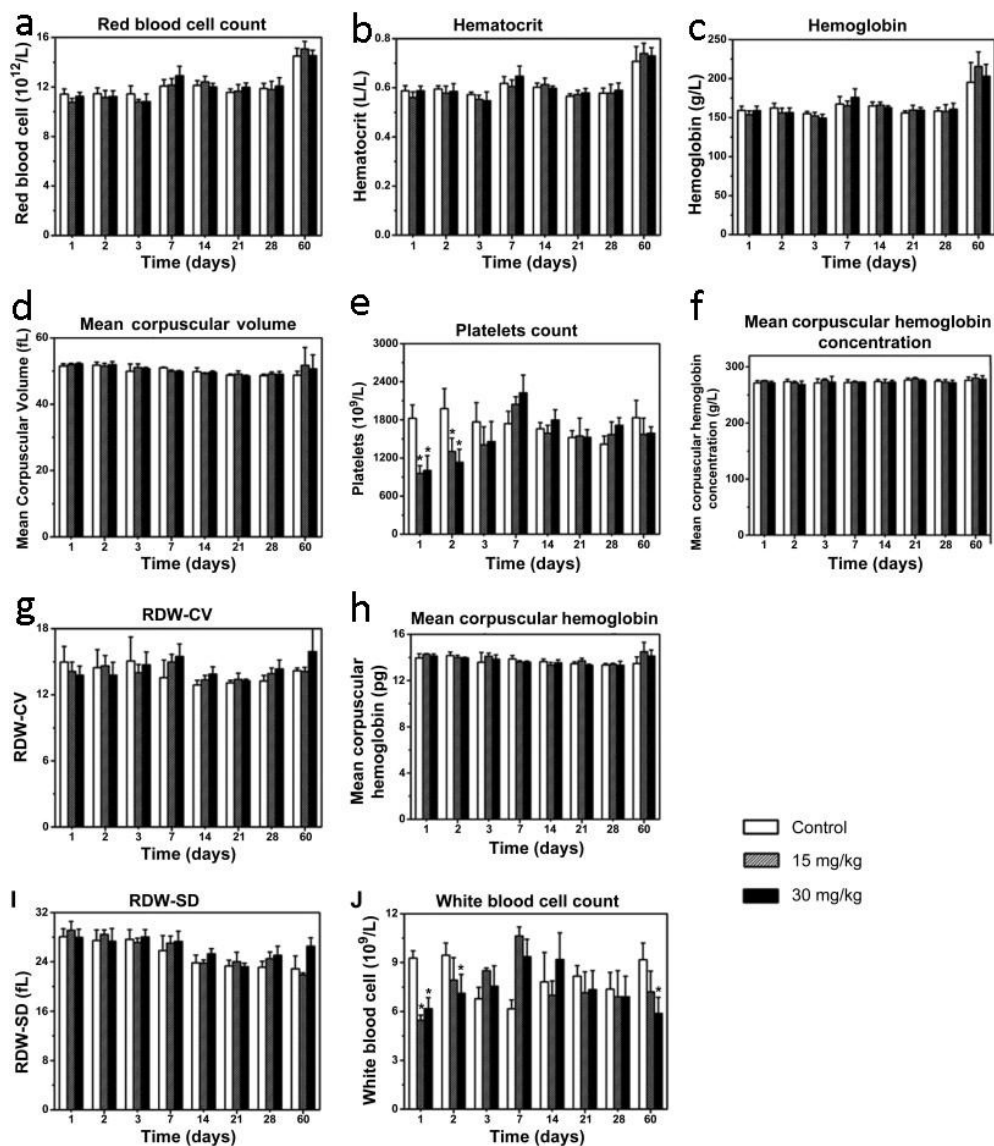


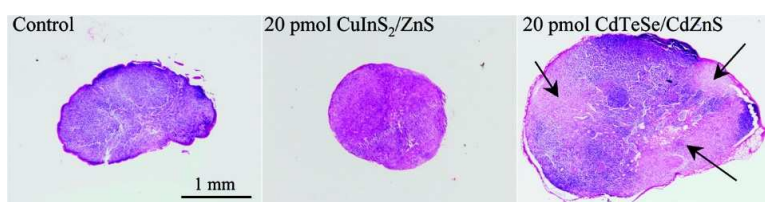
**Figure 72.** Hematology data on female BALB/c mice treated with PEGylated-Ag<sub>2</sub>S QDs at 0, 15 and 30 mg/kg at 1, 2, 3, 7, 14, 28, and 60 days p.i. \*:  $P < 0.05$ . Reprinted with permission from Zhang *et al.*<sup>289</sup> Copyright 2013 Elsevier.

1  
2  
3 Liu *et al.* employed histological imaging to determine the toxicity of micelle-encapsulated  
4 AgInS<sub>2</sub> QDs in mice.<sup>331</sup> After completing MTT assays using Panc-1 cells, the authors carried out  
5  
6  
7  
8  
9  
10  
11  
12  
13  
14  
15  
16  
17  
18  
19  
20  
21  
22  
23  
24  
25  
26  
27  
28  
29  
30  
31  
32  
33  
34  
35  
36  
37  
38  
39  
40  
41  
42  
43  
44  
45  
46  
47  
48  
49  
50  
51  
52  
53  
54  
55  
56  
57  
58  
59  
60

Liu *et al.* employed histological imaging to determine the toxicity of micelle-encapsulated AgInS<sub>2</sub> QDs in mice.<sup>331</sup> After completing MTT assays using Panc-1 cells, the authors carried out histological studies of acute toxicity induced by QDs on the lung, liver, spleen, kidney, heart and brain of mice. Small animals treated with Pluronic micelle-encapsulated AgInS<sub>2</sub> QDs did not show any tissue injury in any of these organs. No drastic differences in body weight were observed between treated and control mice for more than a week. Together, these results support the lack of acute toxicity of the Pluronic micelle-encapsulated AgInS<sub>2</sub> formulations in small animals.

The inflammatory response of the axillary lymph node (LN) was examined in mice treated with CdTeSe/CdZnS and CuInS<sub>2</sub>/ZnS QDs.<sup>390</sup> QD dispersions were subcutaneously injected in the right anterior paw of mice. The two types of QDs displayed similar performance in LN imaging, because the QDs possessed similar extinction coefficients, QYs, and hydrodynamic sizes. The weights of the right axillary LN (RALN) and right lateral thoracic LN (RLTLN) dissected at 7 days post injection were analyzed. The percentage of the total injected dose taken up by the RALN at 7 days post-injection was larger for CuInS<sub>2</sub>/ZnS QDs (4%) compared to CdTeSe/CdZnS (1.5%) (**Figure 73**). The authors mentioned that for both QD formulations, there is a clear dose-dependent increase in weight of the RALNs and this indicates the increasing toxicity of the QDs. Also, they found a distinct difference in the toxicity between the two types of QDs. Inflammation was observed in mice treated with 10 pmol of CdTeSe/CdZnS QDs, and the mass of the RALN was drastically increased. Similar inflammation was detected for the injection of 100 pmol of CuInS<sub>2</sub>/ZnS. Histological analysis was also performed on sections of

1  
2  
3 the RALNs at 7 days post-injection. The RALN of mice treated with 20 pmol  $\text{CuInS}_2/\text{ZnS}$   
4 displayed no signs of inflammation, whereas the same dose of  $\text{CdTeSe}/\text{CdZnS}$  QDs induced  
5 inflammation in RALN of the treated mice. Signs of inflammation observed from the histological  
6 samples include polynuclear cells, histiocytes, and vacuoles of digestion in the examined regions  
7 of interest. The inflammatory response of the axillary LN induced by  $\text{CuInS}_2/\text{ZnS}$  QDs was  
8 much lower than that induced by  $\text{CdTeSe}/\text{CdZnS}$  QDs, and the minimum dose of  $\text{CuInS}_2/\text{ZnS}$   
9 QDs used for RALN detection was 50 times lower than the minimum dose that induced RALN  
10 inflammation. This comparison between Cd-based and Cd-free QDs show that the window of  
11 operation between the dose needed for imaging and that which causes an inflammatory response  
12 was much wider for the  $\text{CuInS}_2/\text{ZnS}$  QDs, illustrating their clear advantage in this application.  
13  
14  
15  
16  
17  
18  
19  
20  
21  
22  
23  
24  
25  
26



35 **Figure 73.** Histological sections of the RALNs resected 7 days post-injection for mice injected  
36 with a saline buffer solution (control),  $\text{CuInS}_2/\text{ZnS}$  QDs and  $\text{CdTeSe}/\text{CdZnS}$  QDs. Black arrows:  
37 inflammation sites. Reprinted with permission from Pons *et al.*<sup>390</sup> Copyright 2010 American  
38 Chemical Society.  
39  
40  
41  
42  
43

### 44 **8.3 Mechanism of Toxicity**

45  
46  
47 A primary mechanism of nanotoxicity associated with QDs is oxidative stress due to  
48 generation of reactive oxygen species (ROS), particularly under light exposure.<sup>3</sup> Chibli *et al.*  
49 investigated the role of ROS generation in the cytotoxicity of  $\text{InP}/\text{ZnS}$  QDs.<sup>547</sup> When QDs are  
50  
51  
52  
53

1  
2  
3 excited by illumination, they may generate various ROS species such as singlet oxygen,  
4 hydrogen peroxide and hydroxyl radicals due to the transfer of their electrons/holes to oxygen  
5 molecules or other acceptors/donors in cells. These reductive and oxidative processes have been  
6 reported when using CdSe QDs and are also expected to occur with InP QDs based on the  
7 similar energy levels of their band edge and defect states. EPR and ROS assays showed that InP  
8 and InP/ZnS QDs generated considerable superoxide and a small amount of hydroxyl radical, but  
9 no singlet oxygen. In a sulforhodamine B (SRB) cytotoxicity assay, no toxicity was observed in  
10 PC12 cells treated with QDs at concentrations up to 500 nM, with or without light exposure. For  
11 KB cells treated with 500 nM of InP/ZnS QDs with one shell-layer of ZnS, a dramatic reduction  
12 in cell growth was observed. On the other hand, InP/ZnS QDs with two shell layers of ZnS  
13 displayed a significant adverse impact only in the presence of light. MDA and 3T3 cells treated  
14 with QDs and subsequently illuminated showed significant signs of toxicity at 200 nM dosage.  
15 The 1-shell layer InP/ZnS QDs were highly toxic to the mouse melanoma cell line B16 at 100  
16 nM, in the presence and absence of light, while 2-shell layer InP/ZnS QDs displayed toxicity at  
17 200 nM only in with light exposure (**Figure 74**). The distinct toxicity reduction and good  
18 electron transfer efficiency for double-shell InP/ZnS QDs in the above-mentioned five cell lines  
19 compared to those observed for CdTe or CdSe/ZnS QDs demonstrates the promise of these Cd-  
20 free QDs as alternatives to Cd-based QDs for photosensitization applications.  
21  
22  
23  
24  
25  
26  
27  
28  
29  
30  
31  
32  
33  
34  
35  
36  
37  
38  
39  
40  
41  
42  
43  
44  
45  
46  
47  
48  
49  
50  
51  
52  
53  
54  
55  
56  
57  
58  
59  
60

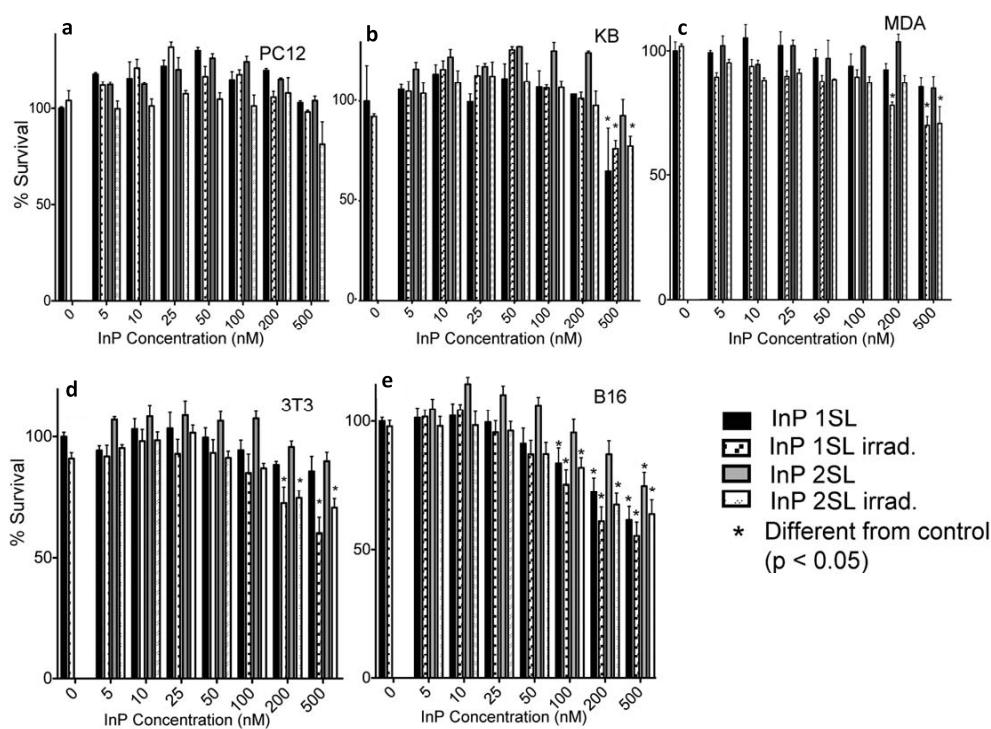


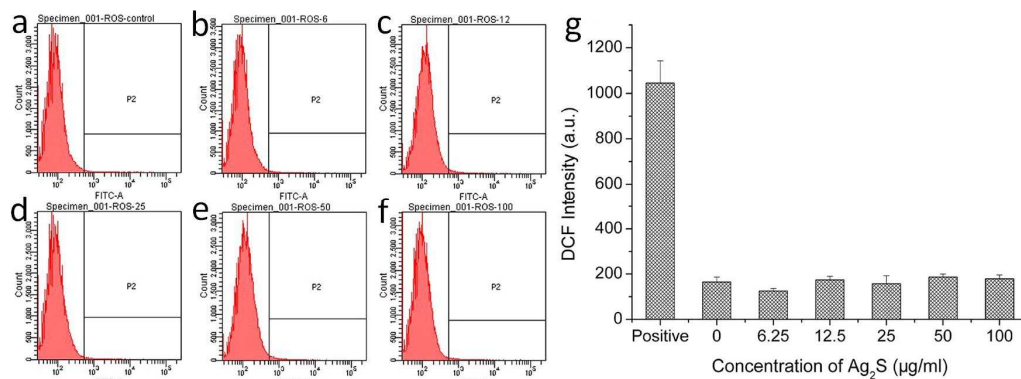
**Figure 74.** Cell viability after treatment with InP/ZnS with one ZnS shell layer (1SL) or two ZnS shell layers (2SL) and either kept in the dark or irradiated (“irrad”). The cell lines included (a) PC12, (b) KB, (c) MDA-231-MB, (d) NIH3T3 and (e) B16. Reprinted with permission from Chibli *et al.*<sup>547</sup> Copyright 2011 Royal Society of Chemistry.

The cytotoxicity of Cd salt, Zn salt, Cd-based QDs and Zn-based QDs was investigated using zebrafish liver cells (ZFL).<sup>548</sup> The  $IC_{50}$  values at 24 h of CdSe/ZnS and InP/ZnS QDs were much larger than that of CdTe QDs, suggesting that ZnS-capped QDs were more biocompatible than CdTe core QDs alone. Isolated mRNA from these QD exposures were employed to determine the expression of metal response genes such as metallothionein (MT), divalent metal transporter (DMT-1), zrt and irt like protein (ZIP-1), metal response element-binding transcription factor

1  
2  
3 (MTF-1), and the zinc transporter (ZnT-1). The expression of metal homeostasis genes was  
4 altered by CdSe/ZnS and InP/ZnS QDs in a manner that is different from the Cd salt, Zn salt or  
5 CdTe QDs. The authors suggest that the coating of ZnS shell on QDs reduces the QD toxicity  
6 that is associated with the release of heavy metal ions, but the coating does not eliminate the  
7 toxic effects associated with the overall NP formulation itself.  
8  
9

10  
11 The cytotoxicity of Ag<sub>2</sub>S QDs, including their influence on ROS generation, cell  
12 proliferation and apoptosis/necrosis, and DNA damage were considered by Zhang *et al.*<sup>290</sup>  
13 Mouse fibroblast L929 cells were used for the cytotoxicity assay. After exposing the L929 cells  
14 to Ag<sub>2</sub>S QDs at five different concentrations (6.25, 12.5, 25, 50, and 100 µg/mL) for 72 h, the  
15 cell proliferation was quantified and determined to be dose-independent. Using Hoechst and EdU  
16 as staining agents for cell counting, the researchers found no statistically significant differences  
17 in the total number of L929 cells or the number of cells with newly synthesized DNA, suggesting  
18 that Ag<sub>2</sub>S QDs did not impact cell proliferation. To investigate apoptosis and necrosis, flow  
19 cytometry with Annexin V-FITC staining and propidium iodide (PI) staining was conducted. The  
20 flow cytometry data showed very low cytotoxicity in terms of generating apoptosis and necrosis  
21 events in the cells after 72 h of treatment. ROS produced by the Ag<sub>2</sub>S QDs was determined by  
22 measuring the fluorescence intensity of 2',7'-dichlorofluorescein (DCF). This ROS assay  
23 involves the use of cell-permeable probe 2',7'-dichlorodihydrofluorescein-diacetate (DCFH-DA),  
24 which diffuses into the cells and is hydrolyzed into nonfluorescent DCFH by cellular esterase.  
25 When ROS are present, the DCFH will be oxidized to DCF and show strong fluorescence. Flow  
26 cytometry measurements showed that cells treated with 100 µg/mL of QDs for 72 h generated  
27  
28  
29  
30  
31  
32  
33  
34  
35  
36  
37  
38  
39  
40  
41  
42  
43  
44  
45  
46  
47  
48  
49  
50  
51  
52

1  
2  
3 very low amounts of ROS, with no statistically significant difference from the negative control  
4  
5  
6 (Figure 75).

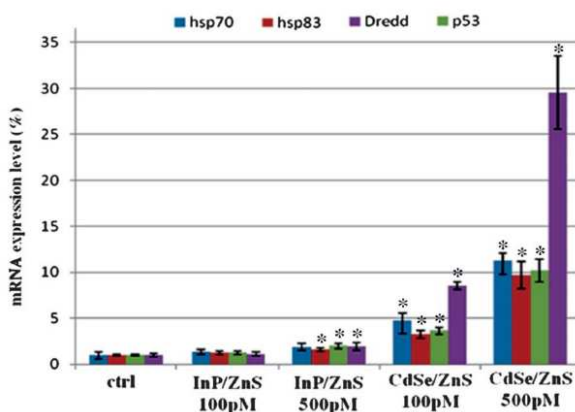


7  
8  
9  
10  
11  
12  
13  
14  
15  
16  
17  
18  
19  
20  
21  
22  
23 **Figure 75.** ROS induced by DHLA-Ag<sub>2</sub>S QDs after 72 h treatment. FACS plots with Ag<sub>2</sub>S QD  
24 concentrations of 0 (a), 6.25 µg/mL (b), 12.5 µg/mL (c), 25 µg/mL (d), 50 µg/mL (e) and 100  
25 µg/mL (f). (g) Quantitative flow cytometry results. Reprinted with permission from Zhang *et*  
26  
27  
28  
29  
30 *al.*<sup>290</sup> Copyright 2012 American Chemical Society.

31  
32  
33  
34 Brunetti *et al.* conducted a detailed *in vitro* and *in vivo* toxicity study of an InP/ZnS QD  
35 formulation.<sup>276</sup> Toxicity of CdSe/ZnS QDs is largely associated with the release of Cd<sup>2+</sup> ions  
36 from the QD surface. Approximately the same amount of In<sup>3+</sup> ions was released from the  
37 InP/ZnS QDs surface. However, the toxicity of In<sup>3+</sup> is much lower than that of Cd<sup>2+</sup>. In this work,  
38 human lung carcinoma A549 cells, an epithelial cell line, and human neuroblastoma SH SY5Y  
39 cells, a neuronal cell line, were used to investigate cytotoxicity of CdSe/ZnS and InP/ZnS QDs  
40 over a concentration range of 1 pM-5 nM. Cell viability was determined using the WST-8 assay  
41 at 24 and 48 h of incubation. CdSe/ZnS QDs caused stronger adverse impact to the cell viability  
42  
43  
44  
45  
46  
47  
48  
49  
50  
51  
52  
53

1  
2  
3 than InP/ZnS QDs. At 24 h incubation, the toxic effect of CdSe/ZnS QDs was detectable at a  
4  
5 concentration of 1 nM. After 48 h incubation, cell viability loss was detected for CdSe/ZnS QDs  
6  
7 even at 10 pM. The highest toxicity was observed for the neuronal cell line with a 27% and 46%  
8  
9 viability loss after 24 h and 48 h of incubation with 5 nM CdSe/ZnS QDs. The A549 cells were  
10  
11 less sensitive to the QDs. A 33% reduction in cell viability was detected after 48 h of incubation  
12  
13 with 5 nM CdSe/ZnS QDs. On the other hand, incubation of the same cell line with 5 nM  
14  
15 InP/ZnS QDs did not cause any significant reduction in cell viability. To further probe the  
16  
17 molecular mechanism underlying the reduction in cell viability, the authors carried out a series of  
18  
19 different assays. The lactate dehydrogenase (LDH) leakage assay was employed to evaluate cell  
20  
21 membrane damage. The assay revealed that the presence of 1 pM CdSe/ZnS QDs produced  
22  
23 significant membrane damage in the cell types mentioned above. In contrast, no change in LDH  
24  
25 was detected upon exposing the cells to InP/ZnS QDs. Oxidative stress within the QD-treated  
26  
27 cells was also analyzed. A positive DCF-DA (dichlorofluorescein diacetate) assay showed that  
28  
29 cell cultures treated with 1 pM Cd-containing QDs for 24 h generated intracellular reactive  
30  
31 oxygen species (ROS). To further confirm the generation of ROS caused by oxidative stress,  
32  
33 real-time qPCR was used to determine the expression levels of CAT, Gpx, SOD1 and SOD2  
34  
35 genes coding for antioxidant and detoxifying enzymes. The expression profiles determined  
36  
37 without photoactivation of QDs revealed that the treated cells experienced oxidative stress when  
38  
39 they were exposed with CdSe/ZnS QDs. The same concentration of InP/ZnS QDs did not cause  
40  
41 any detectable over-expression of genes correlated with oxidative stress. The results revealed  
42  
43 that epithelial cell line A549 was less susceptible to QD-induced damage than the neuronal cell  
44  
45  
46  
47  
48  
49  
50  
51  
52

1  
2  
3 line SH SY5Y. The authors also studied the toxicity of CdSe/ZnS and InP/ZnS QDs in fruit flies  
4 by feeding them QD-supplemented food. The authors used real-time qPCR to investigate the  
5 mechanisms of QD toxicity. For instance, they investigated variations in expression levels of  
6 genes associated with DNA damage and stress response. *Drosophila* flies were fed with food  
7 containing CdSe/ZnS or InP/ZnS QDs, or with standard food as a control. Gene expression was  
8 observed in the fruit flies fed with food containing 100 pM and 500 pM CdSe/ZnS QDs,  
9 revealing systemic toxicity involving increased ROS production, the generation of abnormal  
10 proteins, and the presence of genomic perturbation. Gene expression in fruit flies treated with the  
11 InP/ZnS QDs was much closer to that of the control group (**Figure 76**).  
12  
13  
14  
15  
16  
17  
18  
19  
20  
21  
22  
23  
24  
25  
26  
27



28  
29  
30  
31  
32  
33  
34  
35  
36  
37  
38  
39  
40  
41  
42  
43 **Figure 76.** mRNA expression levels of *Drosophila* flies treated with InP/ZnS or CdSe/ZnS QDs.

44  
45 \* $P < 0.05$  compared with control ( $n = 8$ ). Reprinted with permission from Brunetti *et al.*<sup>276</sup>

46  
47  
48 Copyright 2013 Royal Society of Chemistry.

## 9.0. Concluding Remarks and Perspectives

This review summarized recent developments in Cd-free QDs for biophotonics and nanomedicine applications. Thanks to tremendous efforts invested in the synthesis and functionalization of these QDs, the past decade has witnessed a substantial improvement in their optical properties, stability and biocompatibility. Although the first Cd-free QDs exhibited low QY and/or poor optical or colloidal stability, recent studies of InP, CuInS<sub>2</sub> and AgInS<sub>2</sub> QDs have reported much improved QY, in many cases over 50%, with broad wavelength tunability. The use of Ag<sub>2</sub>S and Ag<sub>2</sub>Se QDs extends the accessible emission wavelengths to the NIR-II window, which was not possible using conventional Cd-based QDs. Meanwhile, Si QDs and emerging graphene QDs provide advantages in terms of biocompatibility, the abundance of their component elements, and the ability to form covalent bonds with organic ligands. The best-quality Cd-free QDs have achieved optical performance matching that of Cd-based QDs in several applications. The low toxicity of their components has relieved some of the concerns associated with their use *in vivo* and has improved their prospects for future clinical applications. Moreover, these Cd-free QDs exhibit diverse and unique optical properties such as long PL lifetime, large multi-photon absorbance cross section, considerable near-IR absorbance, and upconverted emission. These distinguishing features can expand their use to novel applications including time-gated imaging, multi-photon imaging, photoacoustic imaging, and upconversion imaging. Nonetheless, many opportunities remain to improve the engineering of Cd-free QDs to achieve better physicochemical properties and to further enrich their surface chemistry. Further

1  
2  
3 investigations of their fate and toxicological impact in different biological models are urgently  
4  
5 needed. New techniques and instrumentation that fully exploit the advantages of these materials  
6  
7 must be further developed, standardized, and commercialized. Based on this comprehensive  
8  
9 survey of the Cd-free QD literature, here we summarize the current status, trends, and emerging  
10  
11 directions in the synthesis and biomedical applications of Cd-free QDs.  
12  
13  
14

15 **(1) Quantum Dot Synthesis and Functionalization:**  
16

- 17 (a) Mature and reproducible synthesis methods are needed for consistent production of  
18  
19 monodispersed Cd-free QDs with high PL intensity, narrow PL spectral width and broad  
20  
21 wavelength tunability. The optimization of synthesis is a case-by-case challenge depending  
22  
23 on the specific type of Cd-free QD. Also, strategies to avoid or to deliberately introduce  
24  
25 defects must be investigated based on PL mechanism (*e.g.* band-edge emission or  
26  
27 internal/surface defect-related emission) of the Cd-free QDs. For CuInS<sub>2</sub>, AgInS<sub>2</sub> and ZnO  
28  
29 QDs, high QY has been reported in recent studies, but their emission spectra remain broad,  
30  
31 primarily due to polydispersity, and this can limit their use in multiplexed imaging and  
32  
33 other advanced applications. Improved synthesis methods, with better control of size,  
34  
35 stoichiometry, and surface passivation, along with improved fundamental understanding of  
36  
37 all sources of emission broadening are needed to expand the range of applications of these  
38  
39 QDs. Although InP QDs exhibit high QY with narrower emission spectra, they are  
40  
41 typically prepared from expensive and pyrophoric precursors that discourage larger-scale  
42  
43 production and application. For Ag<sub>2</sub>S and Ag<sub>2</sub>Se QDs, improving the PL QY in the near-IR  
44  
45 range remains an important goal. Si QDs remain relatively less understood, with  
46  
47  
48  
49  
50  
51  
52

1  
2  
3 dramatically different results obtained from QDs produced by solution-phase and high-  
4  
5 temperature gas-phase synthesis. Although high QYs have been reported, such materials  
6  
7 can be produced by very few labs, limiting their broader application. Controlled synthesis  
8  
9 of graphene QDs is less mature than the other materials discussed here. Improving the  
10  
11 wavelength tunability of these QDs and using inexpensive and environmentally-friendly  
12  
13 starting materials are important research directions. In contrast to the best developed Cd-  
14  
15 based QDs, particularly CdSe/ZnS QDs, which are available commercially as relatively  
16  
17 standardized products and whose synthesis has been widely replicated, most of the Cd-free  
18  
19 QDs are not commercially available and cannot readily be produced by research groups  
20  
21 without prior QD synthesis experience. Inter-laboratory reproducibility and consistency  
22  
23 remains a major challenge for many of these materials. Standardized, reproducible  
24  
25 protocols are essential for clinical translation of these materials.  
26  
27  
28  
29  
30

- 31  
32 (b) The preparation of Cd-free QDs that retain their bright PL and exhibit long-term colloidal  
33  
34 stability in water and biological media remains an important need. Two general routes to  
35  
36 producing high-performance Cd-free QDs in aqueous media are possible: (1) direct  
37  
38 synthesis of hydrophilic QDs in water or hydrophilic solvents and (2) phase transfer of  
39  
40 hydrophobic QDs into the aqueous phase. The former method requires identification of  
41  
42 appropriate ligands and reaction conditions for nanocrystal growth. For example, several  
43  
44 studies on aqueous synthesis of CuInS<sub>2</sub> QDs selected ligands based on the hard-soft acid-  
45  
46 base theory to balance the reactivity of the different cations. The optimal ligands and  
47  
48 reaction conditions are material-specific, which limits the ability to adapt existing protocols  
49  
50  
51  
52

1  
2  
3 to new QD materials. For phase transfer of Cd-free QDs, researchers can build upon  
4 strategies used for modifying Cd-based QDs and other nanocrystals. However, differences  
5 in both QD composition and surface ligands used during synthesis require unique surface  
6 chemistry, such that methods used for other materials cannot always be directly applied to  
7 Cd-free QDs. For example, exchange of organothiol ligands on Cd-free QDs for  
8 hydrophilic thiol ligands may result in unsuccessful/incomplete ligand exchange or PL  
9 quenching. Encapsulation using polymers or silica shells solves these problems but is  
10 usually accompanied by a substantial size increase. Improved material-specific phase  
11 transfer approaches are still needed for most of the Cd-free QDs.

- 12  
13  
14  
15  
16  
17  
18  
19  
20  
21  
22  
23  
24 (c) The biofunctionalization of Cd-free QDs is in a relatively early stage of development, and  
25 advances are expected to further increase targeting specificity, biomolecule sensitivity, and  
26 gene/drug loading efficiency for a diverse array of applications. The potential of  
27 unfunctionalized Cd-free QDs of appropriate size and surface passivation for tumor  
28 imaging based on passive targeting has been demonstrated for several types of Cd-free  
29 QDs. Molecules including folic acid and anti-VEGF have also been widely used to  
30 functionalize Cd-free QDs for targeting general classes of tumors. In the coming years, we  
31 can expect that ligands for targeting specific tumor markers, multivalent ligands, and  
32 mixed ligands that only target cells expressing specific combinations of biomarkers will  
33 further increase the targeting specificity of Cd-free QDs. For drug/gene delivery,  
34 maximizing loading capacity may lead to compromised optical properties and/or reduced  
35 biocompatibility. For example, increasing the positive surface charge of Cd-free QDs could

1  
2  
3 result in more adsorption of negatively-charged drugs/genes, but the toxicity induced by  
4 the highly positively charged nanocomplexes raises new concerns. In such trade-off  
5 situations, a balance must be found to optimize overall performance in specific delivery  
6 applications. Cd-free QDs will continue to develop in two roles for delivery applications,  
7 (1) those in which QDs are directly conjugated with the drug or gene and (2) those in  
8 which they are encapsulated together with the therapeutic cargo in a larger carrier to serve  
9 as optical probes.

- 10  
11  
12  
13  
14  
15  
16  
17  
18  
19  
20 (d) The integration of Cd-free QDs with other contrast agents (*e.g.* radioactive labels, gold NPs,  
21 magnetic ions or NPs, and Raman tags) for multimodal and multispectral imaging provides  
22 a cross evaluation approach for acquiring comprehensive information to understand the  
23 complex nature of tumors and other disease states. The advantages of optical imaging,  
24 including high spatial resolution, low cost, and high scanning speed, make it  
25 complementary to CT, MRI, PET and SPECT imaging techniques. Initial attempts to  
26 integrate multiple imaging methods have included co-encapsulation of multiple contrast  
27 agents in polymer assemblies or co-synthesis of different types of labels in one reaction  
28 system. Both the design of new multi-modal probes and development of integrated imaging  
29 systems required to fully exploit the possibilities enabled by these new probes will remain  
30 fruitful research areas in the coming years.

31  
32  
33  
34  
35  
36  
37  
38  
39  
40  
41  
42  
43  
44  
45  
46  
47  
48  
49  
50  
51  
52  
53  
54  
55  
56  
57  
58  
59  
60  
**(2) Understanding of Quantum Dot Behavior in Living Systems:**

1  
2  
3 Biodistribution and toxicity profiles of Cd-free QDs must be more fully understood and  
4  
5 mechanistically related to their size, shape, surface properties, administration method and the  
6  
7 applied animal models. Circulation and retention times, which are crucial for long-term imaging,  
8  
9 have been shown to vary substantially for Cd-free QDs of different sizes, with and without  
10  
11 targeting ligands. The most common fates of the Cd-free QDs were 1) accumulation in the RES  
12  
13 organs and 2) excretion. The dominant pathway is mainly determined by hydrodynamic size, in  
14  
15 the actual state of aggregation in which they are present *in vivo*, but is also influenced by the QD  
16  
17 type and surface properties. Toxicity evaluation of Cd-free QDs requires comparative studies  
18  
19 between different types of QDs and more systematic studies on various cell lines and animal  
20  
21 models. Although Cd-free QDs such as InP, CuInS<sub>2</sub>, doped ZnSe and Ag<sub>2</sub>Se QDs do not contain  
22  
23 Cd or other highly toxic elements, their components (*e.g.* In, Se) are not completely benign in  
24  
25 biological systems. The release profile of these elements and biological responses to them must  
26  
27 be more fully characterized. For graphene QDs and Si QDs, which are based on nontoxic  
28  
29 elements, attention should be drawn to toxicity induced by phenomena including immune  
30  
31 response and generation of ROS as well as to their long-term fate. To date, although some  
32  
33 studies have reported reduced toxicity from Cd-free QDs compared to Cd-based QDs at the same  
34  
35 concentration, this information must be carefully evaluated according to their ability to also  
36  
37 achieve the same performance at the same concentration in applications. Moreover, the diversity  
38  
39 of methods used for evaluation of *in vivo* and *in vitro* toxicity profiles make intercomparison of  
40  
41 results challenging or impossible. Going forward, more uniform standards for toxicology studies  
42  
43  
44  
45  
46  
47  
48  
49  
50  
51  
52  
53

1  
2  
3 of QDs, and greater involvement of the traditional toxicology research community, are needed to  
4  
5  
6 move Cd-free QDs closer to clinical application.

7  
8 **(3) New Applications and Technologies**  
9

10 (a) Magnetic manipulation combined with optical imaging using combined or coupled  
11  
12 superparamagnetic and photoluminescent QDs or superparamagnetic and plasmonic NPs  
13  
14 opens up possibilities for highly multiplexed analysis. Such structures enable the use of  
15  
16 external magnetic fields to separate targets by magnetic mobility. Pairing these with  
17  
18 hyperspectral imaging allows multiplexing by emission or absorbance color. Together, this  
19  
20 enables two-dimensional multiplexing for analysis of very complex mixtures of  
21  
22 biomolecules. The same materials can be used for simultaneous cell labeling and magnetic  
23  
24 sorting. Combining magnetic sorting with optical labeling in this way can enhance  
25  
26 sensitivity and specificity of biomarker detection. Such structures can also be used for  
27  
28 magnetically enhanced targeted delivery of drugs and genes. Magnetic-plasmonic QDs can  
29  
30 serve as magnetically guided probes for dark field imaging, photoacoustic tomography in  
31  
32 the IR, photothermal imaging, and photothermal therapy.  
33  
34  
35  
36  
37  
38

39 (b) Another new direction is multivariate near-IR flow cytometry which will allow the use of  
40  
41 this cell-sorting technique with little or no sample preparation<sup>99,549,550</sup>. With near-IR labels,  
42  
43 even whole blood samples can be analyzed, as blood has minimal absorbance in the near-  
44  
45 IR region<sup>132</sup>. The Cd-free QDs discussed here are more stable than the near-IR organic  
46  
47 dyes and also have narrower emission bands and broad excitation spectra, which facilitate  
48  
49 multiplexed detection. This QD technology can also be coupled to microbead capture  
50  
51  
52

1  
2  
3 technology for enhanced detection and analysis of the expression of specific soluble  
4 proteins and of exosomes, which are signatures of specific diseases.  
5  
6

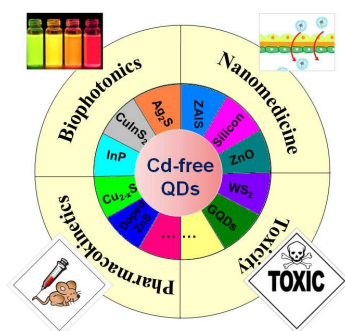
- 7  
8 (c) Newly emerging applications that exploit unique optical properties of Cd-free QDs,  
9 including those mentioned above, will benefit from the development and  
10 commercialization of corresponding imaging systems. For near-IR imaging, multi-photon  
11 imaging and time-gated imaging, a specific QD formulation may require excitation with a  
12 nonstandard wavelength, pulse duration, and/or pulse frequency. The QDs may exhibit PL  
13 at non-standard wavelengths or with PL lifetimes much different from conventional dyes.  
14 Fully exploiting these new probes thus requires specialized optical setups that provide the  
15 excitation and collect the PL in a spatially and temporarily constrained way, which present  
16 a challenge for biological and medical researchers. The availability of standard  
17 configurations of the imaging tools for these methods can increase the signal-to-noise ratio  
18 and allow these imaging techniques to go beyond the current stage of proof-of-concept  
19 studies to widespread practical use. This also extends to multimodal imaging setups that,  
20 for example, combine ultrasound, photoacoustic, and PL imaging in ways that fully exploit  
21 the possibilities opened up by new multimodal imaging probes.  
22  
23  
24  
25  
26  
27  
28  
29  
30  
31  
32  
33  
34  
35  
36  
37  
38  
39  
40  
41  
42  
43

#### 44 **Acknowledgements:**

45  
46 This review was prepared with support from the National Basic Research Program of China  
47 (2012CB85802 & 2015CB352005), National Natural Science Foundation of China (61235012,  
48 61335001, 81301318, & 81501213), Guangdong Natural Science Foundation  
49  
50  
51  
52  
53  
54 238  
55  
56  
57  
58  
59  
60

(2014A030312008), Basic Research Foundation of Shenzhen (JCYJ20140418095735543, JCYJ20140418091413563 & JCYJ20140418182819164), China Scholarship Council (CSC), Singapore Ministry of Education (Grants Tier 2 MOE2010-T2-2-010 (M4020020.040 ARC2/11) and Tier 1 M4010360.040 RG29/10), NTU-NHG Innovation Collaboration Grant (No. M4061202.040), NTU-A\*STAR Silicon Technologies, Centre of Excellence under the program grant No. 11235100003, School of Electrical and Electronic Engineering at NTU. The work in Buffalo was supported by The New York State Center of Excellence in Materials Informatics and by a grant from the Research Foundation of SUNY.

### TOC figure:



### Biographies

1  
2  
3 **Gaixia Xu** is a professor in College of Optoelectronic Engineering at Shenzhen University. She  
4 received her PhD degree from Biomedical Engineering in Zhejiang University in 2005.  
5  
6 Following that, she completed her postdoctoral researches at Shenzhen University from 2005 to  
7  
8 2007 and at the University at Buffalo, State University of New York from 2007 to 2008. Her  
9  
10 interests include the optical tracking/drug delivery/cancer theranostics by using nanoparticles,  
11  
12 and the biomedical applications of multi-modal microscopy and nanoscopy.  
13  
14  
15  
16  
17  
18  
19

20 **Shuwen Zeng** received her Ph.D. from School of Electrical and Electronic Engineering at  
21  
22 Nanyang Technological University. She is currently working as a Postdoctoral Research Fellow  
23  
24 at CNRS-International-NTU-THALES Research Alliances (CINTRA)/UMI 3288, Singapore.  
25  
26 Her main research interests focus on nanomaterials preparation and their sensing applications.  
27  
28  
29  
30

31 **Butian Zhang** is a Ph.D. student under the guidance of Prof. Ken Tye Yong in School of  
32  
33 Electrical and Electronic Engineering at the Nanyang Technological University in Singapore.  
34  
35 She received her B.S. degree of Engineering from Shandong University in China in 2012. Her  
36  
37 research interests include synthesis and surface functionalization of quantum dots for biomedical  
38  
39 applications.  
40  
41  
42  
43  
44  
45

46 **Mark T. Swihart** is a UB Distinguished Professor of Chemical and Biological Engineering and  
47  
48 Executive Director of the New York State Center of Excellence in Materials Informatics at the  
49  
50 University at Buffalo (SUNY). He earned his Ph.D. in chemical engineering from the University  
51  
52

1  
2  
3 at Minnesota in 1997 followed by one year of post-doctoral research in mechanical engineering  
4  
5 at the University of Minnesota. His research interests are in the synthesis and processing of  
6  
7 inorganic nanomaterials for applications from energy harvesting and conversion to nanomedicine.  
8  
9 He has received awards for his research from ACS, the Electrochemical Society, and the  
10  
11 American Association for Aerosol Research, and is a fellow of the American Association for the  
12  
13 Advancement of Science.  
14  
15  
16  
17  
18  
19

20 ***Ken-Tye Yong*** is an Associate Professor in School of Electrical and Electronic Engineering at  
21  
22 the Nanyang Technological University. He received his PhD from Chemical and Biological  
23  
24 Engineering in SUNY at Buffalo in 2006. Following completion of his graduate studies, he did  
25  
26 his post-doc at the Institute for Lasers, Photonics and Biophotonics in SUNY at Buffalo from  
27  
28 2006 to 2009, where his research focus is in the area of biophotonics and nanomedicine.  
29  
30 Currently, His research group interests include engineering nanomaterials for biophotonic and  
31  
32 nanomedicine applications, fabricating of miniaturized devices for drug delivery, developing  
33  
34 nanosensors for biodetection, and devices for nanophotonics studies.  
35  
36  
37  
38  
39  
40

41 ***Paras N. Prasad*** is a SUNY Distinguished Professor of Chemistry, Physics, Electrical  
42  
43 Engineering and Medicine; the Samuel P. Capen Chair of Chemistry; and the Executive Director  
44  
45 of Institute for Lasers, Photonics, and Biophotonics, University at Buffalo, State University of  
46  
47 New York. He was named among the top 50 science and technology leaders in the world by  
48  
49 Scientific American in 2005, and was recognized as the highly cited researcher in both chemistry  
50  
51  
52

1  
2  
3 and materials science fields by Thomas Reuters in 2014. He has published over 750 scientific  
4  
5 and technical papers, four monographs (Introduction to Nanomedicine and Nanobioengineering,  
6  
7 Nanophotonics, Introduction to Biophotonics, Introduction to Nonlinear Optical Effects in  
8  
9 Molecules and Polymers), and eight edited books. He has received many scientific awards and  
10  
11 honors (Morley Medal; Schoellkopf Medal; Guggenheim Fellowship; SPIE President's Gold  
12  
13 Medal ; Honorary Doctorate from KTH , Sweden and from the Aix-Marseille ;Fellow of the APS,  
14  
15 OSA, and SPIE, etc). His interests include biophotonics, nanophotonics, nanomedicine,  
16  
17 metamaterials, and solar cells.  
18  
19  
20  
21  
22  
23  
24  
25  
26  
27  
28  
29  
30  
31  
32  
33  
34  
35  
36  
37  
38  
39  
40  
41  
42  
43  
44  
45  
46  
47  
48  
49  
50  
51  
52  
53

## 10.0 References

- (1) Prasad, P. N. *Nanophotonics*; Wiley: Hoboken, NJ, 2004.
- (2) Prasad, P. N. *Introduction to Biophotonics*; Wiley-Interscience: Hoboken, NJ, 2003.
- (3) Prasad, P. N. *Introduction to Nanomedicine and Nanobioengineering*; John Wiley & Sons: Hoboken, NJ, 2012.
- (4) Liu, J.; Lau, S. K.; Varma, V. A.; Moffitt, R. A.; Caldwell, M.; Liu, T.; Young, A. N.; Petros, J. A.; Osunkoya, A. O.; Krogstad, T. Molecular Mapping of Tumor Heterogeneity on Clinical Tissue Specimens with Multiplexed Quantum Dots. *ACS Nano* **2010**, *4*, 2755-2765.
- (5) Montalti, M.; Cantelli, A.; Battistelli, G. Nanodiamonds and Silicon Quantum Dots: Ultrastable and Biocompatible Luminescent Nanoprobes for Long-Term Bioimaging. *Chem. Soc. Rev.* **2015**, *44*, 4853-4921.
- (6) Liu, Q.; Guo, B.; Rao, Z.; Zhang, B.; Gong, J. R. Strong Two-Photon-Induced Fluorescence from Photostable, Biocompatible Nitrogen-Doped Graphene Quantum Dots for Cellular and Deep-Tissue Imaging. *Nano Lett.* **2013**, *13*, 2436-2441.
- (7) Koneswaran, M.; Narayanaswamy, R. Ultrasensitive Detection of Vitamin B6 Using Functionalised CdS/ZnS Core-Shell Quantum Dots. *Sensor. Actuat. B-Chem.* **2015**, *210*, 811-816.
- (8) Jiang, P.; Zhu, C.-N.; Zhang, Z.-L.; Tian, Z.-Q.; Pang, D.-W. Water-Soluble Ag<sub>2</sub>S Quantum Dots for Near-Infrared Fluorescence Imaging *in vivo*. *Biomaterials* **2012**, *33*, 5130-5135.
- (9) Zhang, B.; Wang, Y.; Yang, C.; Hu, S.; Gao, Y.; Zhang, Y.; Wang, Y.; Demir, H. V.; Liu, L.; Yong, K.-T. The Composition Effect on the Optical Properties of Aqueous Synthesized Cu-In-S and Zn-Cu-In-S Quantum Dot Nanocrystals. *Phys. Chem. Chem. Phys.* **2015**, *17*, 25133-25141.
- (10) Cho, E.; Jang, H.; Lee, J.; Jang, E. Modeling on the Size Dependent Properties of InP Quantum Dots: A Hybrid Functional Study. *Nanotechnology* **2013**, *24*, 215201-215201.
- (11) Vanmaekelbergh, D. I.; Van Vugt, L. K.; Bakker, H. E.; Rabouw, F. T.; Nijs, B. d.; van Dijk-Moes, R. J.; van Huis, M. A.; Baesjou, P. J.; van Blaaderen, A. Shape-Dependent Multiexciton Emission and Whispering Gallery Modes in Supraparticles of CdSe/Multishell Quantum Dots. *ACS Nano* **2015**, *9*, 3942-3950.
- (12) Zhang, B.; Hu, R.; Wang, Y.; Yang, C.; Liu, X.; Yong, K.-T. Revisiting the principles of preparing aqueous quantum dots for biological applications: the effects of surface ligands on the physicochemical properties of quantum dots. *RSC Adv.* **2014**, *4*, 13805-13816.

- 1  
2  
3  
4  
5  
6  
7  
8  
9  
10  
11  
12  
13  
14  
15  
16  
17  
18  
19  
20  
21  
22  
23  
24  
25  
26  
27  
28  
29  
30  
31  
32  
33  
34  
35  
36  
37  
38  
39  
40  
41  
42  
43  
44  
45  
46  
47  
48  
49  
50  
51  
52  
53
- (13) Galloway, J. F.; Winter, A.; Lee, K. H.; Park, J. H.; Dvoracek, C. M.; Devreotes, P.; Searson, P. C. Quantitative Characterization of the Lipid Encapsulation of Quantum Dots for Biomedical Applications. *Nanomed-Nanotechnol.* **2012**, *8*, 1190-1199.
- (14) Ren, M.; Xu, H.; Huang, X.; Kuang, M.; Xiong, Y.; Xu, H.; Xu, Y.; Chen, H.; Wang, A. Immunochromatographic Assay for Ultrasensitive Detection of Aflatoxin B1 in Maize by Highly Luminescent Quantum Dot Beads. *ACS Appl. Mater. Interf.* **2014**, *6*, 14215-14222.
- (15) Zhan, N.; Palui, G.; Mattoussi, H. Preparation of Compact Biocompatible Quantum Dots Using Multicoordinating Molecular-Scale Ligands based on a Zwitterionic Hydrophilic Motif and Lipoic Acid Anchors. *Nat. Protoc.* **2015**, *10*, 859-874.
- (16) Liu, H.; Xu, S.; He, Z.; Deng, A.; Zhu, J.-J. Supersandwich Cytosensor for Selective and Ultrasensitive Detection of Cancer Cells Using Aptamer-DNA Concatamer-Quantum Dots Probes. *Anal. Chem.* **2013**, *85*, 3385-3392.
- (17) Li, M.; Wang, Q.; Shi, X.; Hornak, L. A.; Wu, N. Detection of Mercury (II) by Quantum Dot/DNA/Gold Nanoparticle Ensemble based Nanosensor via Nanometal Surface Energy Transfer. *Anal. Chem.* **2011**, *83*, 7061-7065.
- (18) Wegner, K. D.; Lindén, S.; Jin, Z.; Jennings, T. L.; Khoulati, R. e.; van Bergen en Henegouwen, P. M.; Hildebrandt, N. Nanobodies and Nanocrystals: Highly Sensitive Quantum Dot-Based Homogeneous FRET Immunoassay for Serum-Based EGFR Detection. *Small* **2014**, *10*, 734-740.
- (19) Cassette, E.; Helle, M.; Bezdetnaya, L.; Marchal, F.; Dubertret, B.; Pons, T. Design of New Quantum Dot Materials for Deep Tissue Infrared Imaging. *Adv. Drug Deliv. Rev.* **2013**, *65*, 719-731.
- (20) Sasaki, A.; Tsukasaki, Y.; Komatsuzaki, A.; Sakata, T.; Yasuda, H.; Jin, T. Recombinant Protein (EGFP-Protein G)-Coated PbS Quantum Dots for *in vitro* and *in vivo* Dual Fluorescence (Visible and Second-NIR) Imaging of Breast Tumor. *Nanoscale* **2014**, *7*, 5115-5119.
- (21) Hong, G.; Robinson, J. T.; Zhang, Y.; Diao, S.; Antaris, A. L.; Wang, Q.; Dai, H. *In vivo* Fluorescence Imaging with Ag<sub>2</sub>S Quantum Dots in the Second Near-Infrared Region. *Angew. Chemie* **2012**, *51*, 9818-9821.
- (22) Tan, L.; Wan, A.; Zhao, T.; Huang, R.; Li, H. Aqueous Synthesis of Multidentate-Polymer-Capping Ag<sub>2</sub>Se Quantum Dots with Bright Photoluminescence Tunable in a Second Near-Infrared Biological Window. *ACS Appl. Mater. Interf.* **2014**, *6*, 6217-6222.
- (23) Zrazhevskiy, P.; True, L. D.; Gao, X. Multicolor Multicycle Molecular Profiling with Quantum Dots for Single-Cell Analysis. *Nat. Protoc.* **2013**, *8*, 1852-1869.
- (24) Probst, C. E.; Zrazhevskiy, P.; Bagalkot, V.; Gao, X. Quantum Dots As a Platform for Nanoparticle Drug Delivery Vehicle Design. *Adv. Drug Deliv. Rev.* **2013**, *65*, 703-718.

- 1  
2  
3  
4 (25) Zheng, F.; Zhang, P.; Xi, Y.; Chen, J.; Li, L.; Zhu, J.-J. Aptamer/Graphene Quantum Dots  
5 Nanocomposite Capped Fluorescent Mesoporous Silica Nanoparticles for Intracellular  
6 Drug Delivery and Real-time Monitoring of Drug Release. *Anal. Chem.* **2015**, *87*, 11739-  
7 11745.
- 8  
9 (26) Torchilin, V. P. Multifunctional, Stimuli-Sensitive Nanoparticulate Systems for Drug  
10 Delivery. *Nat. Rev. Drug Discov.* **2014**, *13*, 813-827.
- 11  
12 (27) Bruneau, A.; Fortier, M.; Gagne, F.; Gagnon, C.; Turcotte, P.; Tayabali, A.; Davis, T. A.;  
13 Auffret, M.; Fournier, M. *In vitro* Immunotoxicology of Quantum Dots and Comparison  
14 with Dissolved Cadmium and Tellurium. *Environ. Toxicol.* **2015**, *30*, 9-25.
- 15  
16 (28) Pichaandi, J.; van Veggel, F. C. Near-Infrared Emitting Quantum Dots: Recent Progress  
17 on Their Synthesis and Characterization. *Coord. Chem. Rev.* **2014**, *263*, 138-150.
- 18  
19 (29) Corazzari, I.; Gilardino, A.; Dalmazzo, S.; Fubini, B.; Lovisolo, D. Localization of  
20 CdSe/ZnS Quantum Dots in the Lysosomal Acidic Compartment of Cultured Neurons  
21 and Its Impact on Viability: Potential Role of Ion Release. *Toxicol. in vitro* **2013**, *27*, 752-  
22 759.
- 23  
24 (30) Li, K.; Chen, J.; Bai, S.; Wen, X.; Song, S.; Yu, Q.; Li, J.; Wang, Y. Intracellular  
25 Oxidative Stress and Cadmium Ions Release Induce Cytotoxicity of Unmodified  
26 Cadmium Sulfide Quantum Dots. *Toxicol. in vitro* **2009**, *23*, 1007-1013.
- 27  
28 (31) Yong, K.-T.; Law, W.-C.; Hu, R.; Ye, L.; Liu, L.; Swihart, M. T.; Prasad, P. N.  
29 Nanotoxicity Assessment of Quantum Dots: From Cellular to Primate Studies. *Chem.*  
30 *Soc. Rev.* **2013**, *42*, 1236-1250.
- 31  
32 (32) Tsoi, K. M.; Dai, Q.; Alman, B. A.; Chan, W. C. Are Quantum Dots Toxic? Exploring the  
33 Discrepancy between Cell Culture and Animal Studies. *Acc. Chem. Res.* **2012**, *46*, 662-  
34 671.
- 35  
36 (33) Tan, S. J.; Jana, N. R.; Gao, S.; Patra, P. K.; Ying, J. Y. Surface-Ligand-Dependent  
37 Cellular Interaction, Subcellular Localization, and Cytotoxicity of Polymer-Coated  
38 Quantum Dots. *Chem. Mater.* **2010**, *22*, 2239-2247.
- 39  
40 (34) Johnson, C. M.; Pate, K. M.; Shen, Y.; Viswanath, A.; Tan, R.; Benicewicz, B. C.; Moss,  
41 M. A.; Greytak, A. B. A Methacrylate-based Polymeric Imidazole Ligand Yields  
42 Quantum Dots with Low Cytotoxicity and Low Nonspecific Binding. *J. Colloid Interf.*  
43 *Sci.* **2015**, *458*, 310-314.
- 44  
45 (35) Liu, L.; Yong, K.-T.; Roy, I.; Law, W.-C.; Ye, L.; Liu, J.; Liu, J.; Kumar, R.; Zhang, X.;  
46 Prasad, P. N. Bioconjugated Pluronic Triblock-Copolymer Micelle-Encapsulated  
47 Quantum Dots for Targeted Imaging of Cancer: *in vitro* and *in vivo* Studies. *Theranostics*  
48 **2012**, *2*, 705-713.
- 49  
50  
51  
52  
53  
54  
55  
56  
57  
58  
59  
60

- 1  
2  
3  
4 (36) Deng, D.; Chen, Y.; Cao, J.; Tian, J.; Qian, Z.; Achilefu, S.; Gu, Y. High-Quality  
5 CuInS<sub>2</sub>/ZnS Quantum Dots for *in vitro* and *in vivo* Bioimaging. *Chem. Mater.* **2012**, *24*,  
6 3029-3037.
- 7  
8 (37) Hussain, S.; Won, N.; Nam, J.; Bang, J.; Chung, H.; Kim, S. One-Pot Fabrication of  
9 High-Quality InP/ZnS (Core/Shell) Quantum Dots and Their Application to Cellular  
10 Imaging. *ChemPhysChem* **2009**, *10*, 1466-1470.
- 11  
12 (38) Erogbogbo, F.; Yong, K. T.; Roy, I.; Hu, R.; Law, W. C.; Zhao, W. W.; Ding, H.; Wu, F.;  
13 Kumar, R.; Swihart, M. T. *et al.* *In vivo* Targeted Cancer Imaging, Sentinel Lymph Node  
14 Mapping and Multi-Channel Imaging with Biocompatible Silicon Nanocrystals. *ACS*  
15 *Nano* **2011**, *5*, 413-423.
- 16  
17 (39) Gary, D. C.; Glassy, B. A.; Cossairt, B. M. Investigation of Indium Phosphide Quantum  
18 Dot Nucleation and Growth Utilizing Triarylsilylphosphine Precursors. *Chem. Mater.*  
19 **2014**, *26*, 1734-1744.
- 20  
21 (40) Zan, F.; Ren, J. Gas-Liquid Phase Synthesis of Highly Luminescent InP/ZnS Core/Shell  
22 Quantum Dots Using Zinc Phosphide As a New Phosphorus Source. *J. Mater. Chem.*  
23 **2012**, *22*, 1794-1799.
- 24  
25 (41) Liu, B. R.; Winiarz, J. G.; Moon, J.-S.; Lo, S.-Y.; Huang, Y.-W.; Aronstam, R. S.; Lee, H.-  
26 J. Synthesis, Characterization and Applications of Carboxylated and Polyethylene-  
27 Glycolated Bifunctionalized InP/ZnS Quantum Dots in Cellular Internalization Mediated  
28 by Cell-Penetrating Peptides. *Colloid. Surface B* **2013**, *111*, 162-170.
- 29  
30 (42) Yong, K.-T.; Ding, H.; Roy, I.; Law, W.-C.; Bergey, E. J.; Maitra, A.; Prasad, P. N.  
31 Imaging Pancreatic Cancer Using Bioconjugated InP Quantum Dots. *ACS Nano* **2009**, *3*  
32 (3), 502-510.
- 33  
34 (43) van der Stam, W.; Berends, A. C.; Rabouw, F. T.; Willhammar, T.; Ke, X.; Meeldijk, J. D.;  
35 Bals, S.; de Mello Donega, C. Luminescent CuInS<sub>2</sub> Quantum Dots by Partial Cation  
36 Exchange in Cu<sub>2-x</sub>S Nanocrystals. *Chem. Mater.* **2015**, *27*, 621-628.
- 37  
38 (44) Speranskaya, E. S.; Beloglazova, N. V.; Abé, S.; Aubert, T.; Smet, P. F.; Poelman, D.;  
39 Goryacheva, I. Y.; De Saeger, S.; Hens, Z. Hydrophilic, Bright CuInS<sub>2</sub> Quantum Dots as  
40 Cd-free Fluorescent Labels in Quantitative Immunoassay. *Langmuir* **2014**, *30*, 7567-  
41 7575.
- 42  
43 (45) Kang, X.; Huang, L.; Yang, Y.; Pan, D. Scaling up the Aqueous Synthesis of Visible Light  
44 Emitting Multinary AgInS<sub>2</sub>/ZnS Core/Shell Quantum Dots. *J. Phys. Chem. C* **2015**, *119*,  
45 7933-7940.
- 46  
47 (46) Chang, J.-Y.; Wang, G.-Q.; Cheng, C.-Y.; Lin, W.-X.; Hsu, J.-C. Strategies for  
48 Photoluminescence Enhancement of AgInS<sub>2</sub> Quantum Dots and Their Application as  
49 Bioimaging Probes. *J. Mater. Chem.* **2012**, *22*, 10609-10618.
- 50  
51  
52  
53  
54  
55  
56  
57  
58  
59  
60

- 1  
2  
3  
4 (47) Chen, G.; Tian, F.; Zhang, Y.; Zhang, Y.; Li, C.; Wang, Q. Tracking of Transplanted  
5 Human Mesenchymal Stem Cells in Living Mice using Near-Infrared Ag<sub>2</sub>S Quantum  
6 Dots. *Adv. Funct. Mater.* **2014**, *24*, 2481-2488.
- 7  
8 (48) Geszke-Moritz, M.; Clavier, G.; Lulek, J.; Schneider, R. Copper-or Manganese-Doped  
9 ZnS Quantum Dots as Fluorescent Probes for Detecting Folic Acid in Aqueous Media. *J.*  
10 *Lumin.* **2012**, *132*, 987-991.
- 11  
12 (49) Rajesh, C.; Phadnis, C. V.; Sonawane, K. G.; Mahamuni, S. Synthesis and Optical  
13 Properties of Copper-Doped ZnSe Quantum Dots. *Phys. Scripta* **2015**, *90*, 015803-  
14 015803.
- 15  
16 (50) Bacon, M.; Bradley, S. J.; Nann, T. Graphene Quantum Dots. *Part. Part. Syst. Charact.*  
17 **2014**, *31*, 415-428.
- 18  
19 (51) Zhu, S.; Zhang, J.; Qiao, C.; Tang, S.; Li, Y.; Yuan, W.; Li, B.; Tian, L.; Liu, F.; Hu, R.  
20 Strongly Green-Photoluminescent Graphene Quantum Dots for Bioimaging Applications.  
21 *Chem. Comm.* **2011**, *47*, 6858-6860.
- 22  
23 (52) Dey, S.; Govindaraj, A.; Biswas, K.; Rao, C. Luminescence Properties of Boron and  
24 Nitrogen Doped Graphene Quantum Dots Prepared from Arc-Discharge-Generated  
25 Doped Graphene Samples. *Chem. Phys. Lett.* **2014**, *595*, 203-208.
- 26  
27 (53) Cheng, X.; Lowe, S. B.; Reece, P. J.; Gooding, J. J. Colloidal Silicon Quantum Dots:  
28 From Preparation to the Modification of Self-Assembled Monolayers (SAMs) for Bio-  
29 applications. *Chem. Soc. Rev.* **2014**, *43*, 2680-2700.
- 30  
31 (54) He, Y.; Zhong, Y.; Peng, F.; Wei, X.; Su, Y.; Lu, Y.; Su, S.; Gu, W.; Liao, L.; Lee, S.-T.  
32 One-Pot Microwave Synthesis of Water-Dispersible, Ultraphoto- and pH-Stable, and  
33 Highly Fluorescent Silicon Quantum Dots. *J. Am. Chem. Soc.* **2011**, *133*, 14192-14195.
- 34  
35 (55) Pisanic Ii, T.; Zhang, Y.; Wang, T. Quantum Dots in Diagnostics and Detection: Principles  
36 and Paradigms. *Analyst* **2014**, *139*, 2968-2981.
- 37  
38 (56) Wang, Y.; Hu, R.; Lin, G.; Roy, I.; Yong, K.-T. Functionalized Quantum Dots for  
39 Biosensing and Bioimaging and Concerns on Toxicity. *ACS Appl. Mater. Interf.* **2013**, *5*,  
40 2786-2799.
- 41  
42 (57) Wegner, K. D.; Hildebrandt, N. Quantum Dots: Bright and Versatile *in vitro* and *in vivo*  
43 Fluorescence Imaging Biosensors. *Chem. Soc. Rev.* **2015**, *44*, 4792-4834.
- 44  
45 (58) Cunha-Reis, C.; El Haj, A. J.; Yang, X.; Yang, Y. Fluorescent Labeling of Chitosan for  
46 Use in Non-Invasive Monitoring of Degradation in Tissue Engineering. *J. Tissue Eng.*  
47 *Regen. Med.* **2013**, *7*, 39-50.
- 48  
49 (59) Chen, G.; Ågren, H.; Ohulchanskyy, T. Y.; Prasad, P. N. Light Upconverting Core-Shell  
50 Nanostructures: Nanophotonic Control for Emerging Applications. *Chem. Soc. Rev.* **2015**,  
51 *44*, 1680-1713.

- 1  
2  
3  
4 (60) Mattoussi, H.; Palui, G.; Na, H. B. Luminescent Quantum Dots as Platforms for Probing  
5 *in vitro* and *in vivo* Biological Processes. *Adv. Drug Deliv. Rev.* **2012**, *64*, 138-166.
- 6  
7 (61) Acharya, A. Luminescent Magnetic Quantum Dots for *in vitro/in vivo* Imaging and  
8 Applications in Therapeutics. *J. Nanosci. Nanotechnol.* **2013**, *13*, 3753-3768.
- 9  
10 (62) Lee, J.-E.; In, I.; Lee, H.; Lee, K. D.; Jeong, J. H.; Park, S. Y. Target Delivery and Cell  
11 Imaging Using Hyaluronic Acid-Functionalized Graphene Quantum Dots. *Mol.*  
12 *Pharmaceut.* **2013**, *10*, 3736-3744.
- 13  
14 (63) Minami, S. S.; Sun, B.; Popat, K.; Kauppinen, T.; Pleiss, M.; Zhou, Y.; Ward, M. E.;  
15 Floreancig, P.; Mucke, L.; Desai, T. Selective Targeting of Microglia by Quantum Dots. *J.*  
16 *Neuroinflammation* **2012**, *9*, 22-35.
- 17  
18 (64) Li, J.; Liu, F.; Shao, Q.; Min, Y.; Costa, M.; Yeow, E. K.; Xing, B. Enzyme-Responsive  
19 Cell-Penetrating Peptide Conjugated Mesoporous Silica Quantum Dot Nanocarriers for  
20 Controlled Release of Nucleus-Targeted Drug Molecules and Real-Time Intracellular  
21 Fluorescence Imaging of Tumor Cells. *Adv. Healthc. Mater.* **2014**, *3*, 1230-1239.
- 22  
23 (65) Erogbogbo, F.; Yong, K. T.; Roy, I.; Xu, G.; Prasad, P. N.; Swihart, M. T. Biocompatible  
24 Luminescent Silicon Quantum Dots for Imaging of Cancer Cells. *ACS Nano* **2008**, *2*,  
25 873-878.
- 26  
27 (66) Liu, J.-H.; Cao, L.; LeCroy, G. E.; Wang, P.; Meziani, M. J.; Dong, Y.; Liu, Y.; Luo, P. G.;  
28 Sun, Y.-P. Carbon “Quantum” Dots for Fluorescence Labeling of Cells. *ACS Appl. Mater.*  
29 *Interf.* **2015**, *7*, 19439-19445.
- 30  
31 (67) Aswathy, R. G.; Yoshida, Y.; Maekawa, T.; Kumar, D. S. Near-Infrared Quantum Dots for  
32 Deep Tissue Imaging. *Anal. Bioanal. Chem.* **2010**, *397*, 1417-1435.
- 33  
34 (68) Wang, L.-W.; Peng, C.-W.; Chen, C.; Li, Y. Quantum Dots-based Tissue and *in vivo*  
35 Imaging in Breast Cancer Researches: Current Status and Future Perspectives. *Breast*  
36 *Cancer Res. Treat.* **2015**, *151*, 7-17.
- 37  
38 (69) Markovic, Z. M.; Ristic, B. Z.; Arskin, K. M.; Klisic, D. G.; Harhaji-Trajkovic, L. M.;  
39 Todorovic-Markovic, B. M.; Kopic, D. P.; Kravic-Stevovic, T. K.; Jovanovic, S. P.;  
40 Milenkovic, M. M. Graphene Quantum Dots as Autophagy-Inducing Photodynamic  
41 Agents. *Biomaterials* **2012**, *33*, 7084-7092.
- 42  
43 (70) Ge, J.; Lan, M.; Zhou, B.; Liu, W.; Guo, L.; Wang, H.; Jia, Q.; Niu, G.; Huang, X.; Zhou,  
44 H.*et al.* A Graphene Quantum Dot Photodynamic Therapy Agent with High Singlet  
45 Oxygen Generation. *Nat. Comm.* **2014**, *5*, 4596-4604.
- 46  
47 (71) He, Y.; Wang, X.; Sun, J.; Jiao, S.; Chen, H.; Gao, F.; Wang, L. Fluorescent Blood  
48 Glucose Monitor by Hemin-Functionalized Graphene Quantum Dots based Sensing  
49 System. *Anal. Chim. Acta* **2014**, *810*, 71-78.
- 50  
51  
52  
53

- 1  
2  
3 (72) Nigam, P.; Waghmode, S.; Louis, M.; Wangnoo, S.; Chavan, P.; Sarkar, D. Graphene  
4 Quantum Dots Conjugated Albumin Nanoparticles for Targeted Drug Delivery and  
5 Imaging of Pancreatic Cancer. *J. Mater. Chem. B* **2014**, *2*, 3190-3195.  
6  
7 (73) Carbary-Ganz, J. L.; Welge, W. A.; Barton, J. K.; Utzinger, U. *In vivo* Molecular Imaging  
8 of Colorectal Cancer Using Quantum Dots Targeted to Vascular Endothelial Growth  
9 Factor Receptor 2 and Optical Coherence Tomography/Laser-Induced Fluorescence Dual-  
10 Modality Imaging. *J. Biomed. Opt.* **2015**, *20*, 096015-096015.  
11  
12 (74) Hafian, H.; Sukhanova, A.; Turini, M.; Chames, P.; Baty, D.; Pluot, M.; Cohen, J. H.;  
13 Nabiev, I.; Millot, J.-M. Multiphoton Imaging of Tumor Biomarkers with Conjugates of  
14 Single-Domain Antibodies and Quantum Dots. *Nanomed-Nanotechnol.* **2014**, *10*, 1701-  
15 1709.  
16  
17 (75) van Manen, H.-J.; Otto, C. Hybrid Confocal Raman Fluorescence Microscopy on Single  
18 Cells Using Semiconductor Quantum Dots. *Nano Lett.* **2007**, *7*, 1631-1636.  
19  
20 (76) Bharali, D. J.; Lucey, D. W.; Jayakumar, H.; Pudavar, H. E.; Prasad, P. N. Folate-  
21 Receptor-Mediated Delivery of InP Quantum Dots for Bioimaging Using Confocal and  
22 Two-Photon Microscopy. *J. Am. Chem. Soc.* **2005**, *127*, 11364-11371.  
23  
24 (77) Soenen, S. J.; Manshian, B. B.; Aubert, T.; Himmelreich, U.; Demeester, J.; De Smedt, S.  
25 C.; Hens, Z.; Braeckmans, K. Cytotoxicity of Cadmium-Free Quantum Dots and Their  
26 Use in Cell Bioimaging. *Chem. Res. Toxicol.* **2014**, *27*, 1050-1059.  
27  
28 (78) Qin, Y.; Zhou, Z.-W.; Pan, S.-T.; He, Z.-X.; Zhang, X.; Qiu, J.-X.; Duan, W.; Yang, T.;  
29 Zhou, S.-F. Graphene Quantum Dots Induce Apoptosis, Autophagy, and Inflammatory  
30 Response via p38 Mitogen-Activated Protein Kinase and Nuclear Factor- $\kappa$ B Mediated  
31 Signaling Pathways in Activated THP-1 Macrophages. *Toxicol.* **2015**, *327*, 62-76.  
32  
33 (79) Kara, A.; Ünak, P.; Selçuki, C.; Akça, Ö.; Medine, E. İ.; Sakarya, S. PHA-L Lectin and  
34 Carbohydrate Relationship: Conjugation with CdSe/CdS Nanoparticles, Radiolabeling  
35 and *in vitro* Affinities on MCF-7 cells. *J. Radioanal. Nucl. Chem.* **2014**, *299*, 807-813.  
36  
37 (80) Lee, D.-E.; Koo, H.; Sun, I.-C.; Ryu, J. H.; Kim, K.; Kwon, I. C. Multifunctional  
38 Nanoparticles for Multimodal Imaging and Theragnosis. *Chem. Soc. Rev.* **2012**, *41*, 2656-  
39 2672.  
40  
41 (81) Ding, X.; Liow, C. H.; Zhang, M.; Huang, R.; Li, C.; Shen, H.; Liu, M.; Zou, Y.; Gao, N.;  
42 Zhang, Z. *et al.* Surface Plasmon Resonance Enhanced Light Absorption and  
43 Photothermal Therapy in the Second Near-Infrared Window. *J. Am. Chem. Soc.* **2014**,  
44 *136*, 15684-15693.  
45  
46 (82) Wu, Q.; Chen, L.; Huang, L.; Wang, J.; Liu, J.; Hu, C.; Han, H. Quantum Dots Decorated  
47 Gold Nanorod as Fluorescent-Plasmonic Dual-Modal Contrasts Agent for Cancer  
48 Imaging. *Biosens. Bioelectron.* **2015**, *74*, 16-23.  
49  
50  
51  
52  
53  
54  
55  
56  
57  
58  
59  
60

- 1  
2  
3  
4 (83) Shi, Y.; Pan, Y.; Zhong, J.; Yang, J.; Zheng, J.; Cheng, J.; Song, R.; Yi, C. Facile  
5 Synthesis of Gadolinium (III) Chelates Functionalized Carbon Quantum Dots for  
6 Fluorescence and Magnetic Resonance Dual-Modal Bioimaging. *Carbon* **2015**, *93*, 742-  
7 750.
- 8  
9 (84) Chen, G.; Roy, I.; Yang, C.; Prasad, P. N. Nanochemistry and Nanomedicine for  
10 Nanoparticle-based Diagnostics and Therapy. *Chem. Rev.* **2016**, *116*, 2826-2885.
- 11  
12 (85) Farokhzad, O. C.; Langer, R. Nanomedicine: Developing Smarter Therapeutic and  
13 Diagnostic Modalities. *Adv. Drug Deliv. Rev.* **2006**, *58*, 1456-1459.
- 14  
15 (86) Rizzo, L. Y.; Theek, B.; Storm, G.; Kiessling, F.; Lammers, T. Recent Progress in  
16 Nanomedicine: Therapeutic, Diagnostic and Theranostic Applications. *Curr. Opin.*  
17 *Biotechnol.* **2013**, *24*, 1159-1166.
- 18  
19 (87) Caruso, F.; Hyeon, T.; Rotello, V. M. Nanomedicine. *Chem. Soc. Rev.* **2012**, *41*, 2537-  
20 2538.
- 21  
22 (88) Boisseau, P.; Loubaton, B. Nanomedicine, Nanotechnology in Medicine. *C. R. Phys.*  
23 **2011**, *12*, 620-636.
- 24  
25 (89) Singh, S.; Sharma, A.; Robertson, G. P. Realizing the Clinical Potential of Cancer  
26 Nanotechnology by Minimizing Toxicologic and Targeted Delivery Concerns. *Cancer*  
27 *Res.* **2012**, *72*, 5663-5668.
- 28  
29 (90) Bakalova, R.; Lazarova, D.; Nikolova, B.; Atanasova, S.; Zlateva, G.; Zhelev, Z.; Aoki, I.  
30 Delivery of Size-Controlled Long-Circulating Polymersomes in Solid Tumours,  
31 Visualized by Quantum Dots and Optical Imaging *in vivo*. *Biotechnol. Biotechnol. Equip.*  
32 **2015**, *29*, 175-180.
- 33  
34 (91) Guo, W.; Chen, N.; Tu, Y.; Dong, C.; Zhang, B.; Hu, C.; Chang, J. Synthesis of Zn-Cu-In-  
35 S/ZnS Core/Shell Quantum Dots with Inhibited Blue-Shift Photoluminescence and  
36 Applications for Tumor Targeted Bioimaging. *Theranostics* **2013**, *3*, 99-108.
- 37  
38 (92) Zhang, M.-Z.; Yu, R.-N.; Chen, J.; Ma, Z.-Y.; Zhao, Y.-D. Targeted Quantum Dots  
39 Fluorescence Probes Functionalized with Aptamer and Peptide for Transferrin Receptor  
40 on Tumor Cells. *Nanotechnology* **2012**, *23*, 485104-485104.
- 41  
42 (93) Erogbogbo, F.; Chang, C.-W.; May, J. L.; Liu, L.; Kumar, R.; Law, W.-C.; Ding, H.;  
43 Yong, K. T.; Roy, I.; Sheshadri, M. Bioconjugation of Luminescent Silicon Quantum  
44 Dots to Gadolinium Ions for Bioimaging Applications. *Nanoscale* **2012**, *4*, 5483-5489.
- 45  
46 (94) Liu, Y.; Ai, K.; Yuan, Q.; Lu, L. Fluorescence-Enhanced Gadolinium-Doped Zinc Oxide  
47 Quantum Dots for Magnetic Resonance and Fluorescence Imaging. *Biomaterials* **2011**,  
48 *32*, 1185-1192.
- 49  
50 (95) Guo, W.; Sun, X.; Jacobson, O.; Yan, X.; Min, K.; Srivatsan, A.; Niu, G.; Kiesewetter, D.  
51 O.; Chang, J.; Chen, X. Intrinsically Radioactive <sup>64</sup>Cu CuInS/ZnS Quantum Dots for PET  
52

- 1  
2  
3 and Optical Imaging: Improved Radiochemical Stability and Controllable Cerenkov  
4 Luminescence. *ACS Nano* **2015**, *9*, 488-495.  
5  
6 (96) Tu, C.; Ma, X.; House, A.; Kauzlarich, S. M.; Louie, A. Y. PET Imaging and  
7 Biodistribution of Silicon Quantum Dots in Mice. *ACS Med. Chem. Lett.* **2011**, *2*, 285-  
8 288.  
9  
10 (97) Singh, S. P. Multifunctional Magnetic Quantum Dots for Cancer Theranostics. *J. Biomed.*  
11 *Nanotechnol.* **2011**, *7*, 95-97.  
12  
13 (98) Xia, H.-X.; Yang, X.-Q.; Song, J.-T.; Chen, J.; Zhang, M.-Z.; Yan, D.-M.; Zhang, L.; Qin,  
14 M.-Y.; Bai, L.-Y.; Zhao, Y.-D. Folic Acid-Conjugated Silica-Coated Gold Nanorods and  
15 Quantum Dots for Dual-Modality CT and Fluorescence Imaging and Photothermal  
16 Therapy. *J. Mater. Chem. B* **2014**, *2*, 1945-1953.  
17  
18 (99) Huang, C.-L.; Huang, C.-C.; Mai, F.-D.; Yen, C.-L.; Tzing, S.-H.; Hsieh, H.-T.; Ling, Y.-  
19 C.; Chang, J.-Y. Application of Paramagnetic Graphene Quantum Dots as a Platform for  
20 Simultaneous Dual-Modality Bioimaging and Tumor-Targeted Drug Delivery. *J. Mater.*  
21 *Chem. B* **2015**, *3*, 651-664.  
22  
23 (100) Chen, T.; Zhao, T.; Wei, D.; Wei, Y.; Li, Y.; Zhang, H. Core-Shell Nanocarriers with ZnO  
24 Quantum Dots-Conjugated Au Nanoparticle for Tumor-Targeted Drug Delivery.  
25 *Carbohydr. Polym.* **2013**, *92*, 1124-1132.  
26  
27 (101) Chang, Y.-M.; Shieh, J.; Chu, P.-Y.; Lee, H.-Y.; Lin, C.-M.; Juang, J.-Y. Enhanced Free  
28 Exciton and Direct Band-Edge Emissions at Room Temperature in Ultrathin ZnO Films  
29 Grown on Si Nanopillars by Atomic Layer Deposition. *ACS Appl. Mat. Interf.* **2011**, *3*,  
30 4415-4419.  
31  
32 (102) Gurinovich, L.; Gurin, V.; Ivanov, V.; Bodnar, I.; Molochko, A.; Solovej, N. Crystal  
33 Structure and Optical Properties of CuInS<sub>2</sub> Nanocrystals in a Glass Matrix. *Phys. Status*  
34 *Solidi B* **1998**, *208*, 533-540.  
35  
36 (103) Zhao, N.; Qi, L. Low-Temperature Synthesis of Star-Shaped PbS Nanocrystals in  
37 Aqueous Solutions of Mixed Cationic/Anionic Surfactants. *Adv. Mater.* **2006**, *18*, 359-  
38 362.  
39  
40 (104) Lipovskii, A.; Kolobkova, E.; Petrikov, V.; Kang, I.; Olkhovets, A.; Krauss, T.; Thomas,  
41 M.; Silcox, J.; Wise, F.; Shen, Q. Synthesis and Characterization of PbSe Quantum Dots  
42 in Phosphate Glass. *Appl. Phys. Lett.* **1997**, *71*, 3406-3408.  
43  
44 (105) Kayanuma, Y. Quantum-Size Effects of Interacting Electrons and Holes in  
45 Semiconductor Microcrystals with Spherical Shape. *Phys. Rev. B* **1988**, *38*, 9797-9805.  
46  
47 (106) Bellessa, J.; Voliotis, V.; Grousson, R.; Wang, X.; Ogura, M.; Matsuhata, H. Quantum-  
48 Size Effects on Radiative Lifetimes and Relaxation of Excitons in Semiconductor  
49 Nanostructures. *Phys. Rev. B* **1998**, *58*, 9933-9940.  
50  
51  
52  
53

- 1  
2  
3  
4 (107) Norris, D.; Bawendi, M. Measurement and Assignment of the Size-Dependent Optical  
5 Spectrum in CdSe Quantum Dots. *Phys. Rev. B* **1996**, *53*, 16338-16346.
- 6  
7 (108) Wise, F. W. Lead Salt Quantum Dots: The Limit of Strong Quantum Confinement. *Acc.*  
8 *Chem. Res.* **2000**, *33*, 773-780.
- 9  
10 (109) Brus, L. E. Electron-Electron and Electron-Hole Interactions in Small Semiconductor  
11 Crystallites: The Size Dependence of the Lowest Excited Electronic State. *J. Chem. Phys.*  
12 **1984**, *80*, 4403-4409.
- 13  
14 (110) Bawendi, M. G.; Steigerwald, M. L.; Brus, L. E. The Quantum Mechanics of Larger  
15 Semiconductor Clusters ("Quantum Dots"). *Annu. Rev. Phys. Chem.* **1990**, *41*, 477-496.
- 16  
17 (111) Mirzaei, J.; Reznikov, M.; Hegmann, T. Quantum Dots as Liquid Crystal Dopants. *J.*  
18 *Mater. Chem.* **2012**, *22*, 22350-22365.
- 19  
20 (112) Ediger, M.; Bester, G.; Gerardot, B.; Badolato, A.; Petroff, P.; Karrai, K.; Zunger, A.;  
21 Warburton, R. Fine Structure of Negatively and Positively Charged Excitons in  
22 Semiconductor Quantum Dots: Electron-Hole Asymmetry. *Phys. Rev. Lett.* **2007**, *98*,  
23 036808-036808.
- 24  
25 (113) Ribeiro, F.; Latge, A.; Pacheco, M.; Barticevic, Z. Quantum Dots under Electric and  
26 Magnetic Fields: Impurity-Related Electronic Properties. *J. Appl. Phys.* **1997**, *82*, 270-  
27 274.
- 28  
29 (114) Karabulut, I.; Baskoutas, S. Linear and Nonlinear Optical Absorption Coefficients and  
30 Refractive Index Changes in Spherical Quantum Dots: Effects of Impurities, Electric  
31 Field, Size, and Optical Intensity. *J. Appl. Phys.* **2008**, *103*, 073512-073512.
- 32  
33 (115) Gan, C.; Zhang, Y.; Battaglia, D.; Peng, X.; Xiao, M. Fluorescence Lifetime of Mn-  
34 Doped ZnSe Quantum Dots with Size Dependence. *Appl. Phys. Lett.* **2008**, *92*, 241111-  
35 241111.
- 36  
37 (116) Komarala, V. K.; Xie, C.; Wang, Y.; Xu, J.; Xiao, M. Time-Resolved Photoluminescence  
38 Properties of CuInS<sub>2</sub>/ZnS Nanocrystals: Influence of Intrinsic Defects and External  
39 Impurities. *J. Appl. Phys.* **2012**, *111*, 124314-124314.
- 40  
41 (117) Wen, X.; Yu, P.; Toh, Y.-R.; Ma, X.; Tang, J. On the Upconversion Fluorescence in  
42 Carbon Nanodots and Graphene Quantum Dots. *Chem. Commun.* **2014**, *50*, 4703-4706.
- 43  
44 (118) Tu, C.; Ma, X.; Pantazis, P.; Kauzlarich, S. M.; Louie, A. Y. Paramagnetic, Silicon  
45 Quantum Dots for Magnetic Resonance and Two-Photon Imaging of Macrophages. *J.*  
46 *Am. Chem. Soc.* **2010**, *132*, 2016-2023.
- 47  
48 (119) Geszke, M.; Murias, M.; Balan, L.; Medjahdi, G.; Korczynski, J.; Moritz, M.; Lulek, J.;  
49 Schneider, R. Folic Acid-Conjugated Core/Shell ZnS:Mn/ZnS Quantum Dots as Targeted  
50 Probes for Two Photon Fluorescence Imaging of Cancer Cells. *Acta Biomater.* **2011**, *7*,  
51 1327-1338.

- 1  
2  
3  
4 (120) Deutsch, Z.; Avidan, A.; Pinkas, I.; Oron, D. Energetics and Dynamics of Exciton-  
5 Exciton Interactions in Compound Colloidal Semiconductor Quantum Dots. *Phys. Chem.*  
6 *Chem. Phys.* **2011**, *13*, 3210-3219.
- 7  
8 (121) Acharya, K. P.; Nguyen, H. M.; Paulite, M.; Piryatinski, A.; Zhang, J.; Casson, J. L.; Xu,  
9 H.; Htoon, H.; Hollingsworth, J. A. Elucidation of Two Giants: Challenges to Thick-Shell  
10 Synthesis in CdSe/ZnSe and ZnSe/CdS Core/Shell Quantum Dots. *J. Am. Chem. Soc.*  
11 **2015**, *137*, 3755-3758.
- 12  
13 (122) Chen, C.-W.; Wu, D.-Y.; Chan, Y.-C.; Lin, C. C.; Chung, P.-H.; Hsiao, M.; Liu, R.-S.  
14 Evaluations of the Chemical Stability and Cytotoxicity of CuInS<sub>2</sub> and CuInS<sub>2</sub>/ZnS  
15 Core/Shell Quantum Dots. *J. Phys. Chem. C* **2015**, *119*, 2852-2860.
- 16  
17 (123) Kim, S.; Fisher, B.; Eisler, H.-J.; Bawendi, M. Type-II Quantum Dots: CdTe/CdSe  
18 (Core/Shell) and CdSe/ZnTe (Core/Shell) Heterostructures. *J. Am. Chem. Soc.* **2003**, *125*,  
19 11466-11467.
- 20  
21 (124) Bang, J.; Park, J.; Lee, J. H.; Won, N.; Nam, J.; Lim, J.; Chang, B. Y.; Lee, H. J.; Chon,  
22 B.; Shin, J. ZnTe/ZnSe (Core/Shell) Type-II Quantum Dots: Their Optical and  
23 Photovoltaic Properties. *Chem. Mater.* **2009**, *22*, 233-240.
- 24  
25 (125) Song, Y.; Li, Y.; Wang, X.; Su, X.; Ma, Q. Novel Aqueous Synthesis Methods for  
26 ZnTe/ZnSe and Mn<sup>2+</sup>-Doped ZnTe/ZnSe Type-II Core/Shell Quantum Dots. *RSC Adv.*  
27 **2015**, *5*, 6271-6278.
- 28  
29 (126) Tyrakowski, C. M.; Shamirian, A.; Rowland, C. E.; Shen, H.; Das, A.; Schaller, R. D.;  
30 Snee, P. T. Bright Type II Quantum Dots. *Chem. Mater.* **2015**, *27*, 7276-7281.
- 31  
32 (127) Soni, U.; Pal, A.; Singh, S.; Mittal, M.; Yadav, S.; Elangovan, R.; Sapra, S. Simultaneous  
33 Type-I/Type-II Emission from CdSe/CdS/ZnSe Nano-Heterostructures. *ACS Nano* **2013**,  
34 *8*, 113-123.
- 35  
36 (128) Smith, A. M.; Mohs, A. M.; Nie, S. Tuning the Optical and Electronic Properties of  
37 Colloidal Nanocrystals by Lattice Strain. *Nat. Nanotechnol.* **2009**, *4*, 56-63.
- 38  
39 (129) Liu, C.; Mu, L.; Jia, J.; Zhou, X.; Lin, Y. Boosting the Cell Efficiency of CdSe Quantum  
40 Dot Sensitized Solar Cell Via a Modified ZnS Post-Treatment. *Electrochim. Acta* **2013**,  
41 *III*, 179-184.
- 42  
43 (130) Reiss, P.; Protiere, M.; Li, L. Core/Shell Semiconductor Nanocrystals. *Small* **2009**, *5*,  
44 154-168.
- 45  
46 (131) Ippen, C.; Greco, T.; Wedel, A. InP/ZnSe/ZnS: A Novel Multishell System for InP  
47 Quantum Dots for Improved Luminescence Efficiency and Its application in a Light-  
48 Emitting Device. *J. Inf. Display* **2012**, *13*, 91-95.
- 49  
50 (132) Smith, A. M.; Mancini, M. C.; Nie, S. Bioimaging: Second Window for *in vivo* Imaging.  
51 *Nat. Nanotechnol.* **2009**, *4*, 710-711.

- 1  
2  
3  
4  
5  
6  
7  
8  
9  
10  
11  
12  
13  
14  
15  
16  
17  
18  
19  
20  
21  
22  
23  
24  
25  
26  
27  
28  
29  
30  
31  
32  
33  
34  
35  
36  
37  
38  
39  
40  
41  
42  
43  
44  
45  
46  
47  
48  
49  
50  
51  
52  
53
- (133) Dai, M.; Ogawa, S.; Kameyama, T.; Okazaki, K.-i.; Kudo, A.; Kuwabata, S.; Tsuboi, Y.; Torimoto, T. Tunable Photoluminescence From the Visible to Near-Infrared Wavelength Region of Non-Stoichiometric AgInS<sub>2</sub> Nanoparticles. *J. Mater. Chem.* **2012**, *22*, 12851-12858.
- (134) Chen, B.; Zhong, H.; Zhang, W.; Tan, Z. a.; Li, Y.; Yu, C.; Zhai, T.; Bando, Y.; Yang, S.; Zou, B. Highly Emissive and Color-Tunable CuInS<sub>2</sub>-Based Colloidal Semiconductor Nanocrystals: Off-Stoichiometry Effects and Improved Electroluminescence Performance. *Adv. Funct. Mater.* **2012**, *22*, 2081-2088.
- (135) Li, L.; Pandey, A.; Werder, D. J.; Khanal, B. P.; Pietryga, J. M.; Klimov, V. I. Efficient Synthesis of Highly Luminescent Copper Indium Sulfide-based Core/Shell Nanocrystals with Surprisingly Long-Lived Emission. *J. Am. Chem. Soc.* **2011**, *133*, 1176-1179.
- (136) Cassette, E.; Pons, T.; Bouet, C.; Helle, M.; Bezdetnaya, L.; Marchal, F.; Dubertret, B. Synthesis and Characterization of Near-Infrared Cu–In–Se/ZnS Core/Shell Quantum Dots for *in vivo* Imaging. *Chem. Mater.* **2010**, *22*, 6117-6124.
- (137) Deng, D.; Qu, L.; Zhang, J.; Ma, Y.; Gu, Y. Quaternary Zn–Ag–In–Se Quantum Dots for Biomedical Optical Imaging of RGD-Modified Micelles. *ACS Appl. Mat. Interf.* **2013**, *5*, 10858-10865.
- (138) Jiang, P.; Tian, Z.-Q.; Zhu, C.-N.; Zhang, Z.-L.; Pang, D.-W. Emission-Tunable Near-Infrared Ag<sub>2</sub>S Quantum Dots. *Chem. Mater.* **2011**, *24*, 3-5.
- (139) Dong, B.; Li, C.; Chen, G.; Zhang, Y.; Zhang, Y.; Deng, M.; Wang, Q. Facile Synthesis of Highly Photoluminescent Ag<sub>2</sub>Se Quantum Dots as a New Fluorescent Probe in the Second Near-Infrared Window for *in vivo* Imaging. *Chem. Mater.* **2013**, *25*, 2503-2509.
- (140) Luther, J. M.; Jain, P. K.; Ewers, T.; Alivisatos, A. P. Localized Surface Plasmon Resonances Arising From Free Carriers in Doped Quantum Dots. *Nat. Mater.* **2011**, *10*, 361-366.
- (141) Faucheaux, J. A.; Stanton, A. L. D.; Jain, P. K. Plasmon Resonances of Semiconductor Nanocrystals: Physical Principles and New Opportunities. *J. Phys. Chem. Lett.* **2014**, *5*, 976-985.
- (142) Kriegel, I.; Jiang, C. Y.; Rodriguez-Fernandez, J.; Schaller, R. D.; Talapin, D. V.; da Como, E.; Feldmann, J. Tuning the Excitonic and Plasmonic Properties of Copper Chalcogenide Nanocrystals. *J. Am. Chem. Soc.* **2012**, *134*, 1583-1590.
- (143) Cooper, J. K.; Gul, S.; Lindley, S. A.; Yano, J.; Zhang, J. Z. Tunable Photoluminescent Core/Shell Cu<sup>+</sup>-Doped ZnSe/ZnS Quantum Dots Codoped with Al<sup>3+</sup>, Ga<sup>3+</sup>, or In<sup>3+</sup>. *ACS Appl. Mater. Interf.* **2015**, *7*, 10055-10066.
- (144) Zeng, R.; Shen, R.; Zhao, Y.; Sun, Z.; Li, X.; Zheng, J.; Cao, S.; Zou, B. Water-Soluble, Highly Emissive, Color-Tunable, and Stable Cu-Doped ZnSeS/ZnS Core/Shell Nanocrystals. *CrystEngComm* **2014**, *16*, 3414-3423.

- 1  
2  
3  
4 (145) Tarantino, U.; Fanucci, E.; Iundusi, R.; Celi, M.; Altobelli, S.; Gasbarra, E.; Simonetti,  
5 G.; Manenti, G. Lumbar Spine MRI in Upright Position for Diagnosing Acute and  
6 Chronic Low Back Pain: Statistical Analysis of Morphological Changes. *J. Orthop.*  
7 *Traumatol.* **2013**, *14*, 15-22.
- 8  
9 (146) Li, H.; Hosseini, A.; Li, J.-S.; Gill IV, T. J.; Li, G. Quantitative Magnetic Resonance  
10 Imaging (MRI) Morphological Analysis of Knee Cartilage in Healthy and Anterior  
11 Cruciate Ligament-Injured Knees. *Knee Surg. Sports Traumatol. Arthrosc.* **2012**, *20*,  
12 1496-1502.
- 13  
14 (147) Hart Jr, H.; Bottomley, P.; Edelstein, W.; Karr, S.; Leue, W.; Mueller, O.; Redington, R.;  
15 Schenck, J.; Smith, L.; Vatis, D. Nuclear Magnetic Resonance Imaging: Contrast-To-  
16 Noise Ratio as a Function of Strength of Magnetic Field. *Am. J. Roentgenol.* **1983**, *141*,  
17 1195-1201.
- 18  
19 (148) Hashemi, R. H.; Bradley, W. G.; Lisanti, C. J. *MRI: The Basics*; Lippincott Williams &  
20 Wilkins, Philadelphia, 2012.
- 21  
22 (149) Ogawa, M.; Regino, C. A.; Marcelino, B.; Williams, M.; Kosaka, N.; Bryant Jr, L. H.;  
23 Choyke, P. L.; Kobayashi, H. New Nanosized Biocompatible MR Contrast Agents based  
24 on Lysine-Dendri-Graft Macromolecules. *Bioconjugate Chem.* **2010**, *21*, 955-960.
- 25  
26 (150) Rohrer, M.; Bauer, H.; Mintorovitch, J.; Requardt, M.; Weinmann, H.-J. Comparison of  
27 Magnetic Properties of MRI Contrast Media Solutions at Different Magnetic Field  
28 Strengths. *Invest. Radiol.* **2005**, *40*, 715-724.
- 29  
30 (151) Wang, Y.; Yang, C.; Hu, R.; Toh, H. T.; Liu, X.; Lin, G.; Yin, F.; Yoon, H. S.; Yong, K.-T.  
31 Assembling Mn:ZnSe Quantum Dots-siRNA Nanoplexes for Gene Silencing in Tumor  
32 Cells. *Biomater. Sci.* **2015**, *3*, 192-202.
- 33  
34 (152) Zhang, X.; Brynda, M.; Britt, R. D.; Carroll, E. C.; Larsen, D. S.; Louie, A. Y.;  
35 Kauzlarich, S. M. Synthesis and Characterization of Manganese-Doped Silicon  
36 Nanoparticles: Bifunctional Paramagnetic-Optical Nanomaterial. *J. Am. Chem. Soc.*  
37 **2007**, *129*, 10668-10669.
- 38  
39 (153) Wang, Y.; Wu, B.; Yang, C.; Liu, M.; Sum, T. C.; Yong, K. T. Synthesis and  
40 Characterization of Mn: ZnSe/ZnS/ZnMnS Sandwiched QDs for Multimodal Imaging  
41 and Theranostic Applications. *Small* **2016**, *12*, 534-546.
- 42  
43 (154) Jahanbin, T.; Gaceur, M.; Gros-Dagnac, H.; Benderbous, S.; Merah, S. A. High Potential  
44 of Mn-Doped ZnS Nanoparticles with Different Dopant Concentrations as Novel MRI  
45 Contrast Agents: Synthesis and *in vitro* Relaxivity Studies. *J. Nanopart. Res.* **2015**, *17*,  
46 258-258.
- 47  
48 (155) Lin, B.; Yao, X.; Zhu, Y.; Shen, J.; Yang, X.; Jiang, H.; Zhang, X. Multifunctional  
49 Manganese-Doped Core-Shell Quantum Dots for Magnetic Resonance and Fluorescence  
50 Imaging of Cancer Cells. *New J. Chem.* **2013**, *37*, 3076-3083.
- 51  
52  
53

- 1  
2  
3  
4  
5  
6  
7  
8  
9  
10  
11  
12  
13  
14  
15  
16  
17  
18  
19  
20  
21  
22  
23  
24  
25  
26  
27  
28  
29  
30  
31  
32  
33  
34  
35  
36  
37  
38  
39  
40  
41  
42  
43  
44  
45  
46  
47  
48  
49  
50  
51  
52  
53
- (156) Ding, K.; Jing, L.; Liu, C.; Hou, Y.; Gao, M. Magnetically Engineered Cd-free Quantum Dots as Dual-Modality Probes for Fluorescence/Magnetic Resonance Imaging of Tumors. *Biomaterials* **2014**, *35*, 1608-1617.
- (157) Yang, W.; Guo, W.; Gong, X.; Zhang, B.; Wang, S.; Chen, N.; Yang, W.; Tu, Y.; Fang, X.; Chang, J. Facile Synthesis of Gd–Cu–In–S/ZnS Bimodal Quantum Dots with Optimized Properties for Tumor Targeted Fluorescence/MR *In vivo* Imaging. *ACS Appl. Mat. Interf.* **2015**, *7*, 18759-18768.
- (158) Zheng, Y.; Zou, Y.; Jiang, J. Synthesis of Gd-Doped CuInS<sub>2</sub> Quantum Dots Exhibiting Photoluminescence and High Longitudinal Relaxivity. *Mater. Lett.* **2016**, *168*, 86-89.
- (159) Sitbon, G.; Bouccara, S.; Tasso, M.; Francois, A.; Bezdetnaya, L.; Marchal, F.; Beaumont, M.; Pons, T. Multimodal Mn-Doped I–III–VI Quantum Dots for Near Infrared Fluorescence and Magnetic Resonance Imaging: From Synthesis to *in vivo* Application. *Nanoscale* **2014**, *6*, 9264-9272.
- (160) Xu, S.; Ziegler, J.; Nann, T. Rapid Synthesis of Highly Luminescent InP and InP/ZnS Nanocrystals. *J. Mater. Chem.* **2008**, *18*, 2653-2656.
- (161) Tessier, M. D.; Dupont, D.; De Nolf, K.; De Roo, J.; Hens, Z. Economic and Size-Tunable Synthesis of InP/ZnE (E = S, Se) Colloidal Quantum Dots. *Chem. Mater.* **2015**, *27*, 4893-4898.
- (162) Liu, S.; Zhang, H.; Qiao, Y.; Su, X. One-Pot Synthesis of Ternary CuInS<sub>2</sub> Quantum Dots with Near-Infrared Fluorescence in Aqueous Solution. *RSC Adv.* **2012**, *2*, 819-825.
- (163) Li, L.; Daou, T. J.; Texier, I.; Kim Chi, T. T.; Liem, N. Q.; Reiss, P. Highly Luminescent CuInS<sub>2</sub>/ZnS Core/Shell Nanocrystals: Cadmium-Free Quantum Dots for *In vivo* Imaging. *Chem. Mater.* **2009**, *21*, 2422-2429.
- (164) Li, S.; Chen, Y.; Huang, L.; Pan, D. Simple Continuous-Flow Synthesis of Cu–In–Zn–S/ZnS and Ag–In–Zn–S/ZnS Core/Shell Quantum Dots. *Nanotechnology* **2013**, *24*, 395705-395705.
- (165) Chen, Y.; Li, S.; Huang, L.; Pan, D. Green and Facile Synthesis of Water-Soluble Cu–In–S/ZnS Core/Shell Quantum Dots. *Inorg. Chem.* **2013**, *52*, 7819-7921.
- (166) Xiong, W. W.; Yang, G. H.; Wu, X. C.; Zhu, J. J. Aqueous Synthesis of Color-Tunable CuInS<sub>2</sub>/ZnS Nanocrystals for the Detection of Human Interleukin 6. *ACS Appl Mater Interf.* **2013**, *5*, 8210-8216.
- (167) Ogawa, T.; Kuzuya, T.; Hamanaka, Y.; Sumiyama, K. Synthesis of Ag–In Binary Sulfide Nanoparticles—Structural Tuning and Their Photoluminescence Properties. *J. Mater. Chem.* **2010**, *20*, 2226-2231.
- (168) Hamanaka, Y.; Ozawa, K.; Kuzuya, T. Enhancement of Donor-Acceptor Pair Emissions in Colloidal AgInS<sub>2</sub> Quantum Dots with High Concentrations of Defects. *J. Phys. Chem. C* **2014**, *118*, 14562-14568.

60

- 1  
2  
3  
4 (169) Mao, B.; Chuang, C.-H.; McCleese, C.; Zhu, J.; Burda, C. Near-Infrared Emitting  
5 AgInS<sub>2</sub>/ZnS Nanocrystals. *J. Phys. Chem. C* **2014**, *118*, 13883-13889.
- 6  
7 (170) Torimoto, T.; Adachi, T.; Okazaki, K.-i.; Sakuraoka, M.; Shibayama, T.; Ohtani, B.;  
8 Kudo, A.; Kuwabata, S. Facile Synthesis of ZnS–AgInS<sub>2</sub> Solid Solution Nanoparticles  
9 for a Color-Adjustable Luminophore. *J. Am. Chem. Soc.* **2007**, *129*, 12388-12389.
- 10  
11 (171) Subramaniam, P.; Lee, S. J.; Shah, S.; Patel, S.; Starovoytov, V.; Lee, K. B. Generation of  
12 a Library of Non-Toxic Quantum Dots for Cellular Imaging and siRNA Delivery. *Adv.*  
13 *Mater.* **2012**, *24*, 4014-4019.
- 14  
15 (172) Zhao, Y.; Pan, H.; Lou, Y.; Qiu, X.; Zhu, J.; Burda, C. Plasmonic Cu<sub>2-x</sub>S Nanocrystals:  
16 Optical and Structural Properties of Copper-Deficient Copper(I) Sulfides. *J. Am. Chem.*  
17 *Soc.* **2009**, *131*, 4253-4261.
- 18  
19 (173) Allen, P. M.; Bawendi, M. G. Ternary I– III– VI Quantum Dots Luminescent in the Red  
20 to Near-Infrared. *J. Am. Chem. Soc.* **2008**, *130*, 9240-9241.
- 21  
22 (174) Li, C.; Zhang, Y.; Wang, M.; Zhang, Y.; Chen, G.; Li, L.; Wu, D.; Wang, Q. *In vivo* Real-  
23 Time Visualization of Tissue Blood Flow and Angiogenesis Using Ag<sub>2</sub>S Quantum Dots in  
24 the NIR-II Window. *Biomaterials* **2014**, *35*, 393-400.
- 25  
26 (175) Wang, C.; Gao, X.; Ma, Q.; Su, X. Aqueous Synthesis of Mercaptopropionic Acid  
27 Capped Mn<sup>2+</sup>-Doped ZnSe Quantum Dots. *J. Mater. Chem.* **2009**, *19*, 7016-7022.
- 28  
29 (176) Srivastava, B. B.; Jana, S.; Karan, N. S.; Paria, S.; Jana, N. R.; Sarma, D.; Pradhan, N.  
30 Highly Luminescent Mn-Doped ZnS Nanocrystals: Gram-Scale Synthesis. *J. Phys.*  
31 *Chem. Letters* **2010**, *1*, 1454-1458.
- 32  
33 (177) Kim, S.; Park, J.; Kim, T.; Jang, E.; Jun, S.; Jang, H.; Kim, B.; Kim, S.-W. Reverse Type-  
34 I ZnSe/InP/ZnS Core/Shell/Shell Nanocrystals: Cadmium-Free Quantum Dots for Visible  
35 Luminescence. *Small* **2011**, *7*, 70-73.
- 36  
37 (178) Intartaglia, R.; Barchanski, A.; Bagga, K.; Genovese, A.; Das, G.; Wagener, P.; Di  
38 Fabrizio, E.; Diaspro, A.; Brandi, F.; Barcikowski, S. Bioconjugated Silicon Quantum  
39 Dots From One-Step Green Synthesis. *Nanoscale* **2012**, *4*, 1271-1274.
- 40  
41 (179) Cheng, X.; Lowe, S. B.; Ciampi, S.; Magenau, A.; Gaus, K.; Reece, P. J.; Gooding, J. J.  
42 Versatile “Click Chemistry” Approach to Functionalizing Silicon Quantum Dots:  
43 Applications toward Fluorescent Cellular Imaging. *Langmuir* **2014**, *30*, 5209-5216.
- 44  
45 (180) Sugimoto, H.; Fujii, M.; Fukuda, Y.; Imakita, K.; Akamatsu, K. All-Inorganic Water-  
46 Dispersible Silicon Quantum Dots: Highly Efficient Near-Infrared Luminescence in a  
47 Wide pH Range. *Nanoscale* **2014**, *6*, 122-126.
- 48  
49 (181) Asok, A.; Gandhi, M. N.; Kulkarni, A. R. Enhanced Visible Photoluminescence in ZnO  
50 Quantum Dots by Promotion of Oxygen Vacancy Formation. *Nanoscale* **2012**, *4*, 4943-  
51 4946.

- 1  
2  
3  
4 (182) Xiong, H.-M.; Xu, Y.; Ren, Q.-G.; Xia, Y.-Y. Stable Aqueous ZnO@Polymer Core–Shell  
5 Nanoparticles with Tunable Photoluminescence and Their Application in Cell Imaging. *J.*  
6 *Am. Chem. Soc.* **2008**, *130*, 7522-7523.
- 7  
8 (183) Lin, L.; Xu, Y.; Zhang, S.; Ross, I. M.; Ong, A. C. M.; Allwood, D. A. Fabrication of  
9 Luminescent Monolayered Tungsten Dichalcogenides Quantum Dots with Giant Spin-  
10 Valley Coupling. *ACS Nano* **2013**, *7*, 8214-8223.
- 11  
12 (184) Shen, J. H.; Zhu, Y. H.; Yang, X. L.; Zong, J.; Zhang, J. M.; Li, C. Z. One-Pot  
13 Hydrothermal Synthesis of Graphene Quantum Dots Surface-Passivated by Polyethylene  
14 Glycol and Their Photoelectric Conversion Under Near-Infrared Light. *New J. Chem.*  
15 **2012**, *36*, 97-101.
- 16  
17 (185) Wu, X.; Tian, F.; Wang, W.; Chen, J.; Wu, M.; Zhao, J. X. Fabrication of Highly  
18 Fluorescent Graphene Quantum Dots Using L-Glutamic Acid for *in vitro/in vivo* Imaging  
19 and Sensing. *J. Mater. Chem. C* **2013**, *1*, 4676-4684.
- 20  
21 (186) Mičić, O. I.; Sprague, J.; Lu, Z.; Nozik, A. J. Highly Efficient Band-Edge Emission From  
22 InP Quantum Dots. *Appl. Phys. Lett.* **1996**, *68*, 3150-3152.
- 23  
24 (187) Fu, H.; Zunger, A. InP Quantum Dots: Electronic Structure, Surface Effects, and the  
25 Redshifted Emission. *Phys. Rev. B* **1997**, *56*, 1496-1508.
- 26  
27 (188) Mičić, O. I.; Ahrenkiel, S. P.; Nozik, A. J. Synthesis of Extremely Small InP Quantum  
28 Dots and Electronic Coupling in Their Disordered Solid Films. *Appl. Phys. Lett.* **2001**,  
29 *78*, 4022-4024.
- 30  
31 (189) Allen, P. M.; Walker, B. J.; Bawendi, M. G. Mechanistic Insights into the Formation of  
32 InP Quantum Dots. *Angew. Chemie* **2010**, *49*, 760-762.
- 33  
34 (190) Fan, G.; Wang, C.; Fang, J. Solution-based Synthesis of III–V Quantum Dots and Their  
35 Applications in Gas Sensing and Bio-Imaging. *Nano Today* **2014**, *9*, 69-84.
- 36  
37 (191) Mičić, O. I.; Cheong, H. M.; Fu, H.; Zunger, A.; Sprague, J. R.; Mascarenhas, A.; Nozik,  
38 A. J. Size-Dependent Spectroscopy of InP Quantum Dots. *J. Phys. Chem. B* **1997**, *101*,  
39 4904-4912.
- 40  
41 (192) Biju, V.; Mundayoor, S.; Omkumar, R. V.; Anas, A.; Ishikawa, M. Bioconjugated  
42 Quantum Dots for Cancer Research: Present Status, Prospects and Remaining Issues.  
43 *Biotechnol. Adv.* **2010**, *28*, 199-213.
- 44  
45 (193) Stasiuk, G. J.; Tamang, S.; Imbert, D.; Poillot, C.; Giardiello, M.; Tisseyre, C.; Barbier, E.  
46 L.; Fries, P. H.; de Waard, M.; Reiss, P. *et al.* Cell-Permeable Ln(III) Chelate-  
47 Functionalized InP Quantum Dots As Multimodal Imaging Agents. *ACS Nano* **2011**, *5*,  
48 8193-8201.
- 49  
50 (194) Bain, L. E.; Ivanisevic, A. Engineering the Cell–Semiconductor Interface: A Materials  
51 Modification Approach using II-VI and III-V Semiconductor Materials. *Small* **2015**, *11*,  
52 768-780.

- 1  
2  
3  
4 (195) Narayanaswamy, A.; Feiner, L. F.; van der Zaag, P. J. Temperature Dependence of the  
5 Photoluminescence of InP/ZnS Quantum Dots. *J. Phys. Chem. C* **2008**, *112*, 6775-6780.
- 6 (196) Zhang, Z.; Liu, D.; Li, D.; Huang, K.; Zhang, Y.; Shi, Z.; Xie, R.; Han, M.-Y.; Wang, Y.;  
7 Yang, W. Dual Emissive Cu:InP/ZnS/InP/ZnS Nanocrystals: Single-Source “Greener”  
8 Emitters with Flexibly Tunable Emission from Visible to Near-Infrared and Their  
9 Application in White Light-Emitting Diodes. *Chem. Mater.* **2015**, *27*, 1405-1411.
- 10 (197) Thomas, A.; Nair, P. V.; George Thomas, K. InP Quantum Dots: An Environmentally  
11 Friendly Material with Resonance Energy Transfer Requisites. *J. Phys. Chem. C* **2014**,  
12 *118*, 3838-3845.
- 13 (198) Lin, Z.; Ma, Q.; Fei, X.; Zhang, H.; Su, X. A Novel Aptamer Functionalized CuInS<sub>2</sub>  
14 Quantum Dots Probe for Daunorubicin Sensing and Near Infrared Imaging of Prostate  
15 Cancer Cells. *Anal. Chim. Acta* **2014**, *818*, 54-60.
- 16 (199) Foda, M. F.; Huang, L.; Shao, F.; Han, H.-Y. Biocompatible and Highly Luminescent  
17 Near-Infrared CuInS<sub>2</sub>/ZnS Quantum Dots Embedded Silica Beads for Cancer Cell  
18 Imaging. *ACS Appl. Mater. Interf.* **2014**, *6*, 2011-2017.
- 19 (200) Gao, X.; Liu, Z.; Lin, Z.; Su, X. CuInS<sub>2</sub> Quantum Dots/Poly(L-Glutamic Acid)-Drug  
20 Conjugates for Drug Delivery and Cell Imaging. *Analyst* **2014**, *139*, 831-836.
- 21 (201) Cheng, C.-Y.; Ou, K.-L.; Huang, W.-T.; Chen, J.-K.; Chang, J.-Y.; Yang, C.-H.  
22 Gadolinium-Based CuInS<sub>2</sub>/ZnS Nanoprobe for Dual-Modality Magnetic  
23 Resonance/Optical Imaging. *ACS Appl. Mater. Interf.* **2013**, *5*, 4389-4400.
- 24 (202) Kolny-Olesiak, J.; Weller, H. Synthesis and Application of Colloidal CuInS<sub>2</sub>  
25 Semiconductor Nanocrystals. *ACS Appl. Mater. Interf.* **2013**, *5*, 12221-12237.
- 26 (203) Lin, Z.; Fei, X.; Ma, Q.; Gao, X.; Su, X. CuInS<sub>2</sub> Quantum Dots@Silica Near-Infrared  
27 Fluorescent Nanoprobe for Cell Imaging. *New J. Chem.* **2014**, *38*, 90-96.
- 28 (204) Rao, P.; Yao, W.; Li, Z.; Kong, L.; Zhang, W.; Li, L. Highly Stable CuInS<sub>2</sub>@ZnS:Al  
29 Core@Shell Quantum Dots: The Role of Aluminium Self-Passivation. *Chem. Comm.*  
30 **2015**, *51*, 8757-8760.
- 31 (205) Zhang, W.; Lou, Q.; Ji, W.; Zhao, J.; Zhong, X. Color-Tunable Highly Bright  
32 Photoluminescence of Cadmium-Free Cu-Doped Zn-In-S Nanocrystals and  
33 Electroluminescence. *Chem. Mater.* **2014**, *26*, 1204-1212.
- 34 (206) Jiang, T.; Song, J.; Wang, H.; Ye, X.; Wang, H.; Zhang, W.; Yang, M.; Xia, R.; Zhu, L.;  
35 Xu, X. Aqueous Synthesis of Color Tunable Cu Doped Zn-In-S/ZnS Nanoparticles in the  
36 Whole Visible Region for Cellular Imaging. *J. Mater. Chem. B* **2015**, *3*, 2402-2410.
- 37 (207) Li, J.; Kempken, B.; Dzhagan, V.; Zahn, D. R. T.; Grzelak, J.; Mackowski, S.; Parisi, J.;  
38 Kolny-Olesiak, J. Alloyed CuInS<sub>2</sub>-ZnS Nanorods: Synthesis, Structure and Optical  
39 Properties. *CrystEngComm* **2015**, *17*, 5634-5643.

- 1  
2  
3  
4 (208) Hu, S.; Zeng, S.; Zhang, B.; Yang, C.; Song, P.; Hang Danny, T. J.; Lin, G.; Wang, Y.;  
5 Anderson, T.; Coquet, P. *et al.* Preparation of Biofunctionalized Quantum Dots Using  
6 Microfluidic Chips for Bioimaging. *Analyst* **2014**, *139*, 4681-4690.
- 7  
8 (209) Chen, H.; Li, B.; Zhang, M.; Sun, K.; Wang, Y.; Peng, K.; Ao, M.; Guo, Y.; Gu, Y.  
9 Characterization of Tumor-Targeting Ag<sub>2</sub>S Quantum Dots for Cancer Imaging and  
10 Therapy *in vivo*. *Nanoscale* **2014**, *6*, 12580-12590.
- 11  
12 (210) Langevin, M.-A.; Lachance-Quirion, D.; Ritcey, A. M.; Allen, C. N. Size-Dependent  
13 Extinction Coefficients and Transition Energies of Near-Infrared beta-Ag<sub>2</sub>Se Colloidal  
14 Quantum Dots. *J. Phys. Chem. C* **2013**, *117*, 5424-5428.
- 15  
16 (211) Zhang, X.; Liu, M.; Liu, H.; Zhang, S. Low-Toxic Ag<sub>2</sub>S Quantum Dots for  
17 Photoelectrochemical Detection Glucose and Cancer Cells. *Biosens. Bioelectron.* **2014**,  
18 *56*, 307-312.
- 19  
20 (212) Ji, C.; Zhang, Y.; Zhang, T.; Liu, W.; Zhang, X.; Shen, H.; Wang, Y.; Gao, W.; Wang, Y.;  
21 Zhao, J. *et al.* Temperature-Dependent Photoluminescence of Ag<sub>2</sub>Se Quantum Dots. *J.*  
22 *Phys. Chem. C* **2015**, *119*, 13841-13846.
- 23  
24 (213) Wang, C.; Xu, S.; Zhao, Z.; Wang, Z.; Cui, Y. Aqueous Synthesis of Nontoxic  
25 Ag<sub>2</sub>Se/ZnSe Quantum Dots Designing as Fluorescence Sensors for Detection of Ag(I)  
26 and Cu(II) Ions. *J. Fluoresc.* **2015**, *25*, 41-48.
- 27  
28 (214) Duman, F. D.; Hocaoglu, I.; Ozturk, D. G.; Gozuacik, D.; Kiraz, A.; Acar, H. Y. Highly  
29 Luminescent and Cytocompatible Cationic Ag<sub>2</sub>S NIR-Emitting Quantum Dots for Optical  
30 Imaging and Gene Transfection. *Nanoscale* **2015**, *7*, 11352-11362.
- 31  
32 (215) Jiang, P.; Wang, R.; Chen, Z. Thiol-based Non-Injection Synthesis of Near-Infrared  
33 Ag<sub>2</sub>S/ZnS Core/Shell Quantum Dots. *RSC Adv.* **2015**, *5*, 56789-56793.
- 34  
35 (216) Zhang, X.; Liu, J.; Johansson, E. M. J. Efficient Charge-Carrier Extraction From Ag<sub>2</sub>S  
36 Quantum Dots Prepared by the SILAR Method for Utilization of Multiple Exciton  
37 Generation. *Nanoscale* **2015**, *7*, 1454-1462.
- 38  
39 (217) Zhang, Y.; Liu, Y.; Li, C.; Chen, X.; Wang, Q. Controlled Synthesis of Ag<sub>2</sub>S Quantum  
40 Dots and Experimental Determination of the Exciton Bohr Radius. *J. Phys. Chem. C*  
41 **2014**, *118*, 4918-4923.
- 42  
43 (218) Sun, J.; Yu, W.; Usman, A.; Isimjan, T. T.; Dgobbo, S.; Alarousu, E.; Takanahe, K.;  
44 Mohammed, O. F. Generation of Multiple Excitons in Ag<sub>2</sub>S Quantum Dots: Single High-  
45 Energy versus Multiple-Photon Excitation. *J. Phys. Chem. Lett.* **2014**, *5*, 659-665.
- 46  
47 (219) Gui, R.; Wan, A.; Liu, X.; Yuan, W.; Jin, H. Water-Soluble Multidentate Polymers  
48 Compactly Coating Ag<sub>2</sub>S Quantum Dots with Minimized Hydrodynamic Size and Bright  
49 Emission Tunable From Red to Second Near-Infrared Region. *Nanoscale* **2014**, *6*, 5467-  
50 5473.
- 51  
52  
53  
54  
55  
56  
57  
58  
59  
60

- 1  
2  
3  
4 (220) Zhu, C.-N.; Jiang, P.; Zhang, Z.-L.; Zhu, D.-L.; Tian, Z.-Q.; Pang, D.-W. Ag<sub>2</sub>Se Quantum  
5 Dots with Tunable Emission in the Second Near-Infrared Window. *ACS Appl. Mater.*  
6 *Interf.* **2013**, *5*, 1186-1189.
- 7  
8 (221) Park, Y. J.; Oh, J. H.; Han, N. S.; Yoon, H. C.; Park, S. M.; Do, Y. R.; Song, J. K.  
9 Photoluminescence of Band Gap States in AgInS<sub>2</sub> Nanoparticles. *J. Phys. Chem. C* **2014**,  
10 *118*, 25677-25683.
- 11  
12 (222) Shinchi, H.; Wakao, M.; Nagata, N.; Sakamoto, M.; Mochizuki, E.; Uematsu, T.;  
13 Kuwabata, S.; Suda, Y. Cadmium-Free Sugar-Chain-Immobilized Fluorescent  
14 Nanoparticles Containing Low-Toxicity ZnS-AgInS<sub>2</sub> Cores for Probing Lectin and Cells.  
15 *Bioconjugate Chem.* **2014**, *25*, 286-295.
- 16  
17 (223) Tan, L.; Liu, S.; Li, X.; Chronakis, I. S.; Shen, Y. A New Strategy for Synthesizing  
18 AgInS<sub>2</sub> Quantum Dots Emitting Brightly in Near-Infrared Window for *in vivo* Imaging.  
19 *Colloid. Surface. B* **2015**, *125*, 222-229.
- 20  
21 (224) Regulacio, M. D.; Win, K. Y.; Lo, S. L.; Zhang, S.-Y.; Zhang, X.; Wang, S.; Han, M.-Y.;  
22 Zheng, Y. Aqueous Synthesis of Highly Luminescent AgInS<sub>2</sub>-ZnS Quantum Dots and  
23 Their Biological Applications. *Nanoscale* **2013**, *5*, 2322-2327.
- 24  
25 (225) Wang, Q.; Bao, Y.; Ahire, J.; Chao, Y. Co-encapsulation of Biodegradable Nanoparticles  
26 with Silicon Quantum Dots and Quercetin for Monitored Delivery. *Adv. Healthc. Mater.*  
27 **2013**, *2*, 459-466.
- 28  
29 (226) Chinnathambi, S.; Chen, S.; Ganesan, S.; Hanagata, N. Silicon Quantum Dots for  
30 Biological Applications. *Adv. Healthc. Mater.* **2014**, *3*, 10-29.
- 31  
32 (227) Dohnalova, K.; Gregorkiewicz, T.; Kusova, K. Silicon Quantum dots: Surface Matters. *J.*  
33 *Phys. Condens. Matter* **2014**, *26*, 173201-173228.
- 34  
35 (228) Ban, R.; Zheng, F.; Zhang, J. A Highly Sensitive Fluorescence Assay for 2,4,6-  
36 Trinitrotoluene using Amine-Capped Silicon Quantum Dots as a Probe. *Anal. Methods*  
37 **2015**, *7*, 1732-1737.
- 38  
39 (229) Ohta, S.; Yamura, K.; Inasawa, S.; Yamaguchi, Y. Aggregates of Silicon Quantum Dots as  
40 a Drug Carrier: Selective Intracellular Drug Release based on pH-Responsive  
41 Aggregation/Dispersion. *Chem. Comm.* **2015**, *51*, 6422-6425.
- 42  
43 (230) Wang, L.; Li, Q.; Wang, H.-Y.; Huang, J.-C.; Zhang, R.; Chen, Q.-D.; Xu, H.-L.; Han, W.;  
44 Shao, Z.-Z.; Sun, H.-B. Ultrafast Optical Spectroscopy of Surface-Modified Silicon  
45 Quantum Dots: Unraveling the Underlying Mechanism of the Ultrabright and Color-  
46 Tunable Photoluminescence. *Light Sci. Appl.* **2015**, *4*, e245-e253.
- 47  
48 (231) Hua, F.; Swihart, M. T.; Ruckenstein, E. Efficient Surface Grafting of Luminescent  
49 Silicon Quantum Dots by Photoinitiated Hydrosilylation. *Langmuir* **2005**, *21*, 6054-6062.
- 50  
51  
52  
53

- 1  
2  
3  
4 (232) Li, X.; He, Y.; Swihart, M. T. Surface Functionalization of Silicon Nanoparticles  
5 Produced by Laser-Driven Pyrolysis of Silane Followed by HF-HNO<sub>3</sub> Etching. *Langmuir*  
6 **2004**, *20*, 4720-4727.
- 7  
8 (233) Li, X.; He, Y.; Talukdar, S. S.; Swihart, M. T. Process for Preparing Macroscopic  
9 Quantities of Brightly Photoluminescent Silicon Nanoparticles with Emission Spanning  
10 the Visible Spectrum. *Langmuir* **2003**, *19*, 8490-8496.
- 11  
12 (234) Sato, S.; Swihart, M. T. Propionic-Acid-Terminated Silicon Nanoparticles: Synthesis and  
13 Optical Characterization. *Chem. Mater.* **2006**, *18*, 4083-4088.
- 14  
15 (235) Mangolini, L.; Thimsen, E.; Kortshagen, U. High-Yield Plasma Synthesis of Luminescent  
16 Silicon Nanocrystals. *Nano Lett.* **2005**, *5*, 655-659.
- 17  
18 (236) Jurbergs, D.; Rogojina, E.; Mangolini, L.; Kortshagen, U. Silicon Nanocrystals with  
19 Ensemble Quantum Yields Exceeding 60%. *Appl. Phys. Lett.* **2006**, *88*, 3116-3116.
- 20  
21 (237) Veinot, J. G. Synthesis, Surface Functionalization, and Properties of Freestanding Silicon  
22 Nanocrystals. *Chem. Comm.* **2006**, 4160-4168.
- 23  
24 (238) Gupta, A.; Swihart, M. T.; Wiggers, H. Luminescent Colloidal Dispersion of Silicon  
25 Quantum Dots from Microwave Plasma Synthesis: Exploring the Photoluminescence  
26 Behavior Across the Visible Spectrum. *Adv. Funct. Mater.* **2009**, *19*, 696-703.
- 27  
28 (239) He, G. S.; Zheng, Q. D.; Yong, K. T.; Erogbogbo, F.; Swihart, M. T.; Prasad, P. N. Two-  
29 and Three-Photon Absorption and Frequency Upconverted Emission of Silicon Quantum  
30 Dots. *Nano Lett.* **2008**, *8*, 2688-2692.
- 31  
32 (240) Dasog, M.; Yang, Z.; Regli, S.; Atkins, T. M.; Faramus, A.; Singh, M. P.; Muthuswamy,  
33 E.; Kauzlarich, S. M.; Tilley, R. D.; Veinot, J. G. Chemical Insight into the Origin of Red  
34 and Blue Photoluminescence Arising From Freestanding Silicon Nanocrystals. *ACS Nano*  
35 **2013**, *7*, 2676-2685.
- 36  
37 (241) Hua, F.; Erogbogbo, F.; Swihart, M. T.; Ruckenstein, E. Organically Capped Silicon  
38 Nanoparticles with Blue Photoluminescence Prepared by Hydrosilylation Followed by  
39 Oxidation. *Langmuir* **2006**, *22*, 4363-4370.
- 40  
41 (242) Liu, J.; Erogbogbo, F.; Yong, K.-T.; Ye, L.; Liu, J.; Hu, R.; Chen, H.; Hu, Y.; Yang, Y.;  
42 Yang, J. *et al.* Assessing Clinical Prospects of Silicon Quantum Dots: Studies in Mice and  
43 Monkeys. *ACS Nano* **2013**, *7*, 7303-7310.
- 44  
45 (243) Zhou, T.; Anderson, R. T.; Li, H.; Bell, J.; Yang, Y.; Gorman, B. P.; Pylypenko, S.; Lusk,  
46 M. T.; Sellinger, A. Bandgap Tuning of Silicon Quantum Dots by Surface  
47 Functionalization with Conjugated Organic Groups. *Nano Lett.* **2015**, *15*, 3657-3663.
- 48  
49 (244) Swihart, M. T. In *Nanotechnology in Biology and Medicine: Methods, Devices, and*  
50 *Applications*; Vo-Dinh, T., Eds.; CRC Press: Boca Raton, FL, 2007; Vol. 4.
- 51  
52  
53

- 1  
2  
3  
4 (245) Zhu, S.; Song, Y.; Zhao, X.; Shao, J.; Zhang, J.; Yang, B. The Photoluminescence  
5 Mechanism in Carbon Dots (Graphene Quantum Dots, Carbon Nanodots, and Polymer  
6 Dots): Current State and Future Perspective. *Nano Res.* **2015**, *8*, 355-381.
- 7  
8 (246) Ju, J.; Chen, W. In Situ Growth of Surfactant-Free Gold Nanoparticles on Nitrogen-  
9 Doped Graphene Quantum Dots for Electrochemical Detection of Hydrogen Peroxide in  
10 Biological Environments. *Anal. Chem.* **2015**, *87*, 1903-1910.
- 11  
12 (247) Sk, M. A.; Ananthanarayanan, A.; Huang, L.; Lim, K. H.; Chen, P. Revealing the Tunable  
13 Photoluminescence Properties of Graphene Quantum Dots. *J. Mater. Chem. C* **2014**, *2*,  
14 6954-6960.
- 15  
16 (248) Kumar, G. S.; Roy, R.; Sen, D.; Ghorai, U. K.; Thapa, R.; Mazumder, N.; Saha, S.;  
17 Chattopadhyay, K. K. Amino-Functionalized Graphene Quantum dots: Origin of Tunable  
18 Heterogeneous Photoluminescence. *Nanoscale* **2014**, *6*, 3384-3391.
- 19  
20 (249) Lin, L.; Rong, M.; Luo, F.; Chen, D.; Wang, Y.; Chen, X. Luminescent Graphene  
21 Quantum Dots as New Fluorescent Materials for Environmental and Biological  
22 Applications. *Trends Anal. Chem.* **2014**, *54*, 83-102.
- 23  
24 (250) Sun, J.; Yang, S.; Wang, Z.; Shen, H.; Xu, T.; Sun, L.; Li, H.; Chen, W.; Jiang, X.; Ding,  
25 *Get al.* Ultra-High Quantum Yield of Graphene Quantum Dots: Aromatic-Nitrogen  
26 Doping and Photoluminescence Mechanism. *Part. Part. Syst. Charact.* **2015**, *32*, 434-  
27 440.
- 28  
29 (251) Yang, H.; Holloway, P. H.; Ratna, B. B. Photoluminescent and Electroluminescent  
30 Properties of Mn-Doped ZnS Nanocrystals. *J. Appl. Phys.* **2003**, *93*, 586-592.
- 31  
32 (252) Erwin, S. C.; Zu, L.; Haftel, M. I.; Efros, A. L.; Kennedy, T. A.; Norris, D. J. Doping  
33 Semiconductor Nanocrystals. *Nature* **2005**, *436*, 91-94.
- 34  
35 (253) Wu, P.; Yan, X.-P. Doped Quantum Dots for Chemo/Biosensing and Bioimaging. *Chem.*  
36 *Soc. Rev.* **2013**, *42*, 5489-5521.
- 37  
38 (254) Wu, P.; Zhang, J.; Wang, S.; Zhu, A.; Hou, X. Sensing during In Situ Growth of Mn-  
39 Doped ZnS QDs: A Phosphorescent Sensor for Detection of H<sub>2</sub>S in Biological Samples.  
40 *Chem. Eur. J.* **2014**, *20*, 952-956.
- 41  
42 (255) Sapra, S.; Prakash, A.; Ghangrekar, A.; Periasamy, N.; Sarma, D. D. Emission Properties  
43 of Manganese-Doped ZnS Nanocrystals. *J. Phys. Chem. B* **2005**, *109*, 1663-1668.
- 44  
45 (256) Geszke-Moritz, M.; Piotrowska, H.; Murias, M.; Balan, L.; Moritz, M.; Lulek, J.;  
46 Schneider, R. Thioglycerol-Capped Mn-Doped ZnS Quantum Dot Bioconjugates as  
47 Efficient Two-Photon Fluorescent Nano-Probes for Bioimaging. *J. Mater. Chem. B* **2013**,  
48 *1*, 698-706.
- 49  
50 (257) Yu, J. H.; Kwon, S.-H.; Petrasek, Z.; Park, O. K.; Jun, S. W.; Shin, K.; Choi, M.; Il Park,  
51 Y.; Park, K.; Na, H. *et al.* High-Resolution Three-Photon Biomedical Imaging Using  
52 Doped ZnS Nanocrystals. *Nat. Mater.* **2013**, *12*, 359-366.

- 1  
2  
3  
4 (258) Ertas, N.; Kara, H. E. S. L-Cysteine Capped Mn-Doped ZnS Quantum Dots as a Room  
5 Temperature Phosphorescence Sensor for in-vitro Binding Assay of Idarubicin and DNA.  
6 *Biosens. Bioelectron.* **2015**, *70*, 345-350.
- 7  
8 (259) Gul, S.; Cooper, J. K.; Glans, P.-A.; Guo, J.; Yachandra, V. K.; Yano, J.; Zhang, J. Z.  
9 Effect of Al<sup>3+</sup> Co-doping on the Dopant Local Structure, Optical Properties, and Exciton  
10 Dynamics in Cu<sup>+</sup>-Doped ZnSe Nanocrystals. *ACS Nano* **2013**, *7*, 8680-8692.
- 11  
12 (260) Jain, P. K. Plasmon-in-a-Box: On the Physical Nature of Few-Carrier Plasmon  
13 Resonances. *J. Phys. Chem. Lett.* **2014**, *5*, 3112-3119.
- 14  
15 (261) Liu, X.; Swihart, M. T. Heavily-Doped Colloidal Semiconductor and Metal Oxide  
16 Nanocrystals: An Emerging New Class of Plasmonic Nanomaterials. *Chem. Soc. Rev.*  
17 **2014**, *43*, 3908-3920.
- 18  
19 (262) Zeng, S.; Yong, K.-T.; Roy, I.; Dinh, X.-Q.; Yu, X.; Luan, F. A Review on Functionalized  
20 Gold Nanoparticles for Biosensing Applications. *Plasmonics* **2011**, *6*, 491-506.
- 21  
22 (263) Zeng, S.; Baillargeat, D.; Ho, H.-P.; Yong, K.-T. Nanomaterials enhanced Surface  
23 Plasmon Resonance for Biological and Chemical Sensing Applications. *Chem. Soc. Rev.*  
24 **2014**, *43*, 3426-3452.
- 25  
26 (264) Zeng, S.; Sreekanth, K. V.; Shang, J.; Yu, T.; Chen, C.-K.; Yin, F.; Baillargeat, D.;  
27 Coquet, P.; Ho, H.-P.; Kabashin, A. V. *et al.* Graphene-Gold Metasurface Architectures  
28 for Ultrasensitive Plasmonic Biosensing. *Adv. Mater.* **2015**, *27*, 6163-6169.
- 29  
30 (265) Niezgoda, J. S.; Harrison, M. A.; McBride, J. R.; Rosenthal, S. J. Novel Synthesis of  
31 Chalcopyrite Cu<sub>x</sub>In<sub>y</sub>S<sub>2</sub> Quantum Dots with Tunable Localized Surface Plasmon  
32 Resonances. *Chem. Mater.* **2012**, *24*, 3294-3297.
- 33  
34 (266) Niezgoda, J. S.; Yap, E.; Keene, J. D.; McBride, J. R.; Rosenthal, S. J. Plasmonic  
35 Cu<sub>x</sub>In<sub>y</sub>S<sub>2</sub> Quantum Dots Make Better Photovoltaics Than Their Nonplasmonic  
36 Counterparts. *Nano Lett.* **2014**, *14*, 3262-3269.
- 37  
38 (267) Wang, X.; Swihart, M. T. Controlling the Size, Shape, Phase, Band Gap, and Localized  
39 Surface Plasmon Resonance of Cu<sub>2-x</sub>S and Cu<sub>x</sub>In<sub>y</sub>S Nanocrystals. *Chem. Mater.* **2015**, *27*,  
40 1786-1791.
- 41  
42 (268) Liu, X.; Wang, X.; Zhou, B.; Law, W. C.; Cartwright, A. N.; Swihart, M. T.  
43 Size-Controlled Synthesis of Cu<sub>2-x</sub>E (E= S, Se) Nanocrystals with Strong Tunable  
44 Near-Infrared Localized Surface Plasmon Resonance and High Conductivity in Thin  
45 Films. *Adv. Funct. Mater.* **2013**, *23*, 1256-1264.
- 46  
47 (269) Wang, F.; Li, Q.; Lin, L.; Peng, H.; Liu, Z.; Xu, D. Monodisperse Copper Chalcogenide  
48 Nanocrystals: Controllable Synthesis and the Pinning of Plasmonic Resonance  
49 Absorption. *J. Am. Chem. Soc.* **2015**, *137*, 12006-12012.
- 50  
51 (270) Liu, X.; Wang, X.; Swihart, M. T. Cu<sub>2-x</sub>S<sub>1-y</sub>Se<sub>y</sub> Alloy Nanocrystals with Broadly Tunable  
52 Near-Infrared Localized Surface Plasmon Resonance. *Chem. Mater.* **2013**, *25*, 4402-4408.

- 1  
2  
3  
4 (271) Liu, Z.; Liu, X.; Du, Y.; Ren, J.; Qu, X. Using Plasmonic Copper Sulfide Nanocrystals as  
5 Smart Light-Driven Sterilants. *ACS Nano* **2015**, *9*, 10335-10346.
- 6  
7 (272) Liu, X.; Wang, X.; Swihart, M. T. Composition-Dependent Crystal Phase, Optical  
8 Properties, and Self-Assembly of Cu-Sn-S Colloidal Nanocrystals. *Chem. Mater.* **2015**,  
9 *27*, 1342-1348.
- 10  
11 (273) Liu, M.; Xue, X.; Ghosh, C.; Liu, X.; Liu, Y.; Furlani, E. P.; Swihart, M. T.; Prasad, P. N.  
12 Room-Temperature Synthesis of Covellite Nanoplatelets with Broadly Tunable Localized  
13 Surface Plasmon Resonance. *Chem. Mater.* **2015**, *27*, 2584-2590.
- 14  
15 (274) Lee, K. S.; El-Sayed, M. A. Gold and Silver Nanoparticles in Sensing and Imaging:  
16 Sensitivity of Plasmon Response to Size, Shape, and Metal Composition. *J. Phys. Chem.*  
17 *B* **2006**, *110*, 19220-19225.
- 18  
19 (275) Gary, D. C.; Terban, M. W.; Billinge, S. J. L.; Cossairt, B. M. Two-Step Nucleation and  
20 Growth of InP Quantum Dots via Magic-Sized Cluster Intermediates. *Chem. Mater.* **2015**,  
21 *27*, 1432-1441.
- 22  
23 (276) Brunetti, V.; Chibli, H.; Fiammengo, R.; Galeone, A.; Malvindi, M. A.; Vecchio, G.;  
24 Cingolani, R.; Nadeau, J. L.; Pompa, P. P. InP/ZnS as a Safer Alternative to CdSe/ZnS  
25 Core/Shell Quantum Dots: *in vitro* and *in vivo* Toxicity Assessment. *Nanoscale* **2013**, *5*,  
26 307-317.
- 27  
28 (277) Lin, G.; Ouyang, Q.; Hu, R.; Ding, Z.; Tian, J.; Yin, F.; Xu, G.; Chen, Q.; Wang, X.; Yong,  
29 K.-T. *In vivo* Toxicity Assessment of Non-Cadmium Quantum Dots in BALB/c Mice.  
30 *Nanomed-Nanotechnol.* **2015**, *11*, 341-350.
- 31  
32 (278) Micic, O. I.; Curtis, C. J.; Jones, K. M.; Sprague, J. R.; Nozik, A. J. Synthesis and  
33 Characterization of InP Quantum Dots. *J. Phys. Chem.* **1994**, *98*, 4966-4969.
- 34  
35 (279) Battaglia, D.; Peng, X. Formation of High Quality InP and InAs Nanocrystals in a  
36 Noncoordinating Solvent. *Nano Lett.* **2002**, *2*, 1027-1030.
- 37  
38 (280) Choi, H. S.; Kim, Y.; Park, J. C.; Oh, M. H.; Jeon, D. Y.; Nam, Y. S. Highly Luminescent,  
39 Off-Stoichiometric Cu<sub>x</sub>In<sub>y</sub>S<sub>2</sub>/ZnS Quantum Dots for Near-Infrared Fluorescence Bio-  
40 Imaging. *RSC Adv.* **2015**, *5*, 43449-43455.
- 41  
42 (281) Yong, K.-T.; Roy, I.; Hu, R.; Ding, H.; Cai, H.; Zhu, J.; Zhang, X.; Bergey, E. J.; Prasad,  
43 P. N. Synthesis of Ternary CuInS<sub>2</sub>/ZnS Quantum Dot Bioconjugates and Their  
44 Applications for Targeted Cancer Bioimaging. *Integr. Biol.* **2010**, *2*, 121-129.
- 45  
46 (282) Xie, R.; Rutherford, M.; Peng, X. Formation of High-Quality I-III-VI Semiconductor  
47 Nanocrystals by Tuning Relative Reactivity of Cationic Precursors. *J. Am. Chem. Soc.*  
48 **2009**, *131*, 5691-5697.
- 49  
50 (283) Nam, D.-E.; Song, W.-S.; Yang, H. Facile, Air-Insensitive Solvothermal Synthesis of  
51 Emission-Tunable CuInS<sub>2</sub>/ZnS Quantum Dots with High Quantum Yields. *J. Mater.*  
52 *Chem.* **2011**, *21*, 18220-18226.

- 1  
2  
3  
4 (284) Guo, W.; Chen, N.; Dong, C.; Tu, Y.; Chang, J.; Zhang, B. One-Pot Synthesis of  
5 Hydrophilic ZnCuInS/ZnS Quantum Dots for *in vivo* Imaging. *RSC Adv.* **2013**, *3*, 9470-  
6 9475.
- 7  
8 (285) Tang, R.; Xue, J.; Xu, B.; Shen, D.; Sudlow, G. P.; Achilefu, S. Tunable Ultrasmall  
9 Visible-to-Extended Near-Infrared Emitting Silver Sulfide Quantum Dots for Integrin-  
10 Targeted Cancer Imaging. *ACS Nano* **2015**, *9*, 220-230.
- 11  
12 (286) Gui, R.; Jin, H.; Wang, Z.; Tan, L. Recent Advances in Synthetic Methods and  
13 Applications of Colloidal Silver Chalcogenide Quantum Dots. *Coord. Chem. Rev.* **2015**,  
14 *296*, 91-124.
- 15  
16 (287) Du, Y.; Xu, B.; Fu, T.; Cai, M.; Li, F.; Zhang, Y.; Wang, Q. Near-Infrared  
17 Photoluminescent Ag<sub>2</sub>S Quantum Dots from a Single Source Precursor. *J. Am. Chem.*  
18 *Soc.* **2010**, *132*, 1470-1471.
- 19  
20 (288) Hocaoglu, I.; Cizmeciyan, M. N.; Erdem, R.; Ozen, C.; Kurt, A.; Sennaroglu, A.; Acar, H.  
21 Y. Development of Highly Luminescent and Cytocompatible Near-IR-Emitting Aqueous  
22 Ag<sub>2</sub>S Quantum Dots. *J. Mater. Chem.* **2012**, *22*, 14674-14681.
- 23  
24 (289) Zhang, Y.; Zhang, Y.; Hong, G.; He, W.; Zhou, K.; Yang, K.; Li, F.; Chen, G.; Liu, Z.; Dai,  
25 H. *et al.* Biodistribution, Pharmacokinetics and Toxicology of Ag<sub>2</sub>S Near-Infrared  
26 Quantum Dots in Mice. *Biomaterials* **2013**, *34*, 3639-3646.
- 27  
28 (290) Zhang, Y.; Hong, G.; Zhang, Y.; Chen, G.; Li, F.; Dai, H.; Wang, Q. Ag<sub>2</sub>S Quantum Dot: A  
29 Bright and Biocompatible Fluorescent Nanoprobe in the Second Near-Infrared Window.  
30 *ACS Nano* **2012**, *6*, 3695-3702.
- 31  
32 (291) Wang, Y.; Yan, X.-P. Fabrication of Vascular Endothelial Growth Factor Antibody  
33 Bioconjugated Ultrasmall Near-Infrared Fluorescent Ag<sub>2</sub>S Quantum Dots for Targeted  
34 Cancer Imaging *in vivo*. *Chem. Comm.* **2013**, *49*, 3324-3326.
- 35  
36 (292) Shen, S.; Zhang, Y.; Peng, L.; Du, Y.; Wang, Q. Matchstick-Shaped Ag<sub>2</sub>S-ZnS  
37 Heteronanostructures Preserving both UV/Blue and Near-Infrared Photoluminescence.  
38 *Angew. Chemie* **2011**, *50*, 7115-7118.
- 39  
40 (293) Shen, S.; Zhang, Y.; Liu, Y.; Peng, L.; Chen, X.; Wang, Q. Manganese-Doped Ag<sub>2</sub>S-ZnS  
41 Heteronanostructures. *Chem. Mater.* **2012**, *24*, 2407-2413.
- 42  
43 (294) Gu, Y.-P.; Cui, R.; Zhang, Z.-L.; Xie, Z.-X.; Pang, D.-W. Ultrasmall Near-Infrared Ag<sub>2</sub>Se  
44 Quantum Dots with Tunable Fluorescence for *in vivo* Imaging. *J. Am. Chem. Soc.* **2012**,  
45 *134*, 79-82.
- 46  
47 (295) Song, J.; Jiang, T.; Guo, T.; Liu, L.; Wang, H.; Xia, T.; Zhang, W.; Ye, X.; Yang, M.; Zhu,  
48 L. *et al.* Facile Synthesis of Water-Soluble Zn-Doped AgIn<sub>5</sub>S<sub>8</sub>/ZnS Core/Shell Fluorescent  
49 Nanocrystals and Their Biological Application. *Inorg. Chem.* **2015**, *54*, 1627-1633.
- 50  
51  
52  
53

- 1  
2  
3  
4 (296) Deng, D.; Cao, J.; Qu, L.; Achilefu, S.; Gu, Y. Highly Luminescent Water-Soluble  
5 Quaternary Zn-Ag-In-S Quantum Dots for Tumor Cell-Targeted Imaging. *Phys. Chem.*  
6 *Chem. Phys.* **2013**, *15*, 5078-5083.
- 7  
8 (297) Gao, J.; Chen, K.; Xie, R.; Xie, J.; Lee, S.; Cheng, Z.; Peng, X.; Chen, X. Ultrasmall  
9 Near-Infrared Non-Cadmium Quantum Dots for *in vivo* Tumor Imaging. *Small* **2010**, *6*,  
10 256-261.
- 11  
12 (298) Xie, R.; Peng, X. Synthetic Scheme for High-Quality InAs Nanocrystals Based on Self-  
13 Focusing and One-Pot Synthesis of InAs-Based Core-Shell Nanocrystals. *Angew. Chem.*  
14 *Int. Edit.* **2008**, *47*, 7677-7680.
- 15  
16 (299) Xie, R.; Chen, K.; Chen, X.; Peng, X. InAs/InP/ZnSe Core/Shell/Shell Quantum Dots as  
17 Near-Infrared Emitters: Bright, Narrow-Band, Non-Cadmium Containing, and  
18 Biocompatible. *Nano Res.* **2008**, *1*, 457-464.
- 19  
20 (300) Fan, J.-W.; Vankayala, R.; Chang, C.-L.; Chang, C.-H.; Chiang, C.-S.; Hwang, K. C.  
21 Preparation, Cytotoxicity and *in vivo* Bioimaging of Highly Luminescent Water-Soluble  
22 Silicon Quantum Dots. *Nanotechnology* **2015**, *26*, 215703-215703.
- 23  
24 (301) Shen, P.; Ohta, S.; Inasawa, S.; Yamaguchi, Y. Selective Labeling of the Endoplasmic  
25 Reticulum in Live Cells with Silicon Quantum Dots. *Chem. Commun.* **2011**, *47*, 8409-  
26 8411.
- 27  
28 (302) Shiohara, A.; Prabakar, S.; Faramus, A.; Hsu, C.-Y.; Lai, P.-S.; Northcote, P. T.; Tilley, R.  
29 D. Sized Controlled Synthesis, Purification, and Cell Studies with Silicon Quantum Dots.  
30 *Nanoscale* **2011**, *3*, 3364-3370.
- 31  
32 (303) Xu, S.; Li, D.; Wu, P. One-Pot, Facile, and Versatile Synthesis of Monolayer MoS<sub>2</sub>/WS<sub>2</sub>  
33 Quantum Dots as Bioimaging Probes and Efficient Electrocatalysts for Hydrogen  
34 Evolution Reaction. *Adv. Funct. Mater.* **2015**, *25*, 1127-1136.
- 35  
36 (304) Zeng, S.; Hu, S.; Xia, J.; Anderson, T.; Dinh, X.-Q.; Meng, X.-M.; Coquet, P.; Yong, K.-  
37 T. Graphene-MoS<sub>2</sub> Hybrid Nanostructures Enhanced Surface Plasmon Resonance  
38 Biosensors. *Sensor. Actuat. B-Chem.* **2015**, *207*, 801-810.
- 39  
40 (305) Zheng, X. T.; Ananthanarayanan, A.; Luo, K. Q.; Chen, P. Glowing Graphene Quantum  
41 Dots and Carbon Dots: Properties, Syntheses, and Biological Applications. *Small* **2015**,  
42 *11*, 1620-1636.
- 43  
44 (306) Pan, D. Y.; Zhang, J. C.; Li, Z.; Wu, M. H. Hydrothermal Route for Cutting Graphene  
45 Sheets into Blue-Luminescent Graphene Quantum Dots. *Adv. Mater.* **2010**, *22*, 734-738.
- 46  
47 (307) Peng, J.; Gao, W.; Gupta, B. K.; Liu, Z.; Romero-Aburto, R.; Ge, L.; Song, L.; Alemany,  
48 L. B.; Zhan, X.; Gao, G. *et al.* Graphene Quantum Dots Derived from Carbon Fibers.  
49 *Nano. Lett.* **2012**, *12*, 844-849.
- 50  
51  
52  
53  
54  
55  
56  
57  
58  
59  
60

- 1  
2  
3  
4 (308) Dong, Y.; Chen, C.; Zheng, X.; Gao, L.; Cui, Z.; Yang, H.; Guo, C.; Chi, Y.; Li, C. M.  
5 One-Step and High Yield Simultaneous Preparation of Single- and Multi-Layer Graphene  
6 Quantum Dots from CX-72 Carbon Black. *J. Mater. Chem.* **2012**, *22*, 8764-8766.
- 7  
8 (309) Zhao, H.; Chang, Y.; Liu, M.; Gao, S.; Yu, H.; Quan, X. A Universal Immunosensing  
9 Strategy Based on Regulation of the Interaction between Graphene and Graphene  
10 Quantum Dots. *Chem. Commun.* **2013**, *49*, 234-236.
- 11  
12 (310) Zhu, S.; Zhang, J.; Tang, S.; Qiao, C.; Wang, L.; Wang, H.; Liu, X.; Li, B.; Li, Y.; Yu, W.  
13 *et al.* Surface Chemistry Routes to Modulate the Photoluminescence of Graphene  
14 Quantum Dots: From Fluorescence Mechanism to Up-Conversion Bioimaging  
15 Applications. *Adv. Funct. Mater.* **2012**, *22*, 4732-4740.
- 16  
17 (311) Zhang, J.; Zhu, A.; Zhao, T.; Wu, L.; Wu, P.; Hou, X. Glucose Oxidase-directed, Instant  
18 Synthesis of Mn-Doped ZnS Quantum Dots in Neutral Media with Retained Enzymatic  
19 Activity: Mechanistic Study and Biosensing Application. *J. Mater. Chem. B* **2015**, *3*,  
20 5942-5950.
- 21  
22 (312) Song, Y.; Li, Y.; Liu, Y.; Su, X.; Ma, Q. Highly Sensitive and Selective Detection of  
23 Phosphate Using Novel Highly Photoluminescent Water-Soluble Mn-Doped ZnTe/ZnSe  
24 Quantum Dots. *Talanta* **2015**, *144*, 680-685.
- 25  
26 (313) Cao, S.; Zhao, J.; yang, w.; Li, C.; Zheng, J. Mn<sup>2+</sup>-Doped Zn-In-S Quantum Dots with  
27 Tunable Bandgaps and High Photoluminescence Properties. *J. Mater. Chem. C* **2015**, *3*,  
28 8844-8851.
- 29  
30 (314) Manzoor, K.; Johny, S.; Thomas, D.; Setua, S.; Menon, D.; Nair, S. Bio-Conjugated  
31 Luminescent Quantum Dots of Doped ZnS: a Cyto-Friendly System for Targeted Cancer  
32 Imaging. *Nanotechnology* **2009**, *20*, 065102-065102.
- 33  
34 (315) Wu, P.; He, Y.; Wang, H.-F.; Yan, X.-P. Conjugation of Glucose Oxidase onto Mn-Doped  
35 ZnS Quantum Dots for Phosphorescent Sensing of Glucose in Biological Fluids. *Anal.*  
36 *Chem.* **2010**, *82*, 1427-1433.
- 37  
38 (316) Wu, P.; Miao, L.-N.; Wang, H.-F.; Shao, X.-G.; Yan, X.-P. A Multidimensional Sensing  
39 Device for the Discrimination of Proteins Based on Manganese-Doped ZnS Quantum  
40 Dots. *Angew. Chem. Int. Edit.* **2011**, *50*, 8118-8121.
- 41  
42 (317) Zhou, R.; Li, M.; Wang, S.; Wu, P.; Wu, L.; Hou, X. Low-Toxic Mn-Doped ZnSe/ZnS  
43 Quantum Dots Conjugated with Nano-Hydroxyapatite for Cell Imaging. *Nanoscale* **2014**,  
44 *6*, 14319-14325.
- 45  
46 (318) Yang, H.-J.; Chen, C.-Y.; Yuan, F.-W.; Tuan, H.-Y. Designed Synthesis of Solid and  
47 Hollow Cu<sub>2-x</sub>Te Nanocrystals with Tunable Near-Infrared Localized Surface Plasmon  
48 Resonance. *J. Phys. Chem. C* **2013**, *117*, 21955-21964.
- 49  
50 (319) Vu, T. Q.; Lam, W. Y.; Hatch, E. W.; Lidke, D. S. Quantum Dots for Quantitative  
51 Imaging: from Single Molecules to Tissue. *Cell Tissue Res.* **2015**, *360*, 71-86.
- 52  
53

- 1  
2  
3  
4 (320) Hu, T.; Liu, X.; Liu, S.; Wang, Z.; Tang, Z. Toward Understanding of Transfer  
5 Mechanism between Electrochemiluminescent Dyes and Luminescent Quantum Dots.  
6 *Anal. Chem.* **2014**, *86*, 3939-3946.
- 7  
8 (321) Guo, W.; Yang, W.; Wang, Y.; Sun, X.; Liu, Z.; Zhang, B.; Chang, J.; Chen, X. Color-  
9 Tunable Gd-Zn-Cu-In-S/ZnS Quantum Dots for Dual Modality Magnetic Resonance and  
10 Fluorescence Imaging. *Nano Res.* **2014**, *7*, 1581-1591.
- 11  
12 (322) Chen, H.; Zhang, M.; Li, B.; Chen, D.; Dong, X.; Wang, Y.; Gu, Y. Versatile  
13 Antimicrobial Peptide-Based ZnO Quantum Dots for *in vivo* Bacteria Diagnosis and  
14 Treatment with High Specificity. *Biomaterials* **2015**, *53*, 532-544.
- 15  
16 (323) Johari-Ahar, M.; Barar, J.; Alizadeh, A. M.; Davaran, S.; Omid, Y.; Rashidi, M.-R.  
17 Methotrexate-Conjugated Quantum Dots: Synthesis, Characterisation and Cytotoxicity in  
18 Drug Resistant Cancer Cells. *J. Drug Target.* **2015**, *24*, 120-133.
- 19  
20 (324) Zeng, W.-J.; Peng, C.-W.; Yuan, J.-P.; Cui, R.; Li, Y. Quantum Dot-Based Multiplexed  
21 Imaging in Malignant Ascites: A New Model for Malignant Ascites Classification. *Int. J.*  
22 *Nanomed.* **2015**, *10*, 1759-1768.
- 23  
24 (325) Song, Y. F.; Chen, F.-F.; Xiong, B. Capture and Identification of Heterogeneous Circulating  
25 Tumor Cells Using Transparent Nanomaterials and Quantum Dots-Based Multiplexed  
26 Imaging. *J. Cancer* **2016**, *7*, 69-79.
- 27  
28 (326) Benítez-Martínez, S.; Valcárcel, M. Graphene Quantum Dots in Analytical Science. *Trac-*  
29 *Trend. Anal. Chem.* **2015**, *72*, 93-113.
- 30  
31 (327) Liu, H.; Fan, Y.; Wang, J.; Song, Z.; Shi, H.; Han, R.; Sha, Y.; Jiang, Y. Intracellular  
32 Temperature Sensing: An Ultra-bright Luminescent Nanothermometer with Non-  
33 Sensitivity to pH and Ionic Strength. *Sci. Rep.* **2015**, *5*, 14879-14879.
- 34  
35 (328) Wang, F.; Gu, Z.; Lei, W.; Wang, W.; Xia, X.; Hao, Q. Graphene Quantum Dots as a  
36 Fluorescent Sensing Platform for Highly Efficient Detection of Copper (II) ions. *Sensor.*  
37 *Actuat. B-Chem.* **2014**, *190*, 516-522.
- 38  
39 (329) Liang, R.-P.; Qiu, W.-B.; Zhao, H.-F.; Xiang, C.-Y.; Qiu, J.-D. Electrochemiluminescence  
40 Resonance Energy Transfer between Graphene Quantum Dots and Graphene Oxide for  
41 Sensitive Protein Kinase Activity and Inhibitor Sensing. *Anal. Chim. Acta.* **2016**, *904*, 58-  
42 64.
- 43  
44 (330) Choi, A. O.; Neibert, K. D.; Maysinger, D. In *Quantum Dots: Applications in Biology*;  
45 Fontes, A, Santos, B. S., Eds.; Springer: New York, 2014; pp 191-206.
- 46  
47 (331) Liu, L.; Hu, R.; Roy, I.; Lin, G.; Ye, L.; Reynolds, J. L.; Liu, J.; Liu, J.; Schwartz, S. A.;  
48 Zhang, X. *et al.* Synthesis of Luminescent Near-Infrared AgInS<sub>2</sub> Nanocrystals as Optical  
49 Probes for *in vivo* Applications. *Theranostics* **2013**, *3*, 109-115.
- 50  
51 (332) Deng, D.; Qu, L.; Gu, Y. Near-Infrared Broadly Emissive AgInSe<sub>2</sub>/ZnS Quantum Dots for  
52 Biomedical Optical Imaging. *J. Mater. Chem. C* **2014**, *2*, 7077-7085.

- 1  
2  
3  
4 (333) Dong, C.; Liu, Z.; Zhang, L.; Guo, W.; Li, X.; Liu, J.; Wang, H.; Chang, J. pH-Induced  
5 Charge-Reversible NIR Fluorescence Nanoprobe for Tumor-Specific Imaging. *ACS Appl.*  
6 *Mater. Inter.* **2015**, *7*, 7566-7575.
- 7  
8 (334) Nurunnabi, M.; Khatun, Z.; Nafiujjaman, M.; Lee, D. G.; Lee, Y. K. Surface Coating of  
9 Graphene Quantum Dots Using Mussel-Inspired Polydopamine for Biomedical Optical  
10 Imaging. *ACS Appl. Mater. Inter.* **2013**, *5*, 8246-8253.
- 11  
12 (335) Zhong, Y.; Sun, X.; Wang, S.; Peng, F.; Bao, F.; Su, Y.; Li, Y.; Lee, S.-T.; He, Y. Facile,  
13 Large-Quantity Synthesis of Stable, Tunable-Color Silicon Nanoparticles and Their  
14 Application for Long-Term Cellular Imaging. *ACS Nano* **2015**, *9*, 5958-5967.
- 15  
16 (336) Gao, X.; Zhang, H.; Li, Y.; Su, X. Mn-Doped ZnSe D-Dots-Based Alpha-Methylacyl-  
17 CoA Racemase Probe for Human Prostate Cancer Cell Imaging. *Anal. Bioanal. Chem.*  
18 **2012**, *402*, 1871-1877.
- 19  
20 (337) Yu, Z.; Ma, X.; Yu, B.; Pan, Y.; Liu, Z. Synthesis and Characterization of ZnS:Mn/ZnS  
21 Core/Shell Nanoparticles for Tumor Targeting and Imaging *in vivo*. *J. Biomater. Appl.*  
22 **2013**, *28*, 232-240.
- 23  
24 (338) Mandal, G.; Darragh, M.; Wang, Y. A.; Heyes, C. D. Cadmium-Free Quantum Dots as  
25 Time-Gated Bioimaging Probes in Highly-Autofluorescent Human Breast Cancer Cells.  
26 *Chem. Commun.* **2013**, *49*, 624-626.
- 27  
28 (339) Zhu, S.; Zhou, N.; Hao, Z.; Maharjan, S.; Zhao, X.; Song, Y.; Sun, B.; Zhang, K.; Zhang,  
29 J.; Sun, H. *et al.* Photoluminescent Graphene Quantum Dots for *in vitro* and *in vivo*  
30 Bioimaging Using Long Wavelength Emission. *RSC Adv.* **2015**, *5*, 39399-39403.
- 31  
32 (340) Liu, X.; Law, W.-C.; Jeon, M.; Wang, X.; Liu, M.; Kim, C.; Prasad, P. N.; Swihart, M. T.  
33 Cu<sub>2-x</sub>Se Nanocrystals with Localized Surface Plasmon Resonance as Sensitive Contrast  
34 Agents for *in vivo* Photoacoustic Imaging: Demonstration of Sentinel Lymph Node  
35 Mapping. *Adv. Healthc. Mater.* **2013**, *2*, 952-957.
- 36  
37 (341) Ku, G.; Zhou, M.; Song, S.; Huang, Q.; Hazle, J.; Li, C. Copper Sulfide Nanoparticles As  
38 a New Class of Photoacoustic Contrast Agent for Deep Tissue Imaging at 1064 nm. *ACS*  
39 *Nano* **2012**, *6*, 7489-7496.
- 40  
41 (342) Srinivasan, K.; Thiruppathiraja, C.; Subramanian, K.; Dinakaran, K. Sensitive Detection  
42 of *C. Parvum* Using Near-Infrared Emitting Ag<sub>2</sub>S-Silica Core-Shell Nanospheres. *RSC*  
43 *Adv.* **2014**, *4*, 62399-62403.
- 44  
45 (343) Cui, R.; Gu, Y.-P.; Bao, L.; Zhao, J.-Y.; Qi, B.-P.; Zhang, Z.-L.; Xie, Z.-X.; Pang, D.-W.  
46 Near-Infrared Electrogenerated Chemiluminescence of Ultrasmall Ag<sub>2</sub>Se Quantum Dots  
47 for the Detection of Dopamine. *Anal. Chem.* **2012**, *84*, 8932-8935.
- 48  
49 (344) Yan, S.; Zhang, L.; Tang, Y.; Lv, Y. Synthesis of Water-Soluble Ag<sub>2</sub>Se QDs as a Novel  
50 Resonance Rayleigh Scattering Sensor for Highly Sensitive and Selective ConA  
51 Detection. *Analyst* **2014**, *139*, 4210-4215.

- 1  
2  
3  
4 (345) Liu, S.; Shi, F.; Zhao, X.; Chen, L.; Su, X. 3-Aminophenyl Boronic Acid-Functionalized  
5 CuInS<sub>2</sub> Quantum Dots as a Near-Infrared Fluorescence Probe for the Determination of  
6 Dopamine. *Biosens. Bioelectron.* **2013**, *47*, 379-384.
- 7  
8 (346) Qian, Z. S.; Shan, X. Y.; Chai, L. J.; Ma, J. J.; Chen, J. R.; Feng, H. DNA Nanosensor  
9 Based on Biocompatible Graphene Quantum Dots and Carbon Nanotubes. *Biosens.*  
10 *Bioelectron.* **2014**, *60*, 64-70.
- 11  
12 (347) Cao, J.; Zhu, H.; Deng, D.; Xue, B.; Tang, L.; Mahounga, D.; Qian, Z.; Gu, Y. *In vivo*  
13 NIR Imaging with PbS Quantum Dots Entrapped in Biodegradable Micelles. *J. Biomed.*  
14 *Mater. Res. A* **2012**, *100A*, 958-968.
- 15  
16 (348) Hessel, C. M.; Pattani, V. P.; Rasch, M.; Panthani, M. G.; Koo, B.; Tunnell, J. W.; Korgel,  
17 B. A. Copper Selenide Nanocrystals for Photothermal Therapy. *Nano Lett.* **2011**, *11*,  
18 2560-2566.
- 19  
20 (349) Liu, X.; Li, B.; Fu, F.; Xu, K.; Zou, R.; Wang, Q.; Zhang, B.; Chen, Z.; Hu, J. Facile  
21 Synthesis of Biocompatible Cysteine-Coated CuS Nanoparticles with High Photothermal  
22 Conversion Efficiency for Cancer Therapy. *Dalton T.* **2014**, *43*, 11709-11715.
- 23  
24 (350) Fahmi, M. Z.; Ou, K.-L.; Chen, J.-K.; Ho, M.-H.; Tzing, S.-H.; Chang, J.-Y.  
25 Development of Bovine Serum Albumin-Modified Hybrid Nanoclusters for  
26 Magnetofluorescence Imaging and Drug Delivery. *RSC Adv.* **2014**, *4*, 32762-32772.
- 27  
28 (351) Zhao, C.; Bai, Z.; Liu, X.; Zhang, Y.; Zou, B.; Zhong, H. Small GSH-Capped CuInS<sub>2</sub>  
29 Quantum Dots: MPA-Assisted Aqueous Phase Transfer and Bioimaging Applications.  
30 *ACS Appl. Mater. Inter.* **2015**, *7*, 17623-17629.
- 31  
32 (352) Zhou, J.; Yang, Y.; Zhang, C.-Y. Toward Biocompatible Semiconductor Quantum Dots:  
33 From Biosynthesis and Bioconjugation to Biomedical Application. *Chem. Rev.* **2015**, *115*,  
34 11669-11717.
- 35  
36 (353) Chen, G.; Tian, F.; Li, C.; Zhang, Y.; Weng, Z.; Zhang, Y.; Peng, R.; Wang, Q. *In vivo*  
37 Real-Time Visualization of Mesenchymal Stem cells Tropism for Cutaneous  
38 Regeneration Using NIR-II Fluorescence Imaging. *Biomaterials* **2015**, *53*, 265-273.
- 39  
40 (354) Hu, F.; Li, C.; Zhang, Y.; Wang, M.; Wu, D.; Wang, Q. Real-time *in vivo* Visualization of  
41 Tumor Therapy by a Near-Infrared-II Ag<sub>2</sub>S Quantum Dot-Based Theranostic  
42 Nanoplatform. *Nano Res.* **2015**, *8*, 1637-1647.
- 43  
44 (355) Liu, L.; Hu, R.; Law, W. C.; Roy, I.; Zhu, J.; Ye, L.; Hu, S.; Zhang, X.; Yong, K. T.  
45 Optimizing the Synthesis of Red- and Near-Infrared CuInS<sub>2</sub> and AgInS<sub>2</sub> Semiconductor  
46 Nanocrystals for Bioimaging. *Analyst* **2013**, *138*, 6144-6153.
- 47  
48 (356) Yu, K.; Ng, P.; Ouyang, J.; Zaman, M. B.; Abulrob, A.; Baral, T. N.; Fatehi, D.; Jakubek,  
49 Z. J.; Kingston, D.; Wu, X. *et al.* Low-Temperature Approach to Highly Emissive Copper  
50 Indium Sulfide Colloidal Nanocrystals and Their Bioimaging Applications. *ACS Appl.*  
51 *Mater. Inter.* **2013**, *5*, 2870-2880.

- 1  
2  
3  
4 (357) Fahmi, M. Z.; Chang, J. Y. Forming Double Layer-Encapsulated Quantum Dots for Bio-  
5 imaging and Cell Targeting. *Nanoscale* **2013**, *5*, 1517-1528.
- 6 (358) Bouccara, S.; Fragola, A.; Giovanelli, E.; Sitbon, G.; Lequeux, N.; Pons, T.; Loriette, V.  
7 Time-Gated Cell Imaging Using Long Lifetime Near-Infrared-Emitting Quantum Dots  
8 for Autofluorescence Rejection. *J. Biomed. Opt.* **2014**, *19*, 051208-051208.
- 9  
10 (359) Soenen, S. J.; Rivera-Gil, P.; Montenegro, J.-M.; Parak, W. J.; De Smedt, S. C.;  
11 Braeckmans, K. Cellular Toxicity of Inorganic Nanoparticles: Common Aspects and  
12 Guidelines for Improved Nanotoxicity Evaluation. *Nano Today* **2011**, *6*, 446-465.
- 13 (360) Peng, F.; Su, Y.; Zhong, Y.; Fan, C.; Lee, S.-T.; He, Y. Silicon Nanomaterials Platform for  
14 Bioimaging, Biosensing, and Cancer Therapy. *Accounts Chem. Res.* **2014**, *47*, 612-623.
- 15 (361) Cheng, X.; Hinde, E.; Owen, D. M.; Lowe, S. B.; Reece, P. J.; Gaus, K.; Gooding, J. J.  
16 Enhancing Quantum Dots for Bioimaging Using Advanced Surface Chemistry and  
17 Advanced Optical Microscopy: Application to Silicon Quantum Dots (SiQDs). *Adv.*  
18 *Mater.* **2015**, *27*, 6144-6150.
- 19 (362) Lee, C.; Kim, J.; Zhang, Y.; Jeon, M.; Liu, C.; Song, L.; Lovell, J. F.; Kim, C. Dual-Color  
20 Photoacoustic Lymph Node Imaging Using Nanoformulated Naphthalocyanines.  
21 *Biomaterials* **2015**, *73*, 142-148.
- 22 (363) Chen, P.-J.; Kang, Y.-D.; Lin, C.-H.; Chen, S.-Y.; Hsieh, C.-H.; Chen, Y.-Y.; Chiang, C.-  
23 W.; Lee, W.; Hsu, C.-Y.; Liao, L.-D. *et al.* Multitheragnostic Multi-GNRs Crystal-Seeded  
24 Magnetic Nanoseaurchin for Enhanced *in vivo* Mesenchymal-Stem-Cell Homing,  
25 Multimodal Imaging, and Stroke Therapy. *Adv. Mater.* **2015**, *27*, 6488-6495.
- 26 (364) Ripoll, J.; Koberstein-Schwarz, B.; Ntziachristos, V. Unleashing Optics and  
27 Optoacoustics for Developmental Biology. *Trends Biotechnol.* **2015**, *33*, 679-691.
- 28 (365) Garcia-Urbe, A.; Erpelding, T. N.; Krumholz, A.; Ke, H.; Maslov, K.; Appleton, C.;  
29 Margenthaler, J. A.; Wang, L. V. Dual-Modality Photoacoustic and Ultrasound Imaging  
30 System for Noninvasive Sentinel Lymph Node Detection in Patients with Breast Cancer.  
31 *Sci. Rep.* **2015**, *5*, 15748-15748.
- 32 (366) Mou, J.; Li, P.; Liu, C.; Xu, H.; Song, L.; Wang, J.; Zhang, K.; Chen, Y.; Shi, J.; Chen, H.  
33 Ultrasmall Cu<sub>2-x</sub>S Nanodots for Highly Efficient Photoacoustic Imaging-Guided  
34 Photothermal Therapy. *Small* **2015**, *11*, 2275-2283.
- 35 (367) Wang, H.-Y.; Hua, X.-W.; Wu, F.-G.; Li, B.; Liu, P.; Gu, N.; Wang, Z.; Chen, Z. Synthesis  
36 of Ultrastable Copper Sulfide Nanoclusters via Trapping the Reaction Intermediate:  
37 Potential Anticancer and Antibacterial Applications. *ACS Appl. Mater. Inter.* **2015**, *7*,  
38 7082-7092.
- 39 (368) Gao, D.; Zhang, P.; Liu, C.; Chen, C.; Gao, G.; Wu, Y.; Sheng, Z.; Song, L.; Cai, L.  
40 Compact Chelator-Free Ni-Integrated CuS Nanoparticles with Tunable Near-Infrared  
41  
42  
43  
44  
45  
46  
47  
48  
49  
50  
51  
52  
53

- Absorption and Enhanced Relaxivity for *in vivo* Dual-Modal Photoacoustic/MR Imaging. *Nanoscale* **2015**, *7*, 17631-17636.
- (369) Liu, X.; Lee, C.; Law, W. C.; Zhu, D.; Liu, M.; Jeon, M.; Kim, J.; Prasad, P. N.; Kim, C.; Swihart, M. T. Au-Cu<sub>2-x</sub>Se Heterodimer Nanoparticles with Broad Localized Surface Plasmon Resonance as Contrast Agents for Deep Tissue Imaging. *Nano Lett.* **2013**, *13*, 4333-4339.
- (370) Ding, K.; Zeng, J.; Jing, L.; Qiao, R.; Liu, C.; Jiao, M.; Li, Z.; Gao, M. Aqueous Synthesis of PEGylated Copper Sulfide Nanoparticles for Photoacoustic Imaging of Tumors. *Nanoscale* **2015**, *7*, 11075-11081.
- (371) Yang, K.; Zhu, L.; Nie, L.; Sun, X.; Cheng, L.; Wu, C.; Niu, G.; Chen, X.; Liu, Z. Visualization of Protease Activity *in vivo* Using an Activatable Photo-Acoustic Imaging Probe Based on CuS Nanoparticles. *Theranostics* **2014**, *4*, 134-141.
- (372) Zha, Z.; Zhang, S.; Deng, Z.; Li, Y.; Li, C.; Dai, Z. Enzyme-Responsive Copper Sulphide Nanoparticles for Combined Photoacoustic Imaging, Tumor-Selective Chemotherapy and Photothermal Therapy. *Chem. Commun.* **2013**, *49*, 3455-3457.
- (373) Liu, R.; Jing, L.; Peng, D.; Li, Y.; Tian, J.; Dai, Z. Manganese (II) Chelate Functionalized Copper Sulfide Nanoparticles for Efficient Magnetic Resonance/Photoacoustic Dual-Modal Imaging Guided Photothermal Therapy. *Theranostics* **2015**, *5*, 1144-1153.
- (374) Song, J.; Yang, X.; Jacobson, O.; Lin, L.; Huang, P.; Niu, G.; Ma, Q.; Chen, X. Sequential Drug Release and Enhanced Photothermal and Photoacoustic Effect of Hybrid Reduced Graphene Oxide-Loaded Ultrasmall Gold Nanorod Vesicles for Cancer Therapy. *ACS Nano* **2015**, *9*, 9199-9209.
- (375) Lin, Z.; Pan, D.; Hu, T.; Liu, Z.; Su, X. A Near-Infrared Fluorescent Bioassay for Thrombin Using Aptamer-Modified CuInS<sub>2</sub> Quantum Dots. *Microchim. Acta* **2015**, *182*, 1933-1939.
- (376) Liu, S.; Shi, F.; Chen, L.; Su, X. Dopamine Functionalized CuInS<sub>2</sub> Quantum Dots as a Fluorescence Probe for Urea. *Sensor. Actuat. B-Chem.* **2014**, *191*, 246-251.
- (377) Xiong, W.-W.; Yang, G.-H.; Wu, X.-C.; Zhu, J.-J. Microwave-Assisted Synthesis of Highly Luminescent AgInS<sub>2</sub>/ZnS Nanocrystals for Dynamic Intracellular Cu(II) Detection. *J. Mater. Chem. B* **2013**, *1*, 4160-4165.
- (378) Liu, S.; Na, W.; Pang, S.; Shi, F.; Su, X. A Label-Free Fluorescence Detection Strategy for Lysozyme Assay Using CuInS<sub>2</sub> Quantum Dots. *Analyst* **2014**, *139*, 3048-3054.
- (379) Liu, S.; Pang, S.; Huang, H.; Su, X. 3-Aminophenylboronic Acid-Functionalized CuInS<sub>2</sub> Quantum Dots as a Near-Infrared Fluorescence Probe for the Detection of Dicyandiamide. *Analyst* **2014**, *139*, 5852-5857.

- 1  
2  
3  
4 (380) Wu, P.; Zhao, T.; Tian, Y.; Wu, L.; Hou, X. Protein-Directed Synthesis of Mn-Doped ZnS  
5 Quantum Dots: A Dual-Channel Biosensor for Two Proteins. *Chem-Eur. J.* **2013**, *19*,  
6 7473-7479.
- 7  
8 (381) Ren, H.-B.; Wu, B.-Y.; Chen, J.-T.; Yan, X.-P. Silica-Coated S<sub>2</sub>-Enriched Manganese-  
9 Doped ZnS Quantum Dots as a Photoluminescence Probe for Imaging Intracellular Zn<sup>2+</sup>  
10 Ions. *Anal. Chem.* **2011**, *83*, 8239-8244.
- 11  
12 (382) Wen, L.-N.; Xie, M.-X. Competitive Binding Assay for G-Quadruplex DNA and  
13 Sanguinarine Based on Room Temperature Phosphorescence of Mn-Doped ZnS Quantum  
14 Dots. *J. Photoch. Photobio. A* **2014**, *279*, 24-31.
- 15  
16 (383) Zhu, D.; Chen, Y.; Jiang, L.; Geng, J.; Zhang, J.; Zhu, J.-J. Manganese-Doped ZnSe  
17 Quantum Dots as a Probe for Time-Resolved Fluorescence Detection of 5-Fluorouracil.  
18 *Anal. Chem.* **2011**, *83*, 9076-9081.
- 19  
20 (384) Qian, Z. S.; Shan, X. Y.; Chai, L. J.; Chen, J. R.; Feng, H. Dual-Colored Graphene  
21 Quantum Dots-Labeled Nanoprobes/Graphene Oxide: Functional Carbon Materials for  
22 Respective and Simultaneous Detection of DNA and Thrombin. *Nanotechnology* **2014**,  
23 *25*, 415501-415501.
- 24  
25 (385) Zhang, L.; Zhang, Z. Y.; Liang, R. P.; Li, Y. H.; Qiu, J. D. Boron-Doped Graphene  
26 Quantum Dots for Selective Glucose Sensing Based on the "Abnormal" Aggregation-  
27 Induced Photoluminescence Enhancement. *Anal. Chem.* **2014**, *86*, 4423-4430.
- 28  
29 (386) Jin, T.; Imamura, Y. Applications of Highly Bright PbS Quantum Dots to Non-Invasive  
30 Near-Infrared Fluorescence Imaging in the Second Optical Window. *ECS J. Solid State Sc.*  
31 **2016**, *5*, R3138-R3145.
- 32  
33 (387) Gao, J.; Chen, K.; Xie, R.; Xie, J.; Yan, Y.; Cheng, Z.; Peng, X.; Chen, X. *In vivo* Tumor-  
34 Targeted Fluorescence Imaging Using Near-Infrared Non-Cadmium Quantum Dots.  
35 *Bioconjugate Chem.* **2010**, *21*, 604-609.
- 36  
37 (388) Gao, J.; Chen, K.; Miao, Z.; Ren, G.; Chen, X.; Gambhir, S. S.; Cheng, Z. Affibody-  
38 Based Nanoprobes for HER2-Expressing Cell and Tumor Imaging. *Biomaterials* **2011**,  
39 *32*, 2141-2148.
- 40  
41 (389) Gao, J.; Chen, K.; Luong, R.; Bouley, D. M.; Mao, H.; Qiao, T.; Gambhir, S. S.; Cheng,  
42 Z. A Novel Clinically Translatable Fluorescent Nanoparticle for Targeted Molecular  
43 Imaging of Tumors in Living Subjects. *Nano Lett.* **2012**, *12*, 281-286.
- 44  
45 (390) Pons, T.; Pic, E.; Lequeux, N.; Cassette, E.; Bezdetnaya, L.; Guillemin, F.; Marchal, F.;  
46 Dubertret, B. Cadmium-Free CuInS<sub>2</sub>/ZnS Quantum Dots for Sentinel Lymph Node  
47 Imaging with Reduced Toxicity. *ACS Nano* **2010**, *4*, 2531-2538.
- 48  
49 (391) Helle, M.; Cassette, E.; Bezdetnaya, L.; Pons, T.; Leroux, A.; Plenat, F.; Guillemin, F.;  
50 Dubertret, B.; Marchal, F. Visualisation of Sentinel Lymph Node with Indium-Based  
51

- 1  
2  
3 Near Infrared Emitting Quantum Dots in a Murine Metastatic Breast Cancer Model. *PLoS*  
4 *One* **2012**, *7*, e44433-e44433.  
5  
6 (392) Panthani, M. G.; Khan, T. A.; Reid, D. K.; Hellebusch, D. J.; Rasch, M. R.; Maynard, J.  
7 A.; Korgel, B. A. *In vivo* Whole Animal Fluorescence Imaging of a Microparticle-Based  
8 Oral Vaccine Containing (CuInSe<sub>x</sub>S<sub>2-x</sub>)/ZnS Core/Shell Quantum Dots. *Nano Lett.* **2013**,  
9 *13*, 4294-4298.  
10  
11 (393) Janowski, M.; Bulte, J. W. M.; Walczak, P. Personalized Nanomedicine Advancements  
12 for Stem Cell Tracking. *Adv. Drug Deliver. Rev.* **2012**, *64*, 1488-1507.  
13  
14 (394) Kawabori, M.; Kuroda, S.; Sugiyama, T.; Ito, M.; Shichinohe, H.; Houkin, K.; Kuge, Y.;  
15 Tamaki, N. Intracerebral, but Not Intravenous, Transplantation of Bone Marrow Stromal  
16 Cells Enhances Functional Recovery in Rat Cerebral Infarct: An Optical Imaging Study.  
17 *Neuropathology* **2012**, *32*, 217-226.  
18  
19 (395) Zhao, P.; Zheng, M.; Luo, Z.; Gong, P.; Gao, G.; Sheng, Z.; Zheng, C.; Ma, Y.; Cai, L.  
20 NIR-Driven Smart Theranostic Nanomedicine for On-Demand Drug Release and  
21 Synergistic Antitumour Therapy. *Sci. Rep.* **2015**, *5*, 14258-14258.  
22  
23 (396) Chen, Q.; Ke, H.; Dai, Z.; Liu, Z. Nanoscale Theranostics for Physical Stimulus-  
24 Responsive Cancer Therapies. *Biomaterials* **2015**, *73*, 214-230.  
25  
26 (397) Kang, S.; Bhang, S. H.; Hwang, S.; Yoon, J.-K.; Song, J.; Jang, H.-K.; Kim, S.; Kim, B.-  
27 S. Mesenchymal Stem Cells Aggregate and Deliver Gold Nanoparticles to Tumors for  
28 Photothermal Therapy. *ACS Nano* **2015**, *9*, 9678-9690.  
29  
30 (398) Dong, J.; Zink, J. I. Light or Heat? The Origin of Cargo Release from Nanoimpeller  
31 Particles Containing Upconversion Nanocrystals under IR Irradiation. *Small* **2015**, *11*,  
32 4165-4172.  
33  
34 (399) Oh, M. H.; Yu, J. H.; Kim, I.; Nam, Y. S. Genetically Programmed Clusters of Gold  
35 Nanoparticles for Cancer Cell-Targeted Photothermal Therapy. *ACS Appl. Mater. Inter.*  
36 **2015**, *7*, 22578-22586.  
37  
38 (400) Cao, M.; Wang, P.; Kou, Y.; Wang, J.; Liu, J.; Li, Y.; Li, J.; Wang, L.; Chen, C.  
39 Gadolinium(III)-Chelated Silica Nanospheres Integrating Chemotherapy and  
40 Photothermal Therapy for Cancer Treatment and Magnetic Resonance Imaging. *ACS*  
41 *Appl. Mater. Inter.* **2015**, *7*, 25014-25023.  
42  
43 (401) Guo, J.; Rahme, K.; Fitzgerald, K. A.; Holmes, J. D.; O'Driscoll, C. M. Biomimetic Gold  
44 Nanocomplexes for Gene Knockdown: Will Gold Deliver Dividends for Small Interfering  
45 RNA Nanomedicines? *Nano Res.* **2015**, *8*, 3111-3140.  
46  
47 (402) Jiang, T.; Song, J.; Zhang, W.; Wang, H.; Li, X.; Xia, R.; Zhu, L.; Xu, X. Au-Ag@Au  
48 Hollow Nanostructure with Enhanced Chemical Stability and Improved Photothermal  
49 Transduction Efficiency for Cancer Treatment. *ACS Appl. Mater. Inter.* **2015**, *7*, 21985-  
50 21994.  
51  
52  
53

- 1  
2  
3  
4 (403) Tian, Q.; Jiang, F.; Zou, R.; Liu, Q.; Chen, Z.; Zhu, M.; Yang, S.; Wang, J.; Wang, J.; Hu,  
5 J. Hydrophilic Cu<sub>9</sub>S<sub>5</sub> Nanocrystals: A Photothermal Agent with a 25.7% Heat Conversion  
6 Efficiency for Photothermal Ablation of Cancer Cells *in vivo*. *ACS Nano* **2011**, *5*, 9761-  
7 9771.
- 8  
9 (404) Chen, F.; Cai, W. Nanomedicine for Targeted Photothermal Cancer Therapy: Where Are  
10 We Now? *Nanomedicine-UK* **2015**, *10*, 1-3.
- 11  
12 (405) Chen, Y.; Hou, Z.; Liu, B.; Huang, S.; Li, C.; Lin, J. DOX-Cu<sub>9</sub>S<sub>5</sub>@mSiO<sub>2</sub>-PG Composite  
13 Fibers for Orthotopic Synergistic Chemo- and Photothermal Tumor Therapy. *Dalton T.*  
14 **2015**, *44*, 3118-3127.
- 15  
16 (406) Wang, S.; Riedinger, A.; Li, H.; Fu, C.; Liu, H.; Li, L.; Liu, T.; Tan, L.; Barthel, M. J.;  
17 Pugliese, G. *et al.* Plasmonic Copper Sulfide Nanocrystals Exhibiting Near-Infrared  
18 Photothermal and Photodynamic Therapeutic Effects. *ACS Nano* **2015**, *9*, 1788-1800.
- 19  
20 (407) Lu, F.; Wang, J.; Yang, L.; Zhu, J.-J. A Facile One-Pot Synthesis of Colloidal Stable,  
21 Monodisperse, Highly PEGylated CuS@mSiO<sub>2</sub> Nanocomposites for the Combination of  
22 Photothermal Therapy and Chemotherapy. *Chem. Commun.* **2015**, *51*, 9447-9450.
- 23  
24 (408) Liu, X.; Ren, Q.; Fu, F.; Zou, R.; Wang, Q.; Xin, G.; Xiao, Z.; Huang, X.; Liu, Q.; Hu, J.  
25 CuS@mSiO<sub>2</sub>-PEG Core-Shell Nanoparticles as a NIR Light Responsive Drug Delivery  
26 Nanoplatform for Efficient Chemo-Photothermal Therapy. *Dalton T.* **2015**, *44*, 10343-  
27 10351.
- 28  
29 (409) Lin, B.; Yao, X.; Zhu, Y.; Shen, J.; Yang, X.; Li, C. Multifunctional Gadolinium-Labeled  
30 Silica-Coated Core/Shell Quantum Dots for Magnetic Resonance and Fluorescence  
31 Imaging of Cancer Cells. *RSC Adv.* **2014**, *4*, 20641-20648.
- 32  
33 (410) Shen, J.; Li, Y.; Zhu, Y.; Yang, X.; Yao, X.; Li, J.; Huang, G.; Li, C. Multifunctional  
34 Gadolinium-Labeled Silica-Coated Fe<sub>3</sub>O<sub>4</sub> and CuInS<sub>2</sub> Nanoparticles as a Platform for *in*  
35 *vivo* Tri-Modality Magnetic Resonance and Fluorescence Imaging. *J. Mater. Chem. B*  
36 **2015**, *3*, 2873-2882.
- 37  
38 (411) Mou, J.; Liu, C.; Li, P.; Chen, Y.; Xu, H.; Wei, C.; Song, L.; Shi, J.; Chen, H. A Facile  
39 Synthesis of Versatile Cu<sub>2-x</sub>S Nanoprobe for Enhanced MRI and Infrared  
40 Thermal/Photoacoustic Multimodal Imaging. *Biomaterials* **2015**, *57*, 12-21.
- 41  
42 (412) Hu, R.; Wang, Y.; Liu, X.; Lin, G.; Tan, C. H.; Law, W.-C.; Roy, I.; Yong, K.-T. Rational  
43 Design of Multimodal and Multifunctional InP Quantum Dot Nanoprobes for Cancer: *In*  
44 *vitro* and *in vivo* Applications. *RSC Adv.* **2013**, *3*, 8495-8503.
- 45  
46 (413) Yang, Y.; Wang, J.; Li, X.; Lin, L.; Yue, X. A Near Infrared Fluorescent/Ultrasonic  
47 Bimodal Contrast Agent for Imaging Guided pDNA Delivery via Ultrasound Targeted  
48 Microbubble Destruction. *RSC Adv.* **2015**, *5*, 8404-8414.
- 49  
50  
51  
52  
53

- 1  
2  
3  
4 (414) Yang, Y.; Wu, H.; Shi, B.; Guo, L.; Zhang, Y.; An, X.; Zhang, H.; Yang, S. Hydrophilic  
5 Cu<sub>3</sub>BiS<sub>3</sub> Nanoparticles for Computed Tomography Imaging and Photothermal Therapy.  
6 *Part. Part. Syst. Char.* **2015**, *32*, 668-679.
- 7  
8 (415) Poulouse, A. C.; Veerananarayanan, S.; Mohamed, M. S.; Nagaoka, Y.; Aburto, R. R.;  
9 Mitcham, T.; Ajayan, P. M.; Bouchard, R. R.; Sakamoto, Y.; Yoshida, Y. *et al.* Multi-  
10 stimuli Responsive Cu<sub>2</sub>S Nanocrystals as Trimodal Imaging and Synergistic Chemo-  
11 Photothermal Therapy Agents. *Nanoscale* **2015**, *7*, 8378-8388.
- 12  
13 (416) Chen, F.; Hong, H.; Goel, S.; Graves, S. A.; Orbay, H.; Ehlerding, E. B.; Shi, S.; Theuer,  
14 C. P.; Nickles, R. J.; Cai, W. *In vivo* Tumor Vasculature Targeting of CuS@MSN Based  
15 Theranostic Nanomedicine. *ACS Nano* **2015**, *9*, 3926-3934.
- 16  
17 (417) Song, X.-R.; Wang, X.; Yu, S.-X.; Cao, J.; Li, S.-H.; Li, J.; Liu, G.; Yang, H.-H.; Chen, X.  
18 Co<sub>9</sub>Se<sub>8</sub> Nanoplates as a New Theranostic Platform for Photoacoustic/Magnetic  
19 Resonance Dual-Modal-Imaging-Guided Chemo-Photothermal Combination Therapy.  
20 *Adv. Mater.* **2015**, *27*, 3285-3291.
- 21  
22 (418) Moghimi, S. M.; Hunter, A. C.; Murray, J. C. Nanomedicine: Current Status and Future  
23 Prospects. *Faseb J.* **2005**, *19*, 311-330.
- 24  
25 (419) Jain, R. K.; Stylianopoulos, T. Delivering Nanomedicine to Solid Tumors. *Nat. Rev. Clin.*  
26 *Oncol.* **2010**, *7*, 653-664.
- 27  
28 (420) Huang, P.; Gao, Y.; Lin, J.; Hu, H.; Liao, H.-S.; Yan, X.; Tang, Y.; Jin, A.; Song, J.; Niu,  
29 G. *et al.* Tumor-Specific Formation of Enzyme-Instructed Supramolecular Self-  
30 Assemblies as Cancer Theranostics. *ACS Nano* **2015**, *9*, 9517-9527.
- 31  
32 (421) Chen, F.; Nayak, T. R.; Goel, S.; Valdovinos, H. F.; Hong, H.; Theuer, C. P.; Barnhart, T.  
33 E.; Cai, W. *In vivo* Tumor Vasculature Targeted PET/NIRF Imaging with TRC105(Fab)-  
34 Conjugated, Dual-Labeled Mesoporous Silica Nanoparticles. *Mol. Pharmaceut.* **2014**, *11*,  
35 4007-4014.
- 36  
37 (422) He, Q.; Kiesewetter, D. O.; Qu, Y.; Fu, X.; Fan, J.; Huang, P.; Liu, Y.; Zhu, G.; Liu, Y.;  
38 Qian, Z. *et al.* NIR-Responsive On-Demand Release of CO from Metal Carbonyl-Caged  
39 Graphene Oxide Nanomedicine. *Adv. Mater.* **2015**, *27*, 6741-6746.
- 40  
41 (423) Landgraf, L.; Christner, C.; Storck, W.; Schick, I.; Krumbein, I.; Daehring, H.; Haedicke,  
42 K.; Heinz-Herrmann, K.; Teichgraber, U.; Reichenbach, J. R. *et al.* A Plasma Protein  
43 Corona Enhances the Biocompatibility of Au@Fe<sub>3</sub>O<sub>4</sub> Janus Particles. *Biomaterials* **2015**,  
44 *68*, 77-88.
- 45  
46 (424) Song, J.; Huang, P.; Duan, H.; Chen, X. Plasmonic Vesicles of Amphiphilic Nanocrystals:  
47 Optically Active Multifunctional Platform for Cancer Diagnosis and Therapy. *Accounts*  
48 *Chem. Res.* **2015**, *48*, 2506-2515.
- 49  
50 (425) Boisselier, E.; Astruc, D. Gold Nanoparticles in Nanomedicine: Preparations, Imaging,  
51 Diagnostics, Therapies and Toxicity. *Chem. Soc. Rev.* **2009**, *38*, 1759-1782.
- 52  
53

- 1  
2  
3  
4 (426) Gao, J.; Gu, H.; Xu, B. Multifunctional Magnetic Nanoparticles: Design, Synthesis, and  
5 Biomedical Applications. *Accounts Chem. Res.* **2009**, *42*, 1097-1107.
- 6  
7 (427) Prato, M.; Kostarelos, K.; Bianco, A. Functionalized Carbon Nanotubes in Drug Design  
8 and Discovery. *Accounts Chem. Res.* **2008**, *41*, 60-68.
- 9  
10 (428) Shi, J.; Votruba, A. R.; Farokhzad, O. C.; Langer, R. Nanotechnology in Drug Delivery  
11 and Tissue Engineering: From Discovery to Applications. *Nano Lett.* **2010**, *10*, 3223-  
12 3230.
- 13  
14 (429) Roy, I.; Ohulchanskyy, T. Y.; Bharali, D. J.; Pudavar, H. E.; Mistretta, R. A.; Kaur, N.;  
15 Prasad, P. N. Optical Tracking of Organically Modified Silica Nanoparticles as DNA  
16 Carriers: A Nonviral, Nanomedicine Approach for Gene Delivery. *Proc. Natl. Acad. Sci.*  
17 *USA* **2005**, *102*, 279-284.
- 18  
19 (430) Huang, W.-C.; Chiang, W.-H.; Cheng, Y.-H.; Lin, W.-C.; Yu, C.-F.; Yen, C.-Y.; Yeh, C.-  
20 K.; Chern, C.-S.; Chiang, C.-S.; Chiu, H.-C. Tumortropic Monocyte-Mediated Delivery  
21 of Echogenic Polymer Bubbles and Therapeutic Vesicles for Chemotherapy of Tumor  
22 Hypoxia. *Biomaterials* **2015**, *71*, 71-83.
- 23  
24 (431) Moon, H.; Kang, J.; Sim, C.; Kim, J.; Lee, H.; Chang, J. H.; Kim, H. Multifunctional  
25 Theranostic Contrast Agent for Photoacoustics- and Ultrasound-Based Tumor Diagnosis  
26 and Ultrasound-Stimulated Local Tumor Therapy. *J. Control. Release* **2015**, *218*, 63-71.
- 27  
28 (432) Wu, P.-J.; Ou, K.-L.; Chen, J.-K.; Fang, H.-P.; Tzing, S.-H.; Lin, W.-X.; Chang, J.-Y.  
29 Methotrexate-Conjugated AgInS<sub>2</sub>/ZnS Quantum Dots for Optical Imaging and Drug  
30 Delivery. *Mater. Lett.* **2014**, *128*, 412-416.
- 31  
32 (433) Xu, Z.; Li, B.; Tang, W.; Chen, T.; Zhang, H.; Wang, Q. Glycopolypeptide-Encapsulated  
33 Mn-Doped ZnS Quantum Dots for Drug Delivery: Fabrication, Characterization, and *in*  
34 *vitro* Assessment. *Colloid. Surface. B* **2011**, *88*, 51-57.
- 35  
36 (434) Sanpui, P.; Pandey, S. B.; Chattopadhyay, A.; Ghosh, S. S. Incorporation of Gene Therapy  
37 Vector in Chitosan Stabilized Mn<sup>2+</sup>-Doped ZnS Quantum Dot. *Mater. Lett.* **2010**, *64*,  
38 2534-2537.
- 39  
40 (435) Klein, S.; Zolk, O.; Fromm, M. F.; Schroedl, F.; Neuhuber, W.; Kryschi, C.  
41 Functionalized Silicon Quantum Dots Tailored for Targeted siRNA Delivery. *Biochem.*  
42 *Bioph. Res. Co.* **2009**, *387*, 164-168.
- 43  
44 (436) Liu, S.; Shi, F.; Chen, L.; Su, X. Albumin Coated CuInS<sub>2</sub> Quantum Dots as a Near-  
45 Infrared Fluorescent Probe for NADH, and Their Application to an Assay for Pyruvate.  
46 *Microchim. Acta* **2014**, *181*, 339-345.
- 47  
48 (437) Tu, C.-C.; Chou, Y.-N.; Hung, H.-C.; Wu, J.; Jiang, S.; Lin, L. Y. Fluorescent Porous  
49 Silicon Biological Probes with High Quantum Efficiency and Stability. *Opt. Express*  
50 **2014**, *22*, 29996-30003.
- 51  
52  
53

- 1  
2  
3  
4 (438) Charron, G.; Stuchinskaya, T.; Edwards, D. R.; Russell, D. A.; Nann, T. Insights into the  
5 Mechanism of Quantum Dot-Sensitized Singlet Oxygen Production for Photodynamic  
6 Therapy. *J. Phys. Chem. C* **2012**, *116*, 9334-9342.
- 7  
8 (439) Kim, S. W.; Zimmer, J. P.; Ohnishi, S.; Tracy, J. B.; Frangioni, J. V.; Bawendi, M. G.  
9 Engineering InAs<sub>x</sub>P<sub>1-x</sub>/InP/ZnSe III-V Alloyed Core/Shell Quantum Dots for the Near-  
10 Infrared. *J. Am. Chem. Soc.* **2005**, *127*, 10526-10532.
- 11  
12 (440) Gao, X.; Liu, X.; Lin, Z.; Liu, S.; Su, X. CuInS<sub>2</sub> Quantum Dots as a Near-Infrared  
13 Fluorescent Probe for Detecting Thrombin in Human Serum. *Analyst* **2012**, *137*, 5620-  
14 5624.
- 15  
16 (441) Liu, J.-H.; Yang, S.-T.; Chen, X.-X.; Wang, H. Fluorescent Carbon Dots and  
17 Nanodiamonds for Biological Imaging: Preparation, Application, Pharmacokinetics and  
18 Toxicity. *Curr. Drug Metab.* **2012**, *13*, 1046-1056.
- 19  
20 (442) Aswathy, J.; Seethalekshmy, N.; Hiran, K.; Bindhu, M.; Manzoor, K.; Nair, S. V.; Menon,  
21 D. Mn-Doped Zinc Sulphide Nanocrystals for Immunofluorescent Labeling of Epidermal  
22 Growth Factor Receptors on Cells and Clinical Tumor Tissues. *Nanotechnology* **2014**, *25*,  
23 445102-445102.
- 24  
25 (443) Krejcova, L.; Hynek, D.; Kopel, P.; Rodrigo, M. A. M.; Tmejova, K.; Trnkova, L.; Adam,  
26 V.; Hubalek, J.; Kizek, R. Quantum Dots for Electrochemical Labelling of Neuramidinase  
27 Genes of H5N1, H1N1 and H3N2 Influenza. *Int. J. Electrochem. Sc.* **2013**, *8*, 4457-4471.
- 28  
29 (444) Krejcova, L.; Hynek, D.; Kopel, P.; Rodrigo, M. A. M.; Adam, V.; Hubalek, J.; Babula, P.;  
30 Trnkova, L.; Kizek, R. Development of a Magnetic Electrochemical Bar Code Array for  
31 Point Mutation Detection in the H5N1 Neuraminidase Gene. *Viruses-Basel* **2013**, *5*,  
32 1719-1739.
- 33  
34 (445) Ristic, B. Z.; Milenkovic, M. M.; Dakic, I. R.; Todorovic-Markovic, B. M.;  
35 Milosavljevic, M. S.; Budimir, M. D.; Paunovic, V. G.; Dramicanin, M. D.; Markovic, Z.  
36 M.; Trajkovic, V. S. Photodynamic Antibacterial Effect of Graphene Quantum Dots.  
37 *Biomaterials* **2014**, *35*, 4428-4435.
- 38  
39 (446) Baruah, S.; Ortinero, C.; Shipin, O. V.; Dutta, J. Manganese Doped Zinc Sulfide  
40 Quantum Dots for Detection of Escherichia Coli. *J. Fluoresc.* **2012**, *22*, 403-408.
- 41  
42 (447) Gu, L.; Ruff, L. E.; Qin, Z.; Corr, M.; Hedrick, S. M.; Sailor, M. J. Multivalent Porous  
43 Silicon Nanoparticles Enhance the Immune Activation Potency of Agonistic CD40  
44 Antibody. *Adv. Mater.* **2012**, *24*, 3981-3987.
- 45  
46 (448) Dhyani, H.; Ali, M. A.; Pal, S. P.; Srivastava, S.; Solanki, P. R.; Malhotra, B. D.; Sen, P.  
47 Mediator-Free Biosensor Using Chitosan Capped CdS Quantum Dots for Detection of  
48 Total Cholesterol. *RSC Adv.* **2015**, *5*, 45928-45934.
- 49  
50 (449) Liu, S.; Na, W.; Pang, S.; Su, X. Fluorescence Detection of Pb<sup>2+</sup> Based on the DNA  
51 Sequence Functionalized CdS Quantum Dots. *Biosens. Bioelectron.* **2014**, *58*, 17-21.

- 1  
2  
3  
4 (450) Breger, J.; Delehanty, J. B.; Medintz, I. L. Continuing Progress Toward Controlled  
5 Intracellular Delivery of Semiconductor Quantum Dots. *Wires. Nanomed. Nanobi.* **2015**,  
6 7, 131-151.
- 7 (451) Ferrari, M. Cancer Nanotechnology.: Opportunities and Challenges. *Nat. Rev. Cancer*  
8 **2005**, 5, 161-171.
- 9  
10 (452) Smith, A. M.; Duan, H.; Mohs, A. M.; Nie, S. Bioconjugated Quantum Dots for *in vivo*  
11 Molecular and Cellular Imaging. *Adv. Drug Deliver. Rev.* **2008**, 60, 1226-1240.
- 12 (453) Singh, R.; Lillard, J. W., Jr. Nanoparticle-Based Targeted Drug Delivery. *Exp. Mol.*  
13 *Pathol.* **2009**, 86, 215-223.
- 14 (454) Zhang, Y.; Hou, Z.; Ge, Y.; Deng, K.; Liu, B.; Li, X.; Li, Q.; Cheng, Z.; Ma, P. a.; Li, C.*et*  
15 *al.* DNA-Hybrid-Gated Photothermal Mesoporous Silica Nanoparticles for MR-  
16 Responsive and Aptamer-Targeted Drug Delivery. *ACS Appl. Mater. Inter.* **2015**, 7,  
17 20696-20706.
- 18 (455) Chen, G.; Wang, L.; Cordie, T.; Vokoun, C.; Eliceiri, K. W.; Gong, S. Multi-Functional  
19 Self-Fluorescent Unimolecular Micelles for Tumor-Targeted Drug Delivery and  
20 Bioimaging. *Biomaterials* **2015**, 47, 41-50.
- 21 (456) Win, K. Y.; Teng, C. P.; Ye, E.; Low, M.; Han, M.-Y. Evaluation of Polymeric  
22 Nanoparticle Formulations by Effective Imaging and Quantitation of Cellular Uptake for  
23 Controlled Delivery of Doxorubicin. *Small* **2015**, 11, 1197-1204.
- 24 (457) Wang, Z.; Liu, G.; Zheng, H.; Chen, X. Rigid Nanoparticle-Based Delivery of Anti-  
25 Cancer siRNA: Challenges and Opportunities. *Biotechnol. Adv.* **2014**, 32, 831-843.
- 26 (458) Zhang, L.; Gu, F. X.; Chan, J. M.; Wang, A. Z.; Langer, R. S.; Farokhzad, O. C.  
27 Nanoparticles in Medicine: Therapeutic Applications and Developments. *Clin.*  
28 *Pharmacol. Ther.* **2008**, 83, 761-769.
- 29 (459) Arias, J. L.; Reddy, L. H.; Couvreur, P. Fe<sub>3</sub>O<sub>4</sub>/Chitosan Nanocomposite for Magnetic  
30 Drug Targeting to Cancer. *J. Mater. Chem.* **2012**, 22, 7622-7632.
- 31 (460) Lin, J.; Li, Y.; Li, Y.; Wu, H.; Yu, F.; Zhou, S.; Xie, L.; Luo, F.; Lin, C.; Hou, Z.  
32 Drug/Dye-Loaded, Multifunctional PEG-Chitosan-Iron Oxide Nanocomposites for  
33 Methotrexate Synergistically Self-Targeted Cancer Therapy and Dual Model Imaging.  
34 *ACS Appl. Mater. Inter.* **2015**, 7, 11908-11920.
- 35 (461) Silva, A. K. A.; Luciani, N.; Gazeau, F.; Aubertin, K.; Bonneau, S.; Chauvierre, C.;  
36 Letourneur, D.; Wilhelm, C. Combining Magnetic Nanoparticles with Cell Derived  
37 Microvesicles for Drug Loading and Targeting. *Nanomed-Nanotechnol.* **2015**, 11, 645-  
38 655.
- 39 (462) Zrazhevskiy, P.; Sena, M.; Gao, X. Designing Multifunctional Quantum Dots for  
40 Bioimaging, Detection, and Drug Delivery. *Chem. Soc. Rev.* **2010**, 39, 4326-4354.
- 41  
42  
43  
44  
45  
46  
47  
48  
49  
50  
51  
52  
53

- 1  
2  
3  
4 (463) Chithrani, B. D.; Ghazani, A. A.; Chan, W. C. W. Determining the Size and Shape  
5 Dependence of Gold Nanoparticle Uptake into Mammalian Cells. *Nano Lett.* **2006**, *6*,  
6 662-668.
- 7  
8 (464) Nel, A. E.; Maedler, L.; Velegol, D.; Xia, T.; Hoek, E. M. V.; Somasundaran, P.; Klaessig,  
9 F.; Castranova, V.; Thompson, M. Understanding Biophysicochemical Interactions at the  
10 Nano-Bio Interface. *Nat. Mater.* **2009**, *8*, 543-557.
- 11  
12 (465) Kafshgari, M. H.; Harding, F. J.; Voelcker, N. H. Insights into Cellular Uptake of  
13 Nanoparticles. *Curr. Drug Deliv.* **2015**, *12*, 63-77.
- 14  
15 (466) Xie, J.; Xu, C.; Kohler, N.; Hou, Y.; Sun, S. Controlled PEGylation of Monodisperse  
16 Fe<sub>3</sub>O<sub>4</sub> Nanoparticles for Reduced Non-Specific Uptake by Macrophage Cells. *Adv. Mater.*  
17 **2007**, *19*, 3163-3166.
- 18  
19 (467) Gao, X. L.; Tao, W. X.; Lu, W.; Zhang, Q. Z.; Zhang, Y.; Jiang, X. G.; Fu, S. K. Lectin-  
20 Conjugated PEG-PLA Nanoparticles: Preparation and Brain Delivery after Intranasal  
21 Administration. *Biomaterials* **2006**, *27*, 3482-3490.
- 22  
23 (468) Miller-Kleinhenz, J. M.; Bozeman, E. N.; Yang, L. Targeted Nanoparticles for Image-  
24 Guided Treatment of Triple-Negative Breast Cancer: Clinical Significance and  
25 Technological Advances. *Wires. Nanomed. Nanobi.* **2015**, *7*, 797-816.
- 26  
27 (469) Bhirde, A. A.; Patel, V.; Gavard, J.; Zhang, G.; Sousa, A. A.; Masedunskas, A.; Leapman,  
28 R. D.; Weigert, R.; Gutkind, J. S.; Rusling, J. F. Targeted Killing of Cancer Cells *in vivo*  
29 and *in vitro* with EGF-Directed Carbon Nanotube-Based Drug Delivery. *ACS Nano* **2009**,  
30 *3*, 307-316.
- 31  
32 (470) Hsu, J.-C.; Huang, C.-C.; Ou, K.-L.; Lu, N.; Mai, F.-D.; Chen, J.-K.; Chang, J.-Y. Silica  
33 Nanohybrids Integrated with CuInS<sub>2</sub>/ZnS Quantum Dots and Magnetite Nanocrystals:  
34 Multifunctional Agents for Dual-Modality Imaging and Drug Delivery. *J. Mater. Chem.*  
35 **2011**, *21*, 19257-19266.
- 36  
37 (471) Mathew, M. E.; Mohan, J. C.; Manzoor, K.; Nair, S. V.; Tamura, H.; Jayakumar, R. Folate  
38 Conjugated Carboxymethyl Chitosan-Manganese Doped Zinc Sulphide Nanoparticles for  
39 Targeted Drug Delivery and Imaging of Cancer Cells. *Carbohydr. Polym.* **2010**, *80*, 442-  
40 448.
- 41  
42 (472) Park, J.-H.; Gu, L.; Von Maltzahn, G.; Ruoslahti, E.; Bhatia, S. N.; Sailor, M. J.  
43 Biodegradable Luminescent Porous Silicon Nanoparticles for *in vivo* Applications. *Nat.*  
44 *Mater.* **2009**, *8*, 331-336.
- 45  
46 (473) Xu, Z.; Wang, D.; Guan, M.; Liu, X.; Yang, Y.; Wei, D.; Zhao, C.; Zhang, H.  
47 Photoluminescent Silicon Nanocrystal-Based Multifunctional Carrier for pH-Regulated  
48 Drug Delivery. *ACS Appl. Mater. Inter.* **2012**, *4*, 3424-3431.
- 49  
50  
51  
52  
53

- 1  
2  
3  
4 (474) Hanada, S.; Fujioka, K.; Futamura, Y.; Manabe, N.; Hoshino, A.; Yamamoto, K.  
5 Evaluation of Anti-Inflammatory Drug-Conjugated Silicon Quantum Dots: Their  
6 Cytotoxicity and Biological Effect. *Int. J. Mol. Sci.* **2013**, *14*, 1323-1334.
- 7  
8 (475) Deepagan, V. G.; Sarmiento, B.; Menon, D.; Nascimento, A.; Jayasree, A.;  
9 Sreeranganathan, M.; Koyakutty, M.; Nair, S. V.; Rangasamy, J. *In vitro* Targeted  
10 Imaging and Delivery of Camptothecin Using Cetuximab-Conjugated Multifunctional  
11 PLGA-ZnS Nanoparticles. *Nanomedicine-UK* **2012**, *7*, 507-519.
- 12  
13 (476) Lin, W. J.; Chien, W. H. Peptide-Conjugated Micelles as a Targeting Nanocarrier for  
14 Gene Delivery. *J. Nanopart. Res.* **2015**, *17*, 349-349.
- 15  
16 (477) Naldini, L. Gene Therapy Returns to Centre Stage. *Nature* **2015**, *526*, 351-360.
- 17  
18 (478) Chen, G.; Zhu, J.-Y.; Zhang, Z.-L.; Zhang, W.; Ren, J.-G.; Wu, M.; Hong, Z.-Y.; Lv, C.;  
19 Pang, D.-W.; Zhao, Y.-F. Transformation of Cell-Derived Microparticles into Quantum-  
20 Dot-Labeled Nanovectors for Antitumor siRNA Delivery. *Angew. Chem. Int. Edit.* **2015**,  
21 *54*, 1036-1040.
- 22  
23 (479) Chinnathambi, S.; Chen, S.; Ganesan, S.; Hanagata, N. Binding Mode of CpG  
24 Oligodeoxynucleotides to Nanoparticles Regulates Bifurcated Cytokine Induction via  
25 Toll-Like Receptor 9. *Sci. Rep.* **2012**, *2*, 534-534.
- 26  
27 (480) Zhao, J.; Zhang, B.; Shen, S.; Chen, J.; Zhang, Q.; Jiang, X.; Pang, Z. CREKA Peptide-  
28 Conjugated Dendrimer Nanoparticles for Glioblastoma Multiforme Delivery. *J. Colloid*  
29 *Interf. Sci.* **2015**, *450*, 396-403.
- 30  
31 (481) Benezra, M.; Phillips, E.; Overholtzer, M.; Zanzonico, P. B.; Tuominen, E.; Wiesner, U.;  
32 Bradbury, M. S. Ultrasmall Integrin-Targeted Silica Nanoparticles Modulate Signaling  
33 Events and Cellular Processes in a Concentration-Dependent Manner. *Small* **2015**, *11*,  
34 1721-1732.
- 35  
36 (482) Thovhogi, N.; Sibuyi, N.; Meyer, M.; Onani, M.; Madiehe, A. Targeted Delivery Using  
37 Peptide-Functionalised Gold Nanoparticles to White Adipose Tissues of Obese Rats. *J.*  
38 *Nanopart. Res.* **2015**, *17*, 112-112.
- 39  
40 (483) Schaeffler, M.; Sousa, F.; Wenk, A.; Sitia, L.; Hirn, S.; Schleh, C.; Haberl, N.; Violatto,  
41 M.; Canovi, M.; Andreozzi, P. *et al.* Blood Protein Coating of Gold Nanoparticles as  
42 Potential Tool for Organ Targeting. *Biomaterials* **2014**, *35*, 3455-3466.
- 43  
44 (484) Chatterjee, S.; Mukherjee, T. K. Spectroscopic Investigation of Interaction between  
45 Bovine Serum Albumin and Amine-Functionalized Silicon Quantum Dots. *Phys. Chem.*  
46 *Chem. Phys.* **2014**, *16*, 8400-8408.
- 47  
48 (485) Gonda, K.; Miyashita, M.; Higuchi, H.; Tada, H.; Watanabe, T. M.; Watanabe, M.; Ishida,  
49 T.; Ohuchi, N. Predictive Diagnosis of the Risk of Breast Cancer Recurrence after  
50 Surgery by Single-Particle Quantum Dot Imaging. *Sci. Rep.* **2015**, *5*, 14322-14322.
- 51  
52  
53

- 1  
2  
3  
4 (486) Hu, K.; Wang, H.; Tang, G.; Huang, T.; Tang, X.; Liang, X.; Yao, S.; Nie, D. *In vivo*  
5 Cancer Dual-Targeting and Dual-Modality Imaging with Functionalized Quantum Dots.  
6 *J. Nucl. Med.* **2015**, *56*, 1278-1284.
- 7  
8 (487) Dong, H.; Dai, W.; Ju, H.; Lu, H.; Wang, S.; Xu, L.; Zhou, S.-F.; Zhang, Y.; Zhang, X.  
9 Multifunctional Poly(L-lactide)-Polyethylene Glycol-Grafted Graphene Quantum Dots  
10 for Intracellular MicroRNA Imaging and Combined Specific-Gene-Targeting Agents  
11 Delivery for Improved Therapeutics. *ACS Appl. Mater. Inter.* **2015**, *7*, 11015-11023.
- 12  
13 (488) Bu, L.; Ma, X.; Tu, Y.; Shen, B.; Cheng, Z. Optical Image-Guided Cancer Therapy. *Curr.*  
14 *Pharm. Biotechnol.* **2013**, *14*, 723-732.
- 15  
16 (489) Li, C.-H.; Kuo, T.-R.; Su, H.-J.; Lai, W.-Y.; Yang, P.-C.; Chen, J.-S.; Wang, D.-Y.; Wu, Y.-  
17 C.; Chen, C.-C. Fluorescence-Guided Probes of Aptamer-Targeted Gold Nanoparticles  
18 with Computed Tomography Imaging Accesses for *in vivo* Tumor Resection. *Sci. Rep.*  
19 **2015**, *5*, 15675-15675.
- 20  
21 (490) Xi, L.; Zhou, G.; Gao, N.; Yang, L.; Gonzalo, D. A.; Hughes, S. J.; Jiang, H.  
22 Photoacoustic and Fluorescence Image-Guided Surgery Using a Multifunctional Targeted  
23 Nanoprobe. *Ann. Surg. Oncol.* **2014**, *21*, 1602-1609.
- 24  
25 (491) Tan, L.; Wan, A.; Li, H. Synthesis of Near-Infrared Quantum Dots in Cultured Cancer  
26 Cells. *ACS Appl. Mater. Inter.* **2014**, *6*, 18-23.
- 27  
28 (492) Erogbogbo, F.; Tien, C. A.; Chang, C. W.; Yong, K. T.; Law, W. C.; Ding, H.; Roy, I.;  
29 Swihart, M. T.; Prasad, P. N. Bioconjugation of Luminescent Silicon Quantum Dots for  
30 Selective Uptake by Cancer Cells. *Bioconjugate Chem.* **2011**, *22*, 1081-1088.
- 31  
32 (493) Erogbogbo, F.; Liu, X.; May, J. L.; Narain, A.; Gladding, P.; Swihart, M. T.; Prasad, P. N.  
33 Plasmonic Gold and Luminescent Silicon Nanoplatfoms for Multimode Imaging of  
34 Cancer Cells. *Integr. Biol.* **2013**, *5*, 144-150.
- 35  
36 (494) Wang, J.; Liu, Y.; Peng, F.; Chen, C.; He, Y.; Ma, H.; Cao, L.; Sun, S. A General Route to  
37 Efficient Functionalization of Silicon Quantum Dots for High-Performance Fluorescent  
38 Probes. *Small* **2012**, *8*, 2430-2435.
- 39  
40 (495) Shah, J. P.; Gil, Z. Current Concepts in Management of Oral Cancer - Surgery. *Oral*  
41 *Oncol.* **2009**, *45*, 394-401.
- 42  
43 (496) Tagliabue, M.; Elrefaey, S. H.; Peccatori, F.; Favia, G.; Navach, V.; Pignataro, L.;  
44 Capaccio, P.; Venturino, M.; Tredici, S.; Alterio, D. *et al.* Tongue Cancer During  
45 Pregnancy: Surgery and More, a Multidisciplinary Challenge. *Crit. Rev. Oncol. Hemat.*  
46 **2016**, *98*, 1-11.
- 47  
48 (497) Bozec, A.; Ceruse, P. Head and Neck Oncologic Surgery Today and Tomorrow.  
49 *Oncologie* **2015**, *17*, 220-224.
- 50  
51  
52  
53

- 1  
2  
3  
4 (498) Li, Y.; Li, Z.; Wang, X.; Liu, F.; Cheng, Y.; Zhang, B.; Shi, D. *In vivo* Cancer Targeting  
5 and Imaging-Guided Surgery with Near Infrared-Emitting Quantum Dot Bioconjugates.  
6 *Theranostics* **2012**, *2*, 769-776.
- 7  
8 (499) Zhou, M.; Li, J.; Liang, S.; Sood, A. K.; Liang, D.; Li, C. CuS Nanodots with Ultrahigh  
9 Efficient Renal Clearance for Positron Emission Tomography Imaging and Image-Guided  
10 Photothermal Therapy. *ACS Nano* **2015**, *9*, 7085-7096.
- 11  
12 (500) Ashitate, Y.; Hyun, H.; Kim, S. H.; Lee, J. H.; Henary, M.; Frangioni, J. V.; Choi, H. S.  
13 Simultaneous Mapping of Pan and Sentinel Lymph Nodes for Real-Time Image-Guided  
14 Surgery. *Theranostics* **2014**, *4*, 693-700.
- 15  
16 (501) Rizvi, S. B.; Rouhi, S.; Taniguchi, S.; Yang, S. Y.; Green, M.; Keshtgar, M.; Seifalian, A.  
17 M. Near-Infrared Quantum Dots for HER2 Localization and Imaging of Cancer Cells. *Int.*  
18 *J. Nanomed.* **2014**, *9*, 1323-1337.
- 19  
20 (502) Li, C.; Cao, L.; Zhang, Y.; Yi, P.; Wang, M.; Tan, B.; Deng, Z.; Wu, D.; Wang, Q.  
21 Preoperative Detection and Intraoperative Visualization of Brain Tumors for More  
22 Precise Surgery: A New Dual-Modality MRI and NIR Nanoprobe. *Small* **2015**, *11*, 4517-  
23 4525.
- 24  
25 (503) Zimmer, J. P.; Kim, S. W.; Ohnishi, S.; Tanaka, E.; Frangioni, J. V.; Bawendi, M. G. Size  
26 Series of Small Indium Arsenide-Zinc Selenide Core-Shell Nanocrystals and Their  
27 Application to *in vivo* Imaging. *J. Am. Chem. Soc.* **2006**, *128*, 2526-2527.
- 28  
29 (504) Kotagiri, N.; Li, Z.; Xu, X.; Mondal, S.; Nehorai, A.; Achilefu, S. Antibody Quantum Dot  
30 Conjugates Developed via Copper-Free Click Chemistry for Rapid Analysis of Biological  
31 Samples Using a Microfluidic Microsphere Array System. *Bioconjugate Chem.* **2014**, *25*,  
32 1272-1281.
- 33  
34 (505) Shen, H.; Yuan, H.; Wu, F.; Bai, X.; Zhou, C.; Wang, H.; Lu, T.; Qin, Z.; Ma, L.; Li, L. S.  
35 Facile Synthesis of High-Quality CuInZn<sub>x</sub>S<sub>2+x</sub> Core/Shell Nanocrystals and Their  
36 Application for Detection of C-Reactive Protein. *J. Mater. Chem.* **2012**, *22*, 18623-18630.
- 37  
38 (506) Liu, S.; Shi, F.; Chen, L.; Su, X. Tyrosine-functionalized CuInS<sub>2</sub> Quantum Dots as a  
39 Fluorescence Probe for the Determination of Biothiols, Histidine and Threonine. *Analyst*  
40 **2013**, *138*, 5819-5825.
- 41  
42 (507) Tan, L.; Kang, C.; Xu, S.; Tang, Y. Selective Room Temperature Phosphorescence  
43 Sensing of Target Protein Using Mn-Doped ZnS QDs-Embedded Molecularly Imprinted  
44 Polymer. *Biosens. Bioelectron.* **2013**, *48*, 216-223.
- 45  
46 (508) Tan, L.; Huang, C.; Peng, R.; Tang, Y.; Li, W. Development of Hybrid Organic-Inorganic  
47 Surface Imprinted Mn-Doped ZnS QDs and Their Application as a Sensing Material for  
48 Target Proteins. *Biosens. Bioelectron.* **2014**, *61*, 506-511.
- 49  
50 (509) Yan, H.; Wang, H.-F. Turn-On Room Temperature Phosphorescence Assay of Heparin  
51 with Tunable Sensitivity and Detection Window Based on Target-Induced Self-Assembly  
52

- of Polyethyleneimine Capped Mn-Doped ZnS Quantum Dots. *Anal. Chem.* **2011**, *83*, 8589-8595.
- (510) Klostranec, J. M.; Xiang, Q.; Farcas, G. A.; Lee, J. A.; Rhee, A.; Lafferty, E. I.; Perrault, S. D.; Kain, K. C.; Chan, W. C. W. Convergence of Quantum Dot Barcodes with Microfluidics and Signal Processing for Multiplexed High-Throughput Infectious Disease Diagnostics. *Nano Lett.* **2007**, *7*, 2812-2818.
- (511) Lin, M.; Pei, H.; Yang, F.; Fan, C.; Zuo, X. Applications of Gold Nanoparticles in the Detection and Identification of Infectious Diseases and Biothreats. *Adv. Mater.* **2013**, *25*, 3490-3496.
- (512) Fialova, D.; Krejcova, L.; Janu, L.; Blazkova, I.; Krystofova, O.; Hynek, D.; Kopel, P.; Drbohlavova, J.; Konecna, M.; Vaculovicova, M. Flow Injection Electrochemical Analysis of Complexes of Influenza Proteins with CdS, PbS and CuS Quantum Dots. *Int. J. Electrochem. Sc.* **2013**, *8*, 10805-10817.
- (513) Ballesta, A.; Clairambault, J. Physiologically Based Mathematical Models to Optimize Therapies against Metastatic Colorectal Cancer: A Mini-Review. *Curr. Pharm. Design* **2014**, *20*, 37-48.
- (514) Ulmschneider, M. B.; Searson, P. C. Mathematical Models of the Steps Involved in the Systemic Delivery of a Chemotherapeutic to a Solid Tumor: From Circulation to Survival. *J. Control. Release* **2015**, *212*, 78-84.
- (515) Gordi, T.; Baillie, R.; Vuong, L. T.; Abidi, S.; Dueker, S.; Vasquez, H.; Pegis, P.; Hopper, A. O.; Power, G. G.; Blood, A. B. Pharmacokinetic Analysis of <sup>14</sup>C-Ursodiol in Newborn Infants Using Accelerator Mass Spectrometry. *J. Clin. Pharmacol.* **2014**, *54*, 1031-1037.
- (516) Spring, B. Q.; Rizvi, I.; Xu, N.; Hasan, T. The Role of Photodynamic Therapy in Overcoming Cancer Drug Resistance. *Photoch. Photobio. Sci.* **2015**, *14*, 1476-1491.
- (517) Shen, X.; Li, S.; Li, L.; Yao, S. Q.; Xu, Q. H. Highly Efficient, Conjugated-Polymer-Based Nano-Photosensitizers for Selectively Targeted Two-Photon Photodynamic Therapy and Imaging of Cancer Cells. *Chem-Eur. J.* **2015**, *21*, 2214-2221.
- (518) Termsarasab, U.; Yoon, I.-S.; Park, J.-H.; Moon, H. T.; Cho, H.-J.; Kim, D.-D. Polyethylene Glycol-Modified Arachidyl Chitosan-Based Nanoparticles for Prolonged Blood Circulation of Doxorubicin. *Int. J. Pharmaceut.* **2014**, *464*, 127-134.
- (519) Wang, X.; Yang, C.; Wang, C.; Guo, L.; Zhang, T.; Zhang, Z.; Yan, H.; Liu, K. Polymeric Micelles with  $\alpha$ -Glutamyl-Terminated PEG Shells Show Low Non-Specific Protein Adsorption and a Prolonged *in vivo* Circulation Time. *Mat. Sci. Eng. C-Mater.* **2016**, *59*, 766-772.
- (520) García, K. P.; Zarschler, K.; Barbaro, L.; Barreto, J. A.; O'Malley, W.; Spiccia, L.; Stephan, H.; Graham, B. Zwitterionic-Coated "Stealth" Nanoparticles for Biomedical

- 1  
2  
3 Applications: Recent Advances in Countering Biomolecular Corona Formation and  
4 Uptake by the Mononuclear Phagocyte System. *Small* **2014**, *10*, 2516-2529.
- 5  
6 (521) Huang, H.; Hernandez, R.; Geng, J.; Sun, H.; Song, W.; Chen, F.; Graves, S. A.; Nickles,  
7 R. J.; Cheng, C.; Cai, W. A Porphyrin-PEG Polymer with Rapid Renal Clearance.  
8 *Biomaterials* **2016**, *76*, 25-32.
- 9  
10 (522) Zhang, X. D.; Chen, J.; Min, Y.; Park, G. B.; Shen, X.; Song, S. S.; Sun, Y. M.; Wang, H.;  
11 Long, W.; Xie, J. Metabolizable Bi<sub>2</sub>Se<sub>3</sub> Nanoplates: Biodistribution, Toxicity, and Uses  
12 for Cancer Radiation Therapy and Imaging. *Adv. Funct. Mater.* **2014**, *24*, 1718-1729.
- 13  
14 (523) Lin, G.; Wang, X.; Yin, F.; Yong, K.-T. Passive Tumor Targeting and Imaging by Using  
15 Mercaptosuccinic Acid-Coated Near-Infrared Quantum Dots. *Int. J. Nanomed.* **2015**, *10*,  
16 335-345.
- 17  
18 (524) Keelan, J. A.; Leong, J. W.; Ho, D.; Iyer, K. S. Therapeutic and Safety Considerations of  
19 Nanoparticle-Mediated Drug Delivery in Pregnancy. *Nanomedicine-UK* **2015**, *10*, 2229-  
20 2247.
- 21  
22 (525) Docter, D.; Strieth, S.; Westmeier, D.; Hayden, O.; Gao, M.; Knauer, S. K.; Stauber, R. H.  
23 No King without a Crown-Impact of the Nanomaterial-Protein Corona on  
24 Nanobiomedicine. *Nanomedicine-UK* **2015**, *10*, 503-519.
- 25  
26 (526) Gaudin, A.; Lepetre-Mouelhi, S.; Mouglin, J.; Parrod, M.; Pieters, G.; Garcia-Argote, S.;  
27 Loreau, O.; Goncalves, J.; Chacun, H.; Courbebaisse, Y. Pharmacokinetics,  
28 Biodistribution and Metabolism of Squalenoyl Adenosine Nanoparticles in Mice Using  
29 Dual Radio-Labeling and Radio-HPLC Analysis. *J. Control. Release* **2015**, *212*, 50-58.
- 30  
31 (527) Knudsen, K. B.; Northeved, H.; Gjetting, T.; Permin, A.; Andresen, T. L.; Wegener, K.  
32 M.; Lam, H. R.; Lykkesfeldt, J. Biodistribution of Rhodamine B Fluorescence-Labeled  
33 Cationic Nanoparticles in Rats. *J. Nanopart. Res.* **2014**, *16*, 2221-2221.
- 34  
35 (528) Muhanna, N.; MacDonald, T. D.; Chan, H.; Jin, C. S.; Burgess, L.; Cui, L.; Chen, J.;  
36 Irish, J. C.; Zheng, G. Multimodal Nanoparticle for Primary Tumor Delineation and  
37 Lymphatic Metastasis Mapping in a Head-and-Neck Cancer Rabbit Model. *Adv. Healthc.*  
38 *Mater.* **2015**, *4*, 2164-2169.
- 39  
40 (529) Kim, S. H.; Lee, J. H.; Hyun, H.; Ashitate, Y.; Park, G.; Robichaud, K.; Lunsford, E.; Lee,  
41 S. J.; Khang, G.; Choi, H. S. Near-Infrared Fluorescence Imaging for Noninvasive  
42 Trafficking of Scaffold Degradation. *Sci. Rep.* **2013**, *3*, 1198-1198.
- 43  
44 (530) Choi, H. S.; Ipe, B. I.; Misra, P.; Lee, J. H.; Bawendi, M. G.; Frangioni, J. V. Tissue- and  
45 Organ-Selective Biodistribution of NIR Fluorescent Quantum Dots. *Nano Lett.* **2009**, *9*,  
46 2354-2359.
- 47  
48 (531) Deng, D.; Qu, L.; Achilefu, S.; Gu, Y. Broad Spectrum Photoluminescent Quaternary  
49 Quantum Dots for Cell and Animal Imaging. *Chem. Commun.* **2013**, *49*, 9494-9496.
- 50  
51  
52  
53

- 1  
2  
3  
4 (532) Xu, G.; Yong, K.-T.; Roy, I.; Kopwiththaya, A. FGF2-Labeled Semiconductor  
5 Nanocrystals as Luminescent Biolabels for Imaging Neuroblastoma Cells. *J. Biomed.*  
6 *Nanotechnol.* **2010**, *6*, 641-647.
- 7  
8 (533) Massey, M.; Wu, M.; Conroy, E. M.; Algar, W. R. Mind Your P's and Q's: The Coming of  
9 Age of Semiconducting Polymer Dots and Semiconductor Quantum Dots in Biological  
10 Applications. *Curr. Opin. Biotech.* **2015**, *34*, 30-40.
- 11  
12 (534) Volkov, Y. Quantum Dots in Nanomedicine: Recent Trends, Advances and Unresolved  
13 Issues. *Biochem. Bioph. Res. Co.* **2015**, *468*, 419-427.
- 14  
15 (535) Wu, T.; Zhang, T.; Chen, Y.; Tang, M. Research Advances on Potential Neurotoxicity of  
16 Quantum Dots. *J. Appl. Toxicol.* **2016**, *36*, 345-351.
- 17  
18 (536) Kovalenko, M. V. Opportunities and Challenges for Quantum Dot Photovoltaics. *Nat.*  
19 *Nanotechnol.* **2015**, *10*, 994-997.
- 20  
21 (537) Hougaard, K. S.; Campagnolo, L.; Chavatte-Palmer, P.; Tarrade, A.; Rousseau-Ralliard,  
22 D.; Valentino, S.; Park, M. V.; de Jong, W. H.; Wolterink, G.; Piersma, A. H. A  
23 Perspective on the Developmental Toxicity of Inhaled Nanoparticles. *Reprod. Toxicol.*  
24 **2015**, *56*, 118-140.
- 25  
26 (538) Wu, T.; Tang, M. Toxicity of Quantum Dots on Respiratory System. *Inhal. Toxicol.* **2014**,  
27 *26*, 128-139.
- 28  
29 (539) Kostarelos, K. In *Encyclopedia of Nanotechnology*; Bhushan, B., Eds.; Springer: The  
30 Netherlands, 2012; pp 2197-2200.
- 31  
32 (540) Xu, S.; Cui, J.; Wang, L. Recent Developments of Low-Toxicity NIR II Quantum Dots  
33 for Sensing and Bioimaging. *Trac-Trend. Anal. Chem.* **2015**, *80*, 149-155.
- 34  
35 (541) Soenen, S. J.; Abe, S.; Manshian, B. B.; Aubert, T.; Hens, Z.; De Smedt, S. C.;  
36 Braeckmans, K. The Effect of Intracellular Degradation on Cytotoxicity and Cell  
37 Labeling Efficacy of Inorganic Ligand-Stabilized Colloidal CdSe/CdS Quantum Dots. *J.*  
38 *Biomed. Nanotechnol.* **2015**, *11*, 631-643.
- 39  
40 (542) Hu, R.; Law, W.-C.; Lin, G.; Ye, L.; Liu, J.; Liu, J.; Reynolds, J. L.; Yong, K.-T.  
41 PEGylated Phospholipid Micelle-Encapsulated Near-Infrared PbS Quantum Dots for *in*  
42 *vitro* and *in vivo* Bioimaging. *Theranostics* **2012**, *2*, 723-733.
- 43  
44 (543) Zhang, B.; Wang, Y.; Hu, R.; Roy, I.; Yong, K.-T. In *Handbook of Photonics for*  
45 *Biomedical Engineering*; Ho, A. H.-P., Kim, D., Somekh, M. G., Eds.; Springer: The  
46 Netherlands, 2014.
- 47  
48 (544) Wang, M.; Liu, X.; Cao, C.; Wang, L. Highly Luminescent CuInS<sub>2</sub>-ZnS Nanocrystals:  
49 Achieving Phase Transfer and Nuclear Homing Property Simultaneously Through Simple  
50 TTAB Modification. *J. Mater. Chem.* **2012**, *22*, 21979-21986.

- 1  
2  
3  
4 (545) Huang, L.; Liao, M.; Chen, S.; Demillo, V. G.; Dupre, S. A.; Zhu, X.; Publicover, N. G.;  
5 Hunter Jr, K. W. A Polymer Encapsulation Approach to Prepare Zwitterion-Like,  
6 Biocompatible Quantum Dots with Wide pH and Ionic Stability. *J. Nanopart. Res.* **2014**,  
7 *16*, 2555-2555.  
8  
9 (546) Stern, S. T.; Zolnik, B. S.; McLeland, C. B.; Clogston, J.; Zheng, J.; McNeil, S. E.  
10 Induction of Autophagy in Porcine Kidney Cells by Quantum Dots: A Common Cellular  
11 Response to Nanomaterials? *Toxicol. Sci.* **2008**, *106*, 140-152.  
12  
13 (547) Chibli, H.; Carlini, L.; Park, S.; Dimitrijevic, N. M.; Nadeau, J. L. Cytotoxicity of  
14 InP/ZnS Quantum Dots Related to Reactive Oxygen Species Generation. *Nanoscale*  
15 **2011**, *3*, 2552-2559.  
16  
17 (548) Tang, S.; Allagadda, V.; Chibli, H.; Nadeau, J. L.; Mayer, G. D. Comparison of  
18 Cytotoxicity and Expression of Metal Regulatory Genes in Zebrafish (*Danio rerio*) Liver  
19 Cells Exposed to Cadmium Sulfate, Zinc Sulfate and Quantum Dots. *Metallomics* **2013**,  
20 *5*, 1411-1422.  
21  
22 (549) Ahire, J. H.; Behray, M.; Webster, C. A.; Wang, Q.; Sherwood, V.; Saengkrit, N.;  
23 Ruktanonchai, U.; Woramongkolchai, N.; Chao, Y. Synthesis of Carbohydrate Capped  
24 Silicon Nanoparticles and Their Reduced Cytotoxicity, *in vivo* Toxicity, and Cellular  
25 Uptake. *Adv. Healthc. Mater.* **2015**, *4*, 1877-1886.  
26  
27 (550) Wang, Q.; Bao, Y.; Zhang, X.; Coxon, P. R.; Jayasooriya, U. A.; Chao, Y. Uptake and  
28 Toxicity Studies of Poly-Acrylic Acid Functionalized Silicon Nanoparticles in Cultured  
29 Mammalian Cells. *Adv. Healthc. Mater.* **2012**, *1*, 189-198.  
30  
31  
32  
33  
34  
35  
36  
37  
38  
39  
40  
41  
42  
43  
44  
45  
46  
47  
48  
49  
50  
51  
52